



École doctorale : Sciences de l'Ingénierie et des Systèmes (ED ENGSYS) **Unités de recherche** : Laboratoire de Mécanique Multiphysique et Multiéchelle - UMR 9013 (Université de Lille, Centrale Lille, CNRS)

Thèse présentée par : Ncamisile Preetygirl Khanyile

Pour obtenir le grade de docteur de l'Université de Lille

Discipline/Spécialité : Mécanique, Énergétique, Génie des Procédés, Génie Civil

Titre de la thèse :

NUMERICAL SIMULATION OF CONTACT BY ISOGEOMETRIC ANALYSIS AND APPLICATION TO ACOUSTIC RADIATION OF FORCED-VIBRATING PLATES

SIMULATION NUMÉRIQUE DU CONTACT PAR L'ANALYSE ISOGÉOMÉTRIQUE ET APPLICATION AU RAYONNEMENT ACOUSTIQUE DES PLAQUES VIBRANTES

Soutenue le 6 octobre 2022 devant le jury suivant :

M. Mohamed ICHCHOU	Président	Professeur, LTDS, École Centrale de Lyon
M. Thomas Elguedj	Rapporteur	Professeur, INSA de Lyon
Mme. Emmanuelle ROUHAUD	Rapporteure	Professeur, Université de Technologie de
		Troyes
M. Michel RAOUS	Examinateur	Professeur émérite, Laboratoire de Méca-
		nique et d'Acoustique
M. Géry de Saxcé	Directeur	Professeur, LaMcube, Université de Lille
M. Philippe Dufrénoy	Co-directeur	Professeur, LaMcube, Polytech Lille
Mme. Ahlem Alia	Encadrante	Maître de conférences, LaMcube, Univer-
		sité de Lille

Abstract

Even with the advancement in Finite Element Method (FEM), contact remains a difficult problem to solve in engineering analysis. The main difficulty is due to the non-smoothness that arises from the inequality contact constraints as well as the geometric discontinuities inherent to classical FEM due to mesh generation in the standard C^0 Finite Elements Analysis (FEA). Specifically, the geometric discontinuities of the contact surface in FEM may lead to numerical instabilities including: (1) non-uniqueness of the unit normal vector and the projection point in the local contact search, and (2) non-physical oscillations of the contact forces especially in sliding conditions.

An interesting alternative to partially overcome these difficulties is the use of the Isogeometric Analysis (IGA). Indeed, in IGA the same smooth higher order basis are used for both the geometry and the analysis. The computational geometry is no longer approximate yielding a more robust discretization and more accurate results in comparison to traditional FE approaches. However, IGA is not without drawbacks, the most flagrant being: (1) lack of local refinement capabilities due to the tensor product nature of the NURBS/BSplines basis, (2) data structures non-compatible with existing FE codes due to higher inter-element continuity of the basis functions, (3) solution is sought at the control points which do not necessarily interpolate the geometry and thus can complicate the imposition of boundary conditions, and (4) the significant computation cost as a result of the high regularity of the basis functions.

In this thesis we aim to develop a numerical scheme based on the IGA that can accurately capture the contact stresses arising from surface/surface interactions. This numerical scheme addresses the above mentioned drawbacks in a holistic manner by developing a Bézier-based isogeometric finite element formulation that is both (1) suitable for existing FE codes and (2) able to compute the solution directly at the physical geometry. In doing this, the model then allows for the use of the more simple and more versatile, but accurate and more robust, Node to Surface (NTS) contact formulation frequently featured in FEM for practical applications. This numerical tool is then fully implemented using MATLAB.

The entry point of this Bézier-based method is BSplines basis functions. First, the method takes advantage of the Bézier extraction operator, which allows for an IGA element data structure to be incorporated into existing FE codes. This is then coupled with the full transformation method, using the inverted Bézier transformation matrix, to transform the computational domain from that of control mesh to the physical mesh similar to classical FEM. The Bézier transformation matrix, and its inverse, is computed once and stored for later use. Inspiration from the IGA collocation method is taken when selecting the locations at which the Bézier transformation matrix is computed.

The developed scheme is then used for the treatment of static contact problems (rigid/deformable and deformable/deformable contact interactions), with and without friction, and the numerical model validated against the analytical solution. The results obtained were in good agreement with the analytical solutions. Compared to classical FEM, the scheme was found to be more accurate, on a per-degree-of-freedom basis. Moreover, the model is extended for the treatment of impacted plates by a small sphere, using explicit time integration, to simulate both vibratory and acoustic response. Again, we found that even with a relatively coarse mesh, the IGA based scheme can sufficiently capture the characteristics of the plate response. Finally, the results obtained for the impacted plates were used to interpret and characterize the radiated acoustic field of forced vibrating plate, embedded in a rigid baffle, due to a moving force excitation.

Résumé

Malgré les avancées de la méthode des éléments finis (MEF), le contact reste un problème plus difficile à résoudre en analyse technique. La principale difficulté est attribuable à la non-lissabilité qui résulte des contraintes d'inégalité du contact ainsi qu'aux discontinuités géométriques inhérentes à la MEF classique en raison de la génération du maillage dans l'analyse par éléments finis (AEF) standard C^0 . Plus précisément, les discontinuités géométriques de la surface de contact dans la MEF peuvent conduire à des instabilités numériques, notamment : (1) la non-unicité du vecteur normal unitaire et du point de projection dans la détection locale du contact, et (2) des oscillations non physiques des pressions de contact, en particulier dans des conditions de frottement.

Une bonne alternative pour résoudre partiellement ces difficultés est l'utilisation de l'analyse isogéométrique (IGA). En effet, dans IGA, les mêmes bases lisses d'ordre supérieur sont utilisées à la fois pour la représentation de la géométrie et l'analyse. La géométrie de calcul n'est plus une approximation, ce qui permet une discrétisation plus robuste et des résultats plus précis par rapport aux approches d'éléments finis traditionnelles. Cependant, l'IGA n'est pas sans inconvénients, les plus flagrants étant : (1) le manque de capacités de raffinement local en raison à la nature de produit tensoriel de la base NURBS/BSplines, (2) les structures de données non compatibles avec les codes d'éléments finis existants en raison de la continuité inter-éléments plus élevée des fonctions de base, (3) la solution est recherchée aux points de contrôle qui n'interpolent pas nécessairement la géométrie et peuvent donc compliquer l'application des conditions aux limites, et (4) le coût de calcul significatif en raison de la régularité élevée des fonctions de base.

Dans cette thèse, nous visons à développer un schéma numérique basé sur l'IGA qui peut capturer avec précision les contraintes de contact provenant des interactions surface/surface. Ce schéma numérique aborde les inconvénients mentionnés ci-dessus d'une manière holistique en développant une formulation d'éléments finis isogéométriques basée sur Bézier qui est à la fois (1) adaptée aux codes d'éléments finis existants et (2) capable de calculer la solution directement à la géométrie physique. Ce faisant, le modèle permet d'utiliser la formulation du contact entre nœuds et surfaces (« NTS »), un formulation plus simple et plus polyvalente, mais plus précise et plus robuste, fréquemment utilisée dans les MEF pour des applications pratiques. Cet outil numérique est ensuite implémenté entièrement à l'aide de MATLAB.

Le point d'entrée de cette méthode basée sur Bézier est les fonctions de base BSplines. Tout d'abord, la méthode tire parti de l'opérateur d'extraction de Bézier, qui permet d'incorporer une structure de données d'éléments IGA dans les codes d'éléments finis existants. Ceci est ensuite couplé à la méthode de transformation complète, utilisant la matrice de transformation de Bézier inversée, pour transformer le domaine de calcul de celui de la maille de contrôle à la maille physique similaire à la MEF classique. La matrice de transformation de Bézier, et son inverse,

est calculée une fois et stokés pour une utilisation ultérieure. La sélection des emplacements où la matrice de transformation de Bézier est évaluée s'inspire de la méthode de collocation IGA.

Le schéma développé est ensuite utilisé pour le traitement de problèmes de contact statique (interactions de contact rigide/déformable et déformable/déformable), avec et sans frottement, et le modèle numérique est validé par rapport à la solution analytique. Les résultats obtenus étaient en bon accord avec les solutions analytiques. En comparaison avec la MEF standard, le schéma s'est avéré plus précis, sur une base par degré de liberté. De plus, le modèle est étendu au traitement des plaques impactées par une petite sphère, en utilisant une intégration temporelle explicite, pour simuler la réponse vibratoire et acoustique. Encore une fois, nous avons observé que même avec un maillage relativement grossier, le schéma basé sur l'IGA peut capturer suffisamment les caractéristiques de la réponse de la plaque. Enfin, les résultats obtenus pour les plaques impactées ont été utilisés pour interpréter et caractériser le rayonnement du champ acoustique d'une plaque vibrante forcée, encastrée dans un baffle rigide, en raison de l'excitation d'une force en mouvement.

Acknowledgements

This work was carried out within the *muFrein* (Mécanismes induits par frottement & Freinage) research group at the Laboratoire de Mecanique Multiphysique Multiechelle, under the supervision of M. Géry DE SAXCÉ and M. Philippe DUFRÉNOY. I would like to thank both for having proposed this thesis subject, their belief in me, their welcome to the team, and for providing all the support, freedom, and means necessary to conduct my work in good conditions. I would also like to thank them for their understanding, encouragements, their guidance and support and for always being available whenever needed.

I would like to extend my sincerest gratitude to Mme. Ahlem ALIA, my *encadrante*, for her patience, advice, rich and fruitful discussions, for her technical and programming competences, for her encouragements, and availability. Mostly, for generally caring. I am truly grateful for everything she has done for me.

I would also like extend my gratitude to the jury committee for this thesis: M. ICHCHOU for presiding and chairing the jury, the rapporteurs Mme. ROUHAUD and M. ELGEUDJ, as well as M. RAOUS for his review. Thank you to all for their availability, the interesting discussions, and for the constructive and critical feedback.

Lastly, I would like to thank my colleagues for the warm work environment and their assistance, both in the professional and personal capacity. To my mother Regina, my heavenly father Steven, family, close and far away, and to my friends, thank you for your support during the duration of this thesis.

Table of Contents

LI	St of	Figures	i de la companya de	7
Li	st of	Tables		xi
G	ener	al Intr	oduction	2
1	1.1 1.2		n vation	
	1.3 1.4	Obje	ctives	10
Ι	De	velopr	nent of Bézier-based Isogeometric Analysis	13
2	Fini	te Elem	ent Method based on Isogeometric Analysis	14
	2.1	Intro	$\operatorname{duction}$	14
	2.2	Isoge	eometric Analysis Fundamentals	. 15
		2.2.1	Bézier and Bernstein Polynomials	16
		2.2.2	BSplines	. 18
		2.2.3	Non Uniform Rational BSplines (NURBS)	2
		2.2.4	Bézier Extraction Operator	25
	2.3	The	Isogeometric Finite Element Formulation	28
		2.3.1	Bézier Elements and the Finite Element Framework	
		2.3.2	Bézier-based Isogeometric Analysis	3.
	2.4	Appl	ication of Isogeometric Analysis to Linear Statics	
		2.4.1	Problem Description	
		2.4.2	BSplines-based Isogeometric Analysis	3'
		2.4.3	Bézier-based Isogeometric Analysis	4
	2.5	Sum	mary	46
3	Cor	ntact Pro	oblem and its General Formulation	48
	3.1	Intro	duction	48
	3.2	Gove	erning Equations of the Contact Problem	50
		3 2 1	Problem Description	5

TABLE OF CONTENTS

		3.2.2	Normal Contact	53
			3.2.2.1 Contact Constraints in the Normal Direction	53
			3.2.2.2 The Closest Point Projection Algorithm	55
			3.2.2.3 Constitutive Laws for the Contact Interface in the Normal Direction	56
		3.2.3	Tangential Contact	57
			3.2.3.1 Stick Condition	58
			3.2.3.2 Sliding Condition	58
			3.2.3.3 Constitutive Laws in the Contact Interface for Tangential Contact	60
	3.3	The	Contact Initial Boundary Value Problem	62
		3.3.1	The Strong Form	62
		3.3.2	The Weak Form	63
			3.3.2.1 Variation of the Normal Gap	64
			3.3.2.2 Variation of the Tangential Slip	64
	3.4	Reg	larization of the Contact Constraints	65
		3.4.1	The Lagrange Multipliers Method	66
		3.4.2	The Penalty Method	66
	3.5	Con	act Interface Discretization Techniques	68
	3.6	Con	act Discretization with Bézier-based Isogeometric Analysis	69
		3.6.1	Discretization with Bézier Elements	69
		3.6.2	Local Time Discretization of the Friction Constitutive Law	71
		3.6.3	Linearization of the Contact Contributions	72
		3.6.4	Node to Surface Contact Discretization	74
		3.6.5	The Closest Point Projection Algorithm	77
		3.6.6	The Solution Procedure	77
			3.6.6.1 Newton-Raphson Technique	78
			3.6.6.2 Contact/Impact Algorithm : Global Time Discretization	78
			•	79
			3.6.6.4 Implicit Time Integration : The Newmark Method	81
	3.7	Sum	nary	81
п	Nı	ımeri	al Simulation of Contact Problems, Dynamics and Acous-	
		diatio		85
4	Stat	ic Con	act Problems	86
	4.1	Intro	duction	86
	4.2	App	cation to Frictionless Static Contact Problems	86
		4.2.1	Compression of an Elastic Ball by a Rigid Block on to a Rigid Foundation	87
			4.2.1.1 Axisymmetrical Formulation	88
			4.2.1.2 Numerical Solution	90
		4.2.2	Indentation of an Elastic Half-Space by a Rigid Flat Punch	97
			4.2.2.1 Plane Strain Formulation	97
			4.2.2.2 Numerical Solution	99

TABLE OF CONTENTS

	4.3	Numerical Simulation of Frictional Contact Problems	.03
		4.3.1 Compression of an Elastic Cylinder on a Rigid Substrate	.03
		4.3.2 Frictional Contact Between Deformable Bodies	107
	4.4	Summary	.14
5	Ехр	olicit Dynamics in Impact Simulation and Acoustic Radiation	l 16
	5.1	Introduction	16
	5.2	Problem Description	17
		5.2.1 Governing Equations	18
		5.2.2 Variational Formulation	121
	5.3	Discretization using Bézier Elements	121
	5.4	Numerical Solution	123
		5.4.1 The Dynamic Response	ا25
		5.4.2 The Acoustic Response	127
		5.4.3 Sensitivity Analysis	28
		5.4.3.1 Discretization Order	28
		5.4.3.2 Time Integration Scheme	١29
		5.4.3.3 Time Step Size	131
	5.5	Summary	.32
6	Acc	oustic Radiation of Forced-Vibrating Plates	L 34
	6.1	Introduction	34
	6.2	Application to Impacted Plates	135
		6.2.1 The Dynamic Response	136
		6.2.2 The Acoustic Response	138
		6.2.3 Comparison to Explicit Dynamics	40
	6.3	Application to Vibrating Plates due to a Moving Force	42
		6.3.1 The Dynamic Response	45
		6.3.2 The Acoustic Response	46
	6.4	Summary	.52
C	oncl	usion 1	5 5
7			155
1	Suii	nmary and Perspectives	.əə
A]	ppend	dix A Linearized Contact Integrals	L 60
A j	ppend	dix B Return Mapping Algorithm	L 63
A	ppeno	dix C Analytical Solution for Hertzian Contact Problems	66
	I	Classical Hertz Contact Between an Elastic Sphere and a Rigid Plane	166
	II	Rigid Punch on an Elastic Half-Space Contact Problem	167
	III	Compression of Elastic Cylinder on a Rigid Substrate	69
	$\mathbf{I}\mathbf{V}$	Hertz Contact Between Deformable Bodies	171

BIBLIOGRAPHY 172

List of Figures

1.1	Discretization of a mechanical problem [1]: from the continuum model which describes the mechanics of the problem, to its geometry CAD (smooth) representation, and finally the discrete form which makes up the computational model (Lagrange basis functions for the FEA model and NURBS/BSplines basis for the	
1.2	IGA model) of the problem with the isoparametric concept invoked Contact interface discretization techniques (Yastrebov, 2011): (a) Node to Node discretization, (b) Node to Surface discretization, and (c) Surface to Surface	4
	discretization	7
2.1	Hughes' Proposal: the link between actual geometry and analysis geometry for both IGA and classical FEM, ie, IGA refinement vs classical FEM	15
2.2	A construction of a cubic Bézier curve with the corresponding basis functions, $n_{cpts} = 4$, $p = 3$: (a) Bernstein basis functions, and (b) the constructed Bézier	
2.3	curve	17
2.4	$n_{cpts} = 4, p = 3.$	18
2.4	$\left\{0,0,0,\frac{1}{4},\frac{1}{2},\frac{3}{4},1,1,1\right\}, \text{ (b) } \Xi = \left\{0,0,0,\frac{1}{4},\frac{1}{4},\frac{1}{2},\frac{3}{4},1,1,1\right\}, \text{ (c) } \Xi = \left\{0,0,0,\frac{1}{4},\frac{1}{4},\frac{1}{2},\frac{1}{2},\frac{3}{4},\frac{1}{4},$	1, 1, 1
0.5	and (d) $\Xi = \{0, 0, 0, \frac{1}{4}, \frac{1}{4}, \frac{1}{2}, \frac{1}{2}, \frac{3}{4}, \frac{3}{4}, 1, 1, 1\}$.	20
2.5	Quadratic Bsplines curve with its basis functions, $\Xi = \{0, 0, 0, \frac{1}{3}, \frac{2}{3}, 1, 1, 1\}$ and $p = 2$: (a) a BSplines curve, and (b) BSplines basis functions	21
2.6	BSplines surface with $\Xi = \{0,0,0,0,\frac{1}{3},\frac{2}{3},1,1,1,1\}$ in both ξ,η -direction : (a) the control net, and (b) the constructed surface, cubic polynomials used in both	
	directions	21
2.7	Decomposition of BSplines curve onto composite/piecewise Bézier curves	22
2.8	Transformation of a BSplines curve into composite Bézier curves $(p=3)$: (a)	
	BSplines curve representation, and (b) the composite Bézier curve representation.	22
2.9	NURBS basis functions : (a) quadratic basis, $\Xi = \{0,0,0,1,1,1\}$, and (b) cubic	
	basis, $\Xi = \{0,0,0,0,1,1,1,1\}$	23
2.10	The comparison of NURBS and BSplines approximation of a quarter circle,	
	together with the analytical shape: (a) quadratic approximation, and (b) cubic	0.4
0.11	approximation.	24
2.11	BSplines reconstruction of a quarter circle using the exact interpolation : (a) quadratic approximation, and (b) cubic approximation	24
	- quaqradic addroximation, and (d) cubic addroximation	Z4

2.12	Comparison of IGA discretization technology with the classical FEM Lagrange polynomials: a) Lagrange basis functions, b) Bernstein basis functions, c) BSpline	9.0
2.13	basis functions, d) NURBS basis functions with $w = \{1,0.3,0.5,1\}$ Demonstration of Bézier extraction process of a 4-element BSplines quadratic	26
2 14	surface : (a) the original BSplines surface, and (b) extracted Bézier elements Different spaces considered in the context of BSplines-based IGA : from the	28
2.11	physical space to control space to parameter space finally the parent space	30
2.15	Demonstration of the Bézier extraction process on a single patch 2D quadratic $(p=2)$ BSplines surface containing 4 elements : \circ - BSplines control points, \bullet - additional control points generated for the Bézier elements	32
2.16	Bézier transformation from the control mesh (left) to the physical mesh (right).	32
2.17	Botella and Greville abscissae of BSplines basis supported on knot vector $\Xi = \left\{0,0,0,\frac{1}{3},\frac{1}{2},\frac{2}{3},1,1,1\right\}$	34
2.18	Schematic of 2D quarter of an annulus geometry under prescribed displacement load \bar{u}	37
2.19	BSplines computation points location with respect to the actual physical geometry, with a 3×3 mesh	40
2.20	Displacement field [m] obtained from the BSplines approach : (a) x -component of the diplacement field, and (b) y -component of the displacement field	40
2.21		41
2.22	Bézier control mesh and physical mesh comparison, $(p = 2, 3 \times 3\text{-elements})$: (a)	43
2.23	control mesh, and (b) physical mesh	
2.24	the displacement, and (b) y-component of the displacement	43
2.25	distribution, and (b) Von Mises stress distribution. Bézier based approach with Botella points solution fields: (a) x-component of	44
2.26	the displacement, and (b) y-component of the displacement	44
2.27	distribution, and (b) Von Mises stress distribution	45
	the BSplines-based approach and the Greville Bézier-based approach : (a) solver CPU time, and (b) stiffness matrix assembly CPU time	45
3.1	Deformation of a two-body contact system from the reference configuration to the current configuration : body Ω^1 the slave body, body Ω^2 the master body	51
3.2	Contacting points and their associated unit vector at the boundary	54
3.3 3.4	Master/Slave closest point projection	56
	based on geometric enforcement of the non penetration condition; (b) non-linear constitutive law (1) and a linear regularized law (corresponding to the penalty	
	method)(2)	58

3.5	Relative motion of the projection point $\bar{\mathbf{x}}^2$ of the slave point on the master surface, from a time t_0 to a final time t_n	59
3.6	Non-smooth Coulomb's friction law including the geometrical enforcement of the	
		61
3.7	v - 5	67
3.8	NTS discretization for linear quadrilaterals elements : ♦ - slave nodes, • - master nodes, • closest point projection	74
4.1	A sphere compressed by a rigid block on to a rigid foundation	88
4.2	Coordinates and displacement degree of freedom of an axisymmetric model	89
4.3	The quarter circle model of the Hertz problem, it's boundary conditions, and the multiple patches used for the IGA model: (a) schematic of boundary conditions, and (b) patches for the IGA model	90
4.4	The Hertz problem quarter model contact pairs : the contact patch (bottom surface of the contact patch taken as the slave surface) and the master surface on	91
4.5	The displacement field obtained with a quadratic coarse mesh, $\varepsilon_N = 100E$: (a)	
4.6	r-component of the displacement, and (b) z-component of the displacement Stress field obtained with a quadratic coarse mesh, $\varepsilon_N = 100E$: (a) normal stress	92
	σ_{zz} distribution, and (b) Von Mises stress distribution	92
4.7 4.8	Penetration across the contact area - $4 \times 3 \times 3$ mesh with quadratic elements Comparison between the analytical and numerical contact pressure (normalized)	93
4.9	The effect of the penalty parameter ε_N at fixed mesh resolution - $4 \times 3 \times 3$ quadratic mesh: (a) the evolution of relative error on the contact radius with	94
	increasing ε_N , (b) the evolution of relative error on the contact pressure with increasing ε_N , and (c) the penetration levels at different ε_N	95
4.10	The effect of the penalty parameter ε_N at fixed mesh resolution - $4 \times 3 \times 3$ cubic mesh: (a) the evolution of relative error on the contact radius with increasing ε_N , (b) the evolution of relative error on the contact pressure with increasing ε_N ,	
	and (c) the penetration levels at different ε_N	95
4.11	Indentation process of a rigid punch into an elastic half-space	98
4.12	2D half model of the rigid punch on to an elastic half space contact problem	99
4.13	The rigid punch on an elastic half-space numerical model generated using quadratic	
	Bézier elements : (a) Bézier elements, and (b) mapping of computation points 1	.00
4.14	The displacement field of the indentation process, $p=2$ and $\varepsilon_N=100E$: (a) x	
	component of the displacement, and (b) y component of the displacement 1	.00
4.15	Stress distribution in the normal direction for the indentation process, $p=2$ and	I () 1
/ 16		LO1 LO1
4.10	voil vides suces distribution for the indelitation process, $p-2$ and $\epsilon_N=100E$.	LUJ

4.17	Comparison of the numerical solution, in terms of the contact pressure (normalized with the analytical mean contact pressure p_m) distribution across the contact zone, to the analytical solution for the quadratic and cubic case, $\varepsilon_N = 100E$: (a)	
4.18	quadratic mesh, and (b) cubic mesh	102
	the surface outside the punch, to the analytical solution for the quadratic and	100
1.10	cubic case, $\varepsilon_N = 100E$: (a) quadratic mesh, and (b) cubic mesh	102
4.19 4.20	•	
4.21	an elastic cylinder and a rigid substrate	105
4.22	distribution, σ_{22} , and (d) tangential stress distribution, σ_{12}	106
	(c) 8×2 quadratic mesh, and (d) 8×6 cubic mesh	107
4.23	Schematic of the frictional contact between a deformable cylinder and a deformable	-0,
	plane.	108
4.24	Loading history for contact interaction in fig. 4.23	
4.25	The Bézier mesh of the problem in fig. 4.23 (visualization of elements and the actual location of the computation nodes), 12×6 mesh for the slave body, 7×4 mesh for the master body: (a) visualization of the Bézier elements in the mesh,	
4.26	Analytical contact pressure for the Hertz contact of the deformable cylinder on a	
4.27	deformable plane - see appendix IV	
4.28	of the displacement	110
	and (b) tangential stress, σ_{12} , distribution	111
4.29	Comparison of the analytical and numerical contact pressure (normalized) for the Hertz contact between the deformable bodies	111
4.30	Comparison of the analytical and numerical normal contact pressure (normalized)	
4.31	for the Hertz contact between the deformable bodies. Comparison of the analytical and numerical tangential contact pressure (normalized) for the Hertz contact between the deformable bodies.	112113
5.1	Schematic of the impact of an elastic plate (embedded on a rigid baffle) by an	_3
	elastic sphere: \mathbf{v}_0 the initial velocity of the sphere, and (r,ψ) are the polar coordinates defining the acoustic field point P	118

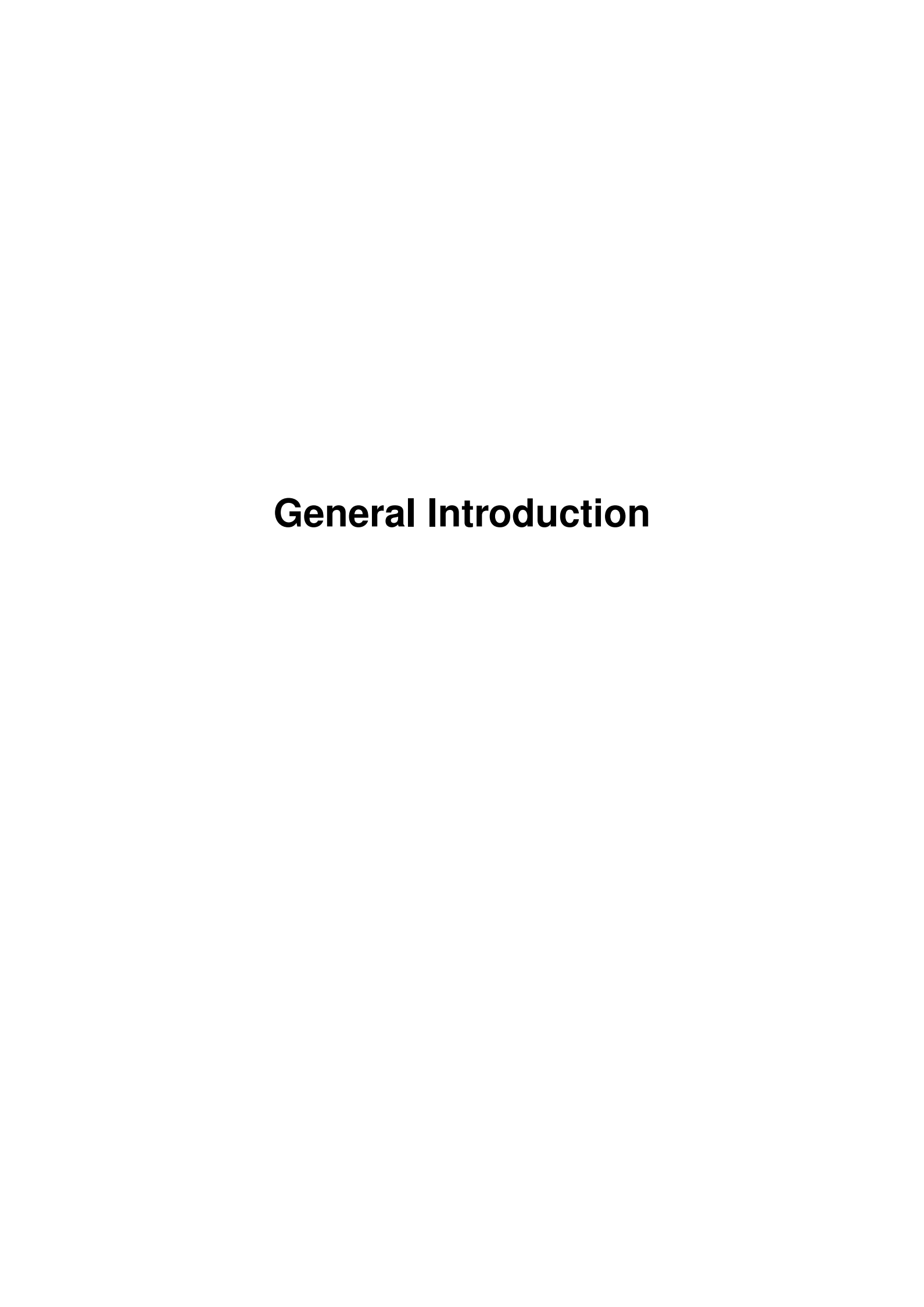
5.2	(a) Mesh of the plate and sphere due to Bézier extraction, (b) sphere zoom and	
	•	124
5.3	Variation of the transverse displacement with respect to the radial distance for	
	1	125
5.4	Variation of the transverse displacement (left) and velocity (right) for the impact	
	point (a,b), and two points located at 30 mm (c-d), and 130 mm (e-f) from the	
ر ر	• •	126
5.5	Acoustic pressure at field points located at $z=60$ mm and polar angles $\psi=$	40-
- 0		127
5.6	Effect of the number of nodes <i>nd</i> per patch edge of the plate on : (a) the relative	
	error committed on the 46 first natural frequencies of the plate for quadratic	
	(n=2) and cubic $(n=3)$ elements, the acoustic pressure (b) on-axis and (c)	100
K 7		129
5.7	Variation of the transverse displacement (left) and velocity (right) for the impact point (a,b) and at 30 mm from the impact point (c-d) calculated by central	
	difference scheme (CD), Noh and Bathe (NB), and Kim and Lee (KL) schemes.	
		131
5.8	Effect of the time step on the contact force between plate and sphere (a-b) and	191
0.0	the acoustic pressure (c-d) when Noh and Bathe (NB) (left) and Kim and Lee	
		132
6.1	Illustration of the problems considered: (a) the impact force computed using	
		135
6.2	Variation, with respect to time, of the transverse displacement (left) and velocity	
0.0		137
6.3	Variation, with respect to the radial distance r , of the transverse displacement of	190
C 1	1	138
6.4	Variation, with respect to time, of the acoustic pressure for field points located at	190
6.5	a distance $z = 50$ mm from the plate	139
0.0	a distance $R = 50$ mm from the plate center with different polar angles ψ	1/10
6.6	Sound pressure distribution in the xz -plane at the vicinity of the plate at three	110
0.0		141
6.7	Acoustic pressure on-axis at $z = 60$ mm using central difference scheme (CD),	111
0.,	Noh and Bathe (NB), and Kim and Lee (KL) schemes in comparison to pressure	
	(Ref) due to applying Ross and Ostiguy contact force directly to the plate without	
	considering the sphere into calculations. (CD), (NB) and (KL) curves are the same.	142
6.8	Contact force between sphere and plate (a) and the effective penetration (b) when	
	central difference (CD), Noh and Bathe (NB), and Kim and Lee (KL) schemes are	
	used. (Ref) is the Ross and Ostiguy contact force. (CD), (NB) and (KL) curves	
	are the same.	143

6.9	Illustration of the problems considered: plate subjected to a moving force.	
	v_m denotes the velocity of the imposed moving force F_{imp} , (r,ψ) are the polar	
	coordinates of the field point belonging to the xz -plane	144
6.10	Variation, with respect to x (left, $y = 0$ mm) and y (right, $x = 0$ mm), of the	
	transverse displacement of the plate for different instants	145
6.11	Transversal displacement distribution of plate at different instants after the	
	movement of the force start. Displacement is given in mm	146
6.12	Variation, with respect to time, of the transverse displacement (left) and velocity	
	(right) of three points on the x-axis of the plate $(y = 0 \text{ mm})$	147
6.13	Variation, with respect to x (left, $y = 0$ mm) and y (right, $x = 0$ mm), of the	
	transverse displacement of the plate for $t = 6.56 \ \mu s.$	148
6.14		
	located on the plate axis at a distance $R=25$ mm from its center ($\psi_0=0^{\circ}$) and	
	(b) its corresponding normalized spectrum with respect to its maximum value.	
	The corresponding plate natural frequencies are indicated by rows in (b) for the	
	more significant peaks.	148
6.15	Variation, with respect to time, of the acoustic pressure for different field points	
0.20	located in xz -plane at a distance $R=25$ mm from the plate center. $\psi_1=30^\circ$,	
	$\psi_2 = 60^\circ$, $\psi_3 = 89^\circ$. The negative values of the angle ψ designate the negative	
		149
6.16	Normalized spectrum, with respect to its maximum value, of the pressure of two	110
0.10	field points located at a distance of 25 mm from the plate center where $\psi_3 = 89^{\circ}$.	
	Some plate natural frequencies are indicated by rows in (a)	150
6.17	Sound pressure distribution in the xz-plane at the vicinity plate at (a) $t = 9.4 \mu s$;	100
0.11	(b) $t = 10.2 \ \mu s$; (c) $t = 14.9 \ \mu s$ after the force start to move. The circles show	
	the current positions of the force. Pressure is given in Pa	151
6 18	Sound pressure distribution in the xz -plane at different instants during the	101
0.10	movement of the force (a) and after its passage (b-d). Pressure is given in Pa	151
6 10		191
0.19	Effect of the time step ($\Delta t_2 = 10\Delta t_1$) on the pressure : (a-c) Variation, with	
	respect to time, of the acoustic pressure for three field points located on xz -plane at a distance $R = 25$ mm from its center $(a/a = 0)^{\circ}$ and (a/b) their	
	at a distance $R=25$ mm from its center ($\psi_0=0^\circ$, $\psi_3=89^\circ$) and (d-f) their	150
<i>c</i> 20	corresponding normalized spectra with respect to their maximum values	152
6.20		
	acoustic pressure for three field points located on xz -plane at a distance $R = \frac{1}{2} \sum_{n=1}^{\infty} \frac{1}{n} \sum_{n=1}^{\infty} 1$	
	25 mm from its center ($\psi_0 = 0^\circ$, $\psi_3 = 89^\circ$) and (d-f) their corresponding	150
	normalized spectra with respect to their maximum values	153
B.1	Unregularized Coulomb's law of friction: (a) Evolution of the frictional traction	
	$\ \mathbf{t}_T\ $ with the tangential slip velocity $\ \dot{\mathbf{g}}_T\ $, and (b) Coulomb's cone	163
B.2	One dimensional schematic of the elasto-perfectly-plastic constitutive law, with	
		164
B.3	Return mapping algorithm in the stress space: (a) initial state - trial state, (b)	
	trial state - solution state	165

C.1	The normalized contact pressure of the sphere across the contact area	167
C.2	Indentation by a cylindrical flat punch	167
C.3	Analytical contact pressure distribution across the contact area due to the inden-	
	tation of the elastic half space	168
C.4	Contact configuration : stick zone and slip region	169
C.5	Purely stick contact analytical solution	170

List of Tables

2.1	Support for the basis functions (Bézier, BSplines/NURBS), $p = 3$	25
2.2	Bézier equivalent Greville points computed from knot vectors $\Xi = \{0,0,0,\frac{1}{3},\frac{1}{2},\frac{2}{3},1,1,1\}$	
	for $p = 2$ and $\Xi = \{0,0,0,0,\frac{1}{3},\frac{1}{2},\frac{2}{3},1,1,1,1\}$ for $p = 3$	34
2.3	Bézier equivalent Botella points computed from knot vectors $\Xi = \{0,0,0,\frac{1}{3},\frac{1}{2},\frac{2}{3},1,1,1\}$	
	for $p = 2$ and $\Xi = \{0,0,0,0,\frac{1}{3},\frac{1}{2},\frac{2}{3},1,1,1,1\}$ for $p = 3$	35
4.1	Properties of the different meshes used for the IGA computation and the results	
	obtained	93
4.2	The effect of the penalty parameter on the numerical results of the Abaqus FEA model, in terms of the maximum contact pressure and the permitted penetration,	
	of the classical friction-less Hertz contact problem	96
4.3	Results obtained from Abaqus (default penalty stiffness) for the classical friction-	
	less Hertz contact problem	97
4.4	The effects of mesh refinement on the numerical solution for the frictional contact	
4 =	between an elastic cylinder and a rigid plane	105
4.5	The contact area semi width a and the stick zone semi width c (contact between	110
4.6	a deformable cylinder on an elastic plane) obtained using the Bézier-based method. Results obtained in terms of the contact area semi width a and the stick zone	112
	semi width c (contact between a deformable cylinder on an elastic plane) from	119
	both the Bézier-based method and using Abaqus	113
5.1	Input parameters and mechanical characteristics of the impacted plate and the	
	impactor sphere as well as the radiating medium	123
B.1	Analogies between friction and plasticity constitutive relations, with γ the plastic	
	multiplier/slip [2]	164
C.1	Input parameters for the contact between an elastic sphere and a rigid plane	166
C.2	Input parameters for the contact between a rigid punch and an elastic half space.	
C.3	Input parameters for the frictional contact problem between an elastic cylinder	
	and a rigid plane	169
C.4	Input parameters for the frictional Hertz contact between two deformable bodies.	171



1

Introduction

1.1 Motivation

Contact is the notion of interactions between separate bodies coming in touch and exchanging loads and energy. This exchange happens without the bodies becoming rigidly attached. Take for instance a simple action such as holding a pen or this manuscript in your hands, there is a contact interaction taking place between your hand and a pen or the pages and fingers. In the case of a book, to page through the document, a certain amount of contact force is required. This contact force between the pages and hand surface will depend on factors such as properties of the surface and material of the pages, i.e. choice of paper, the application of this contact (the point at which fingers interact with the paper), and the angle of application of the force [1]. Moreover, a certain degree of friction is required to prevent slip. Indeed, contact is a phenomenon of every day life, i.e. walking is impossible without frictional contact, in the same way that cars and trains rely on this type of grip to propel themselves forwards [3].

Mechanical loads arise from an interaction between two mechanical entities in contact with each other, for this reason contact interactions practically exist in all structural and mechanical systems [2–6]. These contact interactions may be intentional, such as rolling-element bearings that transmit loading while reducing friction in moving machinery, bridge like structures load carrying capacity, tractive effort generated in wheel/rail contact, braking components, to name a few. Even though these interactions are intentional, they may yet, inadvertently, lead to adverse effects as a result of instabilities (vibrations) specifically in dynamic systems. These include: (1) friction-induced vibrations which may result in squeal, a phenomena common in sliding contact, and also may lead into chatter, and chaos [7–9], (2) structural vibrations leading to fatigue damage failure, (3) impact like events leading to noise pollution that can be detrimental not only to the structure (in terms of operational safety), but also harmful to the environment and hazardous to human health and safety [9–11].

On the other hand we may have unintentional contact interactions. These can include actions like bird strikes on aeroplanes, vehicle crashes, or accidental interactions such as stone striking a

window. Whether we are concerned with increasing efficiency in the case of intentional contact or decreasing the adverse effects if the interaction is unintentional or in the case of dynamic and frictional instabilities, the contact problem, its comprehension and resolution, is of high importance. Essentially, to characterize these mechanical systems in engineering analysis requires the understanding of the contact process.

The phenomenon of contact is governed by complex physics due to its multi-scale and multi-physical nature. Contact constraints arising from this interaction are a set of inequalities and cannot simply be replaced by ordinary boundary conditions imposed on the contacting surfaces [2, 6]. Moreover, the contact interface cannot be considered as an internal surface. This then leads to a great deal of difficulty in deriving analytical solutions, that is if they exist. However, the existence and great strides that have been made in computer aided design, more specifically the numerical technique Finite Element Method (FEM), have allowed for the resolution of these complex problems with somewhat relative ease, however complex the process can be.

In standard Finite Elements Analysis (FEA) the geometry is packaged in CAD (Computer Aided Design) systems and the mesh is generated from the CAD data - effectively the geometry is replaced by an approximate one [12, 13]. In doing this, the geometric approximation which is essential in the mesh generation can bring about accuracy problems. A major contributing factor to these inaccuracies is the lower order polynomial approximation that are usually employed in standard FEA. Naturally one would think to remedy this limitation increasing the order of the polynomials might provided a fix. Szabos et al. [14] explored the use of fixed higher order polynomials (p-FEM) and found that as the solution polynomial order is increased, the error plateaus at some point and can not be reduced further. This can be counter-intuitive as increasing the polynomial order also increases the computation cost. For most engineering problems, like contact problems, the boundaries of the bodies studied are an important location with regards to the physics of the problem.

Often times in classical FEM, boundaries are hot-spots for geometric errors. These geometric errors arise from the facetization induced by meshing in standard C^0 FEA - see figure 1.1: the smooth CAD geometry, typically described with NURBS/BSplines basis is converted into simple polygons using the Lagrange basis approximation. Invoking the isoparametric concept, the unknown solution fields, such as the displacement field \mathbf{u} , are approximated in the same way. To capture the boundaries of the geometry accurately then a fine discretization is needed which leads to prohibitively large numerical models. These require tremendous computation resources in terms of storage and resolution time. A good quality mesh is time consuming and costly in terms of memory resources. Moreover the facetization of the contact surface can lead to numerical instabilities, sub-optimal convergence rates, non-physical behavior and jumps in velocity in the case of dynamic problems [15, 16]. To remedy this, contact formulation can be enriched with smoothing techniques. Several contact smoothing techniques have been used in literature including traditional splines, Bézier surfaces, and NURBS enrichments [6, 15–21], however this can lead to more complex and computationally inefficient methods [22].

Even with the advancement of numerical techniques, particularly in FEM, contact remains a

Continuum Model → Geometry → Computational Model

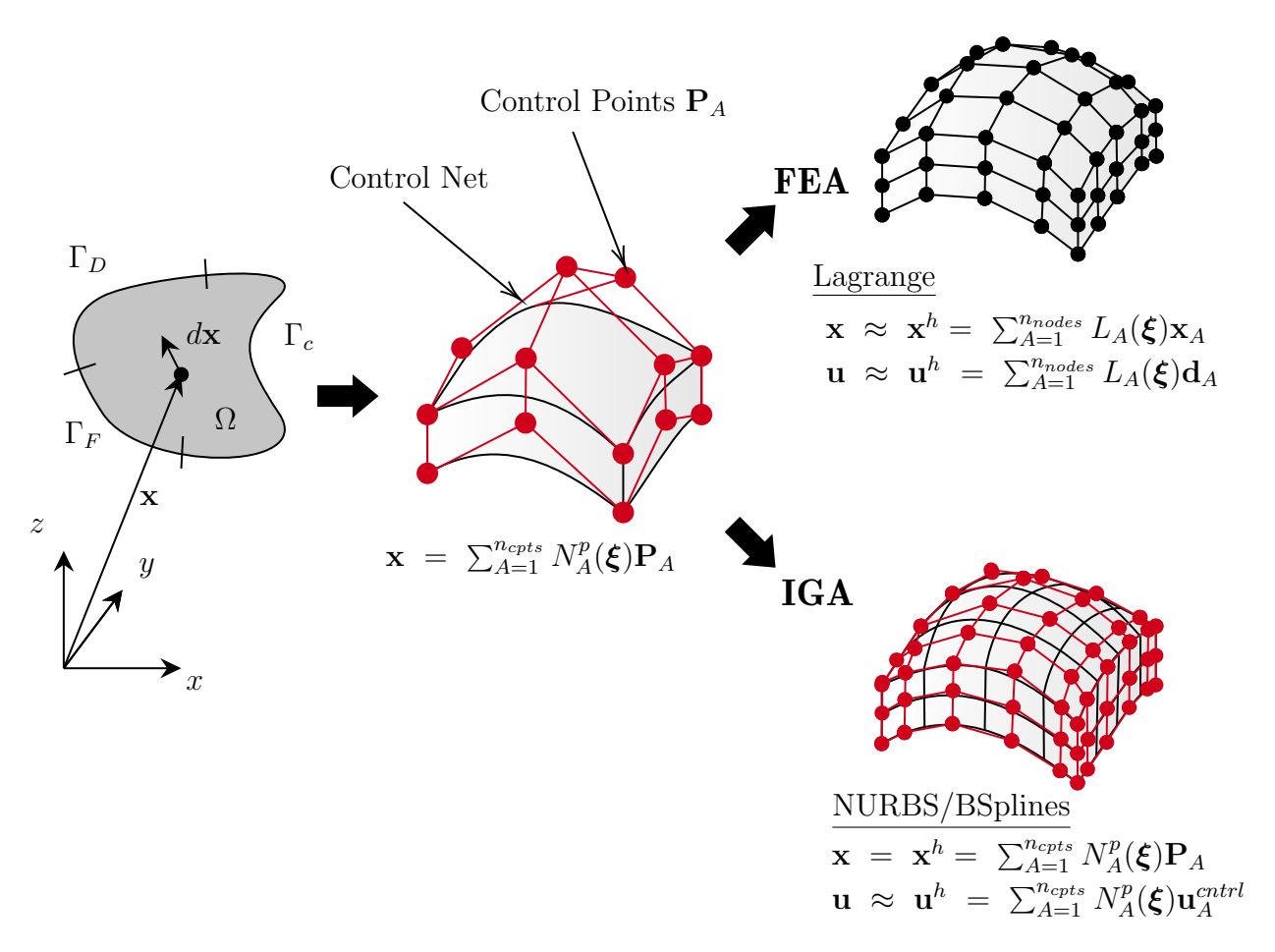


Figure 1.1 – Discretization of a mechanical problem [1]: from the continuum model which describes the mechanics of the problem, to its geometry CAD (smooth) representation, and finally the discrete form which makes up the computational model (Lagrange basis functions for the FEA model and NURBS/BSplines basis for the IGA model) of the problem with the isoparametric concept invoked.

difficult problem to solve in engineering analysis. The main difficulty is due to the non-smoothness that arises from the inequality contact constraints as well as the geometric discontinuities inherent to classical FEM (facetization due to mesh generation in the standard C^0 FEA [22, 23] - fig. 1.1). As already mentioned, the geometric discontinuities of the contact surface in FEA may lead to numerical instabilities. These instabilities typically result from the non-uniqueness of the outward normal vector, and subsequently the projection point in the local contact search, thus causing non-physical oscillations of the contact forces especially in sliding conditions and large deformation problems [15, 16, 22]. Hence the reason Isogeometric Analysis (IGA) approach is an interesting alternative for the numerical analysis of contact problems.

Isogeometric Analysis, first introduced by Hughes et al. [12], has been established as an advantageous alternative to classical C^0 Finite Elements (FE) discretization techniques for various

classes of problems [24]. This is particularly the case for those problems in which the ability to accurately capture the geometry greatly influences the accuracy of the numerical scheme, i.e. geometric errors have a significant influence on the quality of the solution [22, 25]. In IGA the same smooth higher order basis functions used for the representation of the CAD model are used for the analysis [12, 13], hence the name isogeometric - see fig. 1.1.

This approach, IGA, has been shown to have an increased accuracy and robustness [12, 26, 27], in comparison to standard FEA in many applications, including, but not limited to: cohesive zone modeling and debonding [28–30], fatigue and interfacial cracks, and progressive damage with extended isogeometric analysis (XIGA) [31, 32], fluid structure interactions [33], structural vibration, acoustics and wave propagation problems [34–36]. Amongst those classes of problems that IGA has been shown to be advantageous is the treatment of contact problems. The inherent higher-order continuity of the NURBS/BSplines basis in IGA leads to a smooth representation of the contact surfaces. This then yields a more robust discretization and consequently more accurate results in comparison to traditional FE approaches [1, 30, 37–42].

1.2 State of the Art

In the same way as in standard FEA, treatment of contact problems in IGA entails in three main phases, namely: (1) the contact search and detection phase - creating contact elements containing the proximal components of surfaces that may come into contact during resolution, (2) discretization of the contact interface - the parameterization of the contact interface, it predetermines the structure of the contact elements, (3) the contact resolution phase: the choice of method for the regularization and enforcement of contact constraints, and (4) temporal discretization in the case of dynamic contact.

In fact, contact formulations in the IGA setting originate from the more well-established contact algorithms available in classical FEM. For this reason they tend to inherit the favorable and unfavorable aspects of their classical FEM counterparts. De Lorenzis et al. [22] gives a nice detailed review and comparison of isogeometric contact algorithms, and has highlighted how these compare to their FEA counterparts. De Lorenzis et al. [23] is also a good reference, particularly for frictional static problems in standard FEA, advantages and limitations of contact algorithms in classical FEM and how IGA can be a remedy for said limitations. In terms of the implementation aspects of numerical contact problems, the works of Laursen [5] and Wriggers [3], as well as Zhong [4] specifically for contact impact problems, are good material sources. Kikuchi and Oden [43] provides the mathematical framework.

Even though contact detection, contact search to be precise, is a crucial step in the numerical treatment of contact problems - this phase is strongly connected to the nature of contact being studied, the type of contact interface discretization and the differential geometry, and finally the efficiency and robustness of the contact algorithm highly depends on contact detection - it does not form part of our scope. However, this subject has been researched by many authors in

literature and interested readers may consult the works of Wriggers [3], Zhong [4] and Yastrebov [6].

Enforcement of contact constraints amounts to addressing how the penetration of the bodies in contact is prevented (bodies in contact cannot overlap) and the modeling of the generated contact tractions on the contact interface due to this resistance to penetration. Contact constraints are formulated as a set of inequalities [3, 5, 6], something unusual for mechanical Boundary Value Problems (BVP). Due to the nature of these constraints, the rigorous construction of the variational form of the contact BVP writes as a variational inequality. To facilitate treatment of this variational form with existing numerical techniques available for variational equalities requires a regularization of the non smooth contact constraints. Primary methods for this regularization that are available include [3–5]: the (1) Lagrange Multipliers Method, (2) penalty method, and (3) some form of combination of these two methods such as the Augmented Lagrange Multipliers method. The advantage of using the Lagrange multipliers method is the exact enforcement of contact constraints, both for penetrations and contact tractions [6, 23]. However, this method introduces additional degrees of freedom (DOFs) and thus increasing the size of the problem. The penalty method on the other hand does not introduce additional DOFs in the system, however the contact constraints are only enforced in an approximate sense. Moreover the penalty method may lead to nonphysical penetrations, and with increasing penalty parameter, the ill-conditioning of the system of equations [6, 23].

With respect to the parameterization of the contact surfaces, their discretization and how these are incorporated into the variational formulation, different techniques exist to achieve this, namely (see fig. 1.2): (1) Node to Node (NTN) discretization only suitable for small deformation and conforming surface meshes, stable and passes the contact patch test [2, 44], (2) the versatile, multipurpose Node to Surface (NTS) discretization technique suitable for non conforming surface meshes [45], however does not pass the patch test [44] and (3) the stable and robust, however implementationally cumbersome Surface to Surface (STS) discretization [5, 46]. Essentially the contact surface discretization techniques fall into two categories: contact integrals collocated at the nodes/points with penetration conditions satisfied point-wise (NTN, NTS), or contact integrals satisfied in a weak sense and the penetration constraints satisfied in an average sense (STS, mortar methods).

Within the framework of small deformation, linearized mechanics, assumptions of a NTN contact may hold. However, in a general context when non linear kinematics is involved, a more sophisticated approach is required, hence the multi purpose NTS approach. Indeed, in the NTS discretization, the penetration constraints are fulfilled point-wise between a node of the first body (denoted as the slave) and the surface/segment of the second body (denoted as the master). The implementation of this method was pioneered by Hughes et al. [45] and Hallquist [47], primarily to address the limitations of the NTN discretization in the large deformation contact formulation framework. Since then the NTS discretization has been widely featured in the FEA treatment of contact problems [48–51]. Unlike the NTN discretization which is stable and robust, NTS formulation was shown not to pass the contact patch test. Moreover, it is a biased technique,

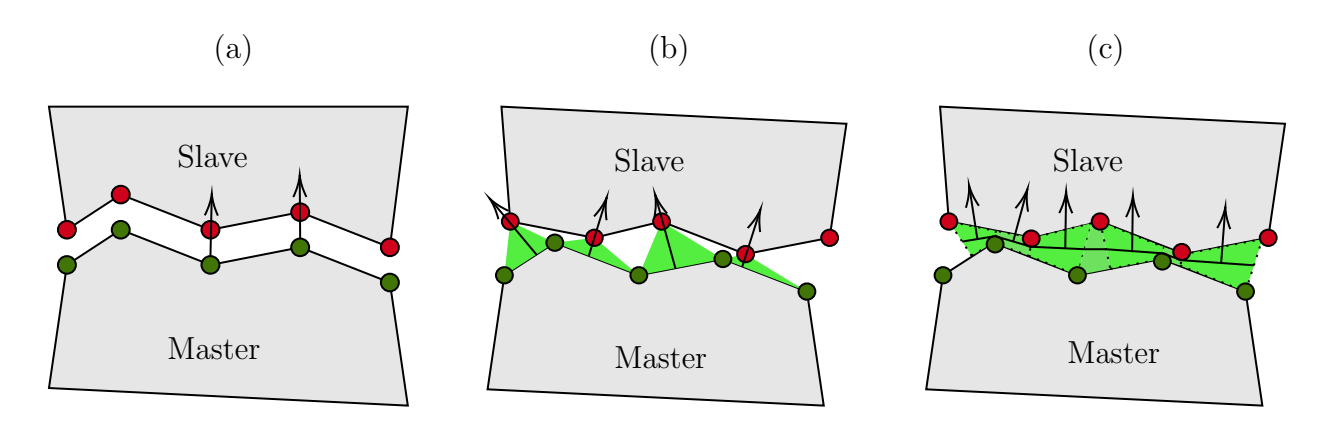


Figure 1.2 – Contact interface discretization techniques (Yastrebov, 2011): (a) Node to Node discretization, (b) Node to Surface discretization, and (c) Surface to Surface discretization.

in a sense that results are highly dependent on the choice of slave/master - see fig. 1.2b which shows the NTS contact elements (green patches). Another drawback of the NTS discretization arises as a result of the piece wise linear discretization in standard FEA which leads to numerical instabilities, particularly in sliding contact conditions, and consequently spurious oscillations of contact tractions. Introducing the smoothing techniques already discussed above was shown to improve the stability of this method. Simple yet highly robust due to its practicality and despite all the drawbacks mentioned, NTS formulation is still the most frequently implemented and used method, specifically in commercial codes.

To address the shortcomings of the NTS formulations, methods that no longer collocate contact integrals at the nodes but rather enforce the contact constraints in a weak sense (as an integral) have been developed. Moreover, the non penetration condition in no longer fulfilled point-wise, but rather in an averaged sense. STS which typically employs a so-called intermediate surface (see fig. 1.2c) over which contact quantities are defined and discretized (segmentation), first proposed by Simo et al. [46] for a two dimensional (2D) case, is one such method. Zavarise and Wriggers [52] presents a consistent linearization of the contact equations for this formulation. With sufficient segmentation of the intermediate surface, this formulation passes the contact patch test. The Gauss-Point-to-Surface (GPTS) formulation, exhibits the same character to an extent, in that: the contact terms contribution to the weak form is integrated in a straightforward manner by locating a predetermined number of Gauss-Legendre quadrature points of the slave contact surface (only at active contact points) [53, 54], however segmentation is not necessary. The GPTS formulation passes the patch test to within integration error. A version of the GPTS that passes the patch test to machine precision (termed the GPTS-2hp) can be found in Sauer [18], Papadopoulos et al. [55] and Sauer and De Lorenzis [56].

Even more further improvement on the contact surface discretization techniques was achieved through the introduction of the mortar methods, an approach inspired by domain decomposition methods [57]. In a similar manner to STS, with mortar formulations contact constraints are enforced in a weak sense. Though, the strength of the mortar methods lies with the rigorous mathematical background thus allowing for a variationally consistent treatment of the contact constraints, in terms of the fulfillment of the non penetration condition and sliding conditions

in frictional contact interactions, therefore guaranteeing optimal convergence rates [23]. Early applications of mortar methods for the treatment contact problems in small deformation framework can be found in Belgacem et al. [58] for friction-less contact and McDevitt and Laursen [59] for frictional contact. Extension into large deformation framework can be found in Puso and Laursen [60], Yang et al. [61] for frictional contact and Puso and Laursen [62] for three dimensional (3D) friction-less contact. Weißenfels [63] gives a detailed compilation and comparison of many mortar based formulations, and more details on this method and its implementation aspects can be found in Wriggers [3].

Mortar methods satisfy both the contact patch test, up to machine precision (they are exact with segmentation), and stability conditions if properly designed [62], and therefore are more accurate and more robust than the other aforementioned contact formulations [6, 62]. However, mortar methods are notorious for their heavy computational resources requirement, in terms of computational costs. Moreover they are highly complex; mortar integrals contain a set of functions of both surfaces (slave/master, or as it is often called in this formulation, mortar and non-mortar surfaces) and therefore can be cumbersome to implement [1, 22, 23]. Segmentation is required for exact computation of the integrals which contributes to the high computation costs [23, 62].

As mentioned, contact formulations in IGA originate from the existing FEM formulations discussed above. In what follows we discuss these contact formulations in the IGA framework.

Node to surface in the IGA setting is tricky to implement as this is a point-wise approach and in IGA, control points which serve the same role as nodes do not necessarily interpolate the physical geometry - see fig. 1.1, thus rendering the actual physical contact boundaries inaccessible at times. The question then becomes, if we are to use this formulation, where do we collocate the integrals? Matzen et al. [37] proposed a work around for this: a point to surface (PTS) method for the treatment of friction-less and frictional contact problems in large deformation, with NURBS as a basis and Lagrange multipliers for contact constraints enforcement. This PTS formulation collocates the contact integrals at the Greville and Botella points. Collocating the integrals at the Greville points was shown to yield better results for the classical Hertz problem, especially for the contact area near the patch boundary. They found the smoothness of the NURBS basis functions to alleviate the major difficulties of the classical NTS method. Even so, the scheme does not pass the patch test, however a two pass version of this scheme, termed PTS+ method, was shown to pass the contact patch test to machine precision [1]. Naturally, some form of smoothing was needed to avoid the oscillations of contact tractions at the contact-no-contact transition zone. In another application, Zhao et al. [64] coupled the NTS, collocated at the Greville points, with the Nitsche's method for contact constraints enforcement, to simulate friction-less 2D contact problems in large deformation. Again, it was found that the approach is more stable and robust compared to its FEA counterpart.

Temizer et al. [38] developed a version of the GPTS-2hp, called the knot to surface (KTS) formulation, with application to various 2D/3D finite deformation thermomechanical contact problems. The KTS formulation delivered satisfactorily results and an even superior convergence

rate, with respect to standard FEA, for 2D deformable bodies in large deformation friction-less sliding contact. However, this formulation is over constrained and thus leads to spurious oscillations of contact tractions, especially close to the contact boundary region. These oscillations due to mechanical contact being over constrained were also observed in De Lorenzis et al. [42] GPTS-2hp formulation with penalty method (the magnitude of the oscillations increased with the penalty parameter), Dimitri et al. [29] coupled the penalized GPTS-2hp formulation with the smoothing post processing scheme of Sauer [18] to reduce the oscillations. Lu [40] also evaluated both the GPTS-2hp and its two pass version.

Even though the GPTS is a good alternative to the non trivial NTS, at least in the IGA setting, that requires the collocation of contact at physical points, this formulation renders the system over constrained which leads to appearance of oscillations in the contact tractions. An alternative is perhaps to reduce the number of Gauss points involved through a patch-wise placement of quadrature points. Doing this results in a fewer points, however this may lead to an under constrained system [40]. Mortar formulations on the other hand provide a consistent treatment of the contact constraints. Here, the mortar projected penetration and traction are computed at each control point of the slave surface. Unlike in the FEM setting, these mortar constraints do not possess an immediate physical meaning due to the non interpolatory nature of the control points, however this has no bearing on the consistent performance of the algorithm. The mortar formulation in IGA setting has been presented in Temizer et al. [38], Kim and Youn [65] for friction-less contact in 2D setting, Temizer et al. [39], De Lorenzis et al. [42, 66], Dittmann et al. [67] for frictional contact in both 2D and 3D setting, and Seitz et al. [68] presents the more efficient dual mortar isogeometric formulation for the the treatment of friction-less contact.

The trade off of using these far superior, in terms of accuracy, and highly smooth NURBS/BSplines based isogeometric finite element methods is computational cost, they are more expensive to process. In the efforts to reduce the computational cost of these methods, a non Galerkin isogeometric collocation (IGA-C) method was developed by Auricchio et al. [69] and extended into multi-patch framework in Auricchio et al. [70] - see Schillinger et al. [71] for the cost comparison of the IGA-C methods to Garlekin IGA and the standard C^0 FEA. This method has been used for treatment of contact problems : De Lorenzis et al. [72] used the collocation method for the treatment of Neumann boundary conditions and enforcement of contact constraints - they proposed a GPTS-2hp formulation enhanced collocation approach that passes the patch test to machine precision which delivered accurate result, improved robustness, even for highly non uniform meshes (unlike the original IGA-C) - , Kruse et al. [73] used the enhanced IGA-C, with a GPTS-2hp and penalty method, for large deformation frictional problems, Nguyen-Thanh et al. [74] developed an isogeometric meshfree collocation method, with Greville collocation points, and applied it to frictional contact problems.

Other interesting contributions in IGA, especially from the implementation point of view, which are useful for numerical simulation of contact problems: (1) Nguyen et al. [75] gives an overview of the IGA method and the aspects of the computational implementation, these include the discretization techniques discussed above, the collocation methods, and the implementationally

friendly NURBS/BSplines that are suitable for existing FE codes derived via the Bézier extraction operator first introduced in Borden et al. [76], Borden [77], (2) to facilitate local refinement capabilities TSplines based IGA methods have been developed by Dimitri et al. [29], and also TSplines coupled with the Bézier extraction operator to formulate a data structure suitable for existing FE codes were developed in Scott et al. [78], Dimitri [79], de Borst and Chen [80], and applied to contact problems by Matzen [1].

Where impact-contact is concerned, the contact interaction is dynamic. Therefore, in addition to the spatial discretizations described above, a temporal discretization of the equations of motion is required. The books of Zhong [4], Laursen [5], Wriggers [3] provide a good fundamental knowledge on the numerical implementation of these problems. In most dynamic problems, the most useful information is contained within the transient phase which typically lasts a duration of a few microseconds, i.e. car crash and blast type loads. For these type of applications, the conditionally stable explicit time integration schemes are recommended. In fact, even if the unconditionally stable implicit schemes are used, a minimum time step size is still imposed to prevent the risk of failure to capture crucial transient characteristics of the solution. Implicit Newmark schemes may be appropriate for low frequency dynamic problems, like vibration of machines or structures under earthquake excitations [3]. More information on friction-less and frictional contact impact problems can be found in Laursen [5], Hughes et al. [81], Laursen and Chawla [82], Armero and Petocz [83] to name a few. Some applications of contact-impact in IGA framework include: a NURBS based continuum approach developed in Lu and Zheng [84] for cloth simulation with an explicit time integration scheme for the dynamic response of the contact impact problem, and Otto et al. [85] developed an explicit contact formulation, based on 3D spectral elements for the bulk domain with an auxiliary NURBS layer in between the bodies to allow for a smooth contact formulation, for treatment of the impact problem and the subsequent wave propagation.

1.3 Objectives

As mentioned is section 1.1, many technical devices exhibit the phenomena of contact. In industrial applications the characterization of these devices, in terms of optimization of the efficiency or reducing adverse effects, requires a good understanding of the contact problem. From the numerical simulation standpoint, a sufficiently accurate recovery of the contact stresses distribution, is paramount. Access to these stresses is an important entry point, especially in quantifying adverse effects that may be detrimental, for simulating phenomena such as initiation and propagation of vibrations induced by friction, generation and acoustic radiation of noise. The use of isogeometric approaches proves advantageous for these applications. Hence the main objective of this work: to develop an advanced isogeometric based numerical tool for the resolution of contact problems, and thus allowing us access to good quality, accurate contact stresses.

However, since in IGA the computation mesh is not necessarily on the physical geometry (typically the solution is computed on the control points and these points may not necessarily live on the physical geometry), methods that require collocation of contact integrals on the physical points (i.e. NTS) can be limiting. Moreover, the higher inter-element continuity in NURBS/BSplines based IGA leads to the overlapping of the basis and interior computation points being shared among-st neighboring elements. For this reason IGA can be cumbersome to implement and its data structures do not fit into existing FE codes. In this work we aim to address these drawbacks in a holistic manner, and propose a scheme not only with data structures suitable for existing FE codes, but also capable to accommodate the more simple and flexible, from the practicality point of view, point collocation contact formulations.

1.4 Scope of Work

The thesis is split into two parts. The first part, which comprises of chapters 2 and 3, is dedicated to the development of the isogeometric based numerical scheme for the treatment of contact problems. In the second part, the remainder of the thesis, the main focus is on the application of the developed numerical scheme.

Unlike classical FEM and Boundary Element Method (BEM), which are based on the notion of elements and nodes, IGA requires the consideration of control points and knots. Familiarity with the numerical aspects of this method and its application for structural problems is essential. Hence the interest of chapter 2 of this manuscript in which an in-depth review of the IGA method, from its fundamental geometric computer aided design point of view, and its characteristics from the numerical analysis point of view, is conducted. With the aim to specifically address the shortcomings of the NURBS-based IGA, particularly for surface/surface interaction problems, we propose a Bézier based scheme, suitable for existing FE codes. Essentially the geometry is discretized with Bézier elements. To study the characteristics of this Bézier based scheme, the scheme is used for the resolution of some classical problem in linear statics. The developed Bézier based scheme is compared to a BSplines (NURBS with identity weights) IGA approach, in terms of its performance, the computational efficiency and quality of the solution.

Chapter 3 entails first the review of the general formulation of contact problems, from the governing equations to the constitutive behavior in the contact interface. Next we detail the variational formulation derivation for the full frictional contact/impact problem, which is then followed by regularization and enforcement of contact constraints and a discussion of the important aspects of contact problems with regards to numerical implementation. Based on this review of contact computational mechanics conducted in sections 3.2 to 3.5, section 3.6 mainly entails the development of the contact algorithm based on the Bézier approach. A full, detailed discrete form, and its linearization is given here. From the geometry spatial discretization with Bézier elements, the time discretization of the friction law, contact interface discretization with NTS, the local search algorithm (contact pairs) and the projection point algorithm, and finally

the global temporal discretization, is given.

In chapter 4 we use the developed contact algorithm for the treatment of friction-less and frictional problems in 2D, with the models verified and validated against analytical solutions. The results obtained using the Bézier based approach are also compared to numerical results obtained using the standard C^0 FEA. This versatility and usefulness of this developed scheme is demonstrated in the penultimate chapter (chapter 5) where the developed scheme is extended to vibro-acoustics for the analysis of dynamics, explicit, and acoustic response of mechanical structures, particularly a forced-vibrating plate. Here, the NTS contact formulation scheme developed is coupled with the Rayleigh integral equation to analyze the vibratory behavior of impacted plates and the resulting acoustic radiation. In chapter 6 the forced vibrating plate considered in chapter 5 is again studied, but now with an implicit integration scheme coupled with an analytical contact force. The results obtained are used to correlate the full complete model used in the simulation in chapter 5. The model is then extended to the treatment of acoustic radiation due to a moving force. Finally, in chapter 7 we summarize the characteristics of the developed scheme, as well some findings from the numerical simulations conducted. A brief discussion on some of the limitations of this scheme, and how we could address these in the future, is also included here.

Part I

Development of Bézier-based Isogeometric Analysis

Finite Element Method based on Isogeometric Analysis

2.1 Introduction

In classical FEM framework the mesh is created from CAD. This leads to adopting a completely different geometric description for analysis. The implication is that the geometry is often replaced by one that is only approximate. Once the mesh is generated should the user desire refinement, communication with the CAD system during each refinement iteration is required and often times this link is unavailable [12, 13]. This perhaps explains why mesh construction is a costly, time consuming process. Furthermore the geometric approximation during mesh generation can lead to accuracy problems as a result of geometric errors.

Isogeometric analysis was introduced by Hughes et al. [12] with the primary goal to be geometrically exact no matter how coarse the mesh. This method also aimed to simplify mesh refinement by eliminating the need to communicate with the original CAD geometry, as well as to enable a tighter connection between CAD and FEA (see fig. 2.1 [86]). Within the IGA framework, the same higher order and smooth basis functions used for the representation of the exact CAD geometry are used for the approximation of the solution fields - hence the term isogeometric [12, 13].

This chapter will serve as an introduction into the IGA framework and how this method fits into the existing more familiar standard C^0 FEA. First we detail the fundamentals of IGA [12, 13, 24, 75] which includes a study on the different parameterization techniques of this method as well the Bézier extraction concept of Borden et al. [76], Borden [77] which allows for the development of the implementationally friendly isogeometric methods which are suitable for existing FE codes data structures. This is followed by the finite element formulation of the isogeometric methods and the development of the Bézier-based IGA approach in Khanyile et al. [87] which couples the Bézier extraction concept of Borden et al. [76] and the full transformation method of Kamoso [88]. Finally we demonstrate this Bézier-based IGA approach and compare

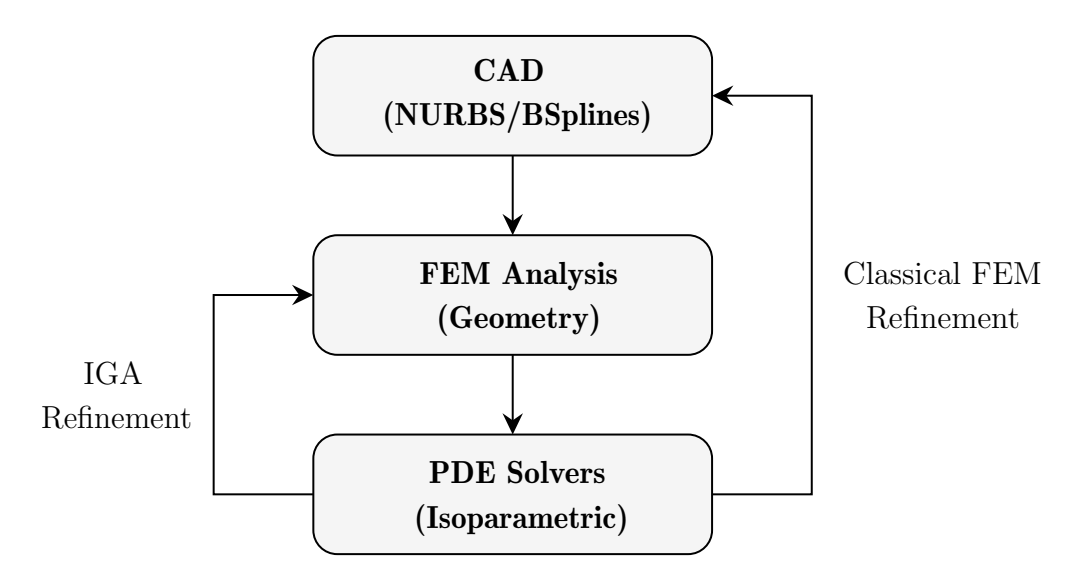


Figure 2.1 – Hughes' Proposal: the link between actual geometry and analysis geometry for both IGA and classical FEM, ie, IGA refinement vs classical FEM.

this method, in terms of performance, to the BSplines-based IGA approach.

2.2 Isogeometric Analysis Fundamentals

Isogeometric analysis is geometrically driven and was inspired by CAD. Therefore to fully comprehend this method it is paramount to have a clear understanding of Computer Aided Geometric Design (CAGD) related discretization technology. More specifically, Bézier, BSplines and NURBS parameterization or rather geometric design techniques, are studied as these are the most commonly used in geometric design [12, 13]. It is worthwhile to note irrespective of the type of technique used in construction of CAD, there exist common characteristics in design of curves, surfaces or solids, namely [89, 90]:

- Control points preselected by the user; the polyline joining these points, the control polygon (control net 2D, a polyhedron in 3D), is an exaggerated shape of the desired curve/surface/solid see fig. 1.2.
- Basis functions these are the blending functions of the model

The aim of this section is to outline the fundamentals of IGA, more specifically the important characteristics of this method, and how this method fits into the existing standard FEA framework. For a more broader and detailed introduction into IGA interested readers are referred to the work of Hughes et al. [12], Cottrell et al. [13], and the work of Nguyen et al. [75] and Agrawal and Gautam [24] for a simplified approach and implementation aspects. Farin [89] and Piegl and Tiller [90] provide a comprehensive review of the underlying geometric concepts and algorithms, particularly for the geometric CAD, an important basis for IGA.

2.2.1 Bézier and Bernstein Polynomials

Bézier parameterization uses Bernstein polynomials as a basis. The univariate Bernstein basis of order p is defined by

$$B_i^p(\xi) = \binom{p}{i} \xi^i (1 - \xi)^{p-i}$$
 (2.1)

where $\xi \in [0,1]$ represents the parameter space and the binomial coefficient in eq. (2.1) is given by eq. (2.2)

An important property of the Bernstein polynomials is that they satisfy the recursion given by eq. (2.3) with condition in eq. (2.4).

$$B_i^p(\xi) = (1 - \xi)B_i^{p-1}(\xi) + \xi B_{i-1}^{p-1}(\xi)$$
(2.3)

$$B_0^0(\xi) \equiv 1 \tag{2.4}$$

Additionally, Bernstein polynomials form a partition of unity. That is,

$$\sum_{i=1}^{n_{\text{cpts}}} B_i^p(\xi) \equiv 1 \tag{2.5}$$

A Bézier curve of the same order p can then be defined as

$$C(\xi) = \sum_{A=1}^{n_{\text{cpts}}} B_A^p(\xi) \mathbf{P}_A \tag{2.6}$$

In eq. (2.6) \mathbf{P}_A contains coordinates of the control points, and $n_{\text{cpts}} = p + 1$ is the number of control points in eqs. (2.5) and (2.6).

Properties of a Bézier curve include [89]:

- (1) **geometry invariance property** a consequence of partition unity leading to shape invariance under affine transformations
- (2) **convex hull property** for all ξ in the parameter space the Bézier curve lies within the convex hull of the control polygon
- (3) variation diminishing property no plane can intersect with the Bézier curve more than it intersects the control polygon this however has not been proven for surfaces/solids
- (4) **endpoint interpolation** in a similar manner to Lagrange polynomial commonly used in standard FEM, Bézier curve is interpolatory at the extremities Figure 2.2 demonstrates this property

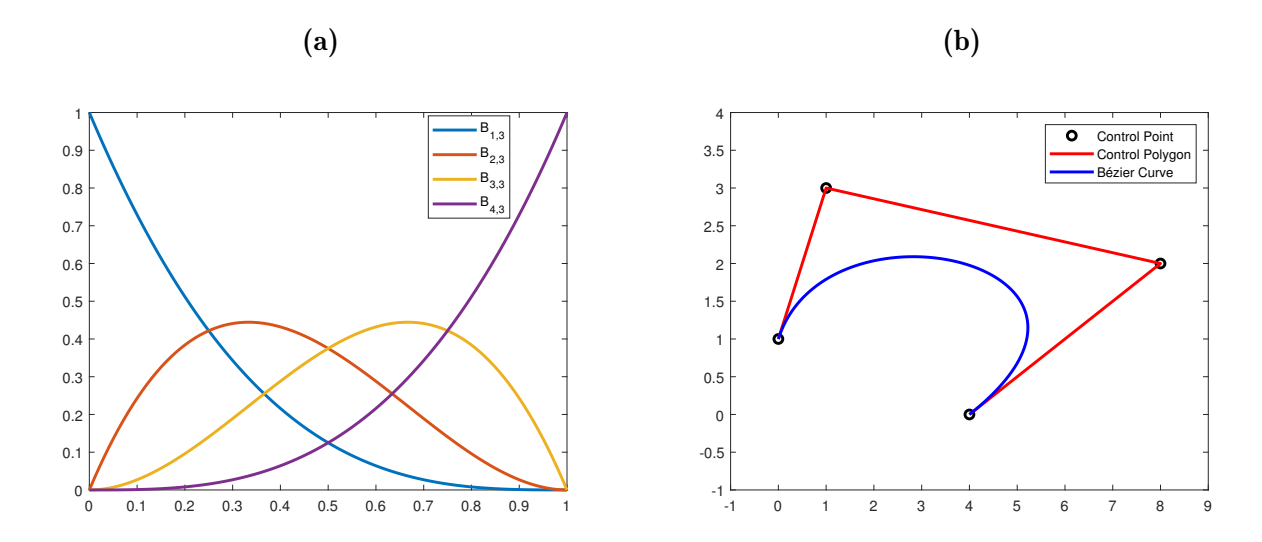


Figure 2.2 – A construction of a cubic Bézier curve with the corresponding basis functions, $n_{cpts} = 4$, p = 3: (a) Bernstein basis functions, and (b) the constructed Bézier curve.

Furthermore, it is worth noting that a derivative of a Bézier curve is a Bézier curve, and the first derivative of the Bernstein polynomials is given by eq. (2.7)

$$\frac{\mathrm{d}B_i^p(\xi)}{\mathrm{d}\xi} = p \left[B_{i-1}^{p-1}(\xi) - B_i^{p-1}(\xi) \right]$$
 (2.7)

with eq. (2.8) holding

$$B_{-1}^{p-1}(\xi) \equiv B_p^{p-1}(\xi) \equiv 0 \tag{2.8}$$

One major advantage of the Bézier technique is the relative easeness when it comes to the implementation. However this technique can be restrictive as the order of the basis functions (Bernstein polynomials) is strongly tied to the number of control points ($p = n_{\text{cpts}} - 1$), which can be disadvantageous. Moreover this technique has a global support across the parameter space; changing one control point changes the entire curve - see fig. 2.3 where a small perturbation of the upper right control point has resulted in the complete change of the shape of the curve (from green curve to blue curve). Another disadvantage of Bézier parameterization, like any parameterization based on polynomials, it cannot exactly represent circles, ellipses and conical shapes [89]. Multivariate Bernstein basis functions are formed from a tensor product of the univariate basis. Suppose a d-dimensional parametric space is considered and univariate basis functions in each parametric direction d are denoted by B_{i,p_d}^p , multivariate basis functions are obtained from eq. (2.9)

$$\mathbf{B}_{\mathbf{i}}^{p}(\boldsymbol{\xi}) = \prod_{d=1}^{n_d} B_{i,p_d}^{p}(\xi_d)$$
 (2.9)

where $n_d = 2$ (bivariate) or $n_d = 3$ (trivariate). Multivariate basis function inherit the key properties of the univariate basis. Surfaces and volumes, similar to curves, are then obtained from a linear combination of the multivariate basis functions and the corresponding control points.

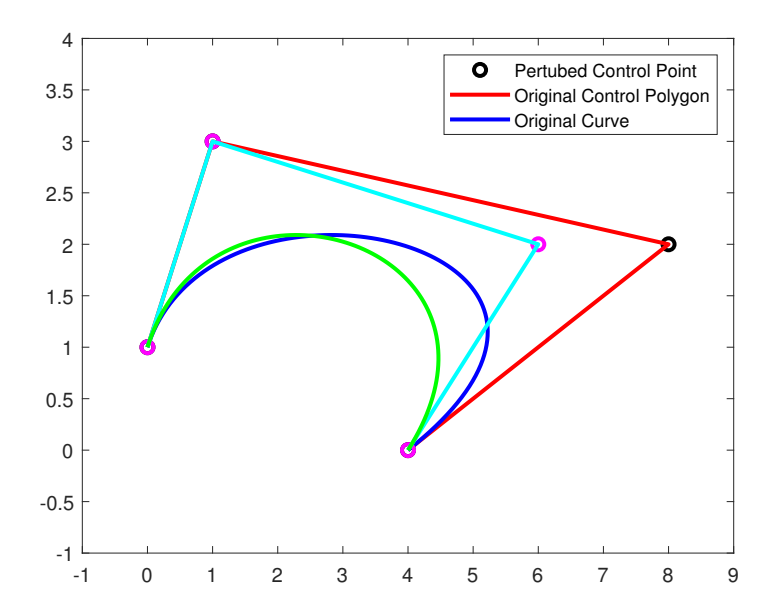


Figure 2.3 – Bézier discretization global support demonstration on a cubic Bézier curve, $n_{cpts} = 4$, p = 3.

2.2.2 BSplines

In terms of design freedom, Bézier curves can be restrictive because the number of control points drives the order of the curve. This means that higher order curves are required to satisfy a large number of constraints, in this case the number of control points required ($n_{\rm cpts} = p + 1$). Numerically, higher order polynomials are inefficient to process, stiff from the design point of view, and can be quite unstable [12, 22]. BSplines, which are piecewise polynomials, are then an appropriate alternative to remedy this limitation of the Bézier technique [89].

In order to construct a BSplines curve, a knot vector is required. A knot vector is a sequence of parameter values, non-decreasing set, that determine where and how the control points affect the BSplines defined shape/curve. Equation (2.10) defines a univariate knot vector.

$$\Xi = \left\{ \xi_1, \xi_2, \xi_3, \cdots, \xi_{n_{\text{cpts}}+p+1} \right\}$$
 (2.10)

Again n_{cpts} is the number of basis functions as well as control points, and p is the order of the polynomial basis function. Each knot span $[\xi_i \ \xi_{i+1}]$, with $\xi_i \neq \xi_{i+1}$, serves the same role as elements in classical FEM. Unlike Bézier basis functions which have a global support over a single curve, BSplines basis functions are defined globally on a patch [89, 90]. A patch is a collection of a number of elements which is equal to the number of knot spans in a knot vector i.e. eq. (2.10) defines a single patch.

For a given knot vector Ξ , the corresponding BSplines basis functions $N_i^p(\xi)$ are defined by the Cox-de-Boor formula in a recursive manner, such that

$$N_i^p(\xi) = \frac{\xi - \xi_i}{\xi_{i+p} - \xi_i} N_i^{p-1}(\xi) + \frac{\xi_{i+p+1} - \xi}{\xi_{i+p+1} - \xi_{i+1}} N_{i+1}^{p-1}(\xi)$$
(2.11)

In eq. (2.11) the fractions of 0/0 are defined as zero, and

$$N_i^0(\xi) = \begin{cases} 1 & \text{if } \xi_i \le \xi < \xi_{i+1} \\ 0 & \text{otherwise} \end{cases}$$
 (2.12)

Properties of BSplines basis functions include (1) partition of unity, (2) linearly independent, (3) each basis function is supported by p + 1 knot spans over the interval $[\xi_i \, \xi_{i+p+1}]$.

An important characteristic to note about BSplines basis functions is that they are non interpolatory at the control points. They exhibit a C^{p-k} -continuity across knots ξ_i , where k is the multiplicity of the knot entry (i.e. how many times the specific knot entry appears in a knot vector). In practice, usually open knots - knot vectors within which the first and last entry have a multiplicity k=p+1, are used [13, 89]. This then means that the designed BSplines curve is interpolatory at the extremities - this is what is known as a clamped BSplines curve. For example consider quadratic BSplines basis function (p=2), knot vector $\Xi = \left\{0 \ 0 \ 0 \ \frac{1}{4} \ \frac{1}{2} \ \frac{3}{4} \ 1 \ 1 \ \right\}$ - fig. 2.4 demonstrates how the continuity of the basis function decreases as the knots are repeated.

A BSplines curve of order p is then defined as

$$C(\xi) = \sum_{A=1}^{n_{\text{cpts}}} N_A^p(\xi) \mathbf{P}_A = \mathbf{P}^T \mathbf{N}$$
(2.13)

Similar to Bézier curves, BSplines curves also possess geometry invariance property, strong convex hull property, as well variation diminishing property. In general they are non-interpolatory on the interior control points, and will interpolate the extremities if the knot vector is open (clamped BSplines). Unlike Bézier curves, BSplines have quasi-local support, that is, if change is made on a specific control point, only the section of the curve that is in the vicinity will be changed [89] - this is the quasi-local modification property. Moreover, similarly to Bézier basis functions, BSplines basis are polynomials and therefore cannot exactly represent conic sections.

Figure 2.5a shows an example of a quadratic (p = 2) BSplines curve and fig. 2.5b shows its basis functions. It can be seen from fig. 2.5a that the BSplines curve does not interpolate interior control points (interior knots have multiplicity of 1); the ends of the curve however are clamped.

Multivariate Bsplines basis functions are obtained from a tensor product as well. Figure 2.6 shows an example of a BSplines surface.

Moreover, Bézier is a special case of BSplines with all knots in the vector repeated p + 1-times. In essence, a BSplines curve can be seen as a composite Bézier curves [89]. The use of composite Bézier curves, rather than a single Bézier curve, can elevate the major drawback of the Bézier technique - the tight dependence of polynomial order to the number of control points : if a curve to be modeled has a highly complex shape, its Bézier representation will have a prohibitively high order [89].

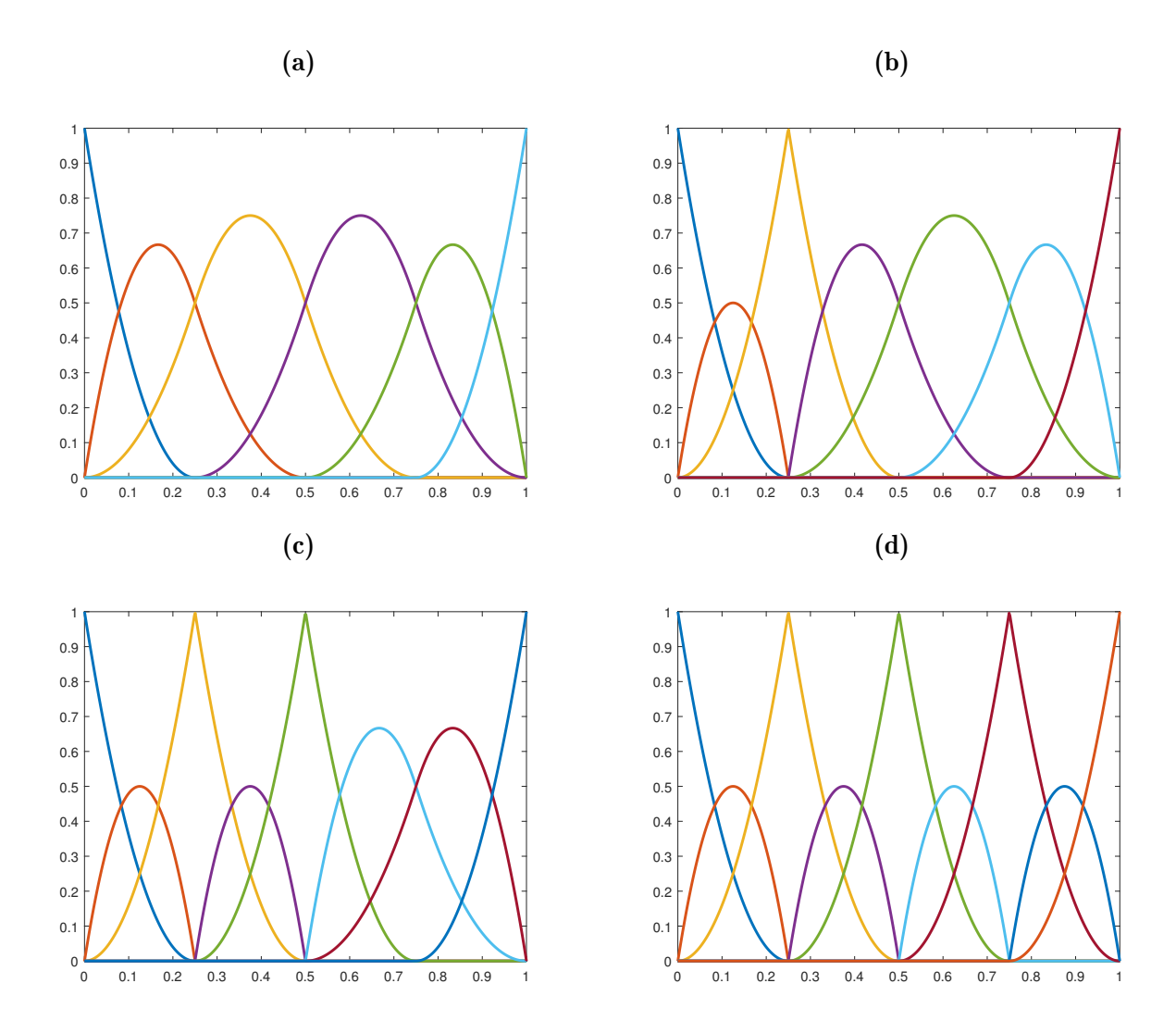


Figure 2.4 – Effect of knot multiplicity on the continuity of basis functions, p = 2: (a) $\Xi = \left\{0, 0, 0, \frac{1}{4}, \frac{1}{2}, \frac{3}{4}, 1, 1, 1\right\}$, (b) $\Xi = \left\{0, 0, 0, \frac{1}{4}, \frac{1}{4}, \frac{1}{2}, \frac{3}{4}, 1, 1, 1\right\}$, (c) $\Xi = \left\{0, 0, 0, \frac{1}{4}, \frac{1}{4}, \frac{1}{2}, \frac{3}{4}, 1, 1, 1\right\}$, and (d) $\Xi = \left\{0, 0, 0, \frac{1}{4}, \frac{1}{4}, \frac{1}{2}, \frac{1}{2}, \frac{3}{4}, \frac{3}{4}, 1, 1, 1\right\}$.

Thus, for any given BSplines control polygon, a composite Bézier can be derived therefore yielding a composite Bézier representation of said curve. Farin [89] demonstrated this transformation for C^1 and C^2 BSplines curves. Figure 2.7 shows how the BSplines global parametric space (ξ) transforms to the local Bézier parameter space $(\hat{\xi})$.

An added advantage of transforming from BSplines control polygon to composite Bézier is that the represented curve will enjoy the local control property exhibited by Bézier curve (BSplines have a quasi local support - the support spreads over several knot spans - whereas the Bézier representation will have global control on a single knot span). Naturally more effort will be required for composite Bézier representation in terms of geometry preparation as will be seen from the Bézier decomposition algorithm that describes the process of transforming a BSplines geometry into a composite Bézier geometry detailed in section 2.2.4. In fig. 2.8 we can see how a highly complex BSplines curve is transformed into composite Bézier curves.

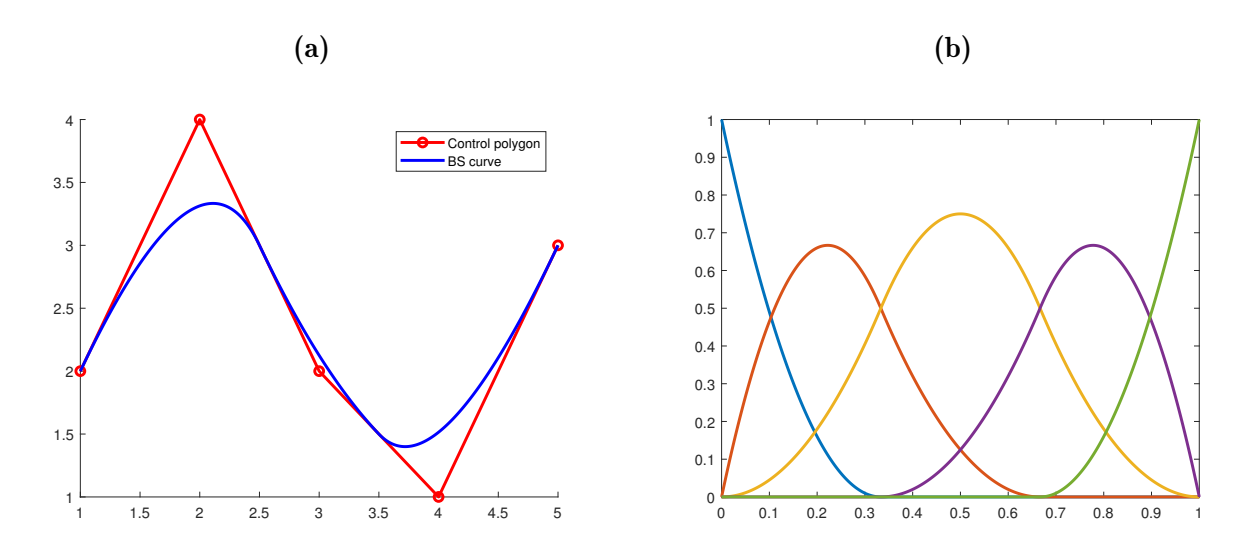


Figure 2.5 – Quadratic Bsplines curve with its basis functions, $\Xi = \{0, 0, 0, \frac{1}{3}, \frac{2}{3}, 1, 1, 1\}$ and p = 2: (a) a BSplines curve, and (b) BSplines basis functions.

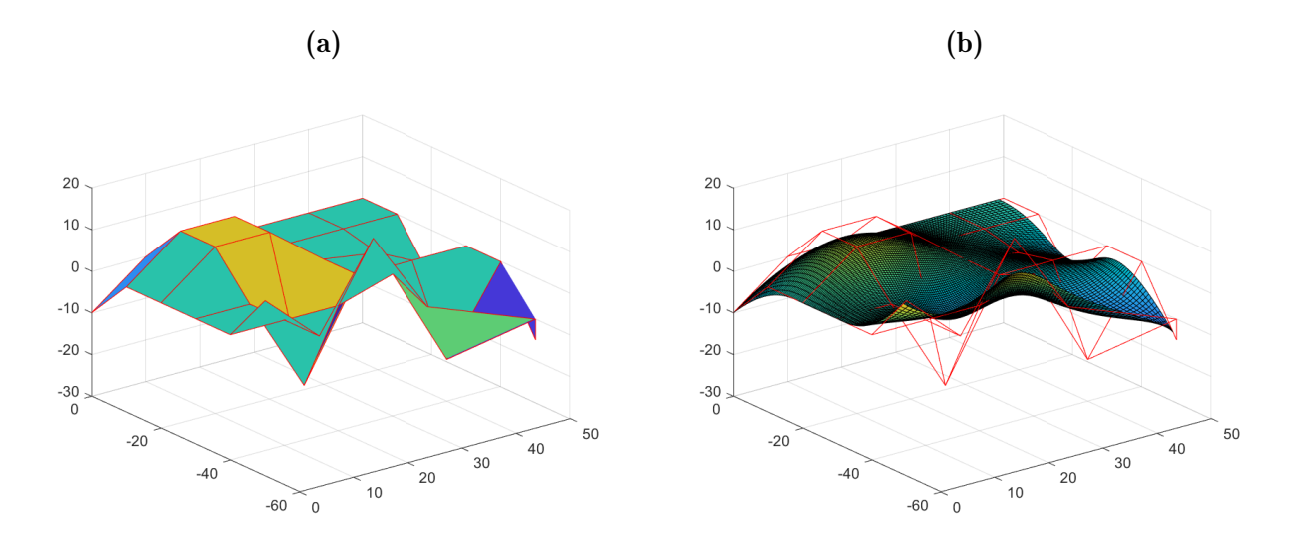


Figure 2.6 – BSplines surface with $\Xi = \{0,0,0,0,\frac{1}{3},\frac{2}{3},1,1,1,1\}$ in both ξ,η -direction : (a) the control net, and (b) the constructed surface, cubic polynomials used in both directions.

For the example shown in fig. 2.8, the BSplines representation consists of : 16 knots in the open knot vector $\Xi = \left\{0^{\langle p+1\rangle}, 0.2, 0.3, 0.4, 0.5, 0.6, 0.7, 0.8, 0.9, 1^{\langle p+1\rangle}\right\}$ (therefore 9 knot spans; $(\bullet)^{\langle p+1\rangle}$ implies knot with p+1 multiplicity), 12 control points, the order of the basis is cubic, and the parameter space is $\xi = [0, 1]$. In transforming this curve into a composite Bézier curve, the number of control points increases from 12 to 28. Each knot span supports a single cubic Bézier curve with a local parameter space $\hat{\xi} = [0, 1]$.

2.2.3 Non Uniform Rational BSplines (NURBS)

Even though BSplines elevate the stiffness, in terms of design flexibility, of the Bézier discretization due to the tight constraints between the number of control points and the order of the basis

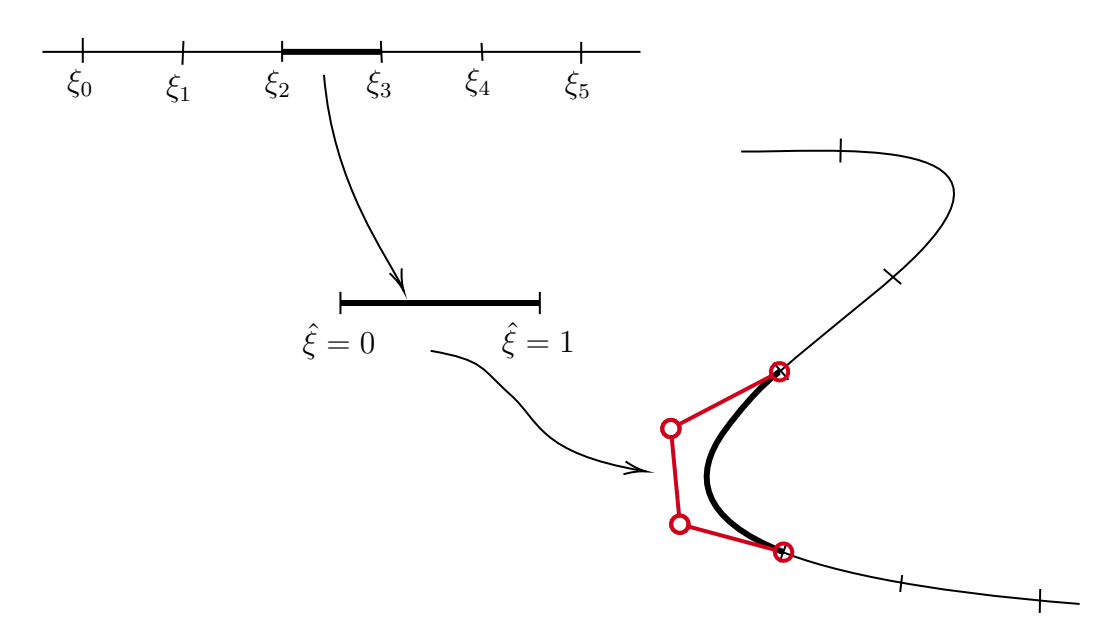


Figure 2.7 – Decomposition of BSplines curve onto composite/piecewise Bézier curves.

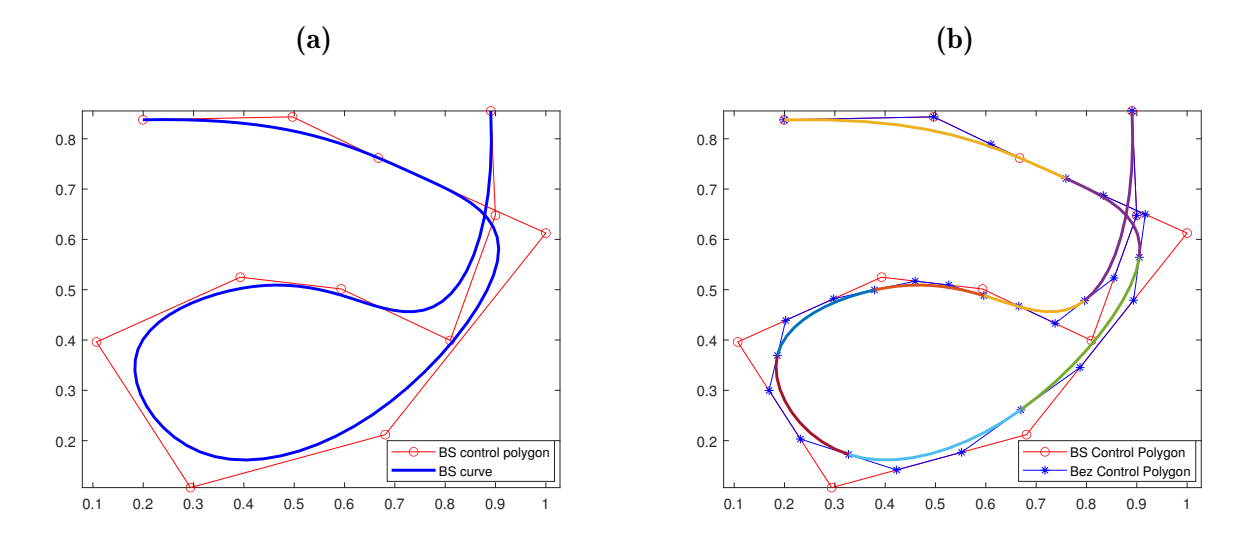


Figure 2.8 – Transformation of a BSplines curve into composite Bézier curves (p = 3): (a) BSplines curve representation, and (b) the composite Bézier curve representation.

functions, they are still polynomials and therefore are not capable of exact construction of conic sections. NURBS (Non Uniform Rational BSplines), a projective transformation of BSplines, can elevate the aforementioned restriction. A univariate NURBS basis function is given by

$$R_i^p(\xi) = \frac{N_i^p(\xi)w_i}{\sum_{j=1}^n N_j^p(\xi)w_j} = \frac{N_i^p(\xi)w_i}{W(\xi)}$$
 (2.14)

where $N_i^p(\xi)$ are the BSplines basis functions (see eq. (2.11) and eq. (2.12)) and $w_i > 0$ are the corresponding weights. Weights indicate the effect of corresponding control points (and therefore the basis) to the final shape of the constructed geometry; weights are an additional parameter for shape modification [13, 89, 91]. BSplines are a specific case of NURBS with unity weights. NURBS basis functions inherit key properties of BSplines basis, namely: partition of unity, non-negativity, C^{p-k} -continuity across knots ξ_i , and quasi local support [89]. Similarly

to Bézier and BSplines, multivariate NURBS basis functions are obtained in a tensor product form. Figure 2.9 shows quadratic and cubic NURBS basis functions, with $\mathbf{w} = \left\{1, \frac{1}{\sqrt{2}}, 1\right\}$ and $\mathbf{w} = \left\{1, \frac{1}{3}\left(1 - \sqrt{2}\right), \frac{1}{3}\left(1 + \sqrt{2}\right), 1\right\}$, respectively.

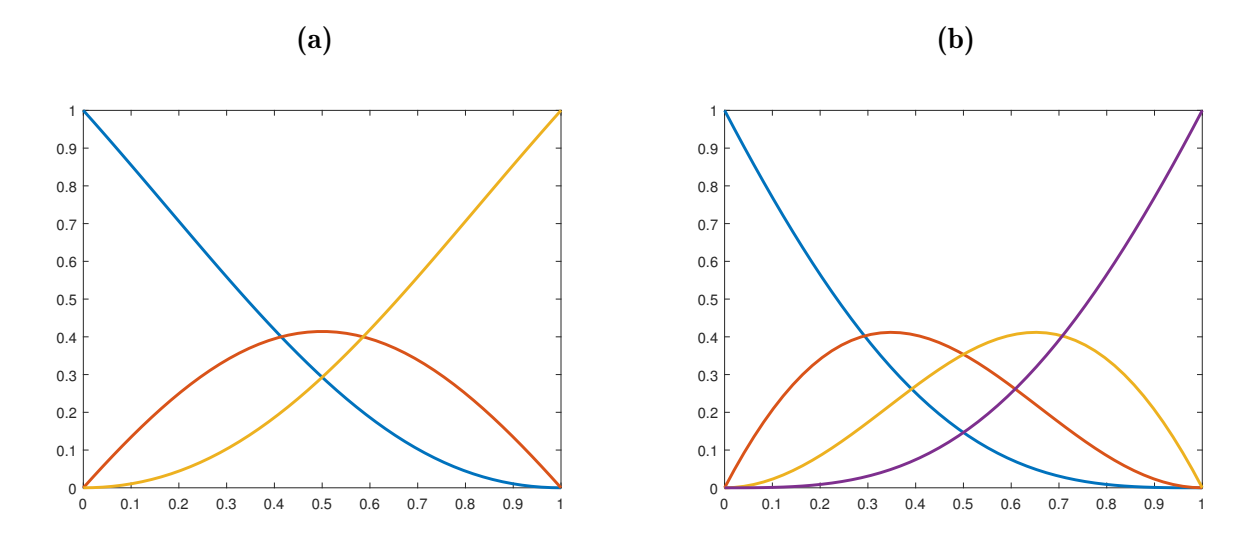


Figure 2.9 – NURBS basis functions : (a) quadratic basis, $\Xi = \{0,0,0,1,1,1\}$, and (b) cubic basis, $\Xi = \{0,0,0,0,1,1,1,1\}$.

A NURBS curve is constructed from a linear combination of basis functions and control points as

$$\mathbf{C}\left(\xi\right) = \sum_{A=1}^{n_{\text{cpts}}} R_A^p\left(\xi\right) \mathbf{P}_A \tag{2.15}$$

NURBS curves also exhibit the same characteristics as BSplines curves: continuity, convex hull property, local modification property, as well as the variation diminishing property [89].

Figure 2.10 shows a quarter circle analytical shape with its reconstruction using NURBS (weights and knot vectors are those used in fig. 2.9) and a BSplines reconstruction achieved by setting the weights to unity ($\mathbf{w} = \mathbf{1}$), for p = 2 and p = 3. It can be seen that NURBS exactly represent the quarter circle (generated shape coincides with the analytical shape), whereas the BSplines curve is only exact at the extremities. As is traditionally observed, increasing the polynomial order improves the approximation; the cubic BSplines representation is much closer to the analytical shape.

It is however possible to minimize the BSplines approximation error at the interior points. This can be achieved through the least squares interpolation - forcing the BSplines curve to go through a set of predetermined points that live on the analytical shape in this case the quarter circle in fig. 2.10. This then entails in finding corresponding control points to ensure that the curve will go through the chosen physical points. For an exact interpolation, p + 1 physical points are sufficient. Inverting the relation in eq. (2.13) amounts to

$$\mathbf{P} = \mathbf{N}^{-1}(\xi)\mathbf{C}(\xi) \tag{2.16}$$

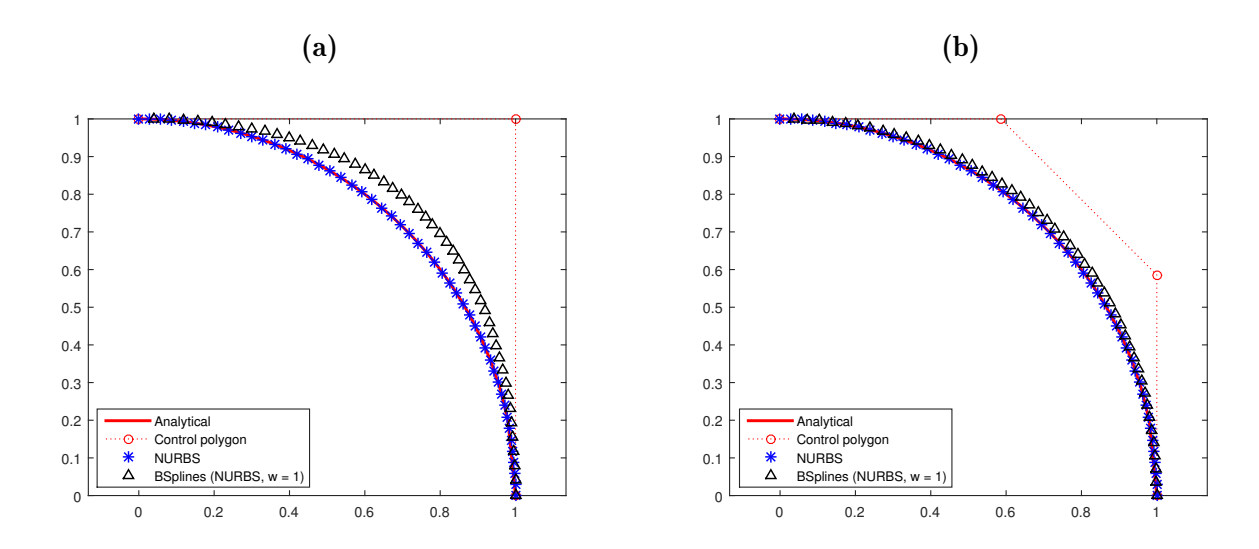


Figure 2.10 – The comparison of NURBS and BSplines approximation of a quarter circle, together with the analytical shape : (a) quadratic approximation, and (b) cubic approximation.

The basis functions $N(\xi)$ and the analytical shape physical points (indicated by $\mathbf{C}(\xi)$) are evaluated at the same parameter values (uniformly distributed over [0,1] for this example). Figure 2.11 shows the reconstructed shape using the exact interpolation. A significant improvement is observed in terms of approximation error, albeit the representation is still not exact.

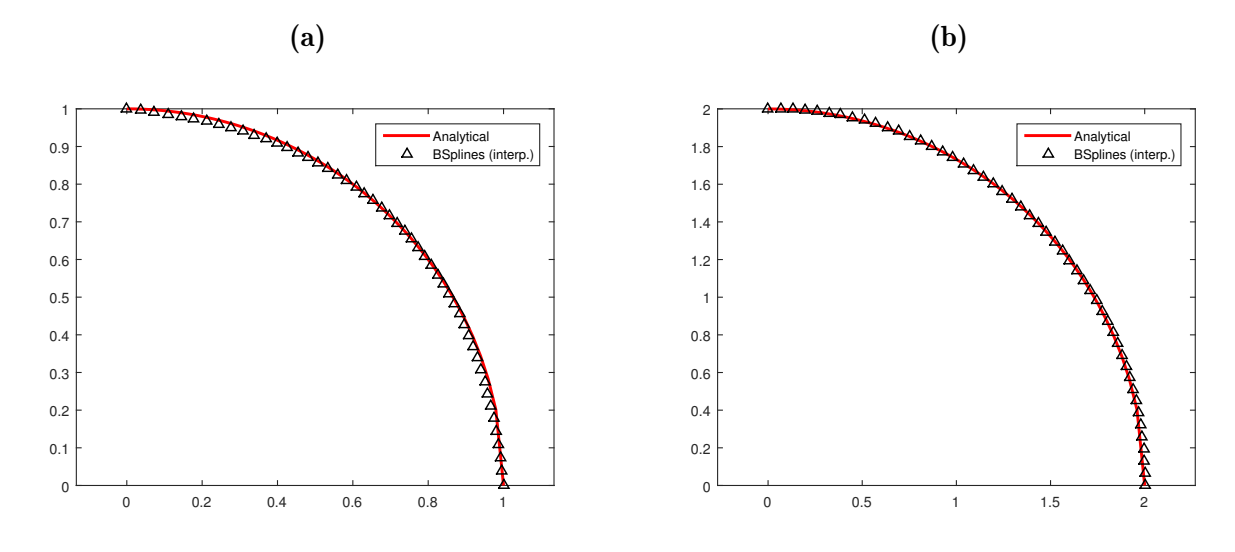


Figure 2.11 – BSplines reconstruction of a quarter circle using the exact interpolation : (a) quadratic approximation, and (b) cubic approximation.

As is observed in fig. 2.10, in line with literature, elevating the order of the polynomial basis functions (BSplines) further improves the approximation. This is what is known as the degree elevation which is analogous to the p-refinement in standard FEM [13, 75, 89, 90]. Another possibility to improve the approximation is through knot insertion (refining the knot vector); this is analogous to the h-refinement in standard FEM [13, 75, 89, 90]. There exists another refinement technique unique to IGA, known as the k-refinement, which is a combination of the knot insertion and degree elevation [13, 75]. In essence, it is possible to obtain an excellent

discretization by simply using BSplines with refinements, however this can be at the expense of resolution time efficiency as this can increase the number of degrees of freedom in the system.

Even though NURBS provide the most advantage with regards to exact construction of the geometry, they are quite cumbersome, in terms of information required, to implement. A lot of effort is required for the problem setup. BSplines, with the right combination of refinements, can be a viable option for achieving acceptable accuracy levels with a little less effort required on problem setup as compared to NURBS. However, the most significant drawback of both NURBS and BSplines, due to their overlapping nature (C^{p-k} -continuity between elements), they can not fit into existing FE data structures automatically [77, 76].

Table 2.1 shows the interaction of basis functions and control points on each knot span for Bézier, BSplines, and NURBS.

Element	Bézier				BSplines/NURBS			
1	P_0	P_1	P_2	P_3	P_0	P_1	P_2	P_3
2	P_3	P_4	P_5	P_6	P_1	P_2	P_3	P_4
:	:	:	÷	:	:	:	:	:
$n_{elem} - 1$	$P_{n_{\text{cpts}}-6}$	$P_{n_{\rm cpts}-5}$	$P_{n_{\text{cpts}}-4}$	$P_{n_{\text{cpts}}-3}$	$P_{n_{\text{cpts}}-4}$	$P_{n_{\text{cpts}}-3}$	$P_{n_{\text{cpts}}-2}$	$P_{n_{\text{cpts}}-1}$
n_{elem}	$P_{n_{\text{cpts}}-3}$	$P_{n_{\text{cpts}}-2}$	$P_{n_{\text{cpts}}-1}$	$P_{n_{\rm cpts}}$	$P_{n_{\text{cpts}}-3}$	$P_{n_{\text{cpts}}-2}$	$P_{n_{\text{cpts}}-1}$	$P_{n_{\mathrm{cpts}}}$

Table 2.1 – Support for the basis functions (Bézier, BSplines/NURBS), p = 3.

Borden et al. [76] proposed an implementationally convenient NURBS (which can be adapted to BSplines) FE data structures derived from the Bézier extraction concept. In a similar manner as in fig. 2.7, the Bézier extraction operator allows for the extraction of Bézier elements which only have global control on each element from NURBS/BSplines. Essentially the NURBS/BSplines topological and global smoothness information are localized to the element level and can be processed in the similar manner as the standard FEM Lagrange basis. In doing this, only the shape function routine requires modification and the rest of the finite element program remains unchanged. This is further discussed in the next section.

2.2.4 Bézier Extraction Operator

One characteristic that is shared amongst the IGA discretization technologies discussed above is the partition of unity of the basis functions as well as non-negativity. The geometries constructed using the 3 techniques also enjoy a strong convex hull property as well as variation diminishing property in terms of one dimensional geometries. Where, similarly to Lagrange basis in FEM, Bézier basis functions have a C^0 -continuity across elements, BSplines and NURBS have a C^{p-k} -continuity. Bézier discretization interpolates inter-elemental boundary control points whereas BSplines and NURBS interpolate the patch boundary.

Figure 2.12 displays a comparison of basis functions for the IGA discretizations and standard FEM Lagrange basis for a 2-elements patch defined by knot vector $\Xi = \{0,0,0,0.5,1,1,1\}$ [22, 24]. As discussed, the undesirable characteristic of NURBS and BSplines with regards to implementation, is that the basis functions are smooth on the patch level which makes them hard to integrate into existing FE codes. In this section, we discuss Borden's proposal [76] for an element structure for IGA that can be incorporated into the existing FE codes through the use of a Bézier extraction operator.

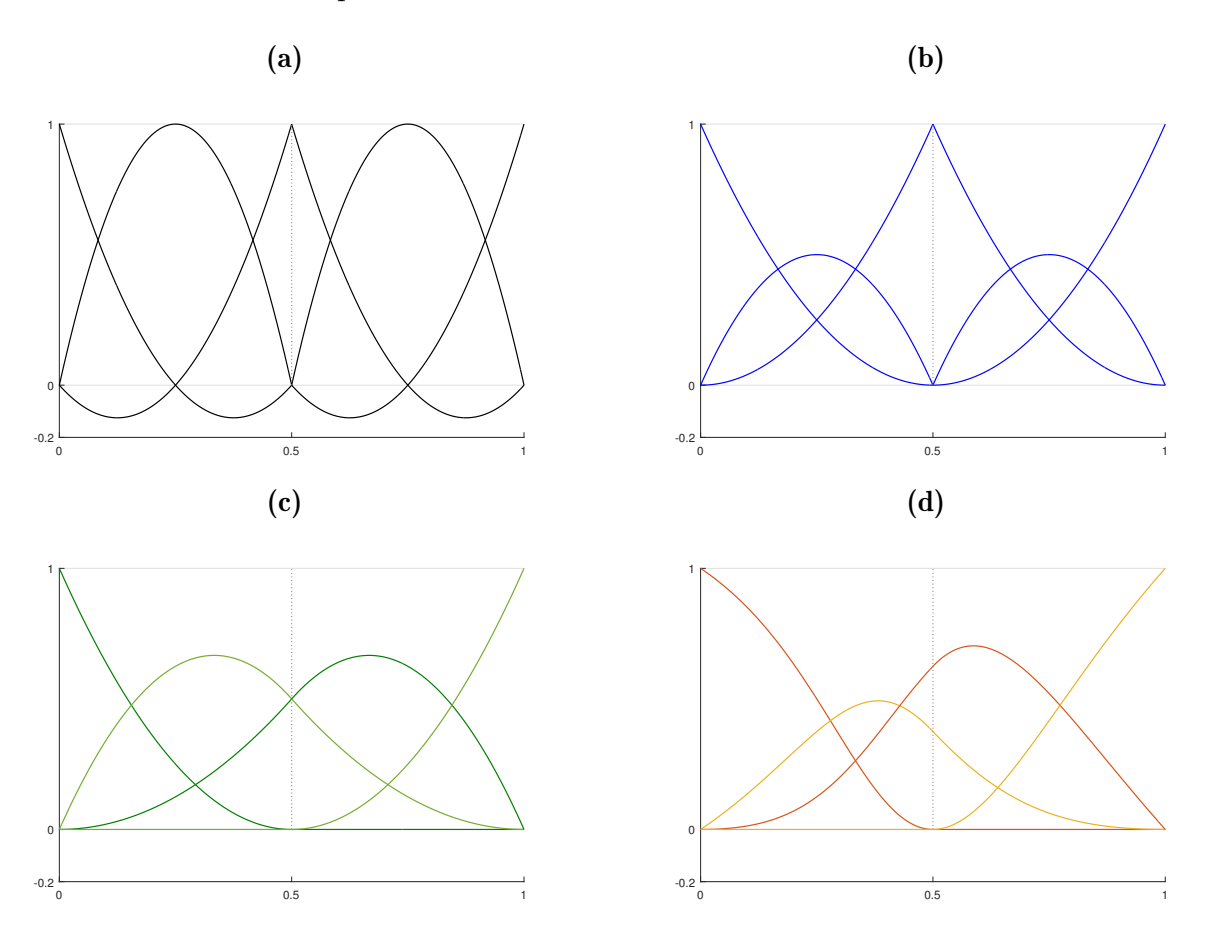


Figure 2.12 – Comparison of IGA discretization technology with the classical FEM Lagrange polynomials: a) Lagrange basis functions, b) Bernstein basis functions, c) BSpline basis functions, d) NURBS basis functions with $w = \{1,0.3,0.5,1\}$.

The Bézier extraction operator maps piecewise Bernstein basis onto BSplines basis thus allowing for the use of C^0 Bézier elements as the FE representation of NURBS/BSplines. Bézier elements of a NURBS geometry are computed through the use of the Bézier decomposition process (see Piegl and Tiller [90] for the algorithm), which typically requires all interior knots be repeated until they have a multiplicity k = p + 1. However for C^0 -continuity, multiplicity k = p is sufficient.

To perform the Bézier decomposition - suppose $\Xi = \{\xi_1, \xi_2, \xi_3, \cdots, \xi_{n_{\text{cpts}}+p+1}\}$ is a given knot vector and it is desired to insert a knot $\bar{\xi} \in [\xi_r, \xi_{r+1}[$ with r > p; it follows that:

- $n_{\rm cpts} + 1$ new basis functions are required for the new knot vector

$$\Xi = \left\{ \xi_1, \xi_2, \xi_3, \cdots, \xi_r, \bar{\xi}, \xi_{r+1}, \cdots, \xi_{n_{\text{cpts}}+p+1} \right\}$$

- $m = n_{\text{cpts}} + 1$ new control points are derived from the original control points as follows

$$\bar{\mathbf{P}}_{A} = \begin{cases}
\mathbf{P}_{1} & \text{if } A = 1 \\
\alpha_{A} \mathbf{P}_{A} + (1 - \alpha_{A}) \mathbf{P}_{A-1} & \text{if } 1 < A < m \\
\mathbf{P}_{n} & \text{if } A = m
\end{cases}$$
(2.17)

where

$$\alpha_{A} = \begin{cases} 1 & \text{if } 1 \leq A \leq r - p \\ \frac{\bar{\xi} - \xi_{A}}{\xi_{A+p} - \xi_{A}} & \text{if } r - p + 1 \leq A \leq r \\ 0 & \text{if } A \geq r + 1 \end{cases}$$
 (2.18)

To compute the Bézier extraction operator for a given knot vector of size $n_{\text{cpts}} + p + 1$ and n_{cpts} control points that define a BSplines curve: first each interior knot must be repeated p-times. Suppose $\{\bar{\xi}_1, \bar{\xi}_2, \cdots, \bar{\xi}_m\}$ is a set knots to be inserted to produce a Bézier decomposition; for each new knot $\bar{\xi}_j$, define α_A^j , $A = 1, 2, \cdots, n_{\text{cpts}} + j$ to be the A^{th} α as is defined in eq. (2.18). Defining $\mathbf{C}^j \in \mathbb{R}^{(n_{\text{cpts}}+j-1)\times(n_{\text{cpts}}+j)}$ as

$$\mathbf{C}^{j} = \begin{bmatrix} \alpha_{1} & 1 - \alpha_{2} & 0 & \cdots & 0 \\ 0 & \alpha_{2} & 1 - \alpha_{3} & 0 & \cdots & 0 \\ 0 & 0 & \alpha_{3} & 1 - \alpha_{4} & 0 & \cdots & 0 \\ \vdots & & & & & \\ 0 & \cdots & & & & \alpha_{n_{\text{cpts}}+j-1} & 1 - \alpha_{n_{\text{cpts}}+j} \end{bmatrix}$$
 (2.19)

To compute corresponding new control points created by knot refinement eq. (2.17) can be rewritten in matrix form as

$$\bar{\mathbf{P}}^{j+1} = \left(\mathbf{C}^j\right)^T \bar{\mathbf{P}}^j \tag{2.20}$$

with $\bar{\mathbf{P}}^1 = \mathbf{P}$ the first/original set of control points and the final set of control points for the Bézier decomposition are given by $\mathbf{P}_{\text{bez}} = \bar{\mathbf{P}}^{m+1}$, respectively. Defining $\mathbf{C}^T = (\mathbf{C}^m)^T (\mathbf{C}^{m-1})^T \cdots (\mathbf{C}^1)^T$, Bézier elements controls points then can be computed as

$$\mathbf{P}_{\text{bez}} = \mathbf{C}^T \mathbf{P} \tag{2.21}$$

It follows then that

$$N = CB_{\text{bez}} \tag{2.22}$$

where \mathbf{N} is the matrix containing BSplines basis functions, \mathbf{B}_{bez} the matrix containing the Bézier basis functions, and \mathbf{C} is the Bézier extraction operator. The computation of \mathbf{C} requires only the knot vector. The Bézier extraction operator therefore does not depend on the control points or basis functions. Note that in practice the global extraction operator \mathbf{C} is never computed, rather algorithms utilize local, element form, extraction operators \mathbf{C}^e .

For surface and volume elements, the univariate element extraction operators in the ξ , η , and ζ direction are \mathbf{C}_{ξ}^{i} , \mathbf{C}_{η}^{j} , and \mathbf{C}_{ζ}^{k} . The multivariate element extraction operator then becomes

$$\mathbf{C}_A^e = \mathbf{C}_\eta^i \otimes \mathbf{C}_\xi^j \tag{2.23}$$

and

$$\mathbf{C}_A^e = \mathbf{C}_\zeta^i \otimes \mathbf{C}_\eta^j \otimes \mathbf{C}_\xi^k \tag{2.24}$$

for surfaces and volumes, respectively.

A demonstration of the Bézier extraction process as well as its application to NURBS is detailed in Borden et al. [76]. Figure 2.13 shows a quadratic 4-elements BSplines surface representation of a quarter annulus and its decomposition into Bézier elements using the extraction operator.

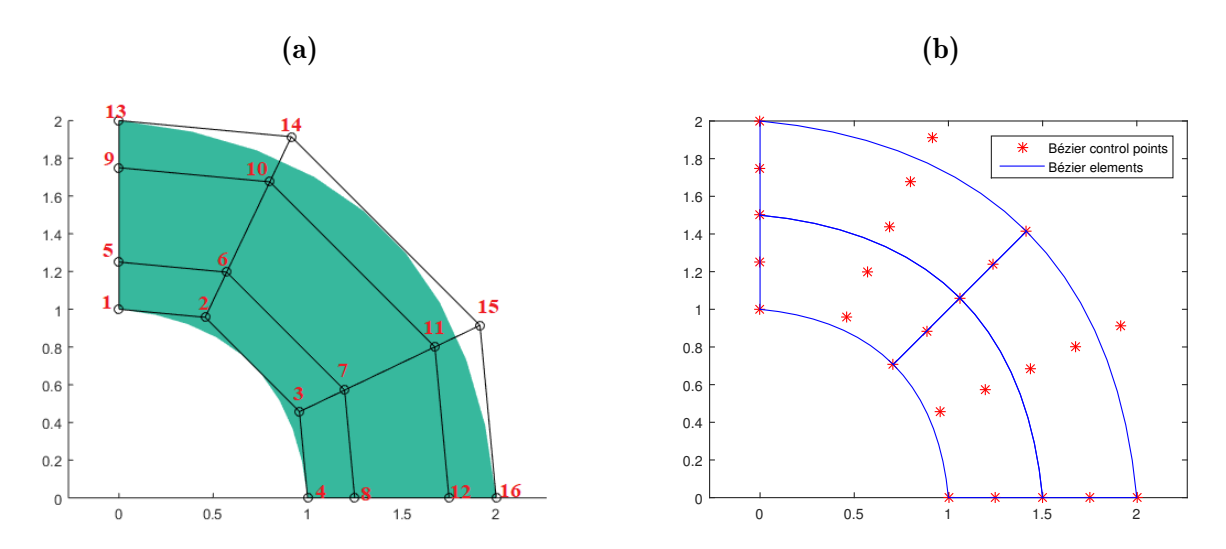


Figure 2.13 – Demonstration of Bézier extraction process of a 4-element BSplines quadratic surface : (a) the original BSplines surface, and (b) extracted Bézier elements.

2.3 The Isogeometric Finite Element Formulation

The purpose of performing Bézier extraction is to obtain an element structure that can be incorporated into existing FE codes [76]. In this section we present the isogeometric finite elements formulation, particularly the Bézier elements extracted as detailed in the previous section and how these fit into the more standard FEM. In the formulation presented we go one step further and address the limitations of the isogeometric methods stemming from the non-interpolatory nature of the basis functions: that is, typically in IGA, control points at which we seek the solution do not necessarily live on the actual geometry. This, as a result, can lead to difficulties during treatment of boundary conditions.

2.3.1 Bézier Elements and the Finite Element Framework

Recalling that in IGA the analysis geometry, in terms of the discretization, adopts the same mapping as the CAD geometry description, the physical points of the discretized geometry are then defined by the mapping:

$$\mathbf{x}(\boldsymbol{\xi}) = \sum_{A=1}^{n_{\text{cpts}}} \mathbf{P}_A N_A(\boldsymbol{\xi})$$
 (2.25)

Note: control points (\mathbf{P}_A) serve the same role as nodes in standard FEM.

The entry point for FEM is the weak form of the problem. Suppose \mathcal{U} is the space of admissible solutions and \mathcal{U}_0 is the space of weighting functions w, the weak formulation writes as

Find $u \in \mathcal{U}$ such that

$$a(w,u) = b(w), \quad \forall w \in \mathcal{U}_0$$
 (2.26)

where $a(\cdot,\cdot)$ and $b(\cdot)$ are bi-linear and linear forms, respectively.

Garlekin's method is then used to construct finite-dimensional approximations of \mathcal{U} and \mathcal{U}_0 as subspaces $\mathcal{U}^h \subset \mathcal{U}$ and $\mathcal{U}_0^h \subset \mathcal{U}_0$ from the geometric basis. The Garlekin formulation writes as:

Find $u^h \in \mathcal{U}^h$ such that

$$a(w^h, u^h) = b(w^h), \quad \forall w^h \in \mathcal{U}_0^h \tag{2.27}$$

Invoking the isoparametric concept, the fields u^h and w^h can be written as

$$w^h = \sum_{A=1}^{n_{\text{cpts}}} c_A N_A \tag{2.28}$$

$$u^h = \sum_{B=1}^{n_{\text{cpts}}} u_B N_B \tag{2.29}$$

 c_A and u_B are control variables (coefficients at the control points). Substituting the above into the Garlekin formulation, we get

$$a(N_A, N_B) = b(N_A) \tag{2.30}$$

in matrix form, the problem writes as

$$\mathbf{K}\mathbf{u} = \mathbf{F} \tag{2.31}$$

where

$$\mathbf{K} = a(N_A, N_B) \tag{2.32}$$

$$\mathbf{u} = \{u_B\} \tag{2.33}$$

$$\mathbf{F} = b(N_A) \tag{2.34}$$

 ${\bf K}$ is the global stiffness matrix and ${\bf F}$ is the global force vector (these can be computed by numerical integration - i.e. through Gaussian quadrature - over each Bézier element and assembling the elemental contributions into their global counterparts), and ${\bf u}$ is the solution vector (computed at the control points).

In standard FEM integration is performed on the parent element space, usually a bi-unit element in 2D or a unit cube in 3D, and then mapped onto the physical space. In isogeometric framework integrals are first pulled back on to the parameter space, and then to the parent space [13, 75, 76] as is shown in fig. 2.14. Therefore the evaluation of the global basis functions and their derivatives, as well as the Jacobian determinant of the mapping from the physical space to the parent space, is required for each quadrature Gauss point in the parent element.

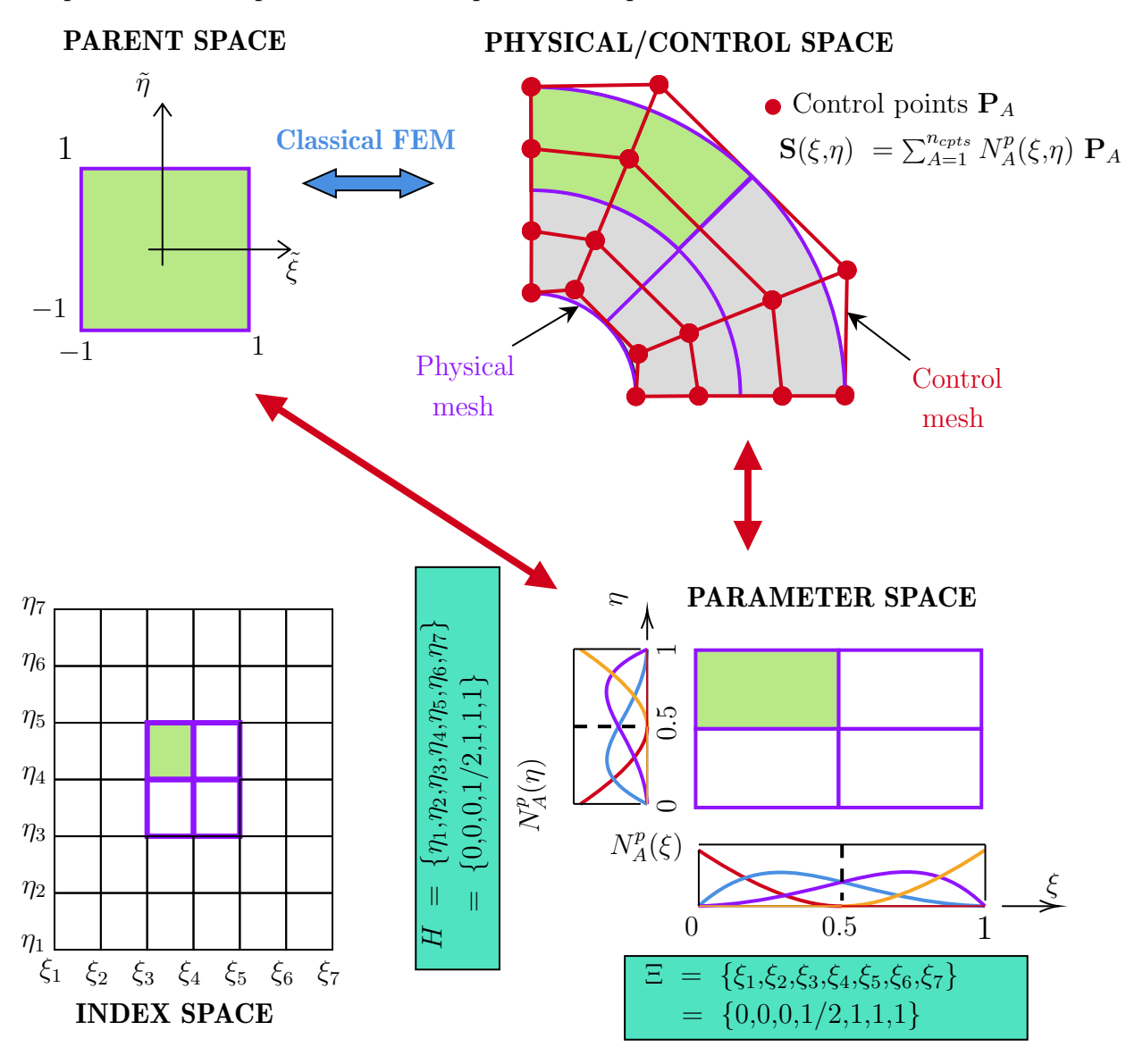


Figure 2.14 – Different spaces considered in the context of BSplines-based IGA : from the physical space to control space to parameter space finally the parent space.

Recall that the global shape functions may be computed from the Bernstein basis and extraction operator as $N = CB_{bez}$. In elemental form this becomes

$$\mathbf{N}^e = \mathbf{C}^e \mathbf{B}_{\text{bez}}^e \tag{2.35}$$

and the derivatives with respect to the parametric coordinates given by eq. (2.36)

$$\frac{\partial \mathbf{N}^e}{\partial \boldsymbol{\xi}} = \mathbf{C}^e \frac{\partial \mathbf{B}_{\text{bez}}^e}{\partial \boldsymbol{\xi}} \tag{2.36}$$

Derivatives of the basis functions with respect to the physical coordinates are computed as

$$\frac{\partial \mathbf{N}^e}{\partial \mathbf{x}} = \frac{\partial \mathbf{N}^e}{\partial \boldsymbol{\xi}} \frac{\partial \boldsymbol{\xi}}{\partial \mathbf{x}} \tag{2.37}$$

with

$$\frac{\partial \boldsymbol{\xi}}{\partial \mathbf{x}} = \left[\frac{\partial \mathbf{x}}{\partial \boldsymbol{\xi}} \right]^{-1} = \left[\mathbf{C}^e \frac{\partial \mathbf{B}_{\text{bez}}^e}{\partial \boldsymbol{\xi}} \mathbf{P}^T \right]^{-1}$$
(2.38)

Finally the determinant of the Jacobian $\det J$ is computed as

$$\det J = \left| \frac{\partial \mathbf{x}}{\partial \boldsymbol{\xi}} \frac{\partial \boldsymbol{\xi}}{\partial \tilde{\boldsymbol{\xi}}} \right| \tag{2.39}$$

If the Bernstein basis are redefined in an interval [-1,1], recursively they write as [76]:

$$B_i^p(\xi) = \frac{1}{2} (1 - \xi) B_i^{p-1}(\xi) + \frac{1}{2} (1 + \xi) B_{i-1}^{p-1}(\xi)$$
 (2.40)

with

$$B_1^0(\xi) \equiv 1$$

and

$$B_i^p(\xi) \equiv 0$$
 if $i < 1$ or $i > p+1$

With eq. (2.39) the mapping from parameter space into parent space is an identity. Finally the determinant of the Jacobian is computed as

$$\det J = \left| \frac{\partial \mathbf{x}}{\partial \boldsymbol{\xi}} \right| \tag{2.41}$$

With this formulation detailed above, the solution is computed at control points which do not necessarily interpolate the actual geometry and as previously mentioned this can pose some difficulties during treatment of boundary conditions. In the next section, we introduce a computational domain transformation method that allows us to directly compute for the actual physical solution instead of the control solution.

2.3.2 Bézier-based Isogeometric Analysis

As mentioned in the previous section, in the IGA framework the solution is sought out at the control points which do not necessarily live on the physical geometry. An additional step is then required to recover the actual physical solution and this can be done through the mapping:

$$\mathbf{u}^{\text{phy}} = \sum_{A=1}^{n_{\text{cpts}}} \mathbf{u}_A^{\text{cntrl}} N_A\left(\boldsymbol{\xi}\right)$$
 (2.42)

However, this non-interpolatory nature of IGA may pose some difficulties during the imposition of boundary conditions. This is particularly the case when boundary conditions are prescribed on boundaries not interpolated by the control points [13, 37, 72, 75, 92], for instance, the inner and outer boundaries of the quarter annulus shown in fig. 2.13. Writing the system of equations

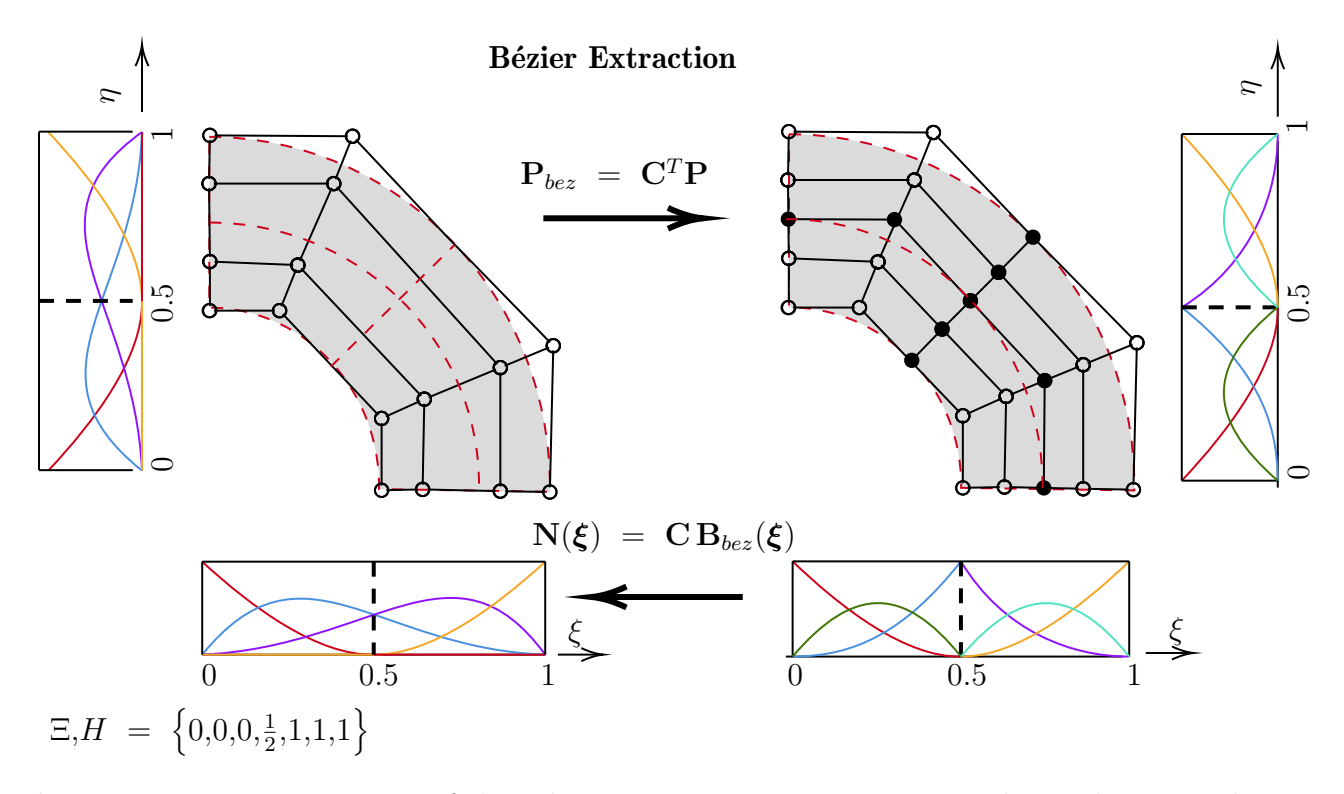


Figure 2.15 – Demonstration of the Bézier extraction process on a single patch 2D quadratic (p=2) BSplines surface containing 4 elements : \circ - BSplines control points, \bullet - additional control points generated for the Bézier elements.

in eqs. (2.30) to (2.34) in terms of the physical solution can alleviate this difficulty. Taking inspiration from the work of Kamoso [88]: suppose we have Bézier elements obtained through the Bézier extraction process of a BSplines surface outlined in section 2.2.4 - see fig. 2.15.

Instead of computing the solution at the Bézier elements control points in fig. 2.15, here the aim is to compute the solution directly at the physical points by performing a full computation space transformation [93] - see fig. 2.16.

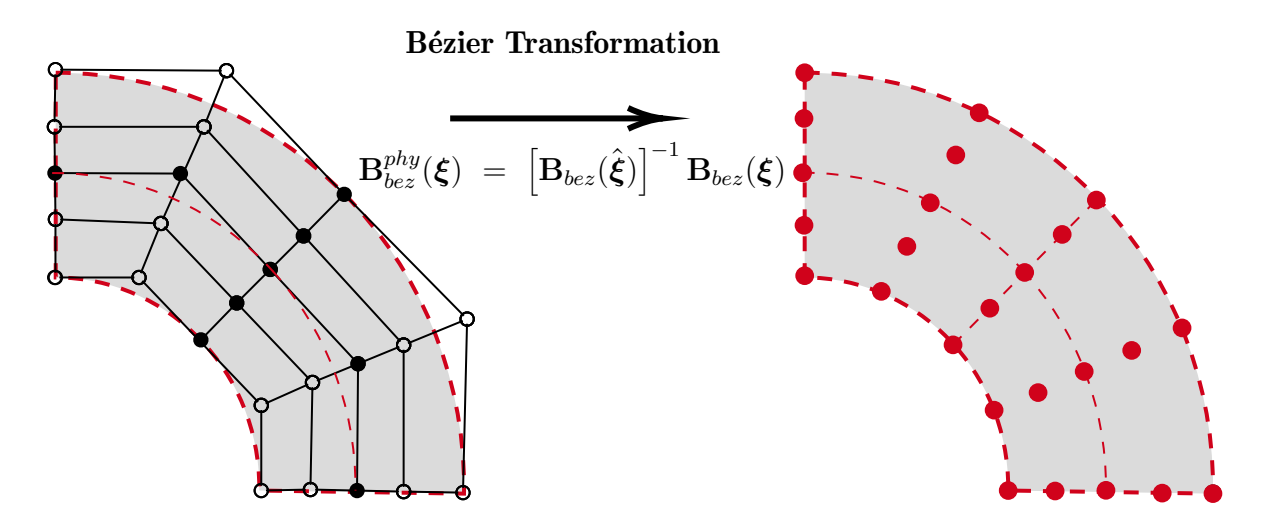


Figure 2.16 – Bézier transformation from the control mesh (left) to the physical mesh (right).

Using Bernstein polynomials as a basis, recalling that the physical variables can be obtained from control variables as follows

$$\mathbf{u}^{\text{phy}} = \mathbf{B}_{\text{bez}} \mathbf{u}^{\text{cntrl}} \tag{2.43}$$

Inverting the relation in eq. (2.43), for each element we can write the control variables in terms of the physical quantities as

$$\mathbf{u}^{\text{cntrl}} = \left[\mathbf{B}_{\text{bez}}\right]^{-1} \mathbf{u}^{\text{phy}} \tag{2.44}$$

 $[\mathbf{B}_{\mathrm{bez}}]^{-1}$ is the *Bézier inverse matrix*. To demonstrate how the Bézier inverse matrix is incorporated in the system of equations : consider linear static equilibrium equations in weak form, for each Bézier element this writes as

$$\int_{\Omega e} \boldsymbol{\sigma} : \boldsymbol{\epsilon} (\delta \mathbf{u}^{\text{cntrl}}) d\Omega - \int_{\Gamma_e} (\delta \mathbf{u}^{\text{cntrl}})^T \cdot \bar{\mathbf{t}}_F d\Gamma = 0$$
(2.45)

Substituting eq. (2.44) into eq. (2.45), we then have

$$\int_{\Omega_{e}} \left[\mathbf{B}_{\text{bez}} \right]^{-T} \left(\boldsymbol{\sigma} : \boldsymbol{\epsilon} (\delta \mathbf{u}^{\text{phy}}) \right) d\Omega - \int_{\Gamma_{e}} \left(\left[\mathbf{B}_{\text{bez}} \right]^{-1} \delta \mathbf{u}^{\text{phy}} \right)^{T} \cdot \bar{\mathbf{t}}_{F} d\Gamma = 0$$
 (2.46)

Resolution of eq. (2.46) amounts to seeking the solution at physical points and with this formulation, boundary conditions can be imposed directly. It remains however to define the Bézier inverse matrix, that is, at which parameter values ξ is this matrix evaluated?

To evaluate the Bézier inverse matrix, we can take inspiration from the isogeometric collocations methods (IGA-C) where typically the BSplines Greville and Botella abscissae are used as collocation points [70, 72, 94]. This is because the number of Botella and Greville points equals to that of the control points. These points are defined as follows:

• Greville points are computed from the following

$$\hat{\xi}_i = \frac{\xi_{i+1} + \dots + \xi_{i+p}}{p} \tag{2.47}$$

• Botella points $\hat{\xi}_i$ are the abscissae of the maxima of the BSplines basis functions

with $\hat{\xi}_i \in [0,1]$. In fig. 2.17 we show the Greville and Botella points together with knot values of a quadratic, p = 2, BSplines supported on knot vector $\Xi = \{0,0,0,\frac{1}{3},\frac{1}{2},\frac{2}{3},1,1,1\}$.

Once we have the Greville and Botella points, we need to derive the equivalent of these points for the Bézier description. To do this, recall that in the design of BSplines, the control polygon has vertices $(\tilde{\xi}_i, d_i)$ where d_i are the control points [89]. Moreover BSplines possess the affine invariance property, that is, the parameter space will transform at the same ratio as the physical space. Since from Bézier extraction process we have

$$\mathbf{P}_{ ext{bez}} = \mathbf{C}^T \mathbf{P}$$

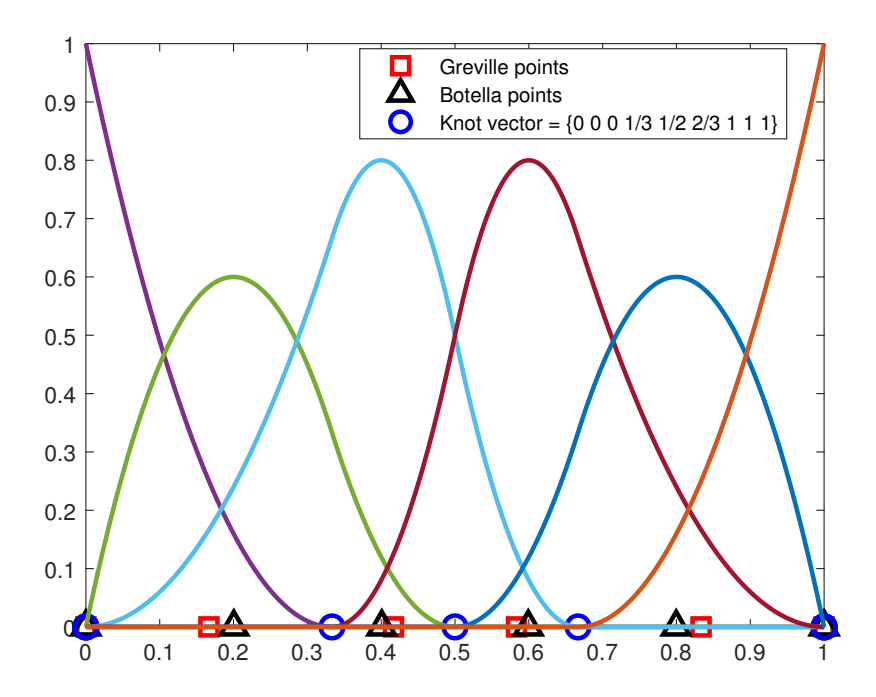


Figure 2.17 – Botella and Greville abscissae of BSplines basis supported on knot vector $\Xi = \{0,0,0,\frac{1}{3},\frac{1}{2},\frac{2}{3},1,1,1\}.$

The Bézier equivalent of the Greville and Botella points can be obtained through the same transformation (Bézier extraction). Using the Bézier extraction operator \mathbf{C}^T , we can compute the Bézier equivalent Greville and Botella points from eq. (2.48) as follows:

$$\hat{\boldsymbol{\xi}}_{\text{bez}} = \mathbf{C}^T \hat{\boldsymbol{\xi}} \tag{2.48}$$

Finally, we perform a linear mapping of the obtained $\hat{\boldsymbol{\xi}}_{bez}$ on to [-1,1] preferred parameter space. The resulting points are then be used to compute the Bézier inverse matrix.

To show an example of these Bézier equivalent points, again consider the BSplines basis in fig. 2.17 consisting of 4 knot spans which is equivalent to 4 elements. We computed both the Greville and Botella equivalent points for the clamped knot vector with quadratic basis functions as well as with cubic basis functions. Table 2.2 and table 2.3 summarizes the results obtained.

Order	Element1	Element 2	Element 3	Element 4
Quadratic, $p = 2$	$-1 \ 0 \ 1$	$-1 \ 0 \ 1$	$-1 \ 0 \ 1$	$-1 \ 0 \ 1$
	-1	-1	-1	-1
Cubic, $p = 3$	$-\frac{1}{3}$	$-\frac{1}{3}$	$-\frac{1}{3}$	$-\frac{1}{3}$
Cubic, $p = 3$	$+\frac{1}{3}$	$+\frac{1}{3}$	$+\frac{1}{3}$	$+\frac{1}{3}$
	+1	+1	+1	+1

Table 2.2 – Bézier equivalent Greville points computed from knot vectors $\Xi = \left\{0,0,0,\frac{1}{3},\frac{1}{2},\frac{2}{3},1,1,1\right\}$ for p=2 and $\Xi = \left\{0,0,0,0,\frac{1}{3},\frac{1}{2},\frac{2}{3},1,1,1,1\right\}$ for p=3.

Order	Element1	Element 2	Element 3	Element 4	
Quadratic, $p = 2$	-1 0.2 1	-1 -0.1952 1	-1 0.1952 1	-1 -0.2 1	
	-1	-1	-1	-1	
Cubic, $p = 3$	-0.2386	-0.3026	-0.3507	-0.4178	
Cubic, $p=3$	+0.4205	+0.3470	+0.3020	+0.2401	
	+1	+1	+1	+1	

Table 2.3 – Bézier equivalent Botella points computed from knot vectors $\Xi = \{0,0,0,\frac{1}{3},\frac{1}{2},\frac{2}{3},1,1,1\}$ for p = 2 and $\Xi = \{0,0,0,0,\frac{1}{3},\frac{1}{2},\frac{2}{3},1,1,1,1\}$ for p = 3.

From the results in table 2.2 and table 2.3, it is observed that with Greville collocation points, the Bézier equivalent points remain the same for all elements. On the other hand, the Botella equivalent points are changing for each element. The implication is then with Greville equivalent points we can compute the Bézier inverse matrix once and then store it for use. However with Botella equivalent points, the Bézier matrix has to be evaluated and inverted for each element, which can then increase the global matrices assembly time.

Once the Bézier inverse matrix is known, we can proceed as in section 2.3.1, however in this case the control points are extracted. This matrix can be incorporated directly into the shape functions routine.

It is important to note that this entails in localizing the global smooth topology (patch level) to the Bézier elemental level. In fact, here, the link to the BSplines is maintained, and therefore at any instance we can always recover the BSplines geometry. More over, due to the affine invariance property of the Bernstein basis (any translation, rotation, expansion, and contraction applied in the physical space, the parameter space is scaled in the same way and vice versa) the Bézier elements automatically satisfy the patch test requirements [12, 13].

2.4 Application of Isogeometric Analysis to Linear Statics

The objective of this section is to demonstrate how to apply isogeometric finite element method to linear elasticity Dirichlet Boundary Value Problem and to study the performance of the proposed Bézier-based IGA method. Two methods with BSplines global geometry description are implemented, namely:

(1) BSplines-based isogeometric analysis

Outlined in section 2.3.1

- the solution is sought out at the global BSplines control points; we solve for $\mathbf{u}^{\text{cntrl}}$.

The physical solution is obtained through a mapping

$$\mathbf{u}^{\text{phy}} = \sum_{A=1}^{n_{\text{cpts}}} u_A^{\text{cntrl}} N_A(\xi)$$

- basis functions are computed through the Bézier extraction operator, that is for each element

$$\mathbf{N}^e = \mathbf{C}^e \mathbf{B}_{\mathrm{bez}}^e$$

(2) Bézier-based isogeometric analysis

Outlined in section 2.3.2

- requires computation of Bézier control points from the global BSplines ones through the use of Bézier extraction operator

$$\mathbf{P}_{\text{bez}} = \mathbf{C}^T \mathbf{P}$$

- through the use of the Bézier inverse matrix, we solve directly for the physical solution $\mathbf{u}^{\mathrm{phy}}$

For improved accuracy in the geometry description, the global geometry is constructed from control points that are computed using the exact interpolation method described in section 2.2.3.

2.4.1 Problem Description

Consider a 2D quarter of an annulus geometry under plane stress conditions, with inner radius $r_{int} = 1$ m and outer radius $r_{ext} = 2$ m, depicted in fig. 2.18, to be occupying a domain Ω , with its boundary denoted by Γ . The body is assumed to be linear elastic with isotropic material properties: Young's modulus E = 10000 Pa, Poisson's ratio $\nu = 0.25$.

There are no body forces acting on domain Ω . The boundary of the domain Γ is decomposed into disjoint parts Γ_F and Γ_D on which tractions \mathbf{t}_F and displacements \mathbf{u}_D are imposed, respectively. In this case only Dirichlet boundary conditions are present: the left edge is fixed (homogeneous Dirichlet boundary conditions, that is $\mathbf{u}(0, y) = \mathbf{0}$), and the bottom horizontal edge is subjected to uniform displacements $\bar{u} = 0.001$ m in the x-direction.

The strong formulation writes as follows: find stress field σ , strain field ϵ , and displacement \mathbf{u} , such that:

$$\operatorname{div} \boldsymbol{\sigma} = \mathbf{0} \quad \text{in} \quad \Omega \tag{2.49a}$$

$$\sigma = \mathbf{D} : \epsilon \quad \text{in} \quad \Omega$$
 (2.49b)

$$\epsilon \simeq \frac{1}{2} \left(\nabla \mathbf{u} + \nabla \mathbf{u}^T \right) \text{ in } \Omega$$
 (2.49c)

$$\mathbf{u} = \mathbf{u}_D \quad \text{on} \quad \Gamma_D \tag{2.49d}$$

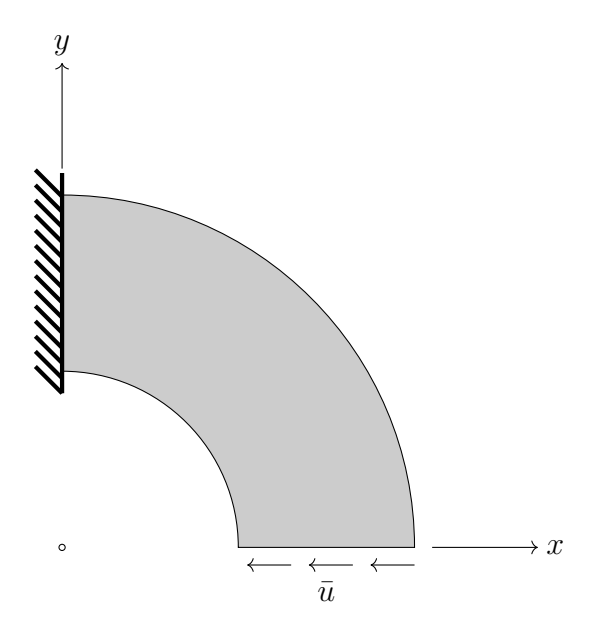


Figure 2.18 – Schematic of 2D quarter of an annulus geometry under prescribed displacement load \bar{u} .

D the elasticity tensor. The weak form of the problem detailed in eqs. (2.49a) to (2.49d) writes as

$$\int_{\Omega} (\nabla \boldsymbol{w})^T : \boldsymbol{\sigma} \ d\Omega = 0, \ \forall \boldsymbol{w} \in \mathcal{U}_0$$
 (2.50)

In plane stress conditions the stress field and strain field can both be reduced to vectorial fields and the elasticity tensor reduces to a 2D tensor as shown in eq. (2.51) below.

$$\boldsymbol{\sigma} = \begin{cases} \sigma_{11} \\ \sigma_{22} \\ \sigma_{12} \end{cases}, \qquad \mathbf{D} = \frac{E}{1 - \nu^2} \begin{bmatrix} 1 & \nu & 0 \\ \nu & 1 & 0 \\ 0 & 0 & 1 - \nu \end{bmatrix}, \qquad \boldsymbol{\epsilon} = \begin{cases} \epsilon_{11} \\ \epsilon_{22} \\ \epsilon_{12} \end{cases}$$
 (2.51)

In classical FEM the above problem solves as

$$Ku = F$$

In the next sections we will demonstrate how this problem solves in an IGA setting. For readability, we use square brackets for matrix form quantities and braces for vector form quantities.

2.4.2 BSplines-based Isogeometric Analysis

Similarly to classical finite element method, in an IGA framework the isoparametric concept is invoked; that is:

$$\boldsymbol{w} = \sum_{A=1}^{n_{\text{cpts}}} c_A^{\text{cntrl}} N_A(\boldsymbol{\xi}) = [\mathbf{N}] \{ \mathbf{c}^{\text{cntrl}} \}$$
 (2.52)

$$\mathbf{u} = \sum_{B=1}^{n_{\text{cpts}}} u_B^{\text{cntrl}} N_B(\boldsymbol{\xi}) = [\mathbf{N}] \{ \mathbf{u}^{\text{cntrl}} \}$$
 (2.53)

In eqs. (2.52) and (2.53) $\{\bullet^{\text{cntrl}}\}$ denotes a control quantity, and **N** are the BSplines basis functions computed for each element using the extraction operator as in eq. (2.54):

$$\mathbf{N} = \mathbf{C}^e \mathbf{B}_{\text{bez}} \tag{2.54}$$

where \mathbf{B}_{bez} is the Bernstein basis. From the weak formulation in eq. (2.50), we compute the derivative of the test function as

$$\nabla \boldsymbol{w} = \nabla([\mathbf{N}]\{\mathbf{c}\}) \tag{2.55}$$

Since $\{c\}$ are coefficients at the control points, eq. (2.55) then becomes

$$\nabla \boldsymbol{w} = \underbrace{\begin{bmatrix} \frac{\partial}{\partial x} & 0\\ 0 & \frac{\partial}{\partial y}\\ \frac{\partial}{\partial y} & \frac{\partial}{\partial x} \end{bmatrix}}_{[\mathbf{B}]} [\mathbf{N}] \{ \mathbf{c} \} = [\mathbf{B}] \{ \mathbf{c} \}$$
(2.56)

In eq. (2.56), matrix [**B**] contains the spatial gradients of the basis functions. From eq. (2.49b) and eq. (2.49c), we can write the stress field as

$$\boldsymbol{\sigma} = [\mathbf{D}] [\mathbf{B}] \left\{ \mathbf{u}^{\text{cntrl}} \right\} \tag{2.57}$$

Substituting eq. (2.56) and eq. (2.57) into the weak form in eq. (2.50) we get

$$\left\{\mathbf{c}\right\}^{T} \left(\left[\int_{\Omega} \left[\mathbf{B}\right]^{T} \left[\mathbf{D}\right] \left[\mathbf{B}\right] \, \det J \, \mathrm{d}\eta \, \, \mathrm{d}\xi \right] \left\{\mathbf{u}^{\mathrm{cntrl}}\right\} + \left[\int_{\Omega} \left[\mathbf{B}\right]^{T} \left[\mathbf{D}\right] \left[\mathbf{B}\right] \, \det J \, \mathrm{d}\eta \, \, \mathrm{d}\xi \right] \left\{\mathbf{u}_{D}\right\} \right) = 0 \quad (2.58)$$

and since $\{\mathbf{c}\}^T$ are arbitrary, eq. (2.58) reduces to :

$$\left[\int_{\Omega} \left[\mathbf{B} \right]^{T} \left[\mathbf{D} \right] \left[\mathbf{N} \right] \, \det J \, \mathrm{d}\eta \, \, \mathrm{d}\xi \right] \left\{ \mathbf{u}^{\mathrm{cntrl}} \right\} + \left[\int_{\Omega} \left[\mathbf{B} \right]^{T} \left[\mathbf{D} \right] \left[\mathbf{B} \right] \, \det J \, \mathrm{d}\eta \, \, \mathrm{d}\xi \right] \left\{ \mathbf{u}_{D} \right\} = 0 \qquad (2.59)$$

In short notation eq. (2.59) can be written as

$$\mathbf{K}\mathbf{u}^{\text{cntrl}} = \mathbf{K}\mathbf{u}_D \tag{2.60}$$

where

$$\mathbf{K} = \int_{\Omega} [\mathbf{B}]^T [\mathbf{D}] [\mathbf{B}] \, \det J \, \mathrm{d}\eta \, \, \mathrm{d}\xi$$
 (2.61)

is the stiffness matrix.

The storage of the degrees of freedom follows the convention below (n_{cpts} is the control points, $2n_{\text{cpts}}$ total number of DOFs)

$$\mathbf{u}^{\text{cntrl}} = \begin{cases} u_1 \\ \vdots \\ u_{n_{\text{cpts}}} \\ v_1 \\ \vdots \\ v_{n_{\text{cpts}}} \end{cases}$$
 (2.62)

Defining the force \mathbf{F}_D as

$$\mathbf{F}_D = -\mathbf{K}\mathbf{u}_D$$

We then seek to solve the system

$$\begin{bmatrix} K_{1,1} & \cdots & K_{1,2n_{\text{cpts}}} \\ \vdots & \ddots & \vdots \\ \vdots & \ddots & \vdots \\ K_{2n_{\text{cpts}},1} & \cdots & K_{2n_{\text{cpts}},2n_{\text{cpts}}} \end{bmatrix} \begin{pmatrix} u_1 \\ \vdots \\ u_{n_{\text{cpts}}} \\ v_1 \\ \vdots \\ v_{n_{\text{cpts}}} \end{pmatrix} = \begin{pmatrix} F_{D_1} \\ \vdots \\ F_{D_{n_{\text{cpts}}}} \\ F_{D_{n_{\text{cpts}}}+1} \\ \vdots \\ F_{D_{2n_{\text{cpts}}}} \end{pmatrix}$$

$$(2.63)$$

Similarly to standard FEM, the integration of the stiffness matrix in eq. (2.61) is performed in the parent element space (through numerical integration specifically Gauss quadrature). Each elemental contributions are then assembled on to the global stiffness matrix in eq. (2.63). The elemental stiffness matrix is computed as:

$$\mathbf{k}^{e} = \sum_{\text{GPs}} [\mathbf{B}]^{T} [\mathbf{D}] [\mathbf{B}] \det J w_{\text{GPs}}$$
(2.64)

Now to compute **B** and $\det J$, for each element first compute the Jacobian matrix **J** as follows

$$\mathbf{J} = \begin{bmatrix} \dots & \frac{\partial N_a(\xi)}{\partial \xi} & \dots \\ \dots & \frac{\partial N_a(\xi)}{\partial \eta} & \dots \end{bmatrix} \begin{bmatrix} \mathbf{P}_x & \mathbf{P}_y \end{bmatrix}, \quad a = 1, \dots, n_{cpts}^e$$
 (2.65)

 \mathbf{P}_x , \mathbf{P}_y are vectors containing the x and y position of the control points and n_{cpts}^e are the number of control points in each element. Finally the spatial derivatives matrix \mathbf{B} is computed as:

$$\mathbf{B} = \begin{bmatrix} \cdots & N_{a,x} & \cdots & 0 & \cdots & 0 \\ 0 & \cdots & 0 & \cdots & N_{a,y} & \cdots \\ \cdots & N_{a,y} & \cdots & \cdots & N_{a,x} & \cdots \end{bmatrix} = [\mathbf{J}]^{-1} \begin{bmatrix} \cdots & \frac{\partial N_a(\boldsymbol{\xi})}{\partial \boldsymbol{\xi}} & \cdots \\ \cdots & \frac{\partial N_a(\boldsymbol{\xi})}{\partial \eta} & \cdots \end{bmatrix}$$
(2.66)

and $\det J = \det([\mathbf{J}])$.

Since for the problem considered here the displacement boundary conditions are specified on the edges at which the control points are interpolated by the physical geometry, they can be imposed directly to the control points. See fig. 2.19 which demonstrates the location of the BSplines control points (which serve the same role of 'nodes' in standard FEM) with respect to the actual geometry for a 3×3 mesh.

The BSpilnes approach described above is then applied to solve the problem described in fig. 2.18. 50 quadratic (p = 2) elements are used to discretize the geometry (10 elements in the ξ -direction, and 5 elements in the η -direction, 10 × 5 mesh), with a total 168 DOFs. Results obtained are shown in fig. 2.20 and fig. 2.21 below.

Figure 2.20 shows the horizontal component (fig. 2.20a) and vertical component (fig. 2.20b) of the displacement field obtained. The maximum displacement is observed in the right bottom tip of the beam.

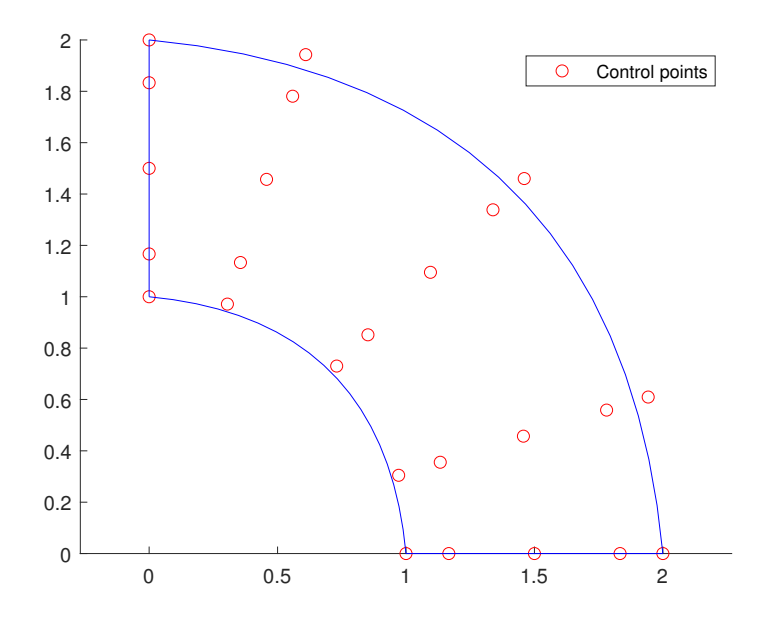


Figure 2.19 – BSplines computation points location with respect to the actual physical geometry, with a 3×3 mesh.

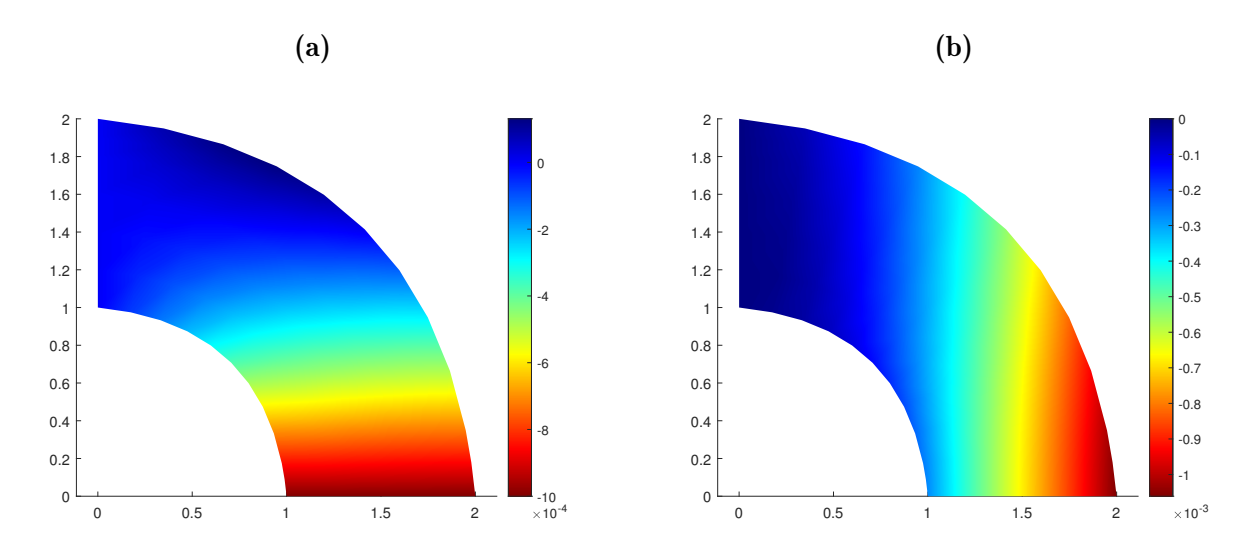


Figure 2.20 – Displacement field [m] obtained from the BSplines approach: (a) x-component of the diplacement field, and (b) y-component of the displacement field.

In fig. 2.21 we show the normal stress distribution (fig. 2.21a) and Von Mises stress distribution (fig. 2.21b). As is typical of bending problems compressive stresses are observed on the inside of the beam and the outside of the beam is in tension. In this problem compressive stresses are more superior than the tensile stresses, hence the non symmetry of the Von Mises stress distribution (curved beam). Maximum Von Mises stress is observed on the inside of the beam.

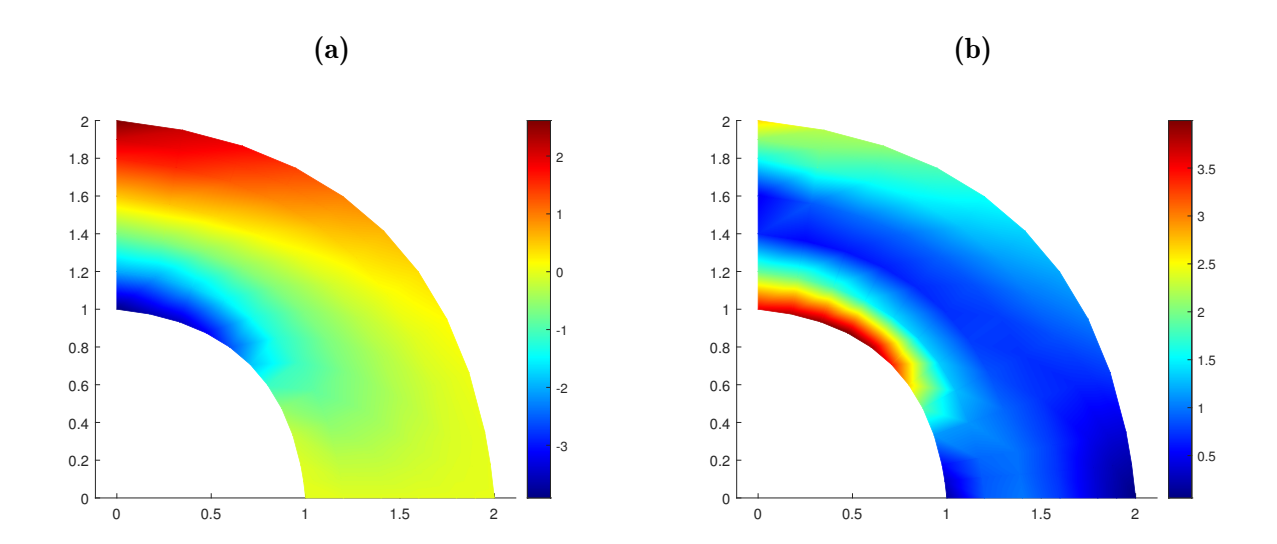


Figure 2.21 – Stress field distribution [Pa] obtained from the BSplines approach : (a) normal stress distribution, σ_{11} , and (b) Von Mises stress distribution.

2.4.3 Bézier-based Isogeometric Analysis

The Bézier based approach also invokes the isogeometric and isoparametric concept however now with Bernstein polynomials as a basis, that is:

$$\boldsymbol{w} = \sum_{A=1}^{n_{\text{cpts}}} c_A^{\text{cntrl}} B_{\text{bez}_A}(\boldsymbol{\xi}) = [\mathbf{B}_{\text{bez}}] \{ \mathbf{c}^{\text{cntrl}} \}$$
(2.67)

$$\mathbf{u} = \sum_{B=1}^{n_{\text{cpts}}} u_B^{\text{cntrl}} B_{\text{bez}_B}(\boldsymbol{\xi}) = [\mathbf{B}_{\text{bez}}] \{ \mathbf{u}^{\text{cntrl}} \}$$
(2.68)

For this approach, the departure point is the BSplines geometry description, as detailed in section 2.3.2, with control points \mathbf{P} . The Bézier control points \mathbf{P}_{bez} (local/element-level) are then derived through the Bézier extraction process as follows:

$$\mathbf{P}_{\text{bez}} = \mathbf{C}^T \mathbf{P} \tag{2.69}$$

Note that in using the Bézier based approach, it amounts to solving a larger model in terms of number of DOFs in the system compared to the BSplines based approach (see fig. 2.13 that demonstrates the extraction of Bézier elements from a BSpline surface). To build the system of equations to be solved, first the derivative of the test function is computed as

$$\nabla \boldsymbol{w} = \nabla([\mathbf{B}_{\text{bez}}]\{\mathbf{c}\}) \tag{2.70}$$

which then becomes

$$\nabla \boldsymbol{w} = \underbrace{\begin{bmatrix} \frac{\partial}{\partial x} & 0\\ 0 & \frac{\partial}{\partial y}\\ \frac{\partial}{\partial y} & \frac{\partial}{\partial x} \end{bmatrix}}_{[\mathbf{B}]} [\mathbf{B}_{\text{bez}}] \{c\} = [\mathbf{B}] \{\mathbf{c}\}$$
(2.71)

The storage of the degrees of freedom follows the convention described in the BSplines based approach (see eq. (2.62)). To compute the spatial derivatives matrix, first compute the Jacobian

matrix as:

$$\mathbf{J} = \begin{bmatrix} \cdots & \frac{\partial B_{\text{bez}_a}(\boldsymbol{\xi})}{\partial \boldsymbol{\xi}} & \cdots \\ \cdots & \frac{\partial B_{\text{bez}_a}(\boldsymbol{\xi})}{\partial \boldsymbol{\eta}} & \cdots \end{bmatrix} \begin{bmatrix} \mathbf{P}_{\text{bez}_x} & \mathbf{P}_{\text{bez}_y} \end{bmatrix}, \quad a = 1, \dots, n_{cpts}^e$$
(2.72)

 $\mathbf{P}_{\text{bez}_x}$, $\mathbf{P}_{\text{bez}_y}$ are the x, y coordinates of the Bézier elements control points. Accordingly, the spatial derivatives matrix \mathbf{B} follows as :

$$\mathbf{B} = \begin{bmatrix} \cdots & B_{\text{bez}_{a,x}} & \cdots & 0 & \cdots & 0 \\ 0 & \cdots & 0 & \cdots & B_{\text{bez}_{a,y}} & \cdots \\ \cdots & B_{\text{bez}_{a,y}} & \cdots & \cdots & B_{\text{bez}_{a,x}} & \cdots \end{bmatrix} = [\mathbf{J}]^{-1} \begin{bmatrix} \cdots & \frac{\partial B_{\text{bez}_{a}}(\boldsymbol{\xi})}{\partial \boldsymbol{\xi}} & \cdots \\ \cdots & \frac{\partial B_{\text{bez}_{a}}(\boldsymbol{\xi})}{\partial \boldsymbol{\eta}} & \cdots \end{bmatrix}$$
(2.73)

and finally $\det J = \det([\mathbf{J}])$.

As detailed in section 2.3.2, with this approach we solve directly for the physical solution \mathbf{u}^{phy} . This is achieved through writing the control solution in eq. (2.60) in terms of the physical solution by inverting the mapping in eq. (2.68), consequently introducing the Bézier inverse matrix into the formulaion [88]. For each element, the control solution then writes as:

$$\mathbf{u}^{\text{cntrl}} = \left[\mathbf{B}_{\text{bez}}\right]^{-1} \left\{\mathbf{u}^{\text{phy}}\right\} \tag{2.74}$$

Substituting eq. (2.74) into eq. (2.60), the elemental stiffness matrix then becomes:

$$\mathbf{k}^{e} = \sum_{\text{CP}} \left[\mathbf{B}_{\text{bez}} \right]^{-T} \left[\mathbf{B} \right]^{T} \left[\mathbf{D} \right] \left[\mathbf{B} \right] \left[\mathbf{B}_{\text{bez}} \right]^{-1} \det J w_{\text{GP}}$$
(2.75)

The Bézier equivalent Greville and Botella points, which are derived using eq. (2.48), are used to evaluate the Bézier inverse matrix.

This method was also implemented and then used to solve the problem in fig. 2.18. Similarly to the BSplines-based model, the geometry is discretized with 50 quadratic Bézier elements, with a total of 462 DOFs. Figure 2.22 demostrates how the computation points in this method differ from those typical in isogeometric analysis (control mesh) for a 3×3 mesh.

Both the Greville points and the Botella points were used to compute the Bézier inverse matrix during the resolution process. The solution obtained, the displacement field and the stress field, is shown in Figures 2.23 to 2.26 using the Bézier Greville points and Botella points, respectively.

It can be seen that both these approaches yield the same solution. With Bézier inverse matrix computed from both the Greville points and Botella points, we found that:

- the maximum deflection is observed on the right bottom tip of the beam, with displacement magnitude of 1.4581×10^{-3} m, vertical displacement -1.0611×10^{-3} m
- maximum compressive stress of 3.9276 Pa is obtained on the inner side of the beam, and maximum tensile stress of 2.6423 Pa on the outside
- \bullet the maximum von Mises stress is found to be 4.0029 Pa

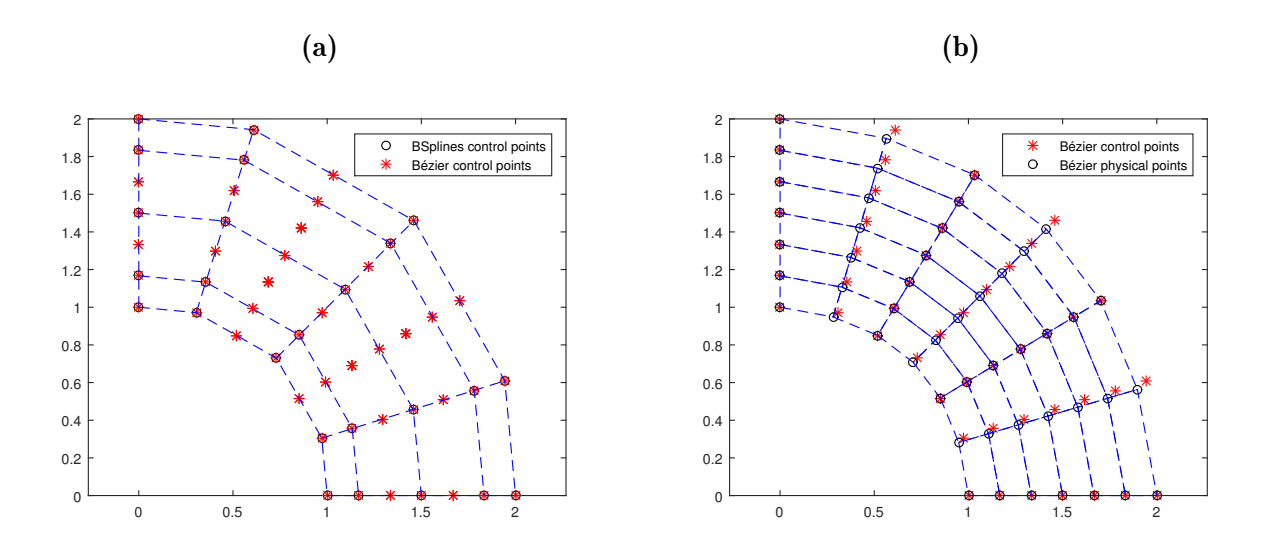


Figure 2.22 – Bézier control mesh and physical mesh comparison, $(p = 2, 3 \times 3\text{-elements})$: (a) control mesh, and (b) physical mesh.

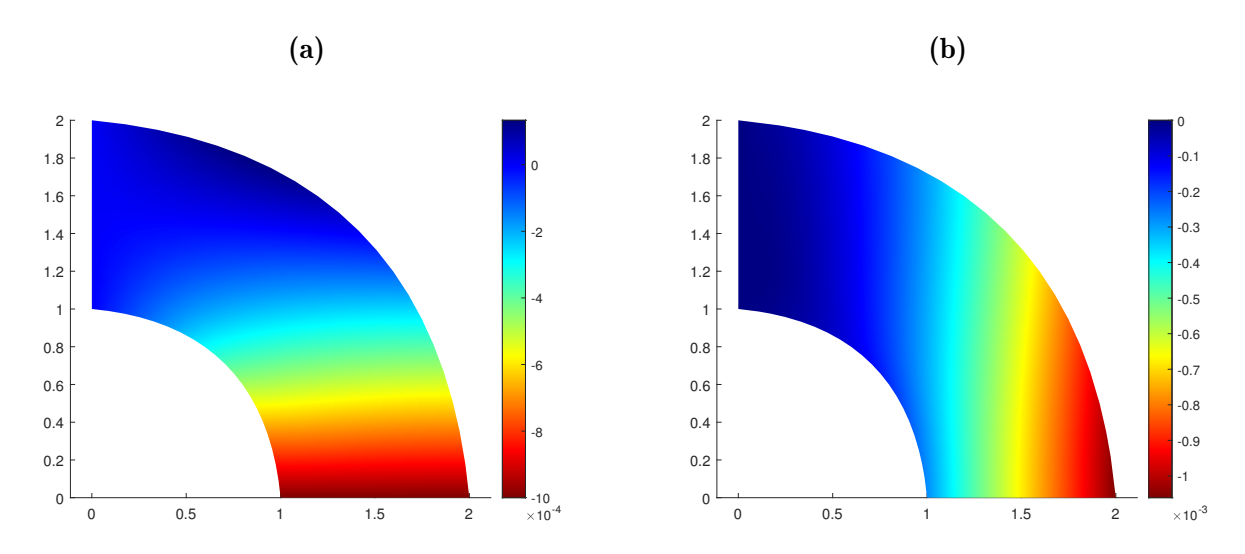


Figure 2.23 – Bézier based approach with Greville points solution fields : (a) x-component of the displacement, and (b) y-component of the displacement.

It is important to note that the solution obtained with this method is equivalent to the solution obtained using the BSplines-based approach. In actual fact, the highlighted maximum values for the displacement and stresses are exactly the same. However, we can observe that the stress distribution obtained from the Bézier-based approach is considerably smoother compared to the BSplines based approach stress distribution. This finer distribution can be attributed to the presence of more computation points in the Bézier approach which play a significant role particularly for the stresses.

Even though the choice of collocation points for the Bézier inverse matrix does not influence the solution, further inspection on the resolution times show that use of the Botella points increases the computation time. This increase arises from the stiffness assembly CPU time: using Botella points for collocation we found the stiffness assembly CPU time to be approximately 3 times

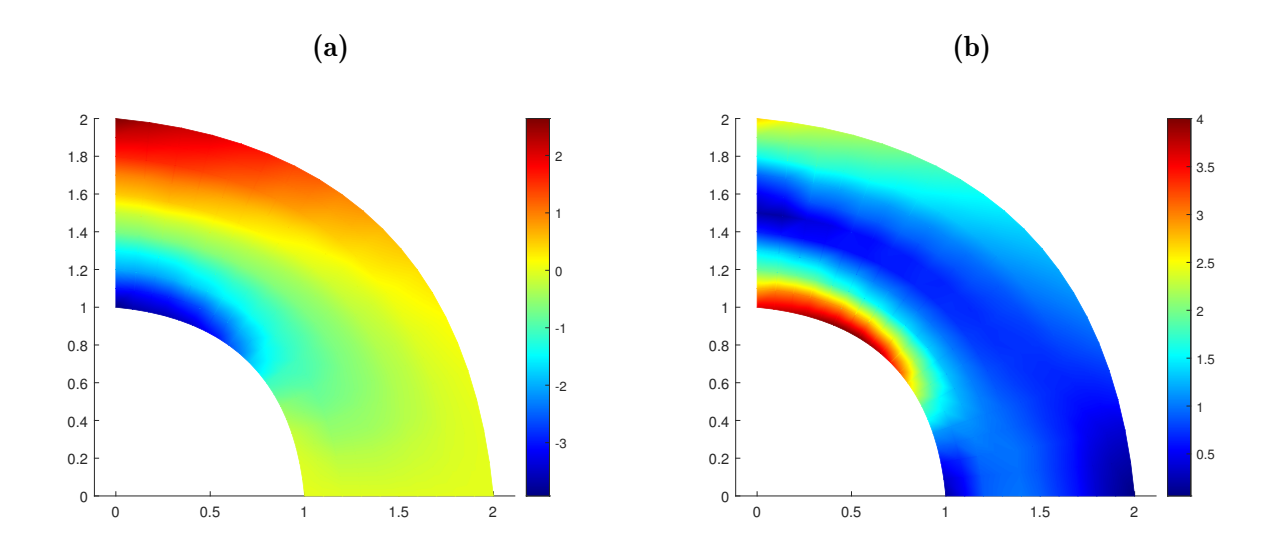


Figure 2.24 – Bézier based approach with Greville points solution fields : (a) normal stress, σ_{11} , distribution, and (b) Von Mises stress distribution.

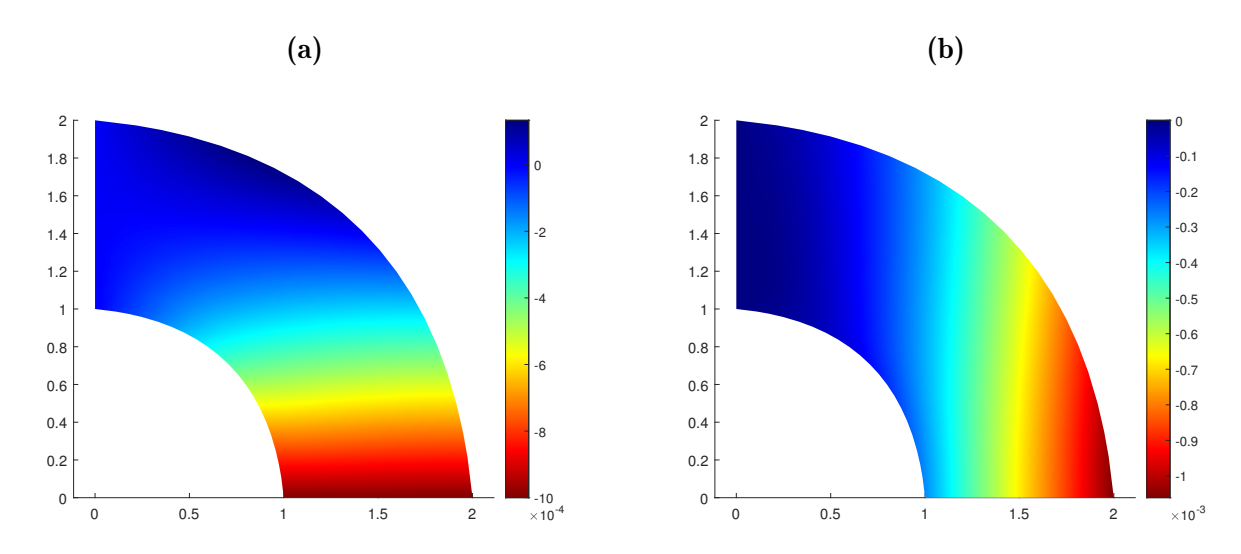


Figure 2.25 – Bézier based approach with Botella points solution fields : (a) x-component of the displacement, and (b) y-component of the displacement.

that of the stiffness time when using Greville points. This is because with Botella points, the Bézier inverse matrix is recomputed for each assembly loop whereas with Greville points this matrix is computed once and stored for use during the assembly.

Moreover, it is important to recall that the Bézier-based approach leads to a larger model, in terms of number of DOFs, compared to the BSplines-based approach model. This is reflected on the solver time for which was 0.45 ms for the BSplines-based method, and 2.19 ms for the Bézier based approach, both with Greville and Botella points. A study on solver computational (CPU) time evolution as a function of the number of elements in the discretization shows a quadratic evolution for BSplines-based approach and cubic evolution for Bézier-based approach - see fig. 2.27a. For this problem specifically, we found that even with a course mesh, we can capture fine stress distribution as well as displacement fields. Therefore a fine mesh was not a

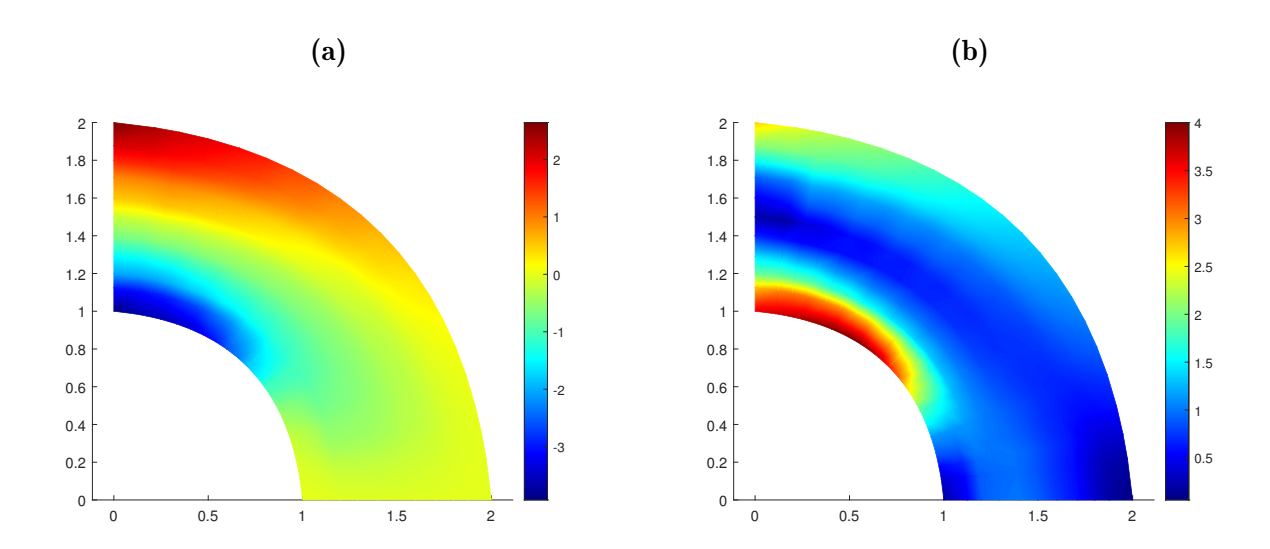


Figure 2.26 – Bézier based approach with Botella points solution fields : (a) normal stress, σ_{11} , distribution, and (b) Von Mises stress distribution.

necessity.

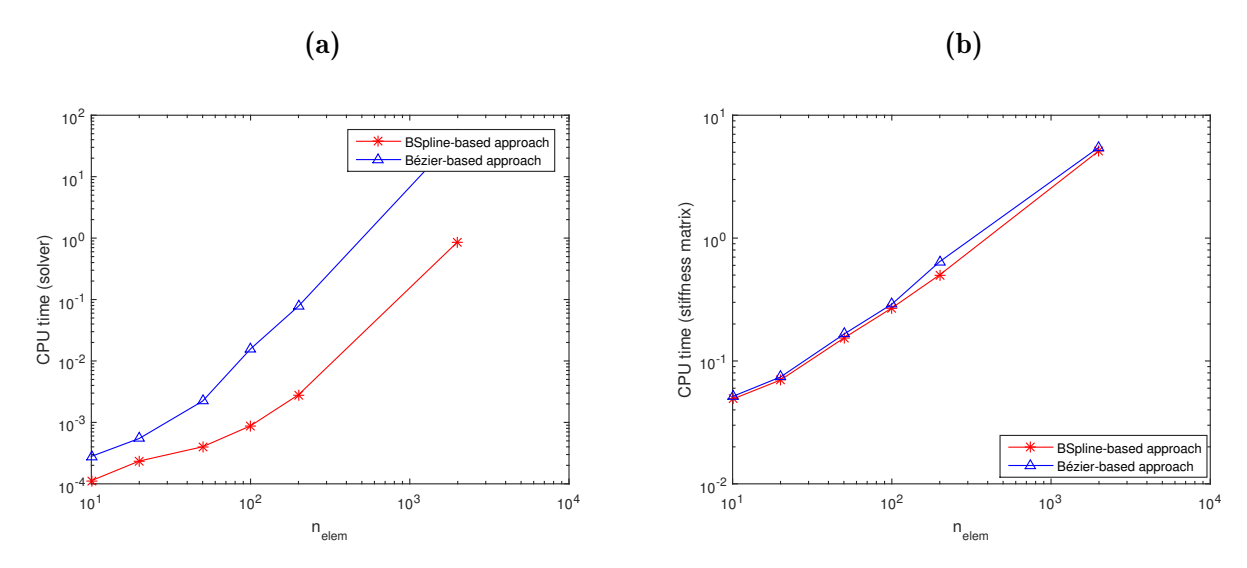


Figure 2.27 – Comparison of the solver CPU time [s] and the global stiffness assembly time for the BSplines-based approach and the Greville Bézier-based approach: (a) solver CPU time, and (b) stiffness matrix assembly CPU time.

However, the added advantage of using the Bézier-based approach is that it is much easier to implement. It requires less operations for the problem setup and computation of quantities involved in the global assembly of the system. Through the use of Bézier approach, we do not necessarily lose that much in terms of accuracy but there is a whole lot to gain in terms of efficient implementation.

Another important advantage of using the Bézier-based approach is the data structures identical to standard finite elements methods. Moreover this method greatly simplifies the application of boundary conditions to the numerical model. With this method we have access to computation

points located on the geometry and therefore can directly apply the boundary conditions.

2.5 Summary

The objective of this chapter was to become familiar with fundamentals of Isogeometric-based FEM and to introduce the Bézier-based isogeometric finite element method which, unlike the typical isogeometric analysis methods, solves directly for the physical solution. The scope of this chapter included first an in depth study of the three main parameterization techniques in isogeometric analysis, namely: (1) Bézier, (2) BSplines, and (3) NURBS. Secondly we detailed isogeometric analysis method in the finite elements framework, which was then followed by a practical demonstration on isogeometric analysis based FEM by modeling a simple structural problem.

Each parameterization technique was explored to study its characteristics (properties, advantages and drawbacks) when used as a discretization tool. We found that even though NURBS offer the most advantages with regards to geometry representation accuracy and design freedom, they tend to be implementationally laborious. Contributing factors to this is firstly the amount of information required for NURBS representation, and secondly their inability to allow for local refinement/control due to their tensor product nature (a trait shared by BSplines as well). However we found that BSplines, with the right combination of refinements, can produce sufficiently accurate geometry representations; they are a valid alternative to the cumbersome NURBS, hence the use of BSplines for the global modeling of the quarter of an annulus studied here.

As mentioned, BSplines lack the local refinement/control capabilities. Borden et al. [76] Bézier extraction concept allowed us to formulate an isogeometric analysis problem compatible with existing finite elements data structures. Since in the isogeometric analysis framework the solution is usually sought out at the control points which are not necessarily on the physical geometry, imposing boundary conditions is not as straight forward as is in classical finite element method. For the specific structural problem studied in this chapter, imposing boundary conditions was a trivial process because of the type of the boundary conditions as well as the location of the boundaries of interest. It is worthwhile to note that imposition of boundary conditions will become very significant in the chapters to come when we have to deal with contact constraints, hence the reason we developed the Bézier-based approach [87].

The Bézier-based approach [87] which directly solves for the physical solution instead of the control solution addresses the above mentioned limitation. Essentially, this approach transforms the BSplines-based problem with control network as computation points, into a larger (in terms of DOFs) Bézier problem with computation points located on the geometry (in a similar manner as in classical finite element method) through the use of the Bézier inverse matrix introduced in section 2.3.2. In effect the data structures are identical with the difference only in the shape functions subroutine. The Bézier inverse matrix which is introduced in the discrete setting of the

system of equations, allows us to express the physical solution in terms of the control solution. The solution field is then obtained at specific computation points which live on the actual geometry. This is achieved though evaluating the Bézier inverse matrix at preselected parameter values corresponding to the specific computational points. These parameter values are chosen as the Bézier equivalent of the familiar BSplines Greville and Botella points. Introduction of this matrix in the weak formulation then allows for the boundary conditions to be applied directly.

It is also worth noting that due to the simplicity of the geometry of the structural problem solved here, a single patch model was sufficient to model the computational domain. In practice however it can be a necessity to describe the domain with multiple patches; for instance, if different material or physical models are to be used at different parts of domains [13]. This can also be the case for complex geometries, i.e. geometries with inclusions, holes, domains that differ topologically from a cube in 3D, etc. For contact problems this is particularly interesting as it permits the possibility to model the contact interface as a single patch. In doing this, it simplifies the contact detection process as it can be carried out patch-wise thus eliminating a great deal of bookkeeping which is a consequence of element-wise searches in classical FEM [22, 23, 37, 40, 95].

Contact Problem and its General Formulation

3.1 Introduction

Any mechanical structure or system may exhibit the phenomenon of contact [43]. This contact phenomenon may be in the form of intentional interaction such that structures like a bridge, can sustain applied mechanical loads or in the case of wheel/rail interaction resulting in the generation of traction effort necessary to propel trains [2–4, 6, 43, 96, 97]. There are also instances where this phenomenon may be unintentional such as vehicle crash or squeal propensity in braking components [23, 96]. Whether we are concerned with increasing efficiency in the case of intentional contact or decreasing the adverse effects that may arise in non-intentional contact [4, 6], it is imperative we gain an understanding of the process of these interactions. For this reason, contact is very important in the mechanics of solids and its engineering applications.

The contact interactions between components or bodies of a mechanical system is a static phenomenon if the bodies in contact are in static equilibrium. Otherwise, the contact is said to be a dynamic phenomenon which often is much more complex than static contact. In real engineering applications most contact processes are "dynamic in a restrictive sense", however for simplicity, many of them may be regarded as static [2, 4]. Moreover, even though the contact phenomenon always involves friction in the interaction [3], the friction effects may be neglected for cases where the frictional forces are sufficiently small.

Contact problems are characterized by their discontinuities. Contact occurs at the interface of two separate continuous bodies/entities. This interaction (in terms of contact constraints) is non smooth and cannot merely be regarded as ordinary boundary conditions imposed on both the interacting surfaces [2, 5]. Furthermore, the contact interface cannot be considered as an internal surface; effectively, we can see it as a zero thickness layer which can only sustain compressive tractions in the normal direction (tensile tractions equate to separation and therefore a vanishing contact interface) [2]. If the contact is frictionless this layer does not sustain tangential efforts,

however, these may arise in the case of frictional contact and require a more sophisticated treatment of the contact state.

Due to the extreme complexity involved in the contact phenomena, to rigorously account for contact effects in conventional engineering analysis is a cumbersome task [43]. This high complexity of mechanical contact problems can be attributed to their inherent non linearity. These problems involve unknown boundary conditions unlike other mechanical problems; the actual contacting surface as well as the stresses and displacements are all unknown a priori [2, 3, 5, 23, 43].

Additionally the presence of friction can raise the degree of complexity even more. This is because a rigorous model of contact with friction is quite difficult as friction depends on many factors, including [2, 4]:

- surface topography
- physical and chemical properties
- type of motion
- temperature of contacting surfaces

As a result, a rigorous analysis of the contact problem while taking into account all the aforementioned complex aspects remains an extremely difficult task. Owing to the advancements of numerical techniques, particularly the FEM, many of these contact problems can now be solved to within useful accuracy [3, 5]. In engineering numerical simulations, the enforcement of contact constraints is incorporated through ad-hoc elements and algorithms that have been developed in the last few decades [2, 3, 5, 23, 97]. Nevertheless, the computational solution of contact is often very challenging and poses many numerical difficulties.

A large number of mechanical problems can be formulated as a Boundary Value Problem (BVP). This formulation, the *strong form*, necessitates the governing differential equations to be fulfilled in the bulk domain Ω under essential boundary conditions applied on its boundary Γ [5, 23]. The weak form of these BVPs, which is a basis of the construction of structural FEM, is obtained by writing the balance of virtual works. On the contrary, contact constraints are formulated as a set of inequalities and cannot be easily incorporated in the weak form [2, 3, 5, 23]. The construction of their weak form then leads to a variational inequality in place of the classical variational equality. Consequently, new solution procedures to handle this mathematical structure are required.

Difficulties may also arise in the rigorous description of the contacting surfaces [2]. The contacting bodies may penetrate each other or there can be separation of a previously established contact. This can then lead to loss of one-to-one mapping between points on the contacting surfaces. Moreover, the weak formulation of contact problems requires the second order variations and therefore access to the differential geometry. With classical FEM (typically a C^0 discretization),

the geometry is rendered into piece-wise smooth surfaces and therefore loss of access to the differential geometry [22]. This then induces mathematical and numerical difficulties. Hence the reason why IGA is an interesting alternative to classical FEM in that, with the IGA all difficulties tied to non smooth discretization can be avoided. IGA offers access to smooth, higher and tailorable continuity basis functions which is very advantageous for the description of interacting surfaces [13, 22, 23]. The smooth representation of surfaces as a result of the use of IGA in contact problems has been shown to be more accurate compared to the standard FEM approach [22, 37–41, 85, 92].

The aim of this chapter is to review the contact problem in its entirety and discuss some of the important numerical implementation aspects for this problem. In section 3.2 we review the general formulation of the contact problem, including both the normal and tangential contact conditions. Without loss of generality, we consider a two body contact system, deformable/deformable contact interaction. A full mechanical problem is briefly outlined, however we are more concerned with contact problem, hence the emphasis and broader discussion of the contact contributions. First we detail the contact problem statement, show the derivation of contact constraints and discuss the contact constitutive laws to formulate the governing equations (section 3.2 and section 3.3). This is then followed by the mathematical formulation of the contact variational form from its strong form. Section 3.4 focuses on contact resolution methods entailing the contact constraints enforcement methods, and finally for completeness, in section 3.5 we review some of the contact interface discretization techniques which we have already touched on in chapter 1.

The final section of this chapter (section 3.6) is dedicated to the development of the Node to surface contact discretization using the Bézier based IGA approach. That is, first give a brief summary of the Bézier based IGA approach proposed in chapter 2. This is followed by the time discretization of the frictional quantities as well as the Node to Surface discretization of the contact term with the penalty method used for the enforcement of contact constraints. For a more generic approach, we develop the discretization for deformable on deformable contact system, naturally the Signorini problem discretization is simply a special case of the more general problem. Finally, we detail the solution algorithm for both quasi static contact system (an implicit, static resolution) and the global time integration (in the case of dynamic contact, the inertial effects non negligible) of this two body contact system with friction.

3.2 Governing Equations of the Contact Problem

In this section we write the description of the mechanical contact problem, its boundary value problem and the contact constraints. All quantities are written in the current configuration. This is because in contact problems two points that are distinct in the reference configuration can in the current configuration occupy the same position. Therefore contact conditions have to be formulated with respect to the current configuration [23].

In general, to detect the occurrence of contact between bodies two steps have to be performed. These steps include first the global search for contact and secondly the setting up the local kinematical relations which are needed to formulate the contact constraints. Our main focus will be on the latter. Step one, which typically involves search algorithms is outside the scope of our discussion. Readers interested by this topic can refer to the works of [3–6].

3.2.1 Problem Description

Without loss of generality, we suppose our contact system consists of two elastic deformable bodies. The Signorini problem, the contact between a deformable body and a rigid body, is then a special case of the more general contact problem.

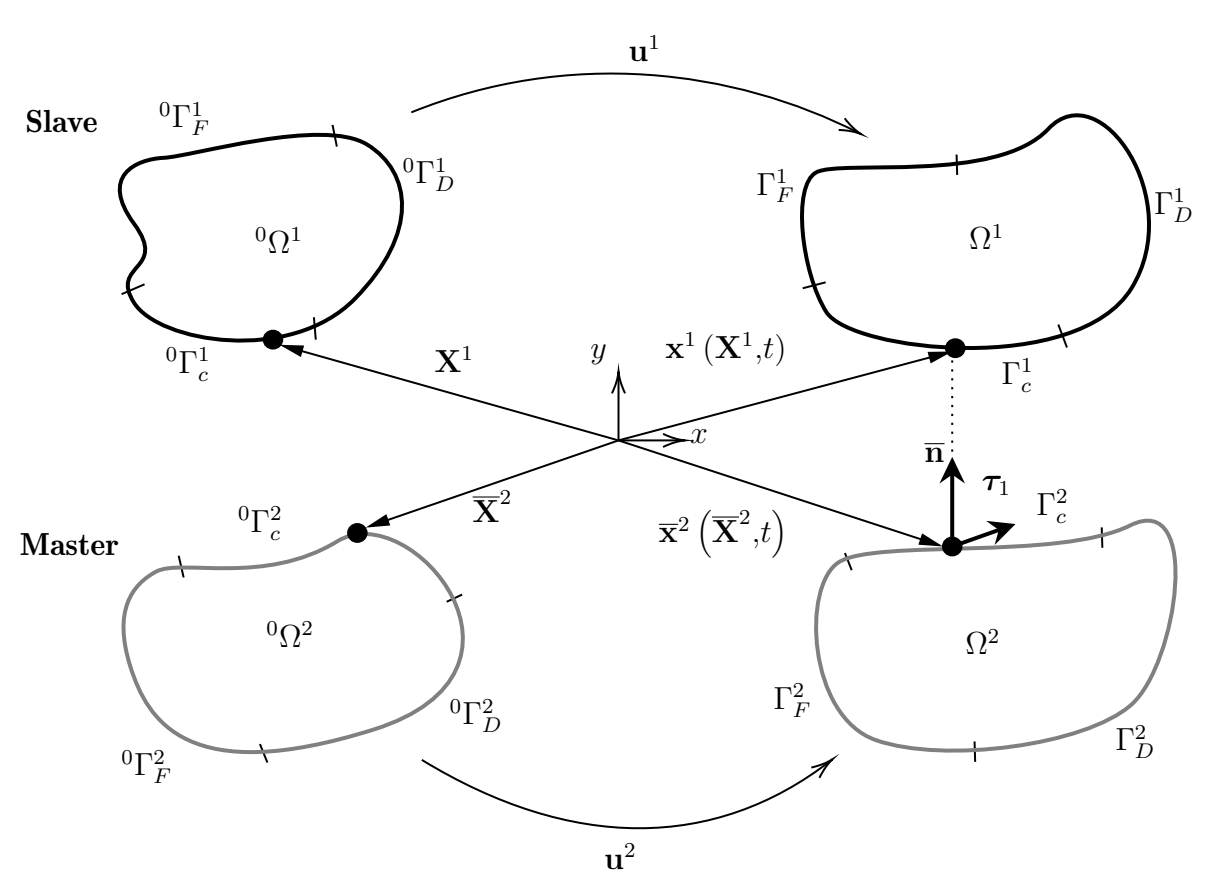


Figure 3.1 – Deformation of a two-body contact system from the reference configuration to the current configuration : body Ω^1 the slave body, body Ω^2 the master body

Let us consider the two-body contact system depicted in fig. 3.1. The two bodies occupy domains ${}^{0}\Omega^{i}$, i = 1,2, the reference configuration corresponding to time t = 0. We denote the closure/boundary of ${}^{t}\Omega^{i}$ with ${}^{t}\Gamma^{i}$ which can be decomposed as follows.

$${}^t\Gamma^i = {}^t\Gamma^i_D \cup {}^t\Gamma^i_F \cup {}^t\Gamma^i_0 \tag{3.1}$$

where, in eq. (3.1), ${}^t\Gamma_D^i$ is the Dirichlet boundary, ${}^t\Gamma_F^i$ is the Neumann boundary, and ${}^t\Gamma_0^i$ part of the boundary where contact may occur.

Each body is subjected to body forces and prescribed boundary loads from time t=0. The bodies deform to occupy new domains ${}^t\Omega^i$ in the current configuration at time t>0. The bodies occupy the \mathbb{R}^{n_d} Euclidean space ($n_d = 2$ specify a 2D space, and $n_d = 3$ specify a 3D space). Again, for generality, unless otherwise specified, we will consider a 3D setting and a 2D setting will be simplification of the generic case. Note: the notation $^t(\bullet)^i$ means the quantity (\bullet) is defined for body i at time t.

We denote the position vector of a point in a body by ${}^{t}\mathbf{x}$ and ${}^{0}\mathbf{x}$ is denoted by \mathbf{X} . The total displacement of the two bodies at any time instance t > 0 is given by eq. (3.2)

$$^{t}\mathbf{u}^{i} = {}^{t}\mathbf{x}^{i} - \mathbf{X}^{i} \tag{3.2}$$

The motion of the bodies occupying ${}^t\Omega^i$ is governed by eq. (3.3)

$$\operatorname{div} {}^{t}\boldsymbol{\sigma}^{i} + {}^{t}\mathbf{b}^{i} = \rho^{i} {}^{t}\ddot{\mathbf{u}}^{i} \tag{3.3}$$

where ${}^t\boldsymbol{\sigma}^i$ is the Cauchy stress field, ${}^t\mathbf{b}^i$ are the volume forces, ρ^i is the mass density assumed to be constant, and ${}^t\ddot{\mathbf{u}}^i$ is the acceleration field. The stress-strain is governed by the Hooke's law such that

$$^{t}\boldsymbol{\sigma}^{i} = \mathbf{D} : {}^{t}\boldsymbol{\epsilon}^{i}$$
 (3.4)

where **D** is the fourth order elasticity tensor, and ${}^{t}\epsilon^{i}$ is the strain field which is related to the displacement ${}^{t}\mathbf{u}^{i}$ through the strain-displacement relation ship in eq. (3.5)

$$\boldsymbol{\epsilon} = \frac{1}{2} \left(\nabla \mathbf{u} + \nabla \mathbf{u}^T \right) = \nabla_s \mathbf{u} \tag{3.5}$$

 ∇_s indicates the symmetric part of the deformation gradient. Prescribed Dirichlet and Neumann boundary conditions can expressed as follows:

$$\mathbf{u}(\mathbf{x},t) = \mathbf{u}_D(\mathbf{x},t) \qquad \mathbf{x} \in \Gamma_D \tag{3.6}$$

$$\sigma(\mathbf{x},t)\vec{\mathbf{n}} = \mathbf{t}_F(\mathbf{x},t) \qquad \mathbf{x} \in \Gamma_F$$
 (3.7)

where $\vec{\mathbf{n}}$ is the outward unit normal vector on the boundary and $\mathbf{u}_D(\mathbf{x},t)$ and $\mathbf{t}_F(\mathbf{x},t)$ are the prescribed displacements and boundary traction, respectively. The initial conditions are expressed in eq. (3.8) and eq. (3.9), where $\dot{\mathbf{u}}$ denotes the velocity field.

$$\mathbf{u}(\mathbf{x},0) = \mathbf{u}_0 \qquad \mathbf{x} \in {}^{0}\Omega^{i}$$

$$\dot{\mathbf{u}}(\mathbf{x},0) = \mathbf{v}_0 \qquad \mathbf{x} \in {}^{0}\Omega^{i}$$
(3.8)

$$\dot{\mathbf{u}}(\mathbf{x},0) = \mathbf{v}_0 \qquad \mathbf{x} \in {}^{0}\Omega^{i} \tag{3.9}$$

 \mathbf{u}_0 and \mathbf{v}_0 are initial displacements and initial velocities, respectively.

Moreover, since all quantities are expressed in current configuration, we drop the t from the convention $^{t}(\bullet)$. Furthermore, as is typical in the expression of contact constraints the notion of slave/master surfaces is adopted; subsequently we take body Ω^1 as a slave and the second body (Ω^2) as the master. The master surface is parameterized using the convective coordinates $\xi^{\alpha} = [\xi^{1}, \xi^{2}]$. We then define the covariant vectors, non unit and generally non-orthogonal vectors that are tangent to the master contact surface, as $\tau_{\alpha} = \mathbf{x}_{,\alpha}^2$, where $(\bullet)_{,\alpha} = \frac{\partial (\bullet)}{\partial \xi^{\alpha}}$. The contra-variant vector $\boldsymbol{\tau}^{\alpha}$ is induced from the inverse of the metric tensor components $m^{\alpha\beta}$ as $\boldsymbol{\tau}^{\alpha} = m^{\alpha\beta}\boldsymbol{\tau}_{\beta}$, with $m_{\alpha\beta} = \boldsymbol{\tau}_{\alpha} \cdot \boldsymbol{\tau}_{\beta}$. The curvature tensor, which is symmetric, then follows from $k_{\alpha\beta} = \boldsymbol{\tau}_{\alpha,\beta} \cdot \vec{\mathbf{n}}^2$. Here, the Greek letters indices refer to the tangent directions in the surface coordinate system, and take values $\alpha,\beta = 1,2$ in 3D, and reduces to 1 in the case of 2D contact problems. As is standard, repetition of the indices imply summation.

3.2.2 Normal Contact

The study of contact problems entails in predicting the behavior of the contact system from time t=0 to time t=T. This behavior is governed by 3 main groups of equations, namely: equations of motion, constitutive equations, and boundary conditions [3, 5, 98]. Boundary conditions may be in the form of prescribed boundary conditions which are deformation independent. However boundary conditions may also be in the form of unknown boundary conditions which are deformation dependent, and among those are the contact conditions and these characterize this study [5]. In this section we will outline the governing equations of contact and formulate its boundary conditions, specifically in the normal direction. Consideration of the tangential contact follows in section 3.2.3.

We now denote Γ_0^i as Γ_c^i , the contact boundary or rather the boundary at which the contact conditions must be satisfied.

3.2.2.1 Contact Constraints in the Normal Direction

Consider slave point \mathbf{x}^1 to be in contact with master point \mathbf{x}^2 as depicted in fig. 3.2.

The unit vectors at the two points are such that:

$$\vec{\mathbf{n}}_j^1 = -\vec{\mathbf{n}}_j^2 \qquad j = 1, 2, 3 \tag{3.10}$$

with unit vectors in 2,3 - direction the tangential units vectors, and $\vec{\mathbf{n}}_1^i$ the outward unit normal vector. If the contact traction vector at the contacting points, for the two bodies, is denoted by \mathbf{t}^i , Newton's third law states that

$$\mathbf{t}^1 = -\mathbf{t}^2 \tag{3.11}$$

If we adopt the notation $\vec{\mathbf{n}}_j^i = \mathbf{n}_j^i$, we can obtain the components of the contact traction vector at the slave and master body as:

$$t_j^i = \mathbf{t}^i \cdot \mathbf{n}_j^i$$
 $i = 1,2 \text{ and } j = 1,2,3$ (3.12)

We distinguish between the three traction vector components and adopt the subscript $(\bullet)_N$ for the normal component and subscript $(\bullet)_{T_\alpha}$, $\alpha = 1,2$, for the tangential components. The traction vector can then be decomposed as follows:

$$\mathbf{t} = \mathbf{t}_N + \mathbf{t}_T, \quad \mathbf{t}_N = t_N \mathbf{n}, \quad \mathbf{t}_T = t_T^{\alpha} \boldsymbol{\tau}_{\alpha} = t_{T_{\alpha}} \boldsymbol{\tau}^{\alpha}$$
 (3.13)

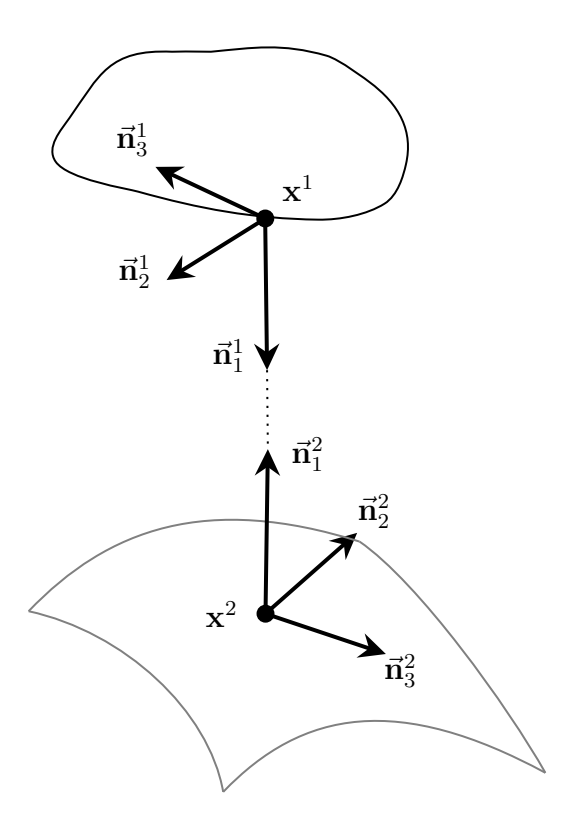


Figure 3.2 – Contacting points and their associated unit vector at the boundary.

Since only compressive stresses are supported on the contact interface in the normal direction and tensile tractions are not allowed, then:

$$t_N \le 0 \tag{3.14}$$

The condition expressed in eq. (3.14) is referred to as the **mechanical contact condition**. Tangential components are related to the normal traction through the friction and can have an arbitrary sign, however they must vanish in the case of frictionless contact [23]. In addition to the mechanical contact constraint, physical constraints require that:

$$\Omega^1 \cap \Omega^2 = \varnothing \tag{3.15}$$

that is, the two bodies in contact may not penetrate each other. The condition in eq. (3.15) is referred to as the **kinematic contact condition**. In the normal direction, this condition defines the contact pairing points of the slave/master surfaces (points that will come into contact with each other) as well as the normal gap between them. If we denote the normal gap function, a function that defines the gap between the contacting slave/master surfaces, as $g_N(\mathbf{x},t)$, such that:

$$g_N(\mathbf{x},t) = \left(\mathbf{x}^1 - \mathbf{x}^2\right) \cdot \mathbf{n}_1^2 \tag{3.16}$$

The kinematic contact condition enforcement, formulated as the non penetration condition of each point of the slave surface into the master body, is then written as an inequality of the normal gap function in eq. (3.16). Denoting the outward unit normal vectors (both to the master

and slave surfaces) \mathbf{n}_1^i as simply \mathbf{n}^i , where i=1,2; it follows:

$$g_N(\mathbf{x},t) = (\mathbf{x}^1 - \mathbf{x}^2) \cdot \mathbf{n}^2$$

$$= (\mathbf{x}^2 - \mathbf{x}^1) \cdot \mathbf{n}^1$$

$$\geq 0$$
(3.17)

Equation (3.17) forms part of the contact constitutive behavior at the interface, as will be seen later.

As mentioned, this kinematic contact constraint facilitates the definition of the master/slave contact pairs. That is, for each slave point we must find the corresponding master contact point, that the slave is likely to come into contact with. The master contact pair will be the master point closest to the slave point. This closest point is found through the closest point projection algorithm which is detailed in the next section. The normal gap function is then evaluated at this projection point and the value obtained is used to determine the contact state.

3.2.2.2 The Closest Point Projection Algorithm

The aim of the closest point projection (CPP) algorithm is, for each given slave point \mathbf{x}^1 , to find its closest point projection $\bar{\mathbf{x}}^2$ on the master surface - see fig. 3.3. This algorithm is described in multiple works including [6, 23, 37, 85, 99], to name a few. For completeness we discuss this algorithm, based on the work in [23], below.

To find the closest point projection, we first define a function that describes the distance between a given slave point \mathbf{x}^1 on Γ_c^1 and an arbitrary point located at $\mathbf{x}^2 = \hat{\mathbf{x}}^2(\boldsymbol{\xi})$ on Γ_c^2 , the master surface. Here, $\boldsymbol{\xi} = \boldsymbol{\xi}^{\alpha} = (\boldsymbol{\xi}^1, \boldsymbol{\xi}^2)$ are the convective coordinates that parameterize the master surface. This distance function is defined as follows

$$d(\mathbf{x}^1, \boldsymbol{\xi}) = \|\mathbf{x}^1 - \hat{\mathbf{x}}^2\| \tag{3.18}$$

If the master surface is, at the very least, locally convex; the closest point projection is the point $\bar{\mathbf{x}}^2 = \hat{\mathbf{x}}^2(\bar{\boldsymbol{\xi}})$ that minimizes eq. (3.18). That is, at every point \mathbf{x}^1 , we can relate point $\bar{\mathbf{x}}^2 = \hat{\mathbf{x}}^2(\bar{\boldsymbol{\xi}})$ through the minimum distance problem:

$$\mathbf{x}^{2}(\bar{\boldsymbol{\xi}}) = \underset{\boldsymbol{\xi} \in D}{\operatorname{arg min}} d(\mathbf{x}^{1}, \boldsymbol{\xi})$$
(3.19)

D is the domain of definition of the convective coordinates $\boldsymbol{\xi}$, and $\bar{\boldsymbol{\xi}}$ are convective coordinates at the closest point projection. The necessary condition for eq. (3.19) is that:

$$\frac{\mathrm{d}}{\mathrm{d}\boldsymbol{\xi}} \, \mathrm{d}(\mathbf{x}^1, \boldsymbol{\xi}) = \frac{\mathbf{x}^1 - \hat{\mathbf{x}}^2(\bar{\boldsymbol{\xi}})}{\|\mathbf{x}^1 - \hat{\mathbf{x}}^2(\bar{\boldsymbol{\xi}})\|} \cdot \hat{\mathbf{x}}_{,\boldsymbol{\xi}}^2(\bar{\boldsymbol{\xi}}) \stackrel{!}{=} 0 \tag{3.20}$$

 $\hat{\mathbf{x}}_{,\boldsymbol{\xi}}^2(\bar{\boldsymbol{\xi}})$ is a non unit tangent vector. This implies that the solution to eq. (3.20) requires orthogonality between the distance vector $\left[\mathbf{x}^1 - \hat{\mathbf{x}}^2(\bar{\boldsymbol{\xi}})\right]$ and the tangent vector $\hat{\mathbf{x}}_{,\boldsymbol{\xi}}^2(\bar{\boldsymbol{\xi}})$. Thus the closest point projection associates the orthogonal projection of each slave point onto the master surface.

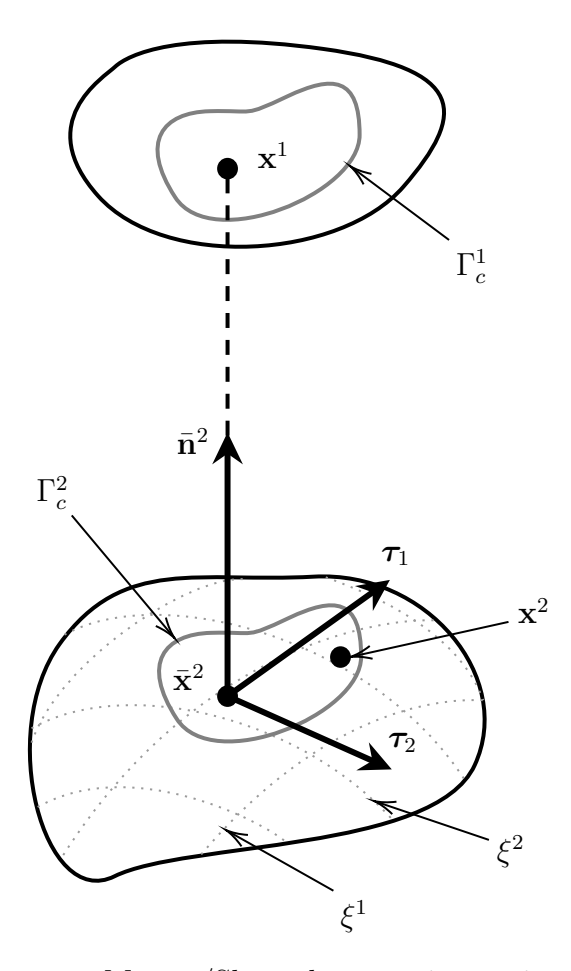


Figure 3.3 – Master/Slave closest point projection.

Once the closest point projection $\bar{\mathbf{x}}^2$ of a given slave point is known, we can compute the normal gap as :

$$g_N = \left(\mathbf{x}^1 - \bar{\mathbf{x}}^2\right) \cdot \bar{\mathbf{n}}^2 \tag{3.21}$$

In eq. (3.21) ($\overline{\bullet}$) denotes quantities evaluated at the closest point projection. It is important to note that it may exist instances where the master surface may be non convex, or any other situation that will render the distance function locally non differentiable, leading to non existence and lack of uniqueness of this projection. This is particularly observed in the case of C^0 continuous FE elements which are only piece-wise continuous, a limitation that may be alleviated through the use of IGA. This is also the case when the model has sharp corners/edges. For these type of problems, a more sophisticated algorithm is then required to obtain the slave points projection [6, 22, 23, 40].

3.2.2.3 Constitutive Laws for the Contact Interface in the Normal Direction

The final ingredient for the description and formulation of normal contact and its contribution to the contact boundary value problem is the contact interface constitutive law. Two different approaches for the definition of the constitutive behavior of contact have been established [3, 5, 23]. These may be:

- constitutive laws based purely on the geometric enforcement of contact constraints
- physically motivated constitutive laws based on empirical knowledge or driven by multiscale models (higher level of complexity)

In this chapter we will consider the geometric based constitutive behavior. With this constitutive law the relationship between the normal contact tractions and the normal gap is deduced from the constraints equation detailed in section 3.2.2.1. In the normal direction, it follows that:

- contacting bodies may not penetrate each other, that is : $g_N \ge 0$
- only compressive tractions are permitted on the contact interface, $t_N \leq 0$
- normal tractions will vanish when the gap is open and they are negative when the gap is closed :

$$\begin{cases} t_N = 0 & \text{if } g_N \ge 0 \\ t_N \le 0 & \text{if } g_N = 0 \end{cases}$$
 (3.22)

Therefore, in the contact interface we have:

$$g_N \ge 0 \qquad t_N \le 0 \qquad t_N \, g_N = 0 \tag{3.23}$$

In eq. (3.23) are what is known as the *Hertz-Signorini-Moreau* conditions in contact mechanics and they correspond to the *Karush-Kuhn-Tucker* (KKT) complementarity conditions typical in constrained problems optimization theory. These conditions lead to a non smooth relationship between the normal gap and the contact pressure as depicted in fig. 3.4 (a) - the red line represents the feasibility region.

Treatment of this non smooth contact law requires appropriate numerical methods. However, there is possibility to regularize this law as it is usually done with penalty methods - see fig. 3.4 (b) - which will be discussed further in section 3.4.

3.2.3 Tangential Contact

When two bodies come into contact in the absence of friction, the behavior in the contact interface is solely governed by the normal contact equations. However, for frictional contact interaction, tangential tractions will arise and therefore we need the governing equations for this contribution. In the tangential direction on the contact interface, we generally need to distinguish between the two cases: the first case is the so called stick state and the second case is the sliding/slip state [3, 5, 23]. We first discuss the kinematics of tangential contact, including the forces exchanged in this direction during contact. This is followed by the discussion of the laws that govern the tangential behavior in the contact interface.

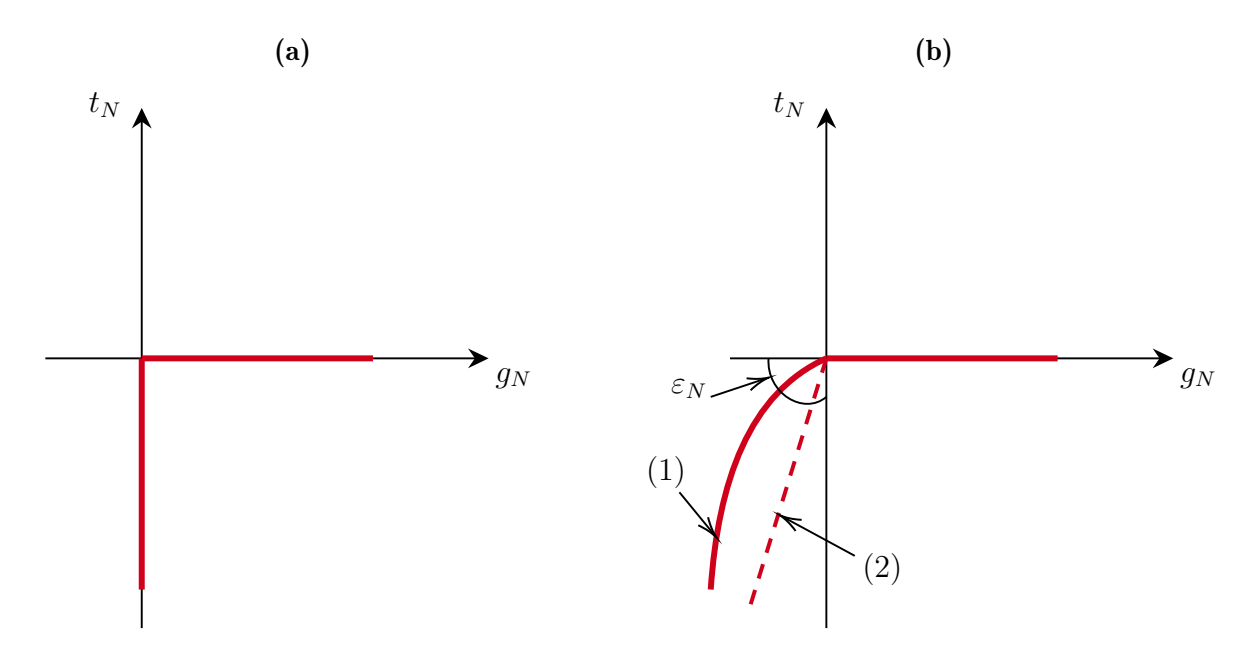


Figure 3.4 – Contact constitutive law in the normal direction : (a) non smooth constitutive law based on geometric enforcement of the non penetration condition; (b) non-linear constitutive law (1) and a linear regularized law (corresponding to the penalty method)(2).

3.2.3.1 Stick Condition

In the stick state the two points in contact, the slave point and its projection point on to the master surface, exchange the tangential forces without any relative sliding in the tangential direction [3, 5, 23]. The mathematical condition for the stick case simply follows from the observation that if the two points in contact do not experience any relative movement in the tangential direction, i.e. the two points stick to each other, then the convective coordinates of the projection point $\bar{\xi}^{\alpha}$ do not change with time. That is:

$$\dot{\bar{\xi}}^{\alpha} = 0 \tag{3.24}$$

Note the convention: $(\bullet) = \frac{\partial(\bullet)}{\partial t}$, where t is the time and could possibly be a fictitious parameter in quasi-static conditions [23]. From eq. (3.24), it follows that the relative displacement in the tangential direction should be zero, therefore we can formulate this condition as:

$$\mathbf{g}_T = g_{T_\alpha} \boldsymbol{\tau}^\alpha = \mathbf{0} \quad \text{with} \quad g_{T_\alpha} = \left(\mathbf{x}^1 - \bar{\mathbf{x}}^2\right) \cdot \boldsymbol{\tau}_\alpha$$
 (3.25)

where in eq. (3.25) \mathbf{g}_T denotes the relative displacement in tangential direction and $\boldsymbol{\tau}_{\alpha}, \boldsymbol{\tau}^{\alpha}$ are evaluated at the projection point and are given by :

$$\tau_{\alpha} = \bar{\mathbf{x}}_{,\alpha}^{2}
\tau^{\alpha} = m^{\alpha\beta} \tau_{\beta}$$
(3.26)

3.2.3.2 Sliding Condition

In the sliding/slip state, a tangential force is exchanged between the two points in contact results in relative movement in the tangential direction along the contact interface [3, 5, 23]. Essentially,

we have that $\dot{\xi}^{\alpha} \neq 0$, that is, the projection point convective coordinates will change over time. The projection point of the slave surface can now slide over the master surface - see fig. 3.5 which depicts the path of this motion beginning from time t_0 to final time t_n . In fig. 3.5 d**g**_T is the incremental tangential relative displacement or the slip vector.

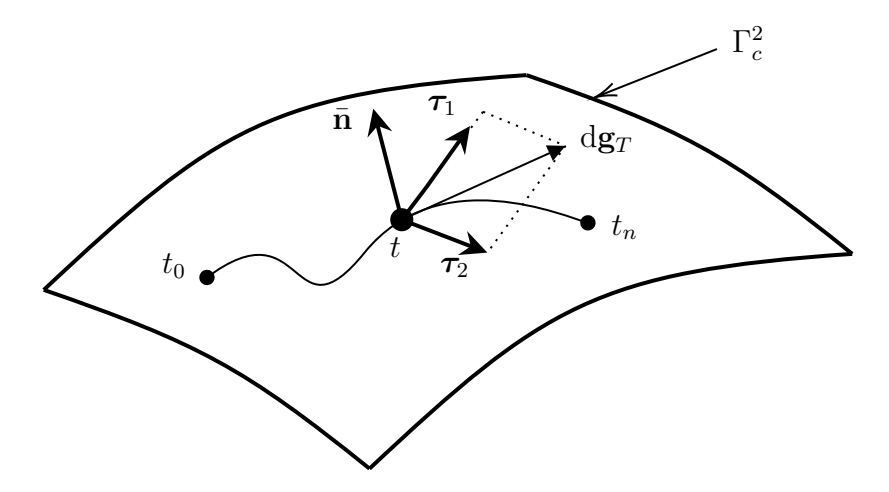


Figure 3.5 – Relative motion of the projection point $\bar{\mathbf{x}}^2$ of the slave point on the master surface, from a time t_0 to a final time t_n .

The path of the slave point on the master surface is not known *a priori*, arbitrary and may, in some instances, even cross itself. For this reason, we cannot make any assumptions of this path during the computations, all that is known is the relative velocity of the sliding point (the rate at which the slave point \mathbf{x}^1 slides on the master surface, in this case the $d\mathbf{g}_T$) [3]. To obtain the path of \mathbf{x}^1 on the master surface we have to integrate its relative velocity $(d\mathbf{g}_T)$. From eq. (3.25), the incremental tangential relative displacement can be derived as:

$$d\mathbf{g}_{T} = \boldsymbol{\tau}_{\alpha} d\bar{\xi}^{\alpha}$$

$$= \bar{\mathbf{x}}_{,\alpha}^{2} d\bar{\xi}^{\alpha}$$

$$= \bar{\mathbf{x}}_{,\alpha}^{2} \dot{\bar{\xi}}^{\alpha} dt$$
(3.27)

and its length given by $dg_T = ||d\mathbf{g}_T||$. The length of the sliding path of $\bar{\mathbf{x}}^2$ is obtained by integrating eq. (3.27) which results in :

$$g_T = \int_{t_0}^t \left\| \bar{\mathbf{x}}_{,\alpha}^2 \, \dot{\bar{\xi}}^{\alpha} \right\| \, \mathrm{d}t \tag{3.28}$$

In eq. (3.28) the expression of $\dot{\xi}^{\alpha}$ is still unknown. To compute this time derivative, first we perform the material time derivative of the orthogonality condition mentioned in section 3.2.2.2 (the necessary condition for the CPP algorithm - see eq. (3.20)). This orthogonality condition writes as:

$$\left(\mathbf{x}^{1} - \bar{\mathbf{x}}^{2}\right) \cdot \boldsymbol{\tau}_{\alpha} = \left(\mathbf{x}^{1} - \bar{\mathbf{x}}^{2}\right) \cdot \bar{\mathbf{x}}_{,\alpha}^{2} = 0 \tag{3.29}$$

Taking the material time derivative of eq. (3.29) yields

$$\left(\mathbf{v}^{1} - \bar{\mathbf{v}}^{2} - \boldsymbol{\tau}_{\beta} \,\dot{\bar{\xi}}^{\beta}\right) \cdot \boldsymbol{\tau}_{\alpha} + \left(\mathbf{x}^{1} - \bar{\mathbf{x}}^{2}\right) \cdot \left(\bar{\mathbf{v}}_{,\alpha}^{2} + \bar{\mathbf{x}}_{,\alpha\beta}^{2} \,\dot{\bar{\xi}}^{\beta}\right) = 0 \tag{3.30}$$

where in eq. (3.30) $\mathbf{v}^i = \frac{\partial \mathbf{x}^i}{\partial t}$. Solving eq. (3.30) for $\dot{\bar{\xi}}^\beta$, we get

$$\dot{\bar{\xi}}^{\beta} = H^{\alpha\beta} \left[\left(\mathbf{v}^1 - \bar{\mathbf{v}}^2 \right) \cdot \boldsymbol{\tau}_{\alpha} + g_N \bar{\mathbf{n}} \cdot \bar{\mathbf{v}}_{,\alpha}^2 \right]$$
 (3.31)

with $H^{\alpha\beta}$ the inverse of the auxiliary variable $H_{\alpha\beta}$, given in eq. (3.32), computed from the metric tensor and components of the curvature tensor

$$H_{\alpha\beta} = \tau_{\alpha} \cdot \tau_{\beta} - g_N \bar{\mathbf{n}} \cdot \bar{\mathbf{x}}_{,\alpha\beta}^2 = m_{\alpha\beta} - g_N k_{\alpha\beta}$$
 (3.32)

and

$$\bar{\mathbf{n}} = \bar{\mathbf{n}}^2 = -\bar{\mathbf{n}}^1 \tag{3.33}$$

3.2.3.3 Constitutive Laws in the Contact Interface for Tangential Contact

Note that in this work, we restrict ourselves to the more simple friction formulations which results in the frictional constitutive equations for dry friction, in particular the classical Coulomb's law of friction.

Coulomb's law of friction states that a point in contact will undergo stick or slip condition depending on the magnitude of the tangential traction vector \mathbf{t}_T [5]. With Coulomb's law, in addition to the contact KKT conditions in eq. (3.23), the magnitude of the tangential traction vector is bounded by the product of the friction of coefficient and the normal traction; that is:

$$\|\mathbf{t}_T\| \le \mu |t_N| \tag{3.34}$$

and

$$\dot{\mathbf{g}}_{T} = \lambda \mathbf{t}_{T}, \text{ with } \begin{cases} \lambda = 0 & \text{if } ||\mathbf{t}_{T}|| < \mu |t_{N}| \\ \lambda \ge 0 & \text{if } ||\mathbf{t}_{T}|| = \mu |t_{N}| \end{cases}$$
(3.35)

where μ is sliding friction coefficient. Equation (3.35) states that if the magnitude of the tangential traction vector does not exceed the μ times the normal traction, then the contact bodies are undergoing stick conditions; there is no relative movement between the bodies.

$$\|\mathbf{t}_T\| < \mu |t_N|, \quad \dot{\mathbf{g}}_T = \mathbf{0} \Leftrightarrow \mathbf{g}_T = \mathbf{0}$$
 (3.36)

The second condition in eq. (3.35) states that when the tangential tractions reaches the limit in eq. (3.34), tangential sliding occurs. Furthermore, any slip that occurs must be co-linear with the tangential tractions exerted by the sliding slave point on the master surface. Figure 3.6 shows the graphical representation of both stick and slip conditions given by the classical Coulomb law of friction - again, the red line denotes the feasibility region.

Similarly to the geometrical enforcement of the non-penetration condition in fig. 3.4a, the classical Coulomb's law of friction and the geometric stick condition is also non smooth in nature, therefore a regularization of the law is needed for computational reasons and will be discussed in section 3.4. Moreover, it can be observed that the behavior of the non-smooth Coulomb's friction

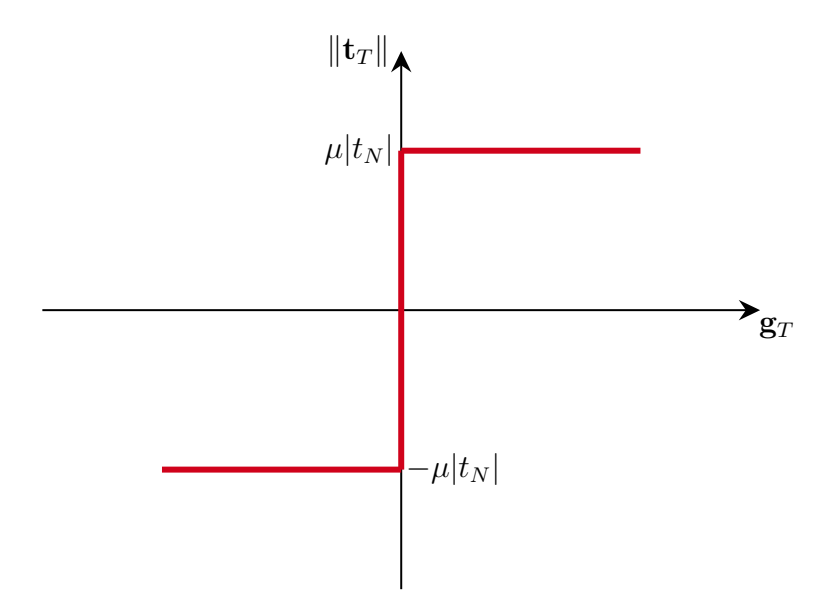


Figure 3.6 – Non-smooth Coulomb's friction law including the geometrical enforcement of the stick constraint.

law in fig. 3.6 is analogous with that observed in plasticity, specifically the rigid-perfectly-plastic constitutive law which is obtained by assuming zero hardening conditions and allowing the elasticity modulus to tend to infinity [5]. In this case the product μt_N may be seen as equivalent to the yield stress: in the same way that in plasticity plastic deformation occurs when we reach the yield stress, tangential contact sliding occurs when the exerted traction reaches μt_N . For more information on plasticity theory and plasticity flow rules, the reader is referred to the work of Crisfield [100] and Simo and Hughes [101]. Laursen [5] also gives a brief discussion of plasticity constitutive laws.

The analogy between frictional constitutive law and plasticity allows for the reformulation of the Coulomb's friction law as a more convenient, in terms of numerical implementation, non-associative Coulomb's friction law [3, 5, 23], which writes as follows

$$\Phi(\mathbf{t}_T, t_N) = \|\mathbf{t}_T\| - \mu |t_N| \le 0 \tag{3.37}$$

Essentially, the tangential stresses are bounded by the slip function Φ . Equation (3.37) can be seen as the 'plastic' slip criterion for a given t_N . The evolution equation for the slip then follows as:

$$\dot{\mathbf{g}}_T = \dot{\gamma} \frac{\partial \Phi}{\partial \mathbf{t}_T} = \dot{\gamma} \frac{\mathbf{t}_T}{\|\mathbf{t}_T\|} \tag{3.38}$$

In eq. (3.38), $\dot{\gamma}$ corresponds to the plastic multiplier in plasticity, and is related to the magnitude of the slip in that $\|\dot{\mathbf{g}}_T\| = |\dot{\gamma}|$. Finally the tangential constraints written as KKT conditions for Coulomb's law of friction are given by:

$$\Phi \le 0, \quad \dot{\gamma} \ge 0, \quad \dot{\gamma}\Phi = 0, \quad \dot{\mathbf{g}}_T = \dot{\gamma} \frac{\mathbf{t}_T}{\|\mathbf{t}_T\|}$$
 (3.39)

The frictional law eq. (3.34) now writes in rate form (eq. (3.39)) which implies that the determination of the tangential stress tractions is path dependent - a time integral is required to find the current stress levels.

3.3 The Contact Initial Boundary Value Problem

We consider the two body contact system outlined in section 3.2.1. From the description in the previous section, the contact problem can be considered as a classical mechanical problem with additional inequality constraints arising from the contact conditions. Similarly to the classical mechanical problem, the numerical treatment of contact requires derivation of the weak form description of the strong form equations. In this section, the formal strong form of the contact problem is given. The principle of virtual work is then used to obtain the weak form of the system. We pay special attention to the contact contribution.

3.3.1 The Strong Form

Given prescribed boundary tractions and prescribed body forces at time t = 0, find the solution displacement $\mathbf{u}(\mathbf{x},t)$ for all time period t = [0,T], such that :

1. The momentum balance

$$\operatorname{div} \boldsymbol{\sigma} + \mathbf{b} = \rho \mathbf{a} \qquad \text{on } \Omega$$

a the acceleration field

2. The constitutive equation

$$\sigma = \mathbf{D} : \boldsymbol{\epsilon}$$
 on Ω

where

$$\epsilon = \nabla_s \mathbf{u}$$

3. The initial conditions

$$\mathbf{u}(\mathbf{X},0) = \mathbf{u}_0$$
 $\mathbf{v}(\mathbf{X},0) = \mathbf{v}_0$
on ${}^0\Omega$

4. The boundary conditions

$$\mathbf{u}(\mathbf{X},t) = \mathbf{u}_D$$
 on Γ_D
 $\boldsymbol{\sigma} \mathbf{n} = \mathbf{t}_F$ on Γ_F

5. The contact conditions

$$g_N(\mathbf{x},t) = 0$$
 $\mathbf{x} \in \Gamma_c^1$ on $\Gamma_c^1 \cup \Gamma_c^2$

(a) Normal contact constraints (as well as frictionless contact)

$$g_N \ge 0 \qquad t_N \le 0 \qquad t_N \, g_N = 0$$

(b) Tangential contact constraints

$$\Phi \le 0, \qquad \dot{\gamma} \ge 0, \qquad \dot{\gamma}\Phi = 0$$

 Φ given in eq. (3.37)

3.3.2 The Weak Form

The departure point for the numerical solution procedure, i.e FEM or IGA, of the non linear contact BVP in section 3.3.1 is the derivation of the weak formulation of the local field equations. As previously stated, the nature of contact constraints (a set of inequalities) renders this derivation a more mathematically delicate process as compared to the classical unconstrained mechanical problems [2, 23]. Contact problems are formulated as variational inequalities.

We consider the principle of virtual work, which states that:

The total virtual work done by the external forces (prescribed forces and contact forces), including inertial forces in the case of a dynamic system, on any kinematically admissible virtual displacement field equals the total virtual work done by the internal stresses on the virtual strain field corresponding to that virtual displacement [4]. That is:

$$\delta W = \delta W_{int} - \delta W_{inert} - \delta W_{ext} - \delta W_c \tag{3.40}$$

where in eq. (3.40) δW_{int} denotes the work done by the internal stresses, and writes as follows

$$\delta W_{int} = \int_{\Omega} \boldsymbol{\sigma} : \delta \boldsymbol{\epsilon} \, \mathrm{d}\Omega \tag{3.41}$$

 δW_{inert} is the work done by the inertial forces and writes as follows:

$$\delta W_{inert} = -\int_{\Omega} \rho \mathbf{a} \cdot \delta \mathbf{u} \, d\Omega \tag{3.42}$$

 δW_{ext} is the work done by the external forces and writes as follows :

$$\delta W_{ext} = \int_{\Omega} \mathbf{b} \cdot \delta \mathbf{u} \, d\Omega + \int_{\Gamma_F} \mathbf{t}_F \cdot \delta \mathbf{u} \, d\Gamma$$
 (3.43)

and δW_c is the work done by the contact forces and writes as follows :

$$\delta W_c = \int_{\Gamma_c^1} \mathbf{t} \cdot \delta \mathbf{u}_c^1 \, d\Gamma + \int_{\Gamma_c^2} \mathbf{t} \cdot \delta \mathbf{u}_c^2 \, d\Gamma$$
 (3.44)

Taking into account eqs. (3.10) to (3.12), we can rewrite eq. (3.44) as:

$$\delta W_c = \int_{\Gamma_c^1} t_j \delta \mathbf{u}_c^1 \cdot \bar{\mathbf{n}}_j^1 \, d\Gamma + \int_{\Gamma_c^2} t_j \delta \mathbf{u}_c^2 \cdot \bar{\mathbf{n}}_j^2 \, d\Gamma \qquad j = 1, 2, 3$$

$$= \int_{\Gamma_c^2} t_j \left(\delta \mathbf{u}_c^2 - \delta \mathbf{u}_c^1 \right) \cdot \bar{\mathbf{n}}_j^2 \, d\Gamma \qquad (3.45)$$

We can decompose eq. (3.45) into its normal and tangential parts. And since in the contact interface we have $\Gamma_c^1 \equiv \Gamma_c^2 \equiv \Gamma_c$, we can write the contact contribution into weak from as:

$$\delta W_c = \int_{\Gamma_c} \left(t_N \bar{\mathbf{n}} + t_{T\alpha} \boldsymbol{\tau}^{\alpha} \right) \cdot \left(\delta \mathbf{u}^1 - \delta \bar{\mathbf{u}}^2 \right) d\Gamma$$
 (3.46)

Consolidating all the contributions to the weak form from the internal and external forces, inertial forces and contact terms, eqs. (3.41) to (3.44), we have:

$$\delta W = \int_{\Omega} \boldsymbol{\sigma} : \delta \boldsymbol{\epsilon} \, d\Omega - \int_{\Omega} \mathbf{b} \cdot \delta \mathbf{u} \, d\Omega - \int_{\Gamma_{F}} \bar{\mathbf{t}}_{F} \cdot \delta \mathbf{u} \, d\Gamma \cdots + \int_{\Gamma_{c}} (t_{N} \bar{\mathbf{n}} + t_{T\alpha} \boldsymbol{\tau}^{\alpha}) \cdot (\delta \mathbf{u}^{1} - \delta \bar{\mathbf{u}}^{2}) \, d\Gamma \cdots + \int_{\Omega} \rho \mathbf{a} \cdot \delta \mathbf{u} \, d\Omega \ge 0$$
(3.47)

Equation (3.45) can be written in terms of the gap function in the normal direction, and the relative sliding displacement (tangential slip) in the tangential direction. This requires the expression for the variation of the normal gap and the variation of the tangential slip.

3.3.2.1 Variation of the Normal Gap

As normal gap is expressed as:

$$g_N \bar{\mathbf{n}} = \left(\mathbf{x}^1 - \bar{\mathbf{x}}^2\right) \tag{3.48}$$

The variation of eq. (3.48) gives:

$$\delta g_N \bar{\mathbf{n}} + g_N \delta \bar{\mathbf{n}} = \left(\delta \mathbf{x}^1 - \delta \bar{\mathbf{x}}^2 - \bar{\mathbf{x}}_{,\alpha}^2 \delta \xi^{\alpha} \right) \cdot \bar{\mathbf{n}} + \left(\mathbf{x}^1 - \bar{\mathbf{x}}^2 \right) \cdot \delta \bar{\mathbf{n}}$$
(3.49)

Taking the dot product of eq. (3.49) with the unit normal vector $\bar{\mathbf{n}}$ and since we have that $\bar{\mathbf{x}}_{,\alpha}^2 \cdot \bar{\mathbf{n}} = 0$ (orthogonality condition), $\bar{\mathbf{n}} \cdot \bar{\mathbf{n}} = 1$, and $\bar{\mathbf{n}} \cdot \delta \bar{\mathbf{n}} = 0$, the virtual variation of the normal gap then becomes:

$$\delta g_N = \left(\delta \mathbf{x}^1 - \delta \bar{\mathbf{x}}^2\right) \cdot \bar{\mathbf{n}} \tag{3.50}$$

However, $\delta \mathbf{u}^1 - \delta \bar{\mathbf{u}}^2 = \delta \mathbf{x}^1 - \delta \bar{\mathbf{x}}^2$ [3]; it follows then that :

$$\delta g_N = \left(\delta \mathbf{u}^1 - \delta \bar{\mathbf{u}}^2\right) \cdot \bar{\mathbf{n}} \tag{3.51}$$

Substituting eq. (3.51) into eq. (3.46), we obtain:

$$\delta W_c = \int_{\Gamma_c} t_N \delta g_N \, d\Gamma + \int_{\Gamma_c} t_{T\alpha} \boldsymbol{\tau}^{\alpha} \cdot \left(\delta \mathbf{u}^1 - \delta \bar{\mathbf{u}}^2 \right) \, d\Gamma$$
 (3.52)

3.3.2.2 Variation of the Tangential Slip

The variation of the tangential slip \mathbf{g}_T can be obtained in the same way as its time derivative computed in eq. (3.27) [3, 5, 6]. We have :

$$\delta \mathbf{g}_T = \delta \bar{\xi}^\alpha \boldsymbol{\tau}_\alpha \tag{3.53}$$

and the variation of ξ^{α} in eq. (3.53) follows in the same way as the time derivative in eq. (3.31)

$$\delta \bar{\xi}^{\beta} = H^{\alpha\beta} \left[\left(\delta \mathbf{u}^{1} - \delta \bar{\mathbf{u}}^{2} \right) \cdot \boldsymbol{\tau}_{\alpha} + g_{N} \bar{\mathbf{n}} \cdot \delta \bar{\mathbf{u}}_{,\alpha}^{2} \right]$$
(3.54)

In the tangential direction we then have:

$$\delta W_{c_T} = \int_{\Gamma_c} \mathbf{t}_T \cdot \delta \mathbf{g}_T \, d\Gamma$$

$$= \int_{\Gamma_c} t_{T\alpha} \boldsymbol{\tau}^{\alpha} \cdot \delta \bar{\xi}^{\beta} \boldsymbol{\tau}_{\beta} \, d\Gamma$$

$$= \int_{\Gamma_c} t_{T\alpha} \delta \bar{\xi}^{\alpha} \, d\Gamma$$
(3.55)

Finally, we can write the weak form as follows

$$\int_{\Omega} \boldsymbol{\sigma} : \delta \boldsymbol{\epsilon} \, d\Omega - \int_{\Omega} \mathbf{b} \cdot \delta \mathbf{u} \, d\Omega - \int_{\Gamma_F} \mathbf{t}_F \cdot \delta \mathbf{u} \, d\Gamma \cdots
- \int_{\Gamma_c} t_N \delta g_N \, d\Gamma - \int_{\Gamma_c} t_{T\alpha} \delta \bar{\xi}^{\alpha} \, d\Gamma \cdots
+ \int_{\Omega} \rho \mathbf{a} \cdot \delta \mathbf{u} \, d\Omega \ge 0$$
(3.56)

The derived weak form is still a constrained problem and therefore poses difficulty in its numerical treatment as it may require different minimization techniques compared to the more conventional well established unconstrained mechanical BVP [2, 5, 23]. In the next section we will discuss how we can remedy this limitation.

3.4 Regularization of the Contact Constraints

We suppose that the bodies in contact are elastic and for simplicity we restrict our discussion to the case of negligible dynamic effects such that the inertial terms may be dropped from eq. (3.56). In the absence of contact, the solution field of the mechanical problem (denoted as G_b) is obtained by writing the BVP as an unconstrained minimization problem. That is:

$$G_b = \int_{\Omega} \boldsymbol{\sigma} : \delta \boldsymbol{\epsilon} \, d\Omega - \int_{\Omega} \mathbf{b} \cdot \delta \mathbf{u} \, d\Omega - \int_{\Gamma_F} \mathbf{\bar{t}}_F \cdot \delta \mathbf{u} \, d\Gamma = 0$$
 (3.57)

However mechanical contact problems are constrained problems and write as variational inequalities (eq. (3.57) no longer holds), and as a consequence, they require new minimization techniques. To remedy this, nowadays most engineering analysis in contact mechanics are based on the so called variational equalities which are much easier to introduce in the FE framework [2]. In doing this, it then permits us to use the already well established minimization techniques.

In order to derive these variational equalities, it is assumed that the contact zone is known. At the same time, the contact zone depends on the solution, and is actually unknown *a priori*. This is why this formulation should be coupled with an active set strategy which is used to identify the potential contact portions of the boundary and update them as the solution evolves [2].

If the contact zone is known then the non linear constrained problem described in the previous sections, through the use of the contact constraints treatment methods, can be transformed into the more familiar, easier to treat unconstrained problem [2]. These contact constraints treatment methods basically facilitate the incorporation of the contact constraints into the variational formulation or rather the imposition of the contact constraints on the boundaries. To do this, two basic methods are available, namely: i) the Lagrange multiplier method, and ii) the penalty method. Other constraints methods based on these aforementioned methods, such as the augmented Lagrange method, also exist.

We denote the variational contact contribution by G_c , with

$$G_c = \int_{\Gamma_c} t_N \delta g_N \, d\Gamma + \int_{\Gamma_c} t_{T\alpha} \delta \bar{\xi}^{\alpha} \, d\Gamma$$
 (3.58)

The form of G_c depends on the choice of method used for the incorporation of the contact constraints in the variational formulation. Next we provide the Lagrange multiplier method variational form and the penalty method variational form.

3.4.1 The Lagrange Multipliers Method

With this method, Lagrange multipliers are used to add contact constraints to the weak formulation [3, 23]. The Lagrange multipliers contact contribution, assuming stick conditions, G_c^{LM} is then given by

$$G_c^{\text{LM, stick}} = -\int_{\Gamma_c} \left[\lambda_N \delta g_N + \boldsymbol{\lambda}_T \cdot \delta \mathbf{g}_T \right] d\Gamma + \int_{\Gamma_c} \left[\delta \lambda_N g_N + \delta \boldsymbol{\lambda}_T \cdot \mathbf{g}_T \right] d\Gamma$$
 (3.59)

where the Lagrange multipliers λ_N, λ_T are additional unknowns.

The first integral in eq. (3.59) is the virtual work of the Lagrange multipliers for the variation of the normal gap function and the variation tangential slip. The second integral results from the enforcement of kinematic contact constraints and variation of the Lagrange multipliers. The terms $\lambda_T \cdot \delta \mathbf{g}_T$ and $\delta \lambda_T \cdot \mathbf{g}_T$ are associated with tangential stick. In the case of stick the relative tangential slip \mathbf{g}_T is zero, this then results in a constraint equation from which λ_T follows as a reaction force. In the case of sliding, the tangential traction can be determined from the sliding conditions constitutive law equation - see eq. (3.39). We can write

$$\lambda_T \cdot \delta \mathbf{g}_T \Rightarrow \mathbf{t}_T \cdot \delta \mathbf{g}_T \tag{3.60}$$

Then for sliding, the contact contribution becomes

$$G_c^{\text{LM, slip}} = -\int_{\Gamma_c} \left[\lambda_N \delta g_N + \mathbf{t}_T \cdot \delta \mathbf{g}_T \right] d\Gamma + \int_{\Gamma_c} \delta \lambda_N g_N d\Gamma$$
 (3.61)

We see that the Lagrange multipliers correspond to the unknown normal and tangential contact tractions (see eq. (3.58)). A condition on these multipliers, $\lambda_N \leq 0$, must be satisfied. In fact, this method does not completely convert into an unconstrained minimization problem as it still needs to satisfy the inequality constraints on the Lagrange multipliers λ_N [23].

The advantage of using the Lagrange multipliers method is that the contact constraints are enforced exactly. However this method introduces additional unknowns, and therefore additional degrees of freedom in the system, which increases the computation cost of the model.

3.4.2 The Penalty Method

In this formulation, the contact constraints are regularized with the penalty method. That is, the normal contact traction is represented as a continuous power function of the penetration:

$$t_N(g_N) = \begin{cases} \varepsilon_N (g_N)^q & g_N \le 0\\ 0 & \text{otherwise} \end{cases}$$
 (3.62)

with degree q, and factor ε_N is a non negative penalty parameter. We can see here that the impenetrability condition is only fulfilled approximately. The contact tractions increase with penetration. In actuality, this approximation implies that the contact does not restrict penetration but rather resists to it and the penalty parameter can be seen as the stiffness of the contact interface [23]. The impenetrability condition is recovered when $\varepsilon_N \to \infty$ - see fig. 3.4b which shows a linear penalty method function.

Similarly to fig. 3.4b, the frictional law can be regularized by introducing a tangential penalty parameter ε_T - see fig. 3.7. The tangential penalty ε_T is not necessarily equal to ε_N .

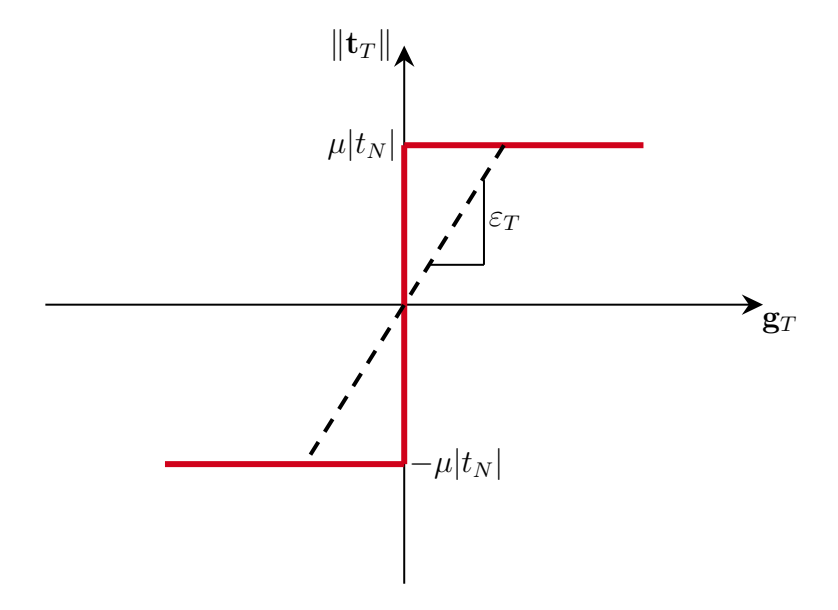


Figure 3.7 – Penalty regularization of the Coulomb friction law exact conditions.

Performing this regularization of eq. (3.39) leads to:

$$\Phi(\mathbf{t}_{T}, t_{N}) = \|\mathbf{t}_{T}\| - \mu |t_{N}| \leq 0$$

$$\dot{\mathbf{t}}_{T} = \varepsilon_{T} \left[\dot{\mathbf{g}}_{T} - \dot{\gamma} \frac{\mathbf{t}_{T}}{\|\mathbf{t}_{T}\|} \right]$$

$$\dot{\gamma} \geq 0$$

$$\dot{\gamma} \Phi = 0$$
(3.63)

Now the regularized Coulomb friction law is analogous to elasto-plasticity behavior, particularly the elasto-perfectly-plastic constitutive law. Again, the exact representation of the Coulomb friction law is only recovered when $\varepsilon_T \to \infty$. The penalty method contact contribution G_c^{PM} then writes as

$$G_c^{\text{PM, stick}} = -\int_{\Gamma_c} \left[\varepsilon_N g_N \delta g_N + \varepsilon_T \mathbf{g}_T \cdot \delta \mathbf{g}_T \right] d\Gamma$$
 (3.64)

 $\varepsilon_N, \varepsilon_T > 0$. We can see that the normal traction and the tangential tractions are approximated as $t_N = \varepsilon_N g_N$ and $\mathbf{t}_T = \varepsilon_T \mathbf{g}_T$, respectively. As it is with the Lagrange multipliers formulation, a slightly different expressions holds for the sliding case. The constitutive equation in eq. (3.63) can be used to compute the tangential contact traction. We then have

$$G_c^{\text{PM, slip}} = -\int_{\Gamma_c} \left[\varepsilon_N g_N \delta g_N + \mathbf{t}_T \cdot \delta \mathbf{g}_T \right] d\Gamma$$
 (3.65)

 \mathbf{t}_T is obtained from the time discretization of constitutive equations in eq. (3.63), typically the Backward Euler time discretization which permits the use of the return mapping for resolution. This is further discussed in section 3.6.2.

The advantage of the penalty method is that it does not require introduction of additional unknowns, there are no additional degrees of freedom added to the system. The penalty contact term depends only on the normal gap function, which in turn is a function of the displacement field. A major drawback of this method is that it leads to an approximate enforcement of contact constraints; the exact solution may only be recovered from this formulation in the limit as $\varepsilon_N, \varepsilon_T \to \infty$. This is however impossible as large penalty parameter values will result in the ill-conditioning of the tangent stiffness matrix [2, 23].

3.5 Contact Interface Discretization Techniques

The treatment of contact constraints in numerical modeling entails in the following: (1) the choice of the method to be used for the enforcement of contact constraints, which we have discussed in section 3.4, and (2) the choice of contact interface (contact integrals) discretization [23]. The second aspect is especially important as it tells us how the contact weak formulation is expressed in discrete form. Different techniques exist for the contact interface discretization, namely:

- Node-to-Node discretization this technique is simple and stable, however it is only suitable for conforming meshes which can only be established for small deformation problems and infinitely small relative sliding.
- Node-to-Surface in 3D setting or Node-to-Segment in 2D setting this technique is less simple but multipurpose and suitable for non conforming meshes. It requires creation of contact pairs; that is, contact constraints are enforced between a node of one contacting body surface (slave surface) and the corresponding surface/segment (master surface). The integrals are collocated at the slave nodes. However this discretization does not pass the patch test, meaning that uniform contact pressure can not be obtained at the contact interface [22]. More over this technique is biased, the solution depends on the choice of the slave/master surface.
- Surface-to-Surface or Segment-to-Segment here the integral is no longer collocated in the slave nodes but rather, the contact constraints are enforced in an integral manner [22]. Unlike NTS, this method passes the patch.

There are also other method available such as the Gauss-Point-To-Surface method (single pass, and the less bias double pass formulation), and more recently the mortar methods which simultaneously satisfy the patch test and stability conditions (at the expense of computational efficiency) [2, 22, 23, 63, 97].

3.6 Contact Discretization with Bézier-based Isogeometric Analysis

We will consider quasi-static contact problems with implicit methods. This means that we assume the inertial forces contribution to be negligible, $\delta W_{inert}^i = 0$. Our departure point is the variational formulation shown in section 3.4. We have that:

$$G_b + G_c = 0 (3.66)$$

with the form of G_b given in equation (3.57), and the full contact contribution G_c formulated by the penalty method (combining the stick and slip contributions) is given by eq. (3.67)

$$G_{c} = \int_{\Gamma_{c}} \varepsilon_{N} g_{N} \delta g_{N} \, d\Gamma + \int_{\Gamma_{c}^{stick}} \varepsilon_{T} \mathbf{g}_{T} \cdot \delta \mathbf{g}_{T} \, d\Gamma + \int_{\Gamma_{c}^{slip}} \mathbf{t}_{T} \cdot \delta \mathbf{g}_{T} \, d\Gamma$$

$$= \int_{\Gamma_{c}} \varepsilon_{N} g_{N} \delta g_{N} \, d\Gamma + \int_{\Gamma_{c}^{slip/stick}} \mathbf{t}_{T} \cdot \delta \mathbf{g}_{T} \, d\Gamma$$

$$= \int_{\Gamma_{c}^{normal}} t_{N} \delta g_{N} \, d\Gamma + \int_{\Gamma_{c}^{tangent}} t_{T\alpha} \delta \bar{\xi}^{\alpha} \, d\Gamma$$

$$(3.67)$$

The boundary conditions are given in section 3.3.1. Equation (3.66) can be rewritten as:

$$\mathbf{F}^{\text{int}} - \mathbf{F}^{\text{ext}} - \mathbf{F}^{\text{c}} = 0 \tag{3.68}$$

with \mathbf{F}^{int} the internal force vector

$$\mathbf{F}^{\text{int}} = \int_{\Omega} \boldsymbol{\sigma} : \boldsymbol{\epsilon}(\delta \mathbf{u}) \, d\Omega \tag{3.69}$$

 $\mathbf{F}^{\mathrm{ext}}$ the external force vector

$$\mathbf{F}^{\text{ext}} = \int_{\Omega} \mathbf{b} \cdot \delta \mathbf{u} \, d\Omega + \int_{\Gamma_F} \mathbf{t}_F \cdot \delta \mathbf{u} \, d\Gamma$$
 (3.70)

and \mathbf{F}^{c} the contact force vector

$$\mathbf{F}^{c} = \int_{\Gamma_{c}} \left(t_{N} \delta g_{N} + t_{T\alpha} \delta \bar{\xi}^{\alpha} \right) d\Gamma \tag{3.71}$$

This problem is discretized with the Bézier-based IGA method detailed in the previous chapter. As the treatment of the internal load vector contribution as well as the external load vectors has already been discussed, in this chapter we will only highlight the final discrete form of the internal and external force vectors. Only the development of the contact force contribution is discussed in detail.

3.6.1 Discretization with Bézier Elements

The Bézier-based IGA approach, detailed in the previous chapter, is used for the numerical modeling of this problem. Bézier basis function, \mathbf{B}_{bez} , are used for both the geometry discretization

and approximation of the solution fields (isoparametric). Unlike the fundamental IGA methods, in which the computational domain does not necessary live on the physical geometry; in this method, through the use of the Bézier inverse matrix, $[\mathbf{B}_{bez}]^{-1}$, we directly solve for the physical solution. This Bézier inverse matrix is evaluated at the Greville points $\hat{\boldsymbol{\xi}}$, which in the Bézier approach with the basis space of [-1,1] equate to:

$$\hat{\boldsymbol{\xi}} = \begin{cases} [-1,0,1] & \text{if quadratic } (p=2) \\ [-1,-\frac{1}{3},\frac{1}{3},1] & \text{if cubic } (p=3) \end{cases}$$
 (3.72)

The Bézier inverse matrix is computed once and then stored for later us. With this approach, the existing FEM contact discretizations can be used without any modification. The only change is in the shape functions subroutine.

Let us denote the Bézier basis functions $B_{\text{bez}}(\boldsymbol{\xi})$ as $\phi(\boldsymbol{\xi})$, $\boldsymbol{\xi} = (\xi, \eta, \zeta)$. The geometry description for each Bézier element is:

$$\mathbf{x}(\boldsymbol{\xi}) = \sum_{a=1}^{n_{\text{cpts}}^e} \phi_a(\boldsymbol{\xi}) \mathbf{x}_a^{\text{cntrl}}$$
(3.73)

accordingly, n_{cpts}^e is the number of nodes in the element and $(\bullet)^{\text{cntrl}}$ implies quantities computed at the control points. The elemental solution field (displacement) is approximated as:

$$\mathbf{u}(\boldsymbol{\xi}) = \sum_{a=1}^{n_{\text{cpts}}^e} \phi_a(\boldsymbol{\xi}) \mathbf{u}_a^{\text{cntrl}}$$
(3.74)

with the solution coefficients at the control points writing as (control solution coefficients):

$$\mathbf{u}_a^{\text{cntrl}} = \left[\mathbf{B}_{\text{bez}}\right]^{-1} \mathbf{u}_a^{\text{phy}} \tag{3.75}$$

 $(\bullet)^{\mathrm{phy}}$ indicates a quantity computed at the physical nodes (nodes located on the actual physical geometry). In matrix form the solution then writes as:

$$\mathbf{u}(\boldsymbol{\xi}) = [\mathbf{Q}] [\mathbf{B}_{\text{bez}}]^{-1} \left\{ \mathbf{u}^{\text{phy}} \right\}$$
 (3.76)

where

$$[\mathbf{Q}] = \begin{bmatrix} \phi_1 & \cdots & \phi_{n_{\text{cpts}}^e} & 0 & \cdots & 0 & 0 & \cdots & 0 \\ 0 & \cdots & 0 & \phi_1 & \cdots & \phi_{n_{\text{cpts}}^e} & 0 & \cdots & 0 \\ 0 & \cdots & 0 & 0 & \cdots & 0 & \phi_1 & \cdots & \phi_{n_{\text{cpts}}^e} \end{bmatrix}$$
(3.77)

and

$$\left\{\mathbf{u}^{\text{phy}}\right\} = \begin{cases}
 u_{1} \\
\vdots \\
 u_{n_{\text{cpts}}^{e}} \\
 v_{1} \\
\vdots \\
 v_{n_{\text{cpts}}^{e}} \\
 w_{1} \\
\vdots \\
 w_{n_{\text{cpts}}^{e}}
\end{cases}$$
(3.78)

The strain-displacement relationship writes as:

$$\epsilon(\mathbf{u}) = \nabla_s \mathbf{u}$$

$$= Q_{i,j} u$$

$$= [\mathbf{B}] [\mathbf{B}_{bez}]^{-1} {\mathbf{u}}$$
(3.79)

[B] contains spatial gradients of the Bézier basis functions. The discrete form with numerical quadrature integration of eq. (3.69) and eq. (3.70), the writes as:

$$\mathbf{F}^{\text{int}} = \sum_{n_{elem}} \left\{ \sum_{i=1}^{n_{GP}} \sum_{j=1}^{n_{GP}} \left[\mathbf{B}_{\text{bez}} \right]^{-T} \left[\mathbf{B} \right]^{T} \left\{ \boldsymbol{\sigma} \right\} w_{i} w_{j} \det J \right\}$$
(3.80)

$$\mathbf{F}^{\text{ext}} = \sum_{n_{elem}} \left\{ \sum_{i=1}^{n_{GP}} \sum_{j=1}^{n_{GP}} \left[\mathbf{B}_{\text{bez}} \right]^{-T} \left[\mathbf{Q} \right] \left\{ \mathbf{b} \right\} w_i w_j \det J + \sum_{i=1}^{n_{GP}} \left[\mathbf{B}_{\text{bez}} \right]^{-T} \left\{ \mathbf{t}_F \right\} w_i \right\}$$
(3.81)

with w_i, w_j the weights for each Gauss point in ξ^1 , ξ^2 directions, n_{GP} the number of Gauss points in each direction, and \mathbf{Q} a matrix containing the basis functions as defined in eq. (3.77).

In next sections, we develop the discrete form of the contact force contribution in eq. (3.71), starting with the time discretization of the incremental friction constitutive law.

3.6.2 Local Time Discretization of the Friction Constitutive Law

The formulation of the tangential constitutive equations in incremental form (eq. (3.63)) leads to a requirement of a time discretization (even in quasi-static settings). Using the penalty regularization for the stick conditions permits the use of the return mapping algorithm which is often used in plasticity problems [3, 5, 23].

Let $\Delta t = t_{n+1} - t_n$ be the chosen time step size. Using the Backward Euler scheme to approximate the rate quantities, the frictional constraints equations can be rewritten in the time discretized setting. The tangential slip defined in incremental form is discretized as follows

$$\dot{\bar{\xi}}^{\alpha} = \frac{\bar{\xi}_{n+1}^{\alpha} - \bar{\xi}_{n}^{\alpha}}{\Delta t} \rightarrow \dot{\mathbf{g}}_{T} = \frac{\mathbf{g}_{T_{n+1}} - \mathbf{g}_{T_{n}}}{\Delta t} = \frac{\bar{\xi}_{n+1}^{\alpha} - \bar{\xi}_{n}^{\alpha}}{\Delta t} \boldsymbol{\tau}_{\alpha}$$
(3.82)

The constitutive law equations in discretized form then write as

$$\Phi_{n+1} = \|\mathbf{t}_{T_{n+1}}\| - \mu |t_{N_{n+1}}| < 0, \quad \Delta \gamma > 0, \quad \Phi_{n+1} \Delta \gamma = 0, \tag{3.83}$$

and the time-discretized tangential traction as

$$t_{T_{\alpha n+1}} = t_{T_{\alpha n}} + \varepsilon_T \left[m_{\alpha \beta} \left(\bar{\xi}_{n+1}^{\beta} - \bar{\xi}_n^{\beta} \right) - \Delta \gamma \frac{t_{T_{\alpha n+1}}}{\|\mathbf{t}_{T_{n+1}}\|} \right]$$
(3.84)

The slip tangential gap follows as

$$\Delta \mathbf{g}_{T_{n+1}^{slip}} = \Delta \gamma \frac{\mathbf{t}_{T_{n+1}}}{\|\mathbf{t}_{T_{n+1}}\|}$$
(3.85)

The frictional sliding traction in the time-discretized setting, which derives from the constitutive law and must be co-linear with the tangential sliding, is given by

$$\mathbf{t}_{T_{n+1}} = \mu \left| t_{N_{n+1}} \right| \frac{\mathbf{g}_{T_{n+1}}}{\left\| \mathbf{g}_{T_{n+1}} \right\|}$$
(3.86)

For the algorithmic update of the frictional tractions, we follow the predictor/corrector return mapping algorithm. Similarly to its application in plasticity, the algorithm involves first integrating the evolution equations under zero incremental tangential slip ($\Delta \gamma = 0$) to obtain the stick state predictor. If the predicted stick state violates the Coulomb's friction law constitutive equations (that is, the state predicted is outside the bounds of Coulomb's friction law, i.e. Coulomb's frictional cone), the predicted stick state tangential tractions are then relaxed (here, mapped on to the surface of the Coulomb's cone) by iteratively correcting the incremental tangential slip. This is done as follows (see appendix B for graphical representation of the return mapping algorithm):

• The departure point is the computation of the normal traction as

$$t_{N_{n+1}} = \varepsilon_N g_{n+1} \tag{3.87}$$

• First assume $\Delta \gamma = 0$, then compute the trial tangential traction

$$t_{T_{\alpha n+1}}^{trial} = t_{T_{\alpha n}} + \varepsilon_T \left[m_{\alpha \beta} \left(\bar{\xi}_{n+1}^{\beta} - \bar{\xi}_{n}^{\beta} \right) \right]$$
 (3.88)

• Using the trial tangential traction in eq. (3.88) and normal traction in eq. (3.87), evaluate the slip function

$$\Phi_{n+1}^{trial} = \left\| \mathbf{t}_{T_{n+1}}^{trial} \right\| - \mu \left| t_{N_{n+1}} \right| \le 0 \tag{3.89}$$

• Based on the stick/slip status from eq. (3.89), update the tangential tractions accordingly

$$t_{T_{\alpha n+1}} = \begin{cases} t_{T_{n+1}}^{trial} & \text{if } \Phi_{n+1}^{trial} \leq 0\\ \mu |t_{N_{n+1}}| \frac{t_{T_{\alpha n+1}}^{trial}}{\|\mathbf{t_{T_{n+1}}}\|} & \text{otherwise} \end{cases}$$
(3.90)

From here on we will express all quantities in the current time step, $t = t_{n+1}$. We then drop the subscript n + 1 for current step quantities, whereas the subscript n referring to quantities in the previous time step is retained.

3.6.3 Linearization of the Contact Contributions

In general, the solution for the contact problem is sought out iteratively and therefore requires the linearization of its weak form contribution. The linearization of eq. (3.67) gives us

$$\Delta G_c = \int_{\Gamma_c^{normal}} \left(\Delta t_N \delta g_N + t_N \Delta \delta g_N \right) d\Gamma + \int_{\Gamma_c^{tangent}} \left(\Delta t_{T\alpha} \delta \bar{\xi}^{\alpha} + t_{T\alpha} \Delta \delta \bar{\xi}^{\alpha} \right) d\Gamma$$
 (3.91)

The variations of both the gap function and the convective coordinates are given in eq. (3.51) and eq. (3.54), respectively. Their linearizations then follows from the variations as:

$$\Delta g_N = \left(\Delta \mathbf{u}^1 - \Delta \bar{\mathbf{u}}^2\right) \cdot \bar{\mathbf{n}} \tag{3.92}$$

$$\Delta \bar{\xi}^{\alpha} = \left[H^{\alpha\beta} \right] \left[\left(\Delta \mathbf{u}^{1} - \Delta \bar{\mathbf{u}}^{2} \right) \cdot \boldsymbol{\tau}_{\beta} + g_{N} \bar{\mathbf{n}} \cdot \Delta \bar{\mathbf{u}}_{,\alpha}^{2} \right]$$
(3.93)

The linearized normal traction follows from eq. (3.92) and writes as $\Delta t_N = \varepsilon_N \Delta g_N$.

It remains now to derive the expressions for the linearized tangential traction, and the linearization of the variation of the normal gap and the tangetial gap. To obtain the expression of the linearized tangential traction we need both $\Delta t_{T\alpha}$ and $\Delta t_{T\alpha}^{trial}$. To derive $\Delta t_{T\alpha}$ we linearize eq. (3.84), which then gives us eq. (3.94).

$$\Delta t_{T\alpha} = \mu p_{T_{\alpha}} \Delta t_N + \frac{\mu t_N}{\left\| \mathbf{t}_T^{trial} \right\|} \Delta t_{T_{\alpha}}^{trial} \left[\delta_{\gamma}^{\beta} - p_T^{\beta} p_{T_{\gamma}} \right] + \mu t_N \mathbf{p}_T \cdot \left[\Delta \bar{\mathbf{u}}_{,\beta}^2 + \bar{\mathbf{x}}_{,\beta\gamma}^2 \Delta \bar{\xi}^{\gamma} \right] p_T^{\beta} p_{T_{\alpha}}$$
(3.94)

where $\mathbf{p}_T = \frac{\mathbf{t}_T^{trial}}{\|\mathbf{t}_T^{trial}\|}$, variable δ_{γ}^{β} is the Kronecker delta (an identity matrix), and

$$p_{T_{\alpha}} = \mathbf{p}_{T} \boldsymbol{\tau}_{\alpha}$$

$$p_{T^{\alpha}} = \mathbf{p}_{T} \boldsymbol{\tau}^{\alpha}$$

$$(3.95)$$

 $\Delta t_{T_{\alpha}}^{trial}$, derived from eq. (3.88), is given in eq. (3.96).

$$\Delta t_{T_{\alpha}}^{trial} = \varepsilon_T \left[m_{\alpha\beta} \Delta \bar{\xi}^{\beta} + 2 \left(\bar{\mathbf{x}}_{,\beta\gamma}^2 \cdot \boldsymbol{\tau}_{\beta} \Delta \bar{\xi}^{\gamma} + \Delta \bar{\mathbf{u}}_{,\beta}^2 \cdot \boldsymbol{\tau}_{\beta} \right) \left(\bar{\xi}^{\alpha} - \bar{\xi}_{n}^{\alpha} \right) \right]$$
(3.96)

The departure point for obtaining the expressions for $\Delta \delta g_N$ and $\Delta \delta \bar{\xi}^{\alpha}$, is the linearization of eq. (3.49), that is:

$$\Delta \left\{ \delta g_N \bar{\mathbf{n}} + g_N \delta \bar{\mathbf{n}} = \delta \mathbf{u}^1 - \delta \bar{\mathbf{u}}^2 - \bar{\mathbf{u}}_{,\alpha}^2 \delta \xi^{\alpha} \right\}$$
 (3.97)

Taking the dot product between eq. (3.97) and the normal vector $\bar{\mathbf{n}}$, we can derive the expression of $\Delta \delta g_N$. Similarly, the dot product of eq. (3.97) with the covariant vector $\boldsymbol{\tau}_{\alpha}$ gives us $\Delta \delta \bar{\xi}^{\alpha}$. Here, we will only detail the final expression for both these variables, the full derivation for both these terms is given the appendix A and can also be found in the works of [2, 3, 5]. Equation (3.98) gives the expression of $\Delta \delta g_N$ and in eq. (3.99) we have the expression for $\Delta \delta \bar{\xi}^{\alpha}$.

$$\Delta \delta g_N = -\left[\delta \bar{\mathbf{u}}_{,\alpha} \Delta \xi^{\alpha} + \Delta \bar{\mathbf{u}}_{,\alpha} \delta \xi^{\alpha} + \bar{\mathbf{x}}_{,\alpha\beta} \Delta \xi^{\alpha} \delta \xi^{\beta}\right] \cdot \bar{\mathbf{n}} + \frac{g_N}{m_{\alpha\beta}} \left[\left(\delta \bar{\mathbf{u}}_{,\alpha} + \bar{\mathbf{x}}_{,\alpha\gamma} \delta \xi^{\gamma}\right) \bar{\mathbf{n}} \otimes \bar{\mathbf{n}} \left(\Delta \bar{\mathbf{u}}_{,\beta} + \bar{\mathbf{x}}_{,\beta\delta} \Delta \xi^{\delta}\right) \right]$$
(3.98)

$$(m_{\alpha\beta} - g_N k_{\alpha\beta}) \Delta \delta \bar{\xi}^{\beta} = -\left(\Delta \bar{\mathbf{u}}_{,\alpha}^2 \delta \bar{\xi}^{\alpha} + \delta \bar{\mathbf{u}}_{,\alpha}^2 \Delta \bar{\xi}^{\alpha}\right) \cdot \boldsymbol{\tau}_{\beta} - \left(\boldsymbol{\tau}_{\alpha} \cdot \boldsymbol{\tau}_{\alpha,\beta} - g_N \bar{\mathbf{n}} \cdot \boldsymbol{\tau}_{\alpha,\alpha\beta}\right) \Delta \bar{\xi}^{\gamma} \delta \bar{\xi}^{\gamma} - g_N \left(\Delta \bar{\mathbf{u}}_{,\alpha\beta}^2 \delta \bar{\xi}^{\alpha} + \delta \bar{\mathbf{u}}_{,\alpha\beta}^2 \Delta \bar{\xi}^{\alpha}\right) \cdot \bar{\mathbf{n}} - \left(\delta \bar{\mathbf{u}}_{,\alpha}^2 + \boldsymbol{\tau}_{\alpha,\gamma} \delta \bar{\xi}^{\gamma}\right) \cdot \boldsymbol{\tau}_{\alpha} \Delta \bar{\xi}^{\beta} - \left(\Delta \bar{\mathbf{u}}_{,\alpha}^2 + \boldsymbol{\tau}_{\alpha,\gamma} \Delta \bar{\xi}^{\gamma}\right) \cdot \boldsymbol{\tau}_{\alpha} \delta \bar{\xi}^{\beta} + \left(\delta \mathbf{u}^1 - \delta \bar{\mathbf{u}}^2\right) \cdot \left(\Delta \bar{\mathbf{u}}_{,\beta}^2 + \boldsymbol{\tau}_{\beta,\alpha} \Delta \bar{\xi}^{\alpha}\right) + \left(\Delta \mathbf{u}^1 - \Delta \bar{\mathbf{u}}^2\right) \cdot \left(\delta \bar{\mathbf{u}}_{,\beta}^2 + \boldsymbol{\tau}_{\beta,\alpha} \delta \bar{\xi}^{\alpha}\right)$$

$$(3.99)$$

3.6.4 Node to Surface Contact Discretization

To cater for the more general non-conforming/non-matching meshes at the contact interface, we discretize the contact contribution using the Node-To-Surface (NTS) technique. We restrict the solution \mathbf{u} to the discretized contact surface Γ_c .

If we take body "1" as the slave and body "2" as the master surface, in the NTS discretization technique the computation of the contact contribution integrals in the weak formulation (see eq. (3.67)) is replaced by the evaluation of these integrals at the slave nodal locations. This is to say, from the variational stand point, this technique amounts to the collocation of the contact integrals at the slave nodes [3, 5, 23].

We define the so-called contact element as the elementary unit of the discretization to which the contact contribution is associated to. Figure 3.8 shows an example of the NTS discretization with the contact pair made of the slave node and the 3 noded master surface (the violet master segments and slave node make up the contact element).

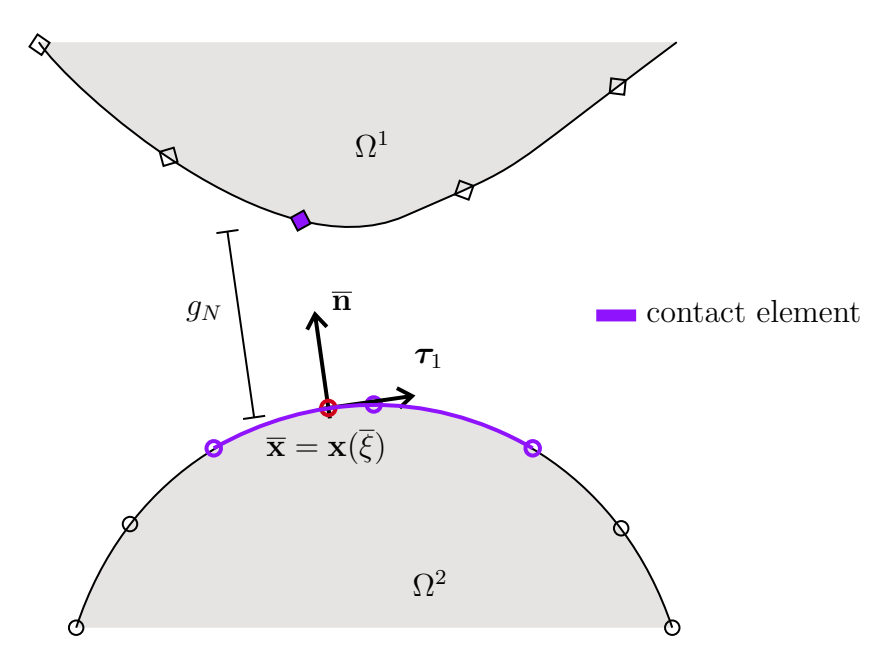


Figure 3.8 – NTS discretization for linear quadrilaterals elements : \Diamond - slave nodes, \circ - master nodes, \circ closest point projection.

The geometry of the contact element is then given by:

$$\mathbf{x}(\xi,\eta) = \sum_{a=1}^{n_c^e} \phi_a(\xi,\eta) \mathbf{x}_a^{\text{cntrl}}$$
(3.100)

 n_c^e is the number of nodes in each contact element. The solution field of the two bodies is approximated as follows:

$$\mathbf{u}^{1} = \sum_{a=1}^{n_{c}^{e}} \phi_{a} \mathbf{u}_{a}^{1^{\text{cntrl}}} \text{ and } \mathbf{u}^{2} = \sum_{a=1}^{n_{c}^{e}} \phi_{a} \mathbf{u}_{a}^{2^{\text{cntrl}}}$$
 (3.101)

and its variation as

$$\delta \mathbf{u}^{1} = \sum_{a=1}^{n_{c}^{e}} \phi_{a} \delta \mathbf{u}_{a}^{1^{\text{cntrl}}} \quad \text{and} \quad \delta \mathbf{u}^{2} = \sum_{a=1}^{n_{c}^{e}} \phi_{a} \delta \mathbf{u}_{a}^{2^{\text{cntrl}}}$$
(3.102)

Recalling that with this Bézier based approach we solve directly for the physical solution. That is, we introduce the Bézier inverse matrix into the shape functions routine, which then allows an implicit map of the solution onto the physical domain, and essentially allows us to have a discretization similar to that of classical FEM however with the benefits of an exact geometry. Let us define $\tilde{\phi}$, such that:

$$\tilde{\phi}_i(\bar{\boldsymbol{\xi}}) = \phi_i(\bar{\boldsymbol{\xi}}) \left[\mathbf{B}_{\text{bez}} \right]^{-1} \tag{3.103}$$

with

$$\phi = \begin{bmatrix} \phi_1 & \phi_2 & \cdots & \phi_{n_{pts}} \end{bmatrix}$$

 $\tilde{\phi}_i$ is then used as a basis, and we can substitute this interpolation into the variations and their linearized counterparts in eqs. (3.92) and (3.93). See eqs. (3.104) to (3.106) for NTS discretization of the normal gap, its variation and the variation of projetion point parametric coordinates.

$$g_N = \left[\tilde{\phi}(\bar{\boldsymbol{\xi}}) \, \mathbf{u}^{2^{\text{cntrl}}} - \mathbf{u}^1 \right] \cdot \bar{\mathbf{n}} \tag{3.104}$$

$$\delta g_N = \left[\tilde{\phi}(\bar{\boldsymbol{\xi}}) \,\delta \mathbf{u}^{2^{\text{cntrl}}} - \delta \mathbf{u}^1\right] \cdot \bar{\mathbf{n}} \tag{3.105}$$

$$\delta \xi^{\beta} = H^{-\alpha\beta} \left[\left(\tilde{\boldsymbol{\phi}}(\bar{\boldsymbol{\xi}}) \delta \mathbf{u}^2 - \delta \mathbf{u}^1 \right) \cdot \boldsymbol{\tau}_{\alpha} - g_N \mathbf{n} \cdot \tilde{\boldsymbol{\phi}}_{,\alpha}(\bar{\boldsymbol{\xi}}) \delta \mathbf{u}^2 \right]$$
(3.106)

We can express the linearized contact integrals in a more compact matrix form as is done in [5]. For a 2D case with $\alpha = 1$ we can define the following NTS vectors:

$$\delta \mathbf{u} = \begin{bmatrix} \delta \mathbf{u}^{1} \\ \delta \bar{\mathbf{u}}_{1}^{2} \\ \delta \bar{\mathbf{u}}_{2}^{2} \\ \vdots \\ \delta \bar{\mathbf{u}}_{n}^{2} \end{bmatrix} \qquad \Delta \mathbf{u} = \begin{bmatrix} \Delta \mathbf{u}^{1} \\ \Delta \bar{\mathbf{u}}_{1}^{2} \\ \Delta \bar{\mathbf{u}}_{2}^{2} \\ \vdots \\ \Delta \bar{\mathbf{u}}_{n}^{2} \end{bmatrix} \qquad \mathbf{N} = \begin{bmatrix} -\bar{\mathbf{n}} \\ \tilde{\phi}_{1}\bar{\mathbf{n}} \\ \tilde{\phi}_{2}\bar{\mathbf{n}} \\ \vdots \\ \tilde{\phi}_{n}\bar{\mathbf{n}} \end{bmatrix} \qquad \mathbf{T} = \begin{bmatrix} -\boldsymbol{\tau}_{1} \\ \tilde{\phi}_{1}\boldsymbol{\tau}_{1} \\ \tilde{\phi}_{2}\boldsymbol{\tau}_{1} \\ \vdots \\ \tilde{\phi}_{n}\boldsymbol{\tau}_{1} \end{bmatrix}$$
(3.107)

$$\mathbf{N}_{1} = \begin{bmatrix} \mathbf{0} \\ \tilde{\phi}_{1,1}\bar{\mathbf{n}} \\ \tilde{\phi}_{2,1}\bar{\mathbf{n}} \\ \vdots \\ \tilde{\phi}_{n,1}\bar{\mathbf{n}} \end{bmatrix} \quad \mathbf{T}_{1} = \begin{bmatrix} \mathbf{0} \\ \tilde{\phi}_{1,1}\boldsymbol{\tau}_{1} \\ \tilde{\phi}_{2,1}\boldsymbol{\tau}_{1} \\ \vdots \\ \tilde{\phi}_{n,1}\boldsymbol{\tau}_{1} \end{bmatrix} \quad \mathbf{N}_{11} = \begin{bmatrix} \mathbf{0} \\ \tilde{\phi}_{1,11}\bar{\mathbf{n}} \\ \tilde{\phi}_{2,11}\bar{\mathbf{n}} \\ \vdots \\ \tilde{\phi}_{n,11}\bar{\mathbf{n}} \end{bmatrix}$$
 (3.108)

For full 3D NTS vectors see [5]. The discrete form of the contact variables variations and linearizations, in a more compact form, then write as

• Normal gap

$$\delta g_N = \delta \mathbf{u}^T \mathbf{N}, \quad \Delta g_N = \mathbf{N}^T \Delta \mathbf{u}$$

• Tangential gap

$$\delta \bar{\xi} = \delta \mathbf{u}^{T} \left\{ H^{-1} \left[\mathbf{T} - g_{N} \mathbf{N}_{1} \right] \right\}$$
$$\Delta \bar{\xi} = \underbrace{\left\{ H^{-1} \left[\mathbf{T} - g_{N} \mathbf{N}_{1} \right] \right\}}_{\mathbf{D}_{1}}^{T} \Delta \mathbf{u}$$

• Stick/trial tangential traction

$$\Delta t_{T_1}^{trial} = \varepsilon_T \left[m_{11} \mathbf{D}_1^{\mathrm{T}} + 2 \left(\tilde{\boldsymbol{\phi}}_{,11} \bar{\mathbf{x}}^2 \cdot \boldsymbol{\tau}_1 \mathbf{D}_1^{\mathrm{T}} + \mathbf{T}_1^{\mathrm{T}} \right) \left(\bar{\boldsymbol{\xi}} - \bar{\boldsymbol{\xi}}_n \right) \right] \Delta \mathbf{u}$$
$$= \varepsilon_T \left[m_{11} \mathbf{D}_1^{\mathrm{T}} + 2 \tilde{\mathbf{T}}_1^{\mathrm{T}} \left(\bar{\boldsymbol{\xi}} - \bar{\boldsymbol{\xi}}_n \right) \right] \Delta \mathbf{u}$$

where

$$\tilde{\mathbf{T}}_1 = \mathbf{T}_1 + \tilde{\boldsymbol{\phi}}_{.11} \bar{\mathbf{x}}^2 \cdot \boldsymbol{\tau}_1 \, \mathbf{D}_1$$

• Sliding tangential traction

$$\Delta t_{T1} = \mu \varepsilon_N \operatorname{sign} \left(t_{T_1}^{trial} \right) \left[\sqrt{m_{11}} \, \mathbf{N}^{\mathrm{T}} + \frac{g_N}{\sqrt{m_{11}}} \left(\tilde{\boldsymbol{\phi}}_{,11} \bar{\mathbf{x}}^2 \cdot \boldsymbol{\tau}_1 \mathbf{D}_1^{\mathrm{T}} + \mathbf{T}_1^{\mathrm{T}} \right) \right] \Delta \mathbf{u}$$
$$= \mu \varepsilon_N \operatorname{sign} \left(t_{T_1}^{trial} \right) \left[\sqrt{m_{11}} \, \mathbf{N}^{\mathrm{T}} + \frac{g_N}{\sqrt{m_{11}}} \tilde{\mathbf{T}}_1^{\mathrm{T}} \right] \Delta \mathbf{u}$$

• Linearized normal gap variation

$$\Delta \delta g_N = -\delta \mathbf{u}^T \left(-\mathbf{N}_1 \mathbf{D}_1^T - \mathbf{D}_1 \mathbf{N}_1^T + k_{11} \mathbf{D}_1 \mathbf{D}_1^T \right) \Delta \mathbf{u}$$
$$+ \delta \mathbf{u}^T \frac{g_N}{m_{11}} \left(-k_{11} \mathbf{N}_1 \mathbf{D}_1^T + k_{11}^2 \mathbf{D}_1 \mathbf{D}_1^T - \mathbf{N}_1 \mathbf{N}_1^T - k_{11} \mathbf{D}_1 \mathbf{N}_1^T \right) \Delta \mathbf{u}$$

define

$$\tilde{\mathbf{N}}_1 = \mathbf{N}_1 - k_{11}\mathbf{D}_1$$

then we have

$$\Delta \delta g_N = \delta \mathbf{u}^{\mathrm{T}} \left\{ \mathbf{N}_1 \mathbf{D}_1^{\mathrm{T}} + \mathbf{D}_1 \mathbf{N}_1^{\mathrm{T}} - k_{11} \mathbf{D}_1 \mathbf{D}_1^{\mathrm{T}} + \frac{g_N}{m_{11}} \tilde{\mathbf{N}}_1 \tilde{\mathbf{N}}_1^{\mathrm{T}} \right\} \Delta \mathbf{u}$$
$$= \delta \mathbf{u}^{\mathrm{T}} \mathbf{K}_{\mathbf{N}_{\delta \Delta}} \Delta \mathbf{u}$$

• Linearized tangential gap variation (detailed in appendix)

$$\begin{split} H\Delta\delta\bar{\xi} &= \delta\mathbf{u}^{T}\left\{-2\left(\mathbf{T}_{1}\mathbf{D}_{1}^{\mathrm{T}} + \mathbf{D}_{1}\mathbf{T}_{1}^{\mathrm{T}}\right) + \left(3\boldsymbol{\tau}_{1}\cdot\tilde{\boldsymbol{\phi}}_{,11}\bar{\mathbf{x}}^{2} - g_{N}\bar{\mathbf{n}}\cdot\tilde{\boldsymbol{\phi}}_{,111}\bar{\mathbf{x}}^{2}\right)\mathbf{D}_{1}\mathbf{D}_{1}^{\mathrm{T}}\right\}\Delta\mathbf{u} \\ &+ \delta\mathbf{u}^{T}\left\{g_{N}\left(\mathbf{N}_{11}\mathbf{D}_{1}^{\mathrm{T}} + \mathbf{D}_{1}\mathbf{N}_{11}^{\mathrm{T}}\right) + \mathbf{N}\tilde{\mathbf{N}}_{1}^{\mathrm{T}} + \tilde{\mathbf{N}}_{1}\mathbf{N}^{\mathrm{T}}\right\}\Delta\mathbf{u} \\ &+ \delta\mathbf{u}^{T}\left\{\frac{1}{m_{11}}\left[\tilde{\mathbf{N}}_{1}\left(\mathbf{T}_{1} - \boldsymbol{\tau}_{1}\cdot\tilde{\boldsymbol{\phi}}_{,11}\bar{\mathbf{x}}^{2}\mathbf{D}_{1}\right)^{\mathrm{T}} + \left(\mathbf{T}_{1} - \boldsymbol{\tau}_{1}\cdot\tilde{\boldsymbol{\phi}}_{,11}\bar{\mathbf{x}}^{2}\mathbf{D}_{1}\right)\tilde{\mathbf{N}}_{1}^{\mathrm{T}}\right]\right\}\Delta\mathbf{u} \\ &= \delta\mathbf{u}^{\mathrm{T}}\mathbf{K}_{\mathrm{T}_{\delta\Delta}}\Delta\mathbf{u} \end{split}$$

• Stiffness and force term for stick conditions

$$\mathbf{K}_{c}^{\text{stick}} = \varepsilon_{N} \mathbf{N} \mathbf{N}^{\text{T}} + \varepsilon_{N} g_{N} \mathbf{K}_{N_{\delta \Delta}} + \varepsilon_{T} m_{11} \mathbf{D}_{1} \mathbf{D}_{1}^{\text{T}} + 2\varepsilon_{T} \mathbf{D}_{1} \tilde{\mathbf{T}}_{1}^{\text{T}} \left(\bar{\xi} - \bar{\xi}_{n}\right) + t_{T_{1}}^{trial} \mathbf{K}_{T_{\delta \Delta}}$$
(3.109)
$$\mathbf{F}_{c}^{\text{stick}} = \varepsilon_{N} g_{N} \mathbf{N} + t_{T_{1}}^{trial} \mathbf{D}_{1}$$
(3.110)

• Stiffness and force term for sliding conditions

$$\mathbf{K}_{c}^{\text{slip}} = \varepsilon_{N} \mathbf{N} \mathbf{N}^{\text{T}} + \varepsilon_{N} g_{N} \mathbf{K}_{N_{\delta\Delta}} + \mu \varepsilon_{N} \operatorname{sign} \left(t_{T_{1}}^{trial} \right) \sqrt{m_{11}} \mathbf{D}_{1} \mathbf{N}^{\text{T}} + \mu \varepsilon_{N} \operatorname{sign} \left(t_{T_{1}}^{trial} \right) \frac{g_{N}}{\sqrt{m_{11}}} \mathbf{D}_{1} \tilde{\mathbf{T}}_{1}^{\text{T}} + t_{T_{1}} \mathbf{K}_{T_{\delta\Delta}}$$

$$(3.111)$$

$$\mathbf{F}_c^{\text{slip}} = \varepsilon_N g_N \mathbf{N} + t_{T1} \mathbf{D}_1 \tag{3.112}$$

Note that the all discrete contact terms, for both stick condition and slip conditions, detailed above must be evaluated at the closest projection point of the slave node onto the master surface. This is achieved through the CPP algorithm introduced in section 3.2.2.2. In the next section we detail the discrete form of the CPP algorithm as well as the resolution method used to compute $\bar{\xi}$.

3.6.5 The Closest Point Projection Algorithm

To obtain the parameter values $\bar{\xi}$ at the closest point projection we must find the solution to eq. (3.20). Using Newton-Raphson method, we have that : suppose f(x) = 0, the solution x to f(x) is obtained as follows

$$x = x_0 + \frac{f(x_0)}{f'(x_0)} \tag{3.113}$$

Therefore the linearized eq. (3.20) writes as

$$\boldsymbol{\xi}^{n+1} = \boldsymbol{\xi}^n + \left[\frac{\partial \mathbf{x}^2}{\partial \boldsymbol{\xi}} \frac{\partial \mathbf{x}^2}{\partial \boldsymbol{\xi}} - \left(\mathbf{x}^1 - \mathbf{x}^2(\boldsymbol{\xi}) \right) \cdot \frac{\partial^2 \mathbf{x}^2}{\partial \boldsymbol{\xi}^2} \right]_{\boldsymbol{\xi}^n}^{-1} \cdot \left[\left(\mathbf{x}^1 - \mathbf{x}^2(\boldsymbol{\xi}) \right) \cdot \frac{\partial \mathbf{x}^2}{\partial \boldsymbol{\xi}} \right]_{\boldsymbol{\xi}^n}$$
(3.114)

We can see that eq. (3.114) requires the first and second derivatives of the basis functions $\phi(\xi)$. These are computed as:

$$\mathbf{x}_{,\boldsymbol{\xi}} = \sum_{a=1}^{n_{\text{cpts}}^{e}} \boldsymbol{\phi}_{a,\boldsymbol{\xi}} \mathbf{x}_{a} = \mathbf{Q}_{,\boldsymbol{\xi}} \left[\mathbf{B}_{\text{bez}} \right]^{-1} \mathbf{P}^{T}$$

$$\frac{\partial^{2} \mathbf{x}}{\partial \boldsymbol{\xi}^{2}} = \sum_{a=1}^{n_{\text{cpts}}^{e}} \boldsymbol{\phi}_{a,\boldsymbol{\xi}\boldsymbol{\xi}} \mathbf{x}_{a} = \mathbf{Q}_{,\boldsymbol{\xi}\boldsymbol{\xi}} \left[\mathbf{B}_{\text{bez}} \right]^{-1} \mathbf{P}^{T}$$
(3.115)

P a vector containing **x** coordinates. The solution to eq. (3.114) is then $\bar{\boldsymbol{\xi}}$. Position **x** is given by eq. (3.100). Once $\bar{\boldsymbol{\xi}}$ is known, we can then evaluate the normal gap function. First we compute the outward normal vector as:

$$\bar{\mathbf{n}} = \frac{\bar{\mathbf{x}}_{,\xi}^2 \times \bar{\mathbf{x}}_{,\eta}^2}{\left\|\bar{\mathbf{x}}_{,\xi}^2 \times \bar{\mathbf{x}}_{,\eta}^2\right\|} \tag{3.116}$$

and compute the normal gap from eq. (3.21). This normal gap is then used to determine the contact state (whether the current slave node is in contact mode or separation mode).

3.6.6 The Solution Procedure

In this section we highlight the algorithmic treatment of the discrete contact problem detailed above. Our problem consists of a contact interface discretized with the NTS technique and contact constraints enforced with the penalty method. The full discrete form of all terms in the weak form (presented in equations eqs. (3.68) to (3.71)) is given in eqs. (3.80) and (3.81) as well as eqs. (3.109) to (3.112).

To complete the formulation detailed in the previous sections, we need a method to identify the active set strategy (a contact search algorithm), which up to this point we have assumed it has already been established. This forms part of contact detection process, a very important aspect of computational contact mechanics, more specifically for large deformation problems [3, 5, 6, 97]. Not only is the contact zone unknown a priori, it may also change considerably within a load step, and in some cases even with the Newton-Raphson iteration.

The search algorithm then facilitates first the global search for entities/elements that may possibly come into contact during the load step, and then the contact detection which is a local search for contact pairs that are actually in contact. Since we are in the IGA framework, we use the multipatch concept to facilitate the global contact search, that is, based on the type of problem (geometry, boundary conditions, etc), we can limit all elements that are likely to come into contact in to a single patch [22, 23]. The local contact detection algorithm is then invoked during the resolution process to identify the true contact status - based on the distance function, we obtain the master segment/surface closest to the slave node and then project the slave node on to this closest master segment using the CPP algorithm detailed in the previous section. Once we have an active set strategy we can proceed with the resolution process.

3.6.6.1 Newton-Raphson Technique

The penalty method is typically implemented with a combination of the active set strategy and a Newton-Raphson iterative procedure. First eq. (3.68) is written as a residual vector $\mathbf{R}(\mathbf{u})$:

$$\mathbf{R}(\mathbf{u}) = \mathbf{F}^{\text{int}}(\mathbf{u}) - \mathbf{F}^{\text{ext}} - \mathbf{F}_{\text{c}}^{\text{stick/slip}}(\mathbf{u})$$
(3.117)

which is then linearized as follows:

$$\frac{\mathrm{d}\mathbf{R}(\mathbf{u})}{\mathrm{d}\mathbf{u}}\Delta\mathbf{u} + \mathbf{R}(\mathbf{u}) = \underbrace{\left[\mathbf{K}^{\mathrm{int}}(\mathbf{u}) + \mathbf{K}_{c}^{\mathrm{stick/slip}}(\mathbf{u})\right]}_{\mathbf{K}_{c}^{\mathbf{P}}(\mathbf{u})} \Delta\mathbf{u} + \mathbf{R}(\mathbf{u}) = \mathbf{0}$$
(3.118)

 $\mathbf{K}^{\mathrm{int}}(\mathbf{u})$ and $\mathbf{K}_{c}^{\mathrm{stick/slip}}(\mathbf{u})$ are the continuum tangent stiffness matrix and the penalty contact contribution stiffness matrix, respectively. The Newton-Raphson procedure then consists in seeking the iterative solution of the linearized equation

$$\mathbf{K}^{\mathbf{P}}(\mathbf{u}^k)\Delta\mathbf{u}^k = -\mathbf{R}^{\mathbf{P}}(\mathbf{u}^k) \tag{3.119}$$

where \mathbf{u}^k is the solution vector at iteration k and $\Delta \mathbf{u}^k = \mathbf{u}^{k+1} - \mathbf{u}^k$ is the incremental solution update at iteration k. To solve eq. (3.119), the incremental solution procedure can be used.

3.6.6.2 Contact/Impact Algorithm: Global Time Discretization

So far we have neglected the inertial effects and therefore assumed quasi static conditions. In reality, contact problems tend to be dynamic, i.e. an impact event. In this case the problem

then entails in : suppose we have the numerical solution fields displacement \mathbf{u}_n , velocity \mathbf{v}_n , and acceleration \mathbf{a}_n , of a dynamic system under contact conditions at time t_n , we would like to find the approximation of these fields \mathbf{u}_{n+1} , \mathbf{v}_{n+1} , \mathbf{a}_{n+1} at time t_{n+1} . Here, Unlike in the case of quasi-static and incremental loading approach, t now represents actual time. The dynamic governing equation given in its weak form in eq. (3.56), in discrete form now writes as:

$$\underbrace{\mathbf{Ma}}_{\mathbf{F}^{inert}} + \mathbf{F}^{int} - \mathbf{F}^{c} = \mathbf{F}^{ext} \tag{3.120}$$

where M is the global mass matrix, computed as follows

$$\mathbf{M} = \rho \sum_{n_{elem}} \left\{ \sum_{i=1}^{n_{GP}} \sum_{j=1}^{n_{GP}} \left[\mathbf{B}_{bez} \right]^{-T} \left[\mathbf{Q} \right] \left[\mathbf{B}_{bez} \right] w_i w_j \det J \right\}$$
(3.121)

assuming a non-compressible material, that is the density ρ is constant and uniform - the mass matrix can be computed at the beginning of the simulation and stored for use. Hilbert-Hughes-Taylor family of temporal integrators are the most commonly featured schemes for time-stepping algorithms [3–5]. For a time step $\Delta t := t_{n+1} - t_n$, this algorithm writes as:

$$\mathbf{Ma}_{n+1} + \mathbf{F}^{int}(u_{n+\alpha}) + \mathbf{F}^{c}(u_{n+\alpha}) = \mathbf{F}^{ext}(t)$$
(3.122)

with

$$\mathbf{u}_{n+\alpha} = \alpha \mathbf{u}_{n+1} + (1 - \alpha) \mathbf{u}_{n}$$

$$\mathbf{u}_{n+1} = \mathbf{u}_{n} + \Delta t \mathbf{v}_{n} + \frac{\Delta t^{2}}{2} \left[(1 - 2\beta) \mathbf{a}_{n} + 2\beta \mathbf{a}_{n+1} \right]$$

$$\mathbf{v}_{n+1} = \mathbf{v}_{n} + \Delta t \left[(1 - \gamma) \mathbf{a}_{n} + \gamma \mathbf{a}_{n+1} \right]$$
(3.123)

where α , β , and γ are algorithmic parameters defining the characteristics of the time integration method in terms of its stability and accuracy. In this family of temporal integrators we consider two most prevalent schemes in finite elements [5]: (1) the conditionally stable, explicit, second order accurate central differences scheme ($\alpha = 1, \beta = 0, \gamma = 1/2$), particularly suitable for high frequency impact systems, and (2) the implicit, unconditionally stable, second order accurate trapezoidal rule, also known as the implicit Newmark method ($\alpha = 1, \beta = 1/4, \gamma = 1/2$).

3.6.6.3 Explicit Time Integration: The Central Difference Method

With the algorithmic parameters $\alpha = 1, \beta = 0, \gamma = 1/2$, we obtain the explicit central differencing time integration scheme, with its discrete form writing as

$$\mathbf{Ma}_{n+1} + \mathbf{F}_{n+1}^{int} - \mathbf{F}_{n+1}^{c} = \mathbf{F}_{n+1}^{ext}$$
(3.124)

$$\mathbf{u}_{n+1} = \mathbf{u}_n + \Delta t \mathbf{v}_n + \frac{\Delta t^2}{2} \mathbf{a}_n \tag{3.125}$$

$$\mathbf{v}_{n+1} = \mathbf{v}_n + \frac{\Delta t}{2} \left(\mathbf{a}_n + \mathbf{a}_{n+1} \right) \tag{3.126}$$

The set of equation in Equations (3.124) to (3.126) are not presented in a manner convenient for implementation. The usual form in which this scheme is implemented follows as [3]: the central differences approximation of the velocity and acceleration fields at time t_n are given by

$$\mathbf{v}_{n} = \frac{\mathbf{u}_{n+1} + \mathbf{u}_{n-1}}{2\Delta t}$$

$$\mathbf{a}_{n} = \frac{\mathbf{u}_{n+1} - 2\mathbf{u}_{n} + \mathbf{u}_{n-1}}{\Delta t^{2}}$$
(3.127)

Substituting the expressions of the velocity and acceleration in eq. (3.127) into eq. (3.124), we get the discrete form of the balance equation at t_n as:

$$\mathbf{M}\left(\frac{\mathbf{u}_{n+1} - 2\mathbf{u}_n + \mathbf{u}_{n-1}}{\Delta t^2}\right) + \mathbf{F}^{int}(\mathbf{u}_n) - \mathbf{F}^c(\mathbf{u}_n) = \mathbf{F}_n^{ext}$$
(3.128)

From eq. (3.128) we obtain a system of equations for the unknown displacements \mathbf{u}_{n+1} at time t_{n+1}

$$\mathbf{M}\mathbf{u}_{n+1} = \Delta t^2 \left[\mathbf{F}_n^{ext} - \mathbf{F}^{int}(\mathbf{u}_n) + \mathbf{F}^c(\mathbf{u}_n) \right] + \mathbf{M} \left(2\mathbf{u}_n - \mathbf{u}_{n-1} \right)$$
(3.129)

Notice that at the start of the central differences scheme eq. (3.129) needs the displacement values \mathbf{u}_{-1} (recall that we only have initial conditions specified at time t_0). The starting values \mathbf{u}_{-1} then require special treatment and can be determined from the initial conditions \mathbf{u}_0 and \mathbf{v}_0 via the Taylor series expansion at time t_{-1} , that is

$$\mathbf{u}_{-1} = \mathbf{u}_0 - \Delta t \mathbf{v}_0 + \frac{\Delta t^2}{2} \mathbf{a}_0 \tag{3.130}$$

With the acceleration \mathbf{a}_0 computed from eq. (3.124) as follows

$$\mathbf{a}_0 = \mathbf{M}^{-1} \left(\mathbf{F}_0^{ext} - \mathbf{F}_0^{int} + \mathbf{F}_0^c \right) \tag{3.131}$$

From eq. (3.129) we can see that the unknown solution \mathbf{u}_{n+1} depends only upon known variables at the previous time step t_n . These methods are easy to implement and can be extremely efficient (no inversion of the costly stiffness matrices), particularly if the mass matrix is approximated by the diagonal lumped mass matrix (the inverse of a diagonal matrix is trivial). As previously mentioned, the central differences method is conditionally stable. The implication is, to achieve stability, the time step size must not exceed the critical time step Δt_{cr} . The critical time step which can be estimated either at element level or at structural level [4, 5], must satisfy the Courant stability limit for a two body system, which writes as

$$\Delta t_{cr}^i \le \frac{2}{\omega_{max}^i}, \quad i = 1,2 \tag{3.132}$$

 ω_{max}^{i} the highest modal natural frequency in the mesh. In the case of the penalty method, the critical time step does not only depend on the FE model (mesh density), but also on the penalty parameter [4]. This is apparent in the contribution of the penalty parameter in the global stiffness matrix, but not the mass matrix, thus further reducing the critical time step.

3.6.6.4 Implicit Time Integration: The Newmark Method

If we substitute the algorithmic parameters $\alpha = 1, \beta = 1/4, \gamma = 1/2$ into eqs. (3.122) and (3.123), we obtain:

$$\mathbf{Ma}_{n+1} + \mathbf{F}_{n+1}^{int} - \mathbf{F}_{n+1}^{c} = \mathbf{F}_{n+1}^{ext}$$
(3.133)

$$\mathbf{u}_{n+1} = \mathbf{u}_n + \Delta t \mathbf{v}_n + \frac{\Delta t^2}{4} \left[\mathbf{a}_n + \mathbf{a}_{n+1} \right]$$
 (3.134)

$$\mathbf{v}_{n+1} = \mathbf{v}_n + \frac{\Delta t}{2} \left[\mathbf{a}_n + \mathbf{a}_{n+1} \right] \tag{3.135}$$

Rearranging eq. (3.134) to get the expression of \mathbf{a}_{n+1} and then substituting this \mathbf{a}_{n+1} into eq. (3.133), we obtain :

$$\frac{4}{\Delta t^{2}} \mathbf{M} \mathbf{u}_{n+1} + \mathbf{F}_{n+1}^{int} - \mathbf{F}_{n+1}^{c} = \mathbf{F}_{n+1}^{ext} + \mathbf{M} \left(\mathbf{a}_{n} + \Delta t \mathbf{v}_{n} + \frac{4}{\Delta t^{2}} \mathbf{u}_{n} \right)
\mathbf{a}_{n+1} = \frac{4}{\Delta t^{2}} \left(\mathbf{u}_{n+1} - \mathbf{u}_{n} \right) - \frac{4}{\Delta t} \mathbf{v}_{n} - \mathbf{a}_{n}
\mathbf{v}_{n+1} = \mathbf{v}_{n} + \frac{\Delta t}{2} \left[\mathbf{a}_{n} + \mathbf{a}_{n+1} \right]$$
(3.136)

Now we can solve our system of equations eq. (3.136) in the same way as in the quasi static case (eqs. (3.117) to (3.119)). The dynamic incremental residual writes as:

$$\mathbf{R}(\mathbf{u}_{n+1}) = \mathbf{F}_{n+1}^{int} - \mathbf{F}_{n+1}^{c} + \frac{4}{\Delta t^2} \mathbf{M} \mathbf{u}_{n+1} - \mathbf{M} \left(\mathbf{a}_n + \Delta t \mathbf{v}_n + \frac{4}{\Delta t^2} \mathbf{u}_n \right) - \mathbf{F}_{n+1}^{ext} = \mathbf{0}$$
 (3.137)

We can solve eq. (3.137) using the Newton-Raphoson technique. The consistent tangent stiffness is given by:

$$\frac{d\mathbf{R}(\mathbf{u}_{n+1})}{d\mathbf{u}_{n+1}} = \mathbf{K}^{P} = \mathbf{K}^{int} + \mathbf{K}_{c}^{stick/slip} + \frac{4}{\Delta t^{2}}\mathbf{M}$$
(3.138)

We then solve, iteratively, the following equation:

$$\mathbf{K}^{\mathbf{P}}(\mathbf{u}_{n+1}^{k})\Delta\mathbf{u}_{n+1}^{k} = -\mathbf{R}^{\mathbf{P}}(\mathbf{u}_{n+1}^{k})$$

$$\Delta\mathbf{u}_{n+1}^{k} = \mathbf{u}_{n+1}^{k+1} - \mathbf{u}_{n+1}^{k}$$
(3.139)

Once the solver has converged, the velocity and acceleration field are updated as in eq. (3.136).

3.7 Summary

The aim of this chapter was to review and discuss the kinematics of the continuum mechanical contact problem, with and without friction, in its entirety and to develop the contact discretization using the Bézier based IGA approach. From the governing equations, the constitutive laws of the behavior of contact at the interface, and the contact constraints, we have introduced the basic equations and concepts that are required to build a strong variational form which is necessary for the development of FE models. The regularization of the contact constraints as well as their

enforcement, i.e. how the contact constraints are incorporated into the variational form, is also detailed. This review forms a basis of section 3.6 where the Bézier based IGA approach proposed in chapter 2 has been used for the discretization of the continuum equations and to formulate a Node to Surface contact formulation.

In section 3.6 we have developed a node to surface, with the penalty method, Bézier-based isogeometric numerical scheme for the treatment of contact problems with friction. The Bézier-based approach (introduced in section 2.3.2 and in [87]) was shown to possess the same characteristics, in terms of mesh and computation points, as the standard FEM and therefore suitable for existing FE codes data structures. The implication is that we can exploit the smooth higher order, and tailorable isogeometric basis, and easily integrate the IGA formulation with the more familiar standard FEM methods. This then allows us to use the contact discretizations developed specifically for FEM i.e. in the work of Laursen [5] and Wriggers [3], with only modifications in the shape functions routine. Majority of the work goes towards the geometry preparation to obtain the elemental structure similar to standard FEA. The contact Newton-Raphson procedure is shown in algorithm 1, the return mapping algorithm essential for frictional contact interaction in algorithm 2, and the quasi static global solution procedure is shown in algorithm 3. The explicit global resolution algorithm for the dynamic system of equations is summarized in algorithm 4. Application of this developed scheme follows in the next chapter.

Algorithm 1 Newton-Raphson procedure for contact with penalty method.

```
Initialize current solution as \mathbf{u}^{(0)} = \mathbf{u}_n
Initialize the active/inactive set
Set the penalty parameter \varepsilon_N, \varepsilon_T
loop over iteration k = 1, 2, \cdots, convergence
    Check the contact status : g_N
    if g_N \leq 0 then
         Contact status: True
         Compute t_N
         Return mapping algorithm 2
         Compute contact contributions \mathbf{K}_{c}^{PM} and \mathbf{R}_{c}^{PM}
    else
         Contact status: False
    end if
    Solve: \mathbf{K}^P(\mathbf{u}^k)\Delta\mathbf{u}^k = -\mathbf{R}^P(\mathbf{u}^k)
    Update solution vector : \mathbf{u}^{k+1} = \mathbf{u}^k + \Delta \mathbf{u}^k
    Check for convergence
    if \|\mathbf{R}^{\mathrm{P}}(\mathbf{u}^{k+1})\| < \text{tol then}
         STOP and exit
    else
         CONTINUE
    end if
    Update active/inactive sets
end loop
```

Algorithm 2 Frictional contact: return mapping algorithm.

```
Compute trial state : t_T^{\text{trial}^k} = t_T^{\text{trial}^{k-1}} + \Delta t_T^{\text{trial}}

Evaluate friction cone function : \Phi^{\text{trial}} = \left\| t_T^{\text{trial}^k} \right\| - \mu t_N

if \Phi^{\text{trial}} \leq 0 then

Stick state : t_T^k = t_T^{\text{trial}^k}

Compute \mathbf{K}_c^{\text{stick}} from eq. (3.110)

else

Slip state : Compute t_T^k from eq. (3.112)

Compute \mathbf{K}_c^{\text{slip}} from eq. (3.111)
```

Algorithm 3 Global solution algorithm : the incremental solution procedure.

```
Loop through all load steps  \begin{aligned} \textbf{loop} \text{ over load steps } n &= 1, 2, \cdots, n_{steps} \\ \text{Get current applied load/displacement} \\ \text{Compute tangent stiffness } \mathbf{K}^{int} \\ \text{Newton-Raphson procedure, algorithm 1} \\ \textbf{end loop} \end{aligned}
```

Algorithm 4 Global solution algorithm : explicit temporal integration.

```
Choose \Delta t
Initialize \mathbf{u}_0 and \mathbf{v}_0
Form M and compute its inverse, store for later use
Compute \mathbf{a}_0 = \mathbf{M}^{-1}(\mathbf{F}_0^{ext} - \mathbf{F}_0^c + \mathbf{F}_0^{int})
Compute \mathbf{u}_{-1}
Loop through all load steps
loop over load steps n = 1, 2, \dots, n_{steps}
     Get current applied load/displacement, form \mathbf{F}_n^{ext}
     Compute \mathbf{F}_n^{int}
     Invoke contact algorithm: search for contacting nodes
     Compute g_N(\mathbf{u}_n)
    if q_N \leq 0 then
         Contact status: True
         Compute contact contributions \mathbf{F}_n^c
     else
         Contact status: False
     end if
     Compute \mathbf{u}_{n+1}
     Update \mathbf{a}_n and \mathbf{v}_n
end loop
```

Part II

Numerical Simulation of Contact Problems, Dynamics and Acoustic Radiation

Static Contact Problems

4.1 Introduction

In this chapter we demonstrate the quality and accuracy of the numerical scheme developed in chapter 3.6 for the treatment of contact problems in 2D. First the scheme is used for the numerical simulation of friction-less unilateral contact problems. The scheme is then extended to the treatment of contact problems with friction. Numerical results are verified and validated against analytical solutions (where available) and its performance, in terms of the quality of the solution, compared to that of standard FEM (in this case solution obtained using contact models in Abaqus 6.13).

4.2 Application to Frictionless Static Contact Problems

In this section, the aim is to demonstrate the validity of the solution procedure discussed in chapter 3.6 for the simulation of unilateral contact problems. We consider two numerical examples, namely: (1) the compression of an elastic sphere by a rigid block onto a rigid foundation, and (2) the indentation of an elastic body by a rigid punch. For both these problems, we assume the contact to be quasi-static, frictionless and that the inertial forces are negligible.

Since we consider a contact system consisting of an elastic body in contact with a rigid obstacle, this is a *Signorini* contact problem and it is governed by the following equations:

1. Static equilibrium equation

$$\operatorname{div} \, \boldsymbol{\sigma} + \mathbf{b} = 0 \quad \text{ on } \Omega$$

2. Prescribed boundary conditions

$$\mathbf{u} = \mathbf{u}_D$$
 on Γ_D

$$\boldsymbol{\sigma} \mathbf{n} = \mathbf{t}_F$$
 on Γ_F

3. Contact conditions

$$g_N \ge 0$$
 $t_N \le 0$ $t_N g_N = 0$ on Γ_c

The stress-strain relationship remains the Hooke's law. The weak formulation of the equations above writes as follows

$$\int_{\Omega} \boldsymbol{\sigma} : \boldsymbol{\epsilon}(\delta \mathbf{u}) \, d\Omega - \int_{\Omega} \mathbf{b} \cdot \delta \mathbf{u} \, d\Omega - \int_{\Gamma} \mathbf{t}_{F} \cdot \delta \mathbf{u} \, d\Gamma - \int_{\Gamma_{\alpha}} \mathbf{t} \cdot \delta \mathbf{u} \, d\Gamma = 0$$
 (4.1)

in discrete form eq. (4.1) writes as

$$\mathbf{R}(\mathbf{u}) = \mathbf{F}^{int} - \mathbf{F}^{ext} - \mathbf{F}^c \tag{4.2}$$

with

$$\mathbf{F}^{int} = \sum_{n_{elem}} \left(\sum_{i=1}^{n_{GPs}} \sum_{j=1}^{n_{GPs}} \left[\mathbf{B}_{bez} \right]^{-T} \left[\mathbf{B} \right]^{T} \left\{ \boldsymbol{\sigma} \right\} w_{i} w_{j} \det J \right)$$

$$\mathbf{F}^{ext} = \sum_{n_{elem}} \left(\sum_{i=1}^{n_{GPs}} \sum_{j=1}^{n_{GPs}} \left[\mathbf{Q} \right] \left[\mathbf{B}_{bez} \right]^{-1} \left\{ \mathbf{b} \right\} w_{i} w_{j} \det J + \sum_{i=1}^{n_{GPs}} \left[\mathbf{Q} \right] \left[\mathbf{B}_{bez} \right]^{-1} \left\{ \mathbf{b} \right\} w_{i} \right)$$

Q is the basis functions matrix given in eq. (3.76). Assuming small deformations state, the contact force vector (with penalty method and NTS discretization reduces into)

$$\mathbf{F}^{c} = \sum_{n_{slaves}} \left(\int_{\Gamma_{c}} \varepsilon_{N} g_{N} \left(\delta \bar{\mathbf{u}}^{2} - \delta \mathbf{u}^{1} \right) \cdot \bar{\mathbf{n}}^{2} d\Gamma \right)$$

$$= \sum_{n_{slaves}} \varepsilon_{N} g_{N} \mathbf{N}$$
(4.3)

and the contact stiffness reduces into

$$\mathbf{K}_{c}^{P} = \sum_{n_{slaves}} \left(\int_{\Gamma_{c}} \varepsilon_{N} g_{N} \mathbf{N} \mathbf{N}^{\mathrm{T}} d\Gamma \right)$$

$$= \sum_{n_{slaves}} \varepsilon_{N} \mathbf{N} \mathbf{N}^{\mathrm{T}}$$
(4.4)

4.2.1 Compression of an Elastic Ball by a Rigid Block on to a Rigid Foundation

In this application we consider an elastic sphere that is being compressed by a rigid block onto a rigid foundation depicted in fig. 4.1. The sphere has radius R=0.05 m, and it's material properties: Young's modulus E=200 GPa, and Poisson's ratio $\nu=0.3$. There are no body forces present, and a total displacement of $\bar{u}=2.7$ mm is prescribed at the top rigid block. This problem is a classical Hertz friction-less contact problem between an elastic sphere and a rigid plane. It is axisymmetric and therefore the axisymmetrical formulation (2D) can be use to obtain its solution.

The elastic sphere on a rigid plane contact problem is well known and has an existing analytical solution and is outlined in [102, 103]. For the prescribed displacement $\bar{u}=2.7$ mm, the analytical contact radius a is found to be 8.215 mm, and the maximum contact pressure p_0 is found to be -2.29×10^{10} Pa - see appendix I for the detailed analytical solution.

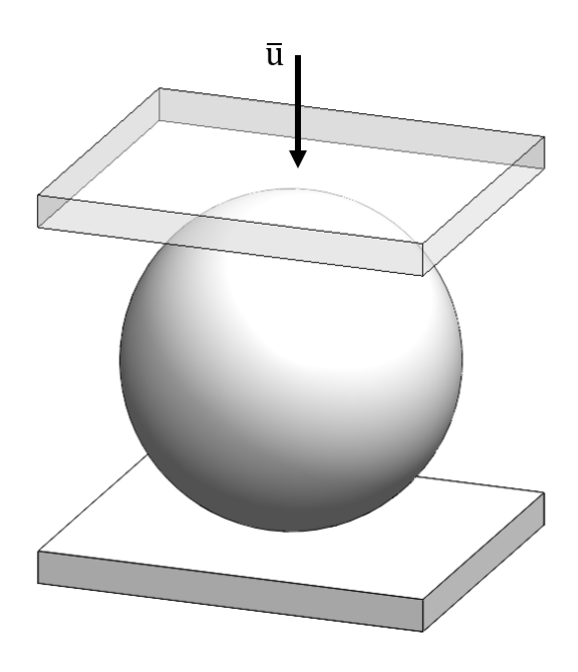


Figure 4.1 – A sphere compressed by a rigid block on to a rigid foundation.

4.2.1.1 Axisymmetrical Formulation

In the absence of body forces and boundary traction, the residual in eq. (4.2) reduces to

$$\mathbf{R}(\mathbf{u}) = \mathbf{F}^{int} - \mathbf{F}^c \tag{4.5}$$

Linearization of eq. (4.5) leads to eq. (4.6)

$$[\mathbf{K}] \{\Delta \mathbf{u}\} + \{\mathbf{F}^{int}\} - \{\mathbf{F}^{c}\} = 0 \tag{4.6}$$

As previously mentioned this is an axisymmetric problem, therefore the solution of this problem can be sufficiently described with only 2 coordinates, see fig. 4.2, namely:

- radial displacements u_r in the *u*-direction
- vertical displacements u_z in the w-direction

Since the load is non-rotational, the rotational displacement vanishes, that is $u_{\theta} = 0$. Furthermore, only the principal direction stress components $\sigma_r, \sigma_{\theta}, \sigma_z$ are present, as well as shear stress σ_{zr} . The strain-displacement relationship is as follows

$$\epsilon_r = u_{,r} \qquad \epsilon_\theta = \frac{u}{r} \qquad \epsilon_z = w_{,z}, \quad \epsilon_{rz} = u_{,z} + w_{,r}$$
(4.7)

In matrix form, we have

$$\{\epsilon\} = \begin{bmatrix} \frac{\partial}{\partial r} & 0\\ \frac{1}{r} & 0\\ 0 & \frac{\partial}{\partial z}\\ \frac{\partial}{\partial z} & \frac{\partial}{\partial r} \end{bmatrix} \begin{Bmatrix} u\\ w \end{Bmatrix}$$

$$(4.8)$$

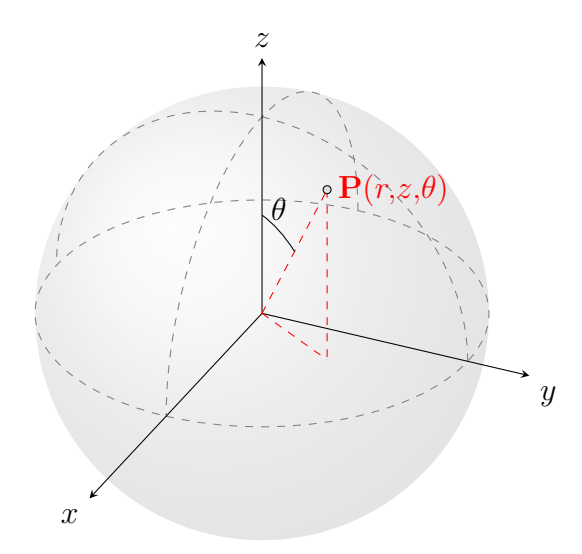


Figure 4.2 – Coordinates and displacement degree of freedom of an axisymmetric model.

with

The strain matrix [B] is then

$$[\mathbf{B}] = \begin{bmatrix} \frac{\partial}{\partial r} & 0\\ \frac{1}{r} & 0\\ 0 & \frac{\partial}{\partial z}\\ \frac{\partial}{\partial z} & \frac{\partial}{\partial r} \end{bmatrix} \begin{bmatrix} \phi_1 & \phi_2 & \cdots & \phi_{n_{\text{cpts}}^e} & 0 & \cdots & 0 & 0\\ 0 & 0 & \cdots & 0 & \phi_1 & \phi_2 & \cdots & \phi_{n_{\text{cpts}}^e} \end{bmatrix} = [\boldsymbol{\partial}] [\mathbf{Q}]$$
(4.10)

The only change with this formulation, compared to the plane stress/strain formulation strain matrix, is the computation of the ϵ_{θ} field which then adds an extra row in the strain matrix. Moreover, modifications of the discrete matrices that require volume integration are as follows

$$[\mathbf{K}] = \sum_{n_{elem}} \left\{ \sum_{GPs} [\mathbf{B}_{bez}]^{-T} [\mathbf{B}]^{T} [\mathbf{D}] [\mathbf{B}] [\mathbf{B}_{bez}]^{-1} 2\pi r \det J \right\}$$
$$\left\{ \mathbf{F}^{int} \right\} = \sum_{n_{elem}} \left\{ \sum_{GPs} [\mathbf{B}_{bez}]^{-T} [\mathbf{B}]^{T} \{\boldsymbol{\sigma}\} 2\pi r \det J \right\}$$

where r is the actual radius at each integration Gauss point, **D** is the material matrix and is given by

$$[\mathbf{D}] = E \frac{(1-\nu)}{(1+\nu)(1-2\nu)} \begin{bmatrix} 1 & \frac{\nu}{1-\nu} & \frac{\nu}{1-\nu} & 0\\ & 1 & \frac{\nu}{1-\nu} & 0\\ & \text{sym} & 1 & 0\\ & & & \frac{1-2\nu}{2(1-\nu)} \end{bmatrix}$$
(4.11)

Analysis of the problem given in fig. 4.1 is performed below.

4.2.1.2 Numerical Solution

Due to double symmetry, we can model the sphere with a quarter circle - see fig. 4.3. To facilitate local refinement and the ease of contact search (minimize bookkeeping), a quadratic multi-patch model is used for the geometry of the sphere. A single patch is used to model the rigid foundation.

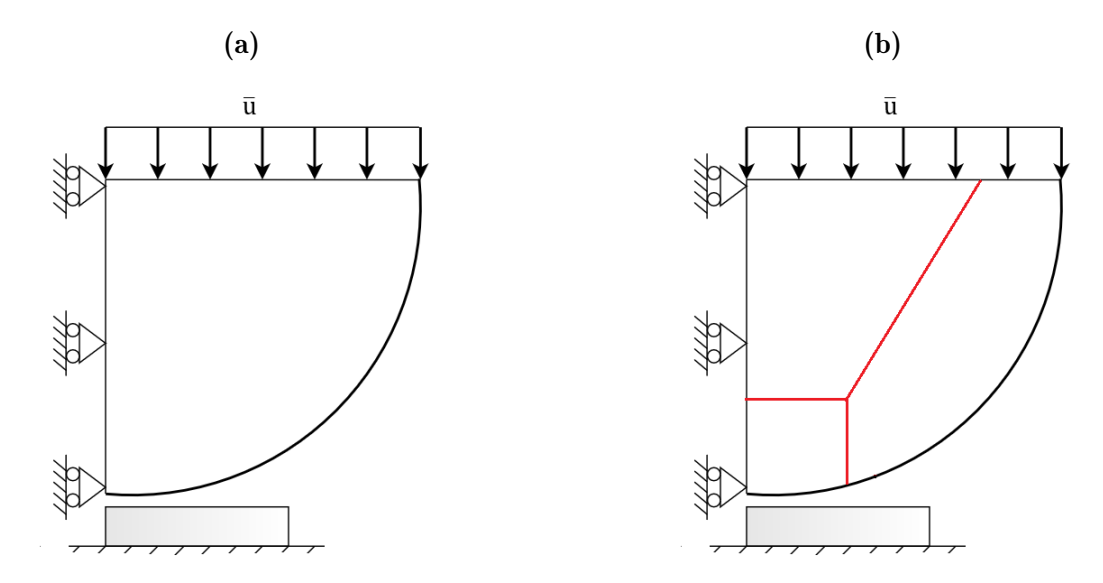


Figure 4.3 – The quarter circle model of the Hertz problem, it's boundary conditions, and the multiple patches used for the IGA model: (a) schematic of boundary conditions, and (b) patches for the IGA model.

The geometry is setup in such a way that slave surface/edge is contained in one patch. This then means only nodes living on this surface are included in the contact algorithm. The entire top edge of the rigid foundation makes up the master surface. See fig. 4.4 for the graphical description. We discretize the model first with quadratic Bézier elements, with the contact patch containing a 4×3 mesh. Each contact pair then contains a single slave node and 3 master nodes for quadratic elements. Since we are in the small displacement framework, the active set strategy is predefined (all surface nodes on the contact patch make up the slave nodes set) and therefore a global contact search algorithm is not necessary. We simply need a contact status check algorithm (local contact search algorithm) - this is the closest projection algorithm detailed in section 3.6.5.

To get started, we use a relatively coarse mesh containing a total of 40 Bézier elements (390 DOFs): 33 elements make up the quarter circle with 12 elements on the contact patch. The rigid block contains 7 elements - see fig. 4.4. The active set strategy then contains 9 slave nodes and the whole top edge of the rigid block is taken as the master surface (contains 15 nodes) with each contact element containing 4 nodes as previously stated. A penalty parameter of $\varepsilon_N = 100E$ is used in the simulation. The choice of the penalty parameter is based on the contact

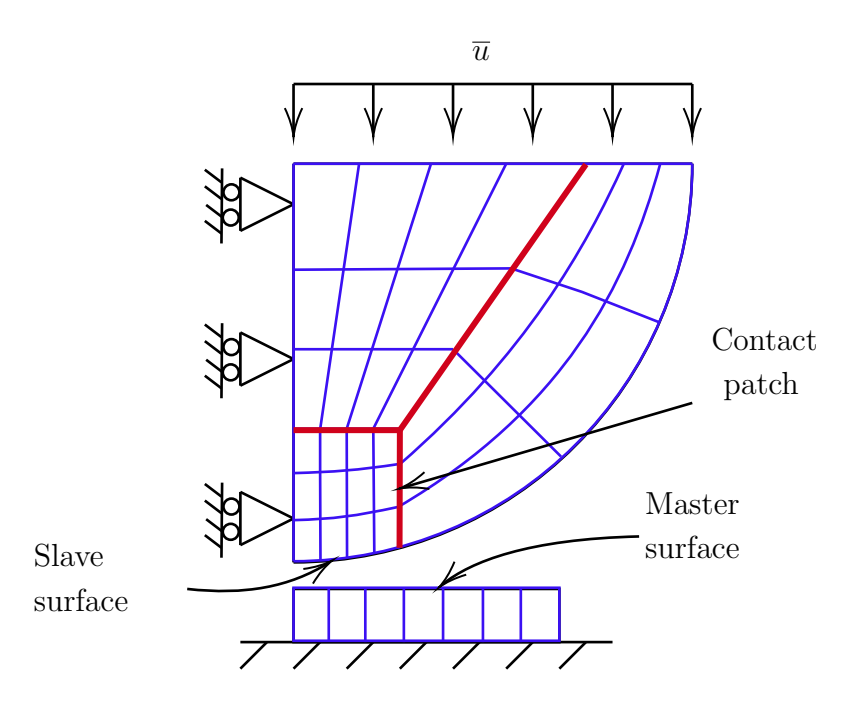


Figure 4.4 – The Hertz problem quarter model contact pairs: the contact patch (bottom surface of the contact patch taken as the slave surface) and the master surface on the rigid block - $4 \times 3 \times 3$ mesh with quadratic elements.

stiffness which in most FEA commercial packages is calculated from the elements modulus and the characteristic element length. For instance ANSYS and Autodesk (and to an extent Abaqus) calculates the underlying element contact stiffness as:

$$k_{\text{contact stiffness}}^e = \frac{E^*}{l^*} \tag{4.12}$$

where E^* is the effective material stiffness and l^* is the element characteristic length, which is defined as

$$l^* = \frac{V}{A_c} \tag{4.13}$$

V the volume of the element and A_c the contact area for each element (essentially the width of each element). This approximation of the contact stiffness in eq. (4.12) depends purely on the material properties and geometry (in terms of the mesh size, the characteristic length in eq. (4.13)) of the bodies in contact. For the $4 \times 3 \times 3$ mesh used in the simulation, the calculated $k_{\text{contact stiffness}}^e = 3.956 \times 10^{13}$ Pa. Hence the reason we set the penalty parameter as $\varepsilon_N = 100E$. Finally, the prescribed displacement \bar{u} is applied in 50 increments ($n_{steps} = 50$). Results obtained, in terms of the horizontal and vertical components of the displacement field are shown in fig. 4.5, and fig. 4.6 shows the normal stress distribution (contact pressure) as well as the Von Mises stress distribution.

The maximum contact pressure is found to be approximately 2.34×10^{10} Pa. The contact area radius is found as $a^h \approx 8.21431$ mm, a value similar to the analytical contact radius. However when taking a closer look at the boundary of the contact zone (transition from contact to no contact region), we can see irregular behavior. We observe more excessive penetration - see fig. 4.7. In actual fact the permitted penetration across the contact area is order 1×10^{-8}

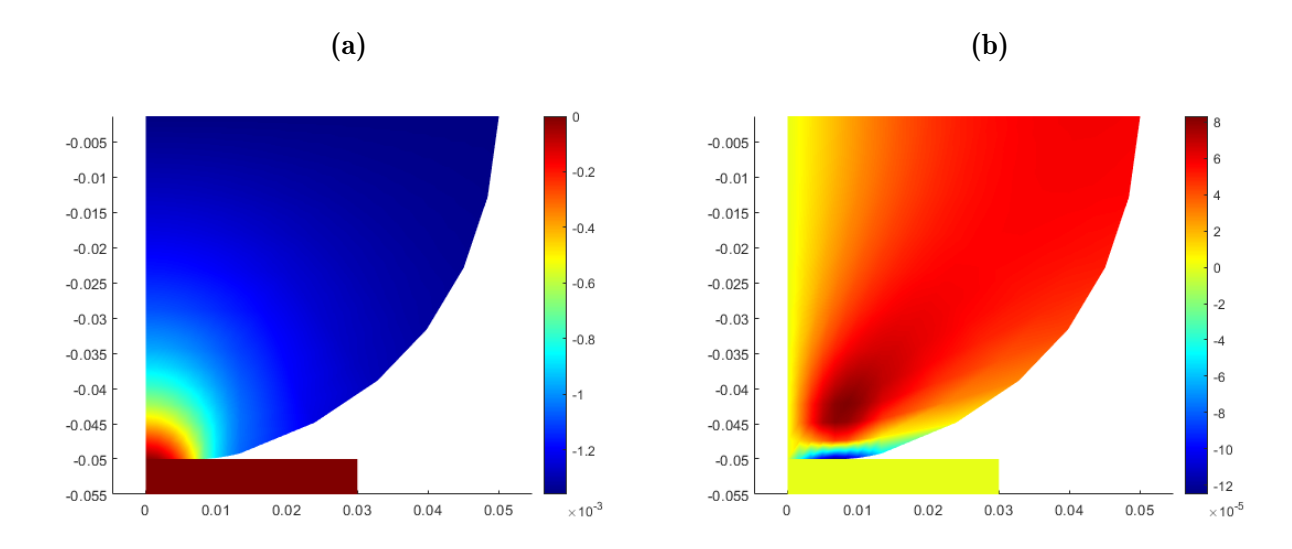


Figure 4.5 – The displacement field obtained with a quadratic coarse mesh, $\varepsilon_N = 100E$: (a) r-component of the displacement, and (b) z-component of the displacement.

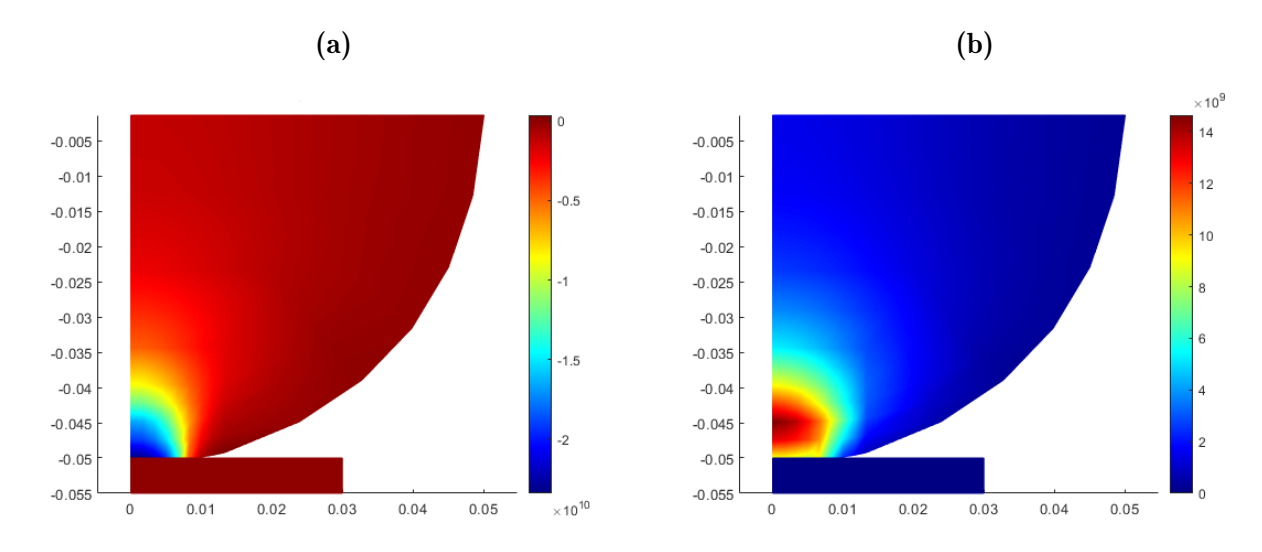


Figure 4.6 – Stress field obtained with a quadratic coarse mesh, $\varepsilon_N = 100E$: (a) normal stress σ_{zz} distribution, and (b) Von Mises stress distribution.

(roughly 0.01 μ m), however close to the contact zone boundary there is a sharp increase of the penetration (penetration 0.1 mm). This behavior could be a consequence of the larger mesh size, with a coarser mesh, the distance between successive nodes is bigger, and therefore may either under-predict or overshoot the contact area boundary (edge of the contact zone).

To improve the results, we performed first the h-refinement where we refined the knot vectors in all directions (doubled the number of elements in the 3 patches that make up the quarter circle). We also performed the p-refinement by raising the basis order from quadratic to cubic, and finally the k-refinement (a combination of h- and p-). The mesh properties for these 3 cases as well as the solution obtained are summarized in table 4.1. Note that the relative error is defined as

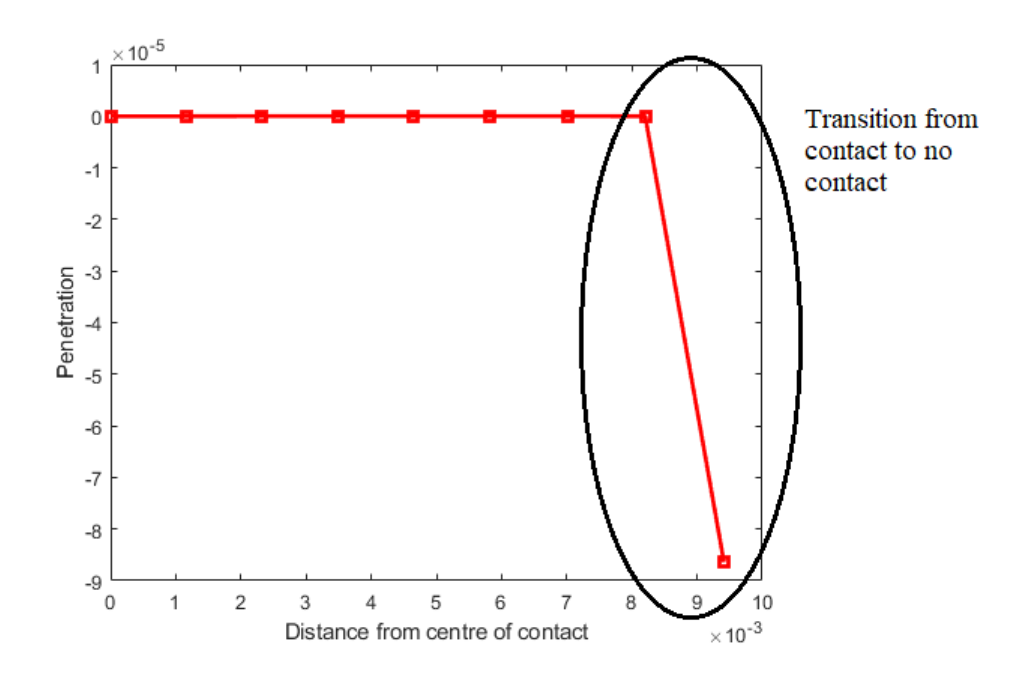


Figure 4.7 – Penetration across the contact area - $4 \times 3 \times 3$ mesh with quadratic elements.

Relative error =
$$\left[\frac{sol_{\text{analytical}} - sol_{\text{numerical}}}{sol_{\text{analytical}}} \right] \times 100$$
 (4.14)

where in eq. (4.14) $sol_{\text{analytical}}$ denotes the analytical solution and $sol_{\text{numerical}}$ denotes the numerical solution.

Parameter	p-refinement	h-refinement	k-refinement	
Total number of elements	40	139	139	
Total number of DOFs	832	1228	2674	
Contact patch elements	4	8	8	
Number of slave nodes	13	17	25	
Contact area radius				
Contact radius a^h [mm]	8.199	8.198	8.190	
Relative error [%]	0.21	0.22	0.32	
Maximum contact pressure				
Max. contact pressure $p_0^h \ [\times 10^{10} \ Pa]$	2.2771	2.3377	2.3394	
Relative error [%]	1	1.64	1.71	

Table 4.1 – Properties of the different meshes used for the IGA computation and the results obtained.

Figure 4.8 shows the comparison of the obtained numerical contact pressure, first using the coarse and then the finer quadratic mesh, across the contact area to the analytical pressure distribution.

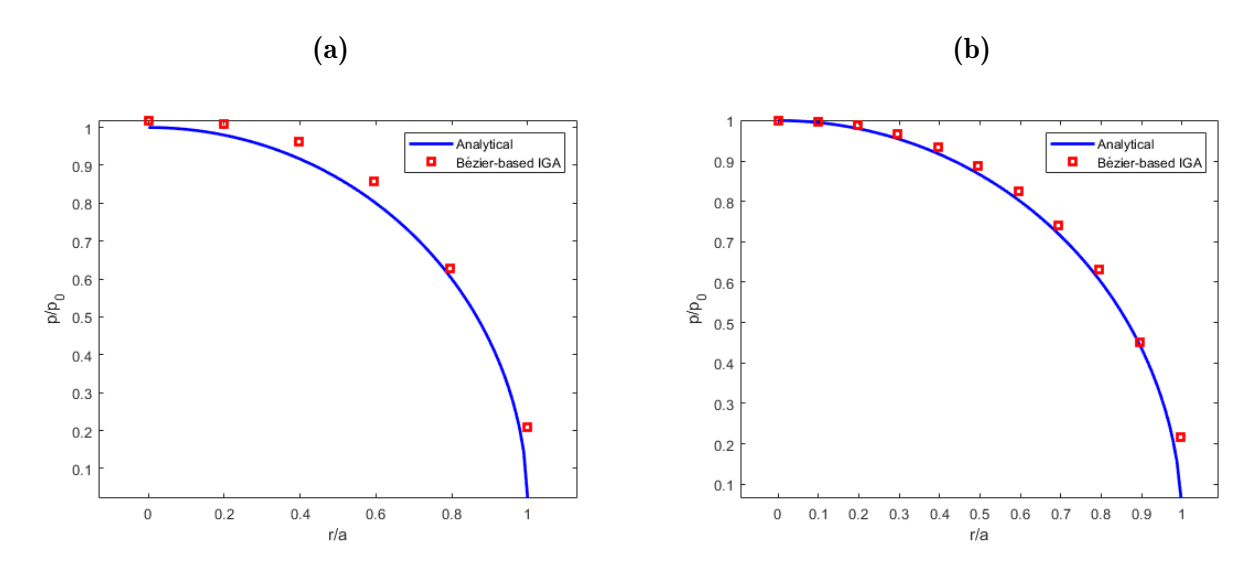


Figure 4.8 – Comparison between the analytical and numerical contact pressure (normalized) across the contact area, quadratic elements: (a) coarse mesh, and (b) fine mesh.

The results we have obtained are in good agreement with the analytical solution, however the accuracy of the solution is highly dependent on the model's ability to capture the contact zone transition region (edge of contact). More points (nodes) around the region are required in order to have a better quality solution. We have demonstrated how we can achieve this with refinement of knot vector as well as degree elevation. It is important to note in this model, we used uniform knot vectors (each patch has a uniform element size). Another alternative to improve the quality of the solution would be to use non-uniform knot vectors; with non-uniform knot-vectors, we can construct meshes that are finer around the transition zone and coarser away from this region. In this way, we could reduce the model size and save on computation cost while maintaining good levels of accuracy.

In the numerical results discussed thus far the penalty parameter has been fixed at $\varepsilon_N = 100E$, a choice based on the approximation of the contact stiffness in eq. (4.12). However, this value was computed specifically for the coarse mesh $(4 \times 3 \times 3)$ with quadratic elements. Recall that with the penalty method the contact constraints are satisfied an approximate sense; the constraints are satisfied exactly if penalty tends to infinity. In essence, increasing the penalty value should improve the quality of the results, however we should be mindful as excessively large penalty parameters lead to the ill-posedness of the tangent stiffness matrix. Hence, it is interesting to observe how the relative error, in terms of the quality of the solution, evolves with the increasing values of the penalty parameter ε_N . This evaluation is shown in fig. 4.9 and fig. 4.10, where we show the evolution of the relative error as well as the penetration levels for the course mesh $(4 \times 3 \times 3)$ with quadratic elements and cubic elements, respectively.

From fig. 4.9 and fig. 4.10 we observe that : (1) for both quadratic and cubic mesh, the relative error on both the contact radius and the contact pressure plateaus at $\varepsilon_N \geq 100E$; the implication is that increasing the penalty parameter value past 100E will not enrich the numerical solution, and (2) even with low penalty parameter values, the maximum penetration on the contact area

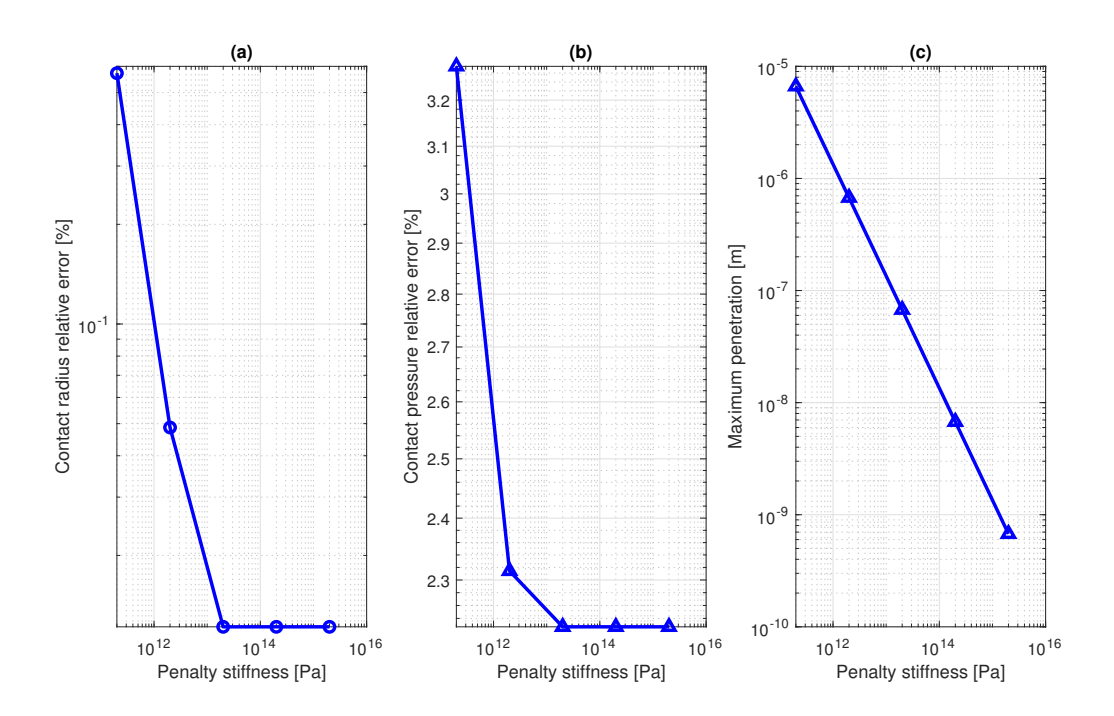


Figure 4.9 – The effect of the penalty parameter ε_N at fixed mesh resolution - $4 \times 3 \times 3$ quadratic mesh: (a) the evolution of relative error on the contact radius with increasing ε_N , (b) the evolution of relative error on the contact pressure with increasing ε_N , and (c) the penetration levels at different ε_N .

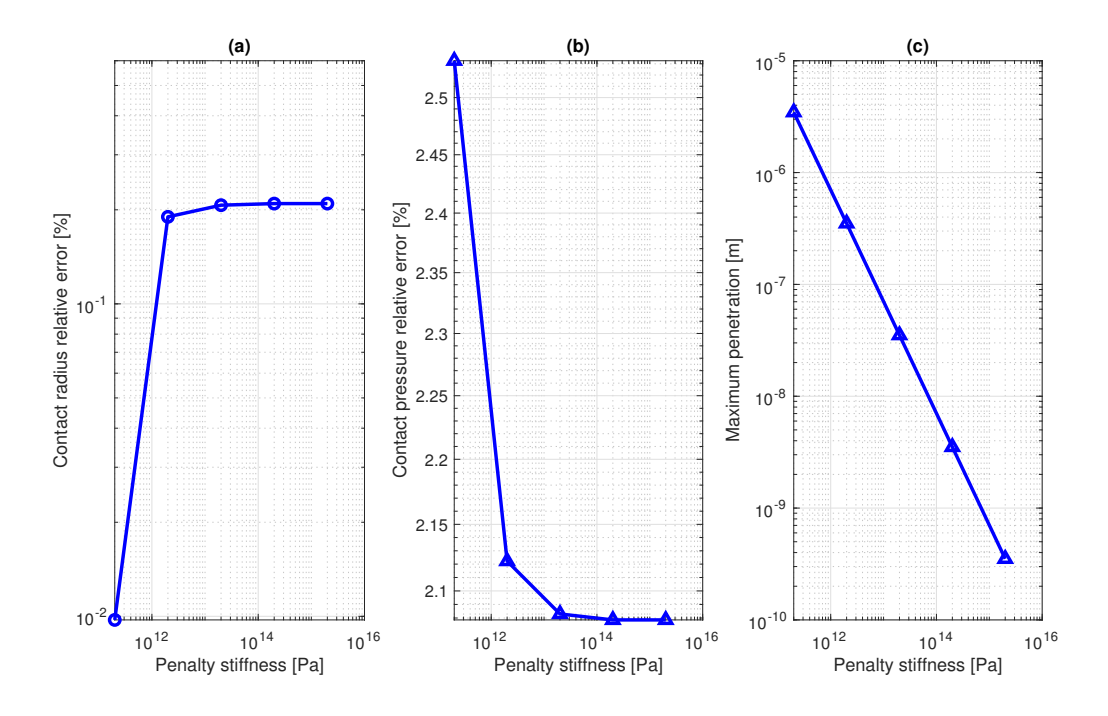


Figure 4.10 – The effect of the penalty parameter ε_N at fixed mesh resolution - $4 \times 3 \times 3$ cubic mesh: (a) the evolution of relative error on the contact radius with increasing ε_N , (b) the evolution of relative error on the contact pressure with increasing ε_N , and (c) the penetration levels at different ε_N .

is very low and the penetration levels decrease linearly with the penalty parameter. This then qualifies the choice made to set the value of the penalty parameter as 100E.

Isogeometric analysis has been proven to have a superior accuracy per degree of freedom in comparison to standard FEM, therefore it is interesting to compare the results obtained from the Bézier based approach to that of standard finite elements analysis. To do this, this Hertz problem was also simulated using Abaqus. For the same model size and element distribution as the $4 \times 3 \times 3$ IGA quadratic mesh, in Abaqus the mesh has properties: 160 linear quadrilateral elements, and 396 DOFs. The contact was modeled using the penalty method and we specified the same penalty parameters as in fig. 4.9 and fig. 4.10. Note due to the threshold on the maximum permissible contact stiffness in Abaqus penalty method model (the penalty stiffness cannot exceed 1000E), we did not include the penalty parameter value 10000E. In fact, Abaqus has a threshold on acceptable penalty parameter values; should the penalty parameter exceed this value the contact model will switch from that of penalty method to Lagrange multipliers method. The results obtained, in terms of the maximum contact pressure p_0 and the maximum permitted penetration order level, are summarized in table 4.2.

Penalty parameter, ε_N	Max. contact pressure, p_0^h [Pa]	Penetration level [m]
$oxed{E}$	-	-
10E	-	-
100E	1.239	1×10^{-3}
1000E	2.222	1×10^{-4}

Table 4.2 – The effect of the penalty parameter on the numerical results of the Abaqus FEA model, in terms of the maximum contact pressure and the permitted penetration, of the classical friction-less Hertz contact problem.

As we can see from table 4.2 no results were obtained for low values of the penalty values; the simulation was unsuccessful as excessive non physical deformation led to convergence failure. Compared to the IGA results, the maximum contact pressure values are much lower than the analytical value and the penetration is higher. To circumvent this limitation, we then modeled the contact interaction using the penalty method with the default setting on the penalty stiffness, which readily determines the suitable contact constraints models based on the mesh size. In doing this, it helps facilitates the mesh refinement process while maintaining relatively low penetrations. The results obtained are shown in table 4.3.

From table 4.3 we see that with 6 slave nodes in the contact interface in the FEA model we found a maximum contact pressure of 2.325×10^{10} Pa which is in good agreement with the analytical value (1.51 % error). However the contact radius was found to be 9.110 mm, which is much higher than the analytical value (~ 10 % error). The penetrations allowed were of order 1×10^{-5} m. With refinements (21 slave nodes) the contact area approximation improved to a value a = 8.4716 mm (~ 3 % error), however the maximum contact pressure increases to a value 2.407×10^{10} Pa which then increases the relative error to ~ 4.8 %. From these results it is clear

Parameter	Coarse mesh	Fine mesh	
Number of slaves	6	21	
Contact radius			
Contact radius, a^h [mm]	9.110	8.4716	
Relative error [%]	10	3	
Maximum contact pressure			
Maximum contact pressure, $p_0^h \ [\times 10^{10} \ Pa]$	2.325	2.407	
Relative error [%]	1.51	4.8	

Table 4.3 – Results obtained from Abaqus (default penalty stiffness) for the classical friction-less Hertz contact problem.

that the Bézier based is more superior and indeed more accurate than FEA on per degree of freedom basis.

4.2.2 Indentation of an Elastic Half-Space by a Rigid Flat Punch

Here we consider the indentation of an elastic half space by a flat rigid punch. This problem is depicted in fig. 4.11. There are no body forces present. The elastic half space has a Young's modulus E = 200 GPa, and Poisson's ratio $\nu = 0.3$. The rigid punch has a flat base of width 2a and it has sharp corners. Furthermore the punch has a thickness (third dimension) much larger than the dimensions in the x,y dimensions, such that we can assume plane-strain conditions.

To achieve the indentation process the rigid punch is displaced by 2 mm, therefore the indentation depth d=2 mm. Similarly to the Hertz problem in the previous section, this problem has a known analytical solution, and it has been outlined in [102–104]. The contact radius a is equal to the base of the rigid punch.

4.2.2.1 Plane Strain Formulation

Similarly to the Hertz problem in fig. 4.1, there are no body forces present, such that the residual in discrete form is given by eq. (4.5) and the linearized form in eq. (4.6). In this case the plane strain formulation is used, consequently we have:

- The behavior of this contact problem can be sufficiently modeled with 2 coordinates: displacements degrees of freedom in the *u* and *v* direction, corresponding to the horizontal (*x*) direction and vertical (*y*) direction, respectively.
- No principal and shear strains in the z-direction; that is:

$$\epsilon_z, \epsilon_{xz}, \epsilon_{uz} = 0 \tag{4.15}$$

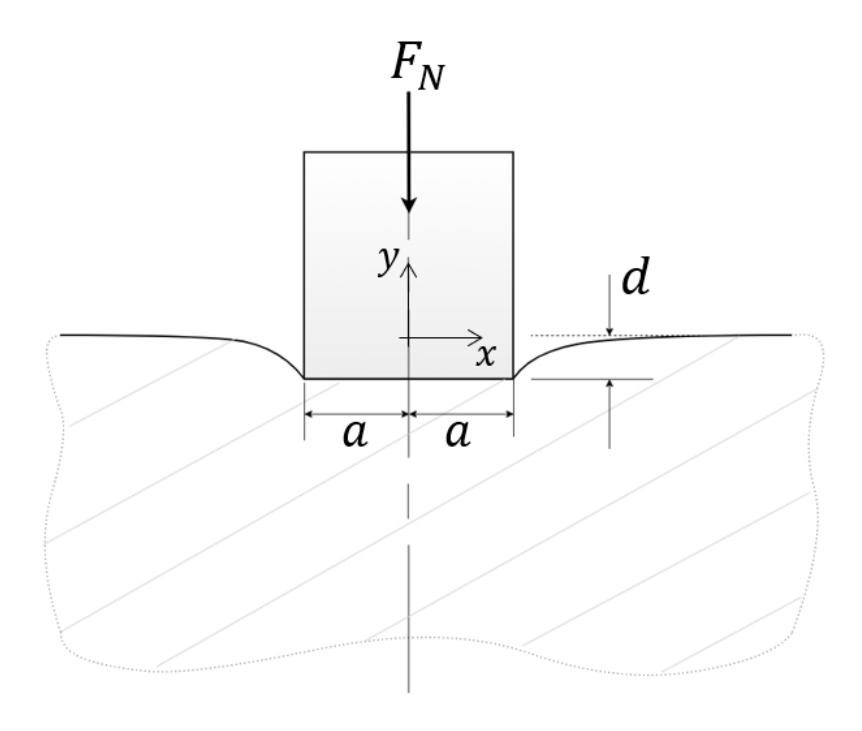


Figure 4.11 – Indentation process of a rigid punch into an elastic half-space.

the non zero strain components are given by

$$\epsilon_x = \frac{\partial u}{\partial x}, \, \epsilon_y = \frac{\partial v}{\partial y}, \, \epsilon_{xy} = \frac{\partial u}{\partial y} + \frac{\partial v}{\partial x}$$
(4.16)

and the constitutive equation is given by

$$\begin{cases}
\sigma_{x} \\
\sigma_{y} \\
\sigma_{xy}
\end{cases} = \frac{E}{(1+\nu)(1-2\nu)} \begin{bmatrix} 1-\nu & \nu & 0 \\
\nu & 1-\nu & 0 \\
0 & 0 & 0.5-\nu \end{bmatrix} \begin{cases} \epsilon_{x} \\
\epsilon_{y} \\
\epsilon_{xy} \end{cases} = \mathbf{D} \begin{cases} \epsilon_{x} \\
\epsilon_{y} \\
\epsilon_{xy} \end{cases} \tag{4.17}$$

The strain-displacement relationship in matrix form is as follows

and the mapping of u,v is given by eq. (4.9). To obtain the strain matrix $[\mathbf{B}]$, we replace $[\boldsymbol{\partial}]$ in eq. (4.10) by the expression of $[\boldsymbol{\partial}]$ from eq. (4.18). Finally, we have :

$$[\mathbf{K}] = \sum_{n_{elem}} \left\{ \sum_{i=1}^{n_{GPs}} \sum_{j=1}^{n_{GPs}} [\mathbf{B}_{bez}]^{-T} [\mathbf{B}]^{T} [\mathbf{D}] [\mathbf{B}] [\mathbf{B}_{bez}]^{-1} w_i w_j \det J \right\}$$
(4.19)

$$\left\{ \mathbf{F}^{int} \right\} = \sum_{n_{elem}} \left\{ \sum_{i=1}^{n_{GPs}} \sum_{j=1}^{n_{GPs}} \left[\mathbf{B}_{bez} \right]^{-T} \left[\mathbf{B} \right]^{T} \left\{ \boldsymbol{\sigma} \right\} w_{i} w_{j} \operatorname{det} J \right\}$$
(4.20)

4.2.2.2 Numerical Solution

Due to symmetry, a half model is used in the analysis - see fig. 4.12. In the numerical model the rigid punch has a base of width a=0.5 m, and the elastic half space has a width of 4a and a depth of 2a. The analytical contact pressure at x=0 is found as $p_0=4.3956\times 10^8$ Pa - analytical solution detailed in appendix II.

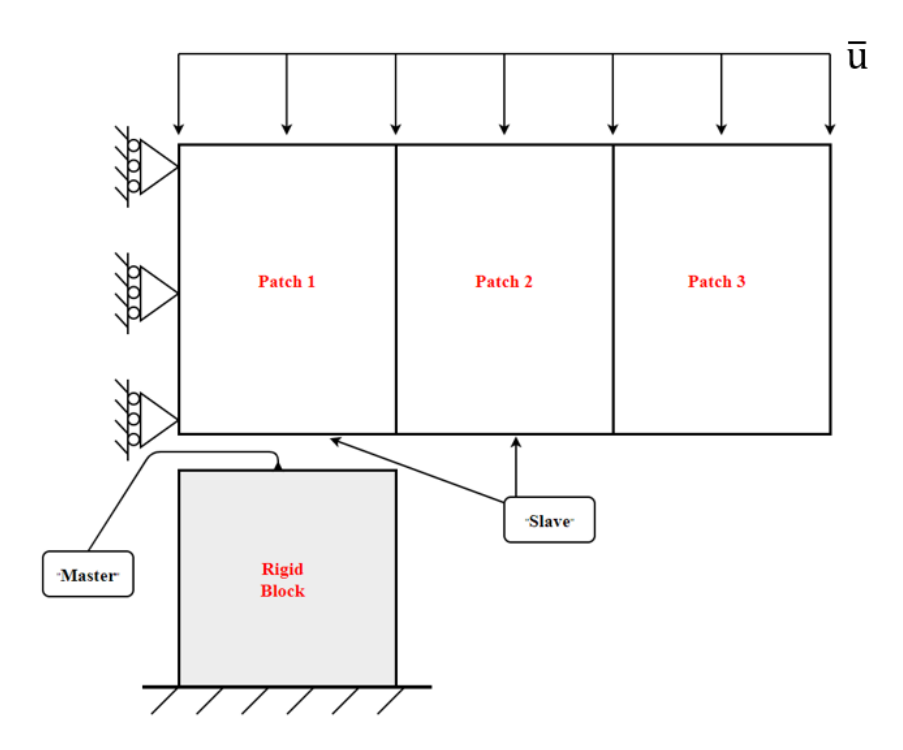


Figure 4.12 – 2D half model of the rigid punch on to an elastic half space contact problem.

To simulate the indentation process:

- the rigid block is modeled explicitly, at the top edge (contact interface of the rigid block) both displacement degrees of freedom (u,v) are fixed
- the motion is applied to the elastic half space to achieve the indentation; symmetry boundary conditions are prescribed on the left edge of the elastic space see fig. 4.12

The elastic half space is taken as the slave and the rigid indenter as the master. A single patch is sufficient to model the rigid indenter. 3 patches are used to model the elastic half space to allow for targeted refinement around the edge of the contact area - non-uniform knot vectors are used for the geometry and chosen in such a way that the size of the Bézier elements (knot spans) gradually increases as move away from the edge of the contact zone. The resulting Bézier geometry as well as the network of it's control points (mesh), for a quadratic discretization, are shown in fig. 4.13.

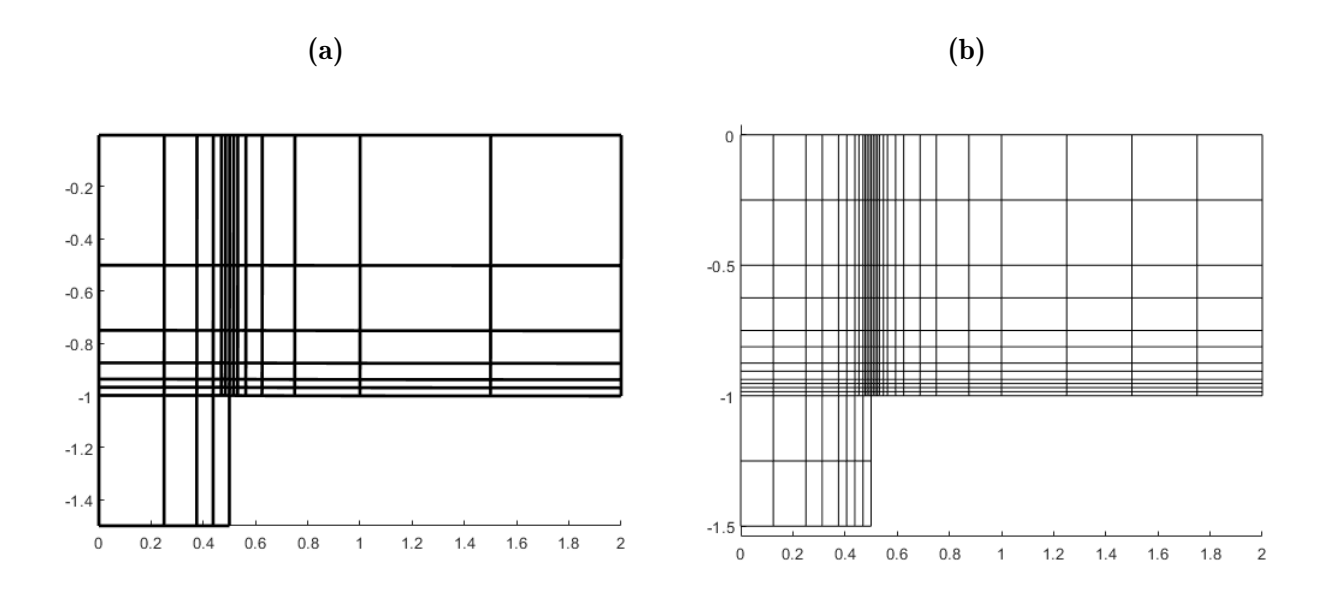


Figure 4.13 – The rigid punch on an elastic half-space numerical model generated using quadratic Bézier elements : (a) Bézier elements, and (b) mapping of computation points.

We discretize the half space with 14 elements along the x-direction, and 6 elements in the y-direction. The rigid block contains 4 elements horizontally and a single elements vertically. In total the model has 808 DOFs with 12 slaves nodes (6 elements on the potential contact zone) and 10 master nodes. The penalty parameter ε_N is set to 100E (again this value is based on the contact stiffness approximation in eq. (4.12), which for quadratic elements was found to be 2.705×10^{13}). The prescribed displacement is applied in 50 increments (load steps). We found $p_0 = 4.2320 \times 10^8$ Pa. Figure 4.14 shows the x- and y- components of the displacement field.

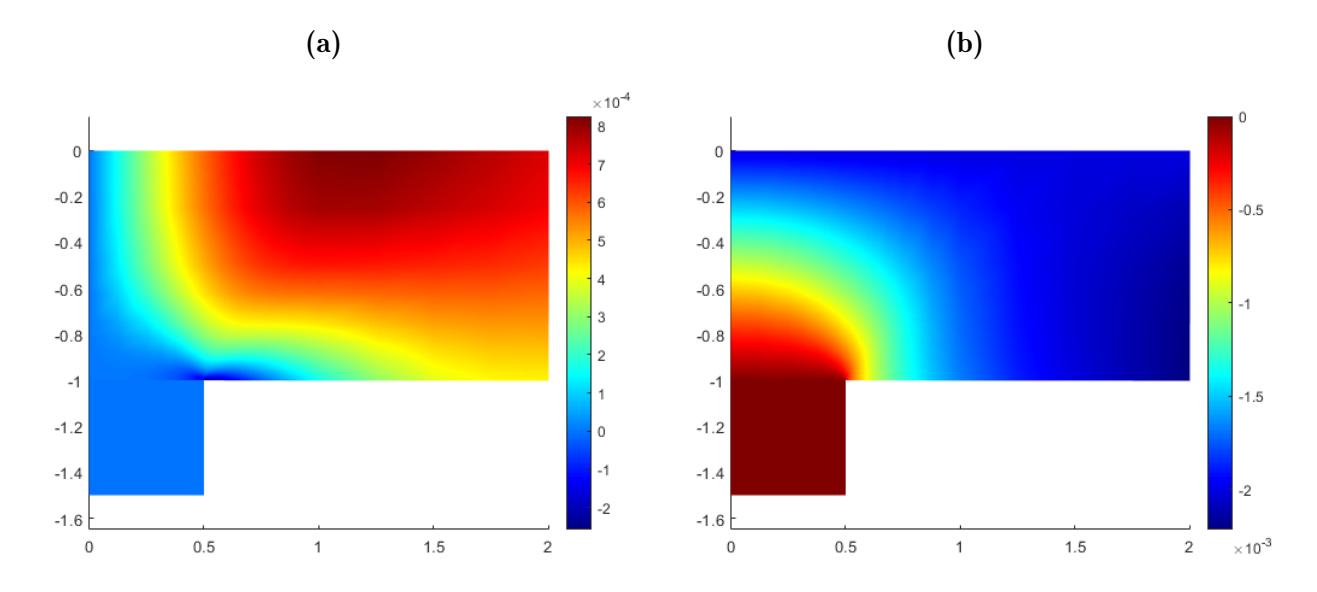


Figure 4.14 – The displacement field of the indentation process, p = 2 and $\varepsilon_N = 100E$: (a) x component of the displacement, and (b) y component of the displacement.

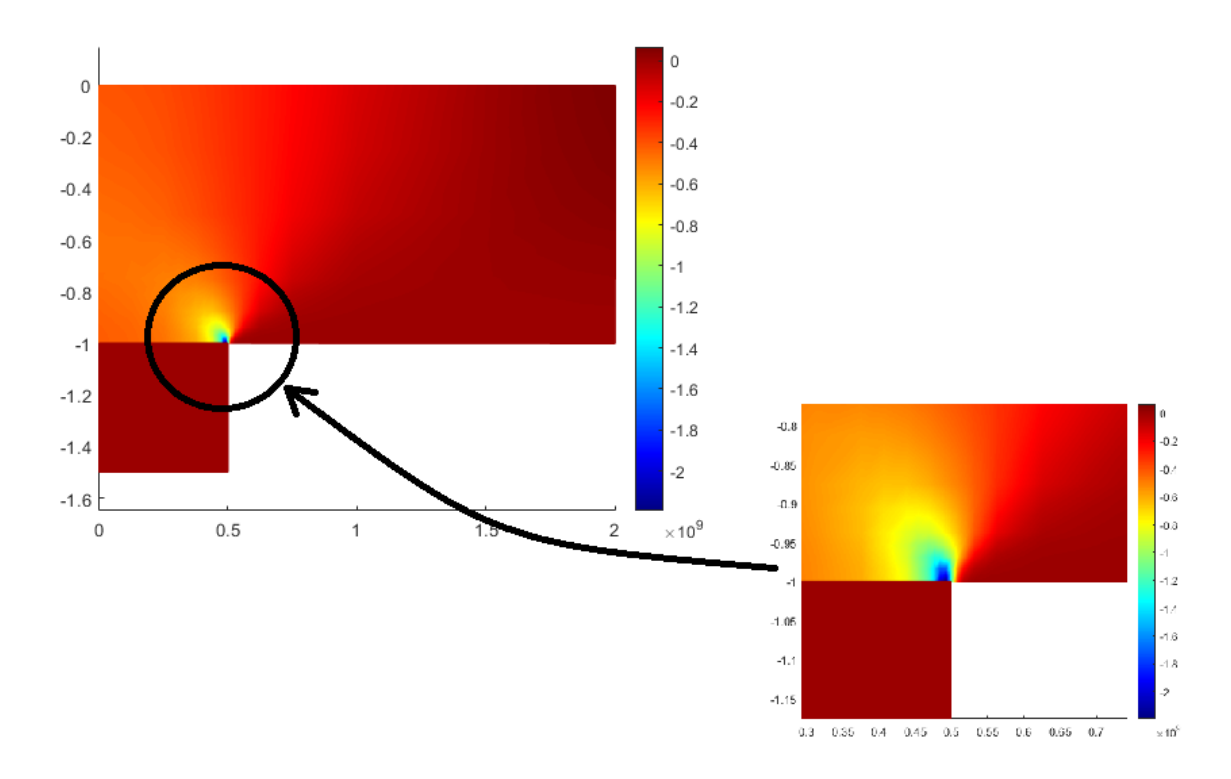


Figure 4.15 – Stress distribution in the normal direction for the indentation process, p=2 and $\varepsilon_N=100E$.

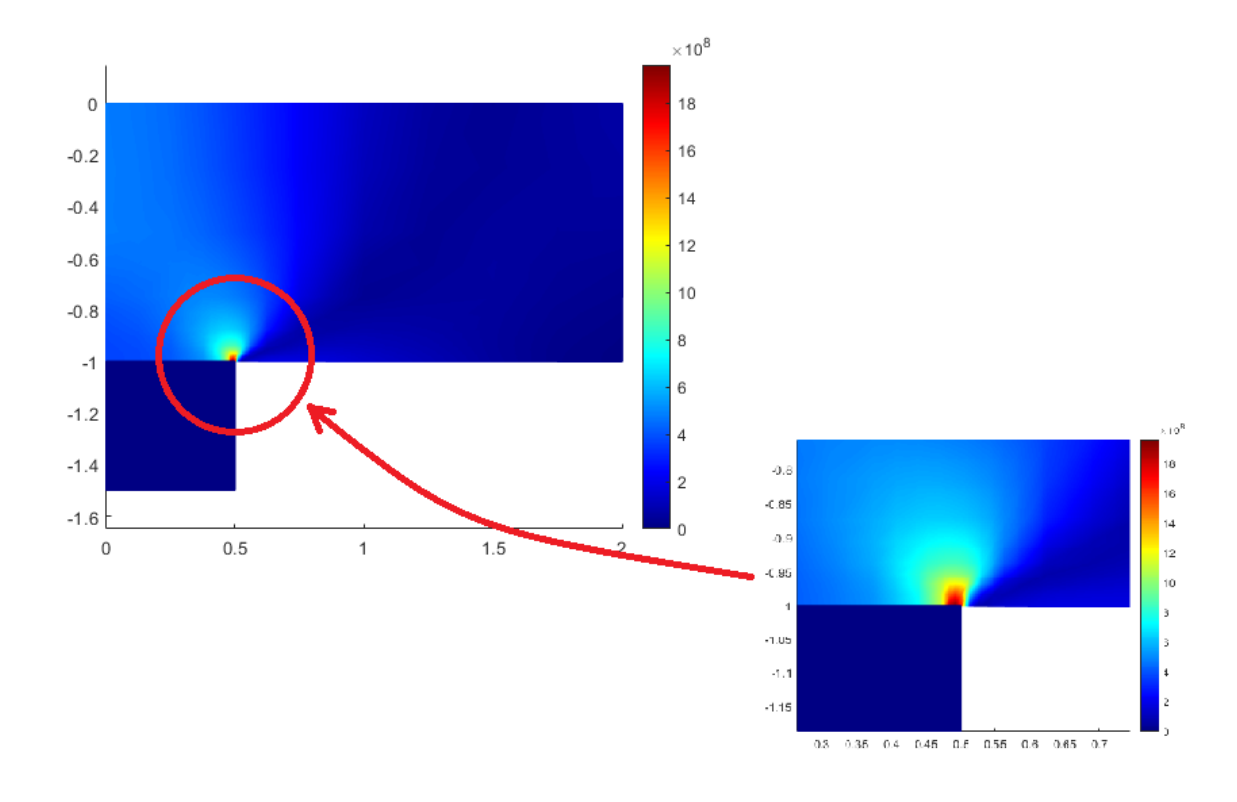


Figure 4.16 – Von Mises stress distribution for the indentation process, p=2 and $\varepsilon_N=100E$.

In fig. 4.15 we show the normal stress distribution and in fig. 4.16 the Von mises stress distribution. As expected, we observe a sharp rise of the stresses at the edge of the contact zone (theoretically the pressure has an infinite value at the edges of the punch $(x = \pm a)$ [104]).

Using a cubic discretization which also has 12 slave nodes we found $p_0^h = 4.2687 \times 10^8$ Pa. We then compared the numerical contact pressure distribution obtained to the analytical pressure distribution, and this comparison is shown in fig. 4.17. In fig. 4.18 we show the comparison of the numerical displacement of the surface outside the punch to the analytical displacement.

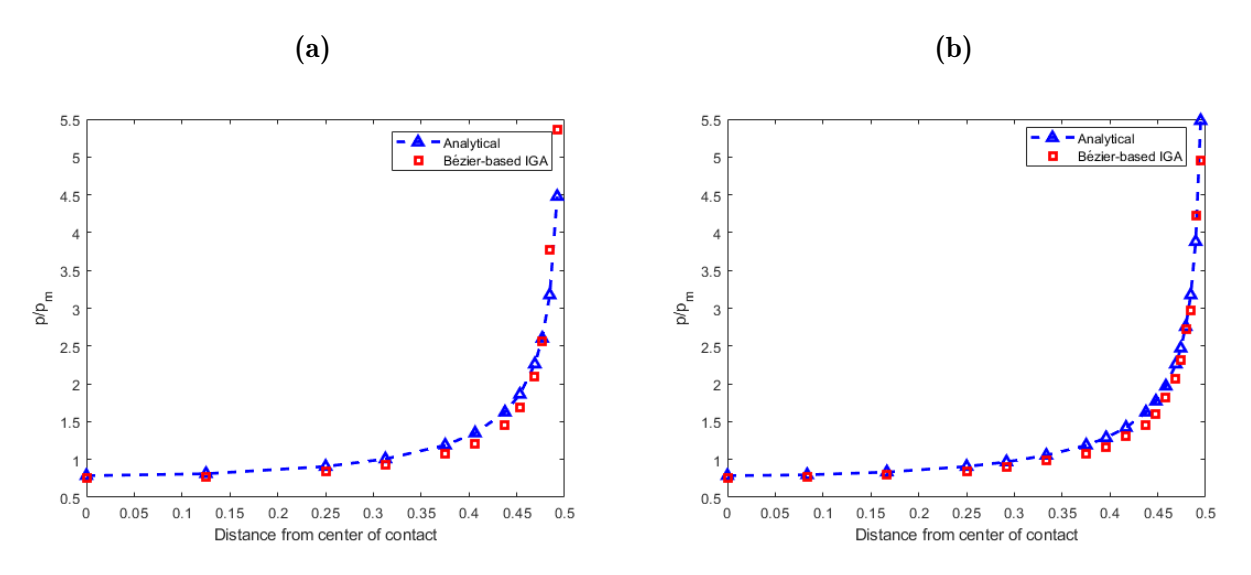


Figure 4.17 – Comparison of the numerical solution, in terms of the contact pressure (normalized with the analytical mean contact pressure p_m) distribution across the contact zone, to the analytical solution for the quadratic and cubic case, $\varepsilon_N = 100E$: (a) quadratic mesh, and (b) cubic mesh.

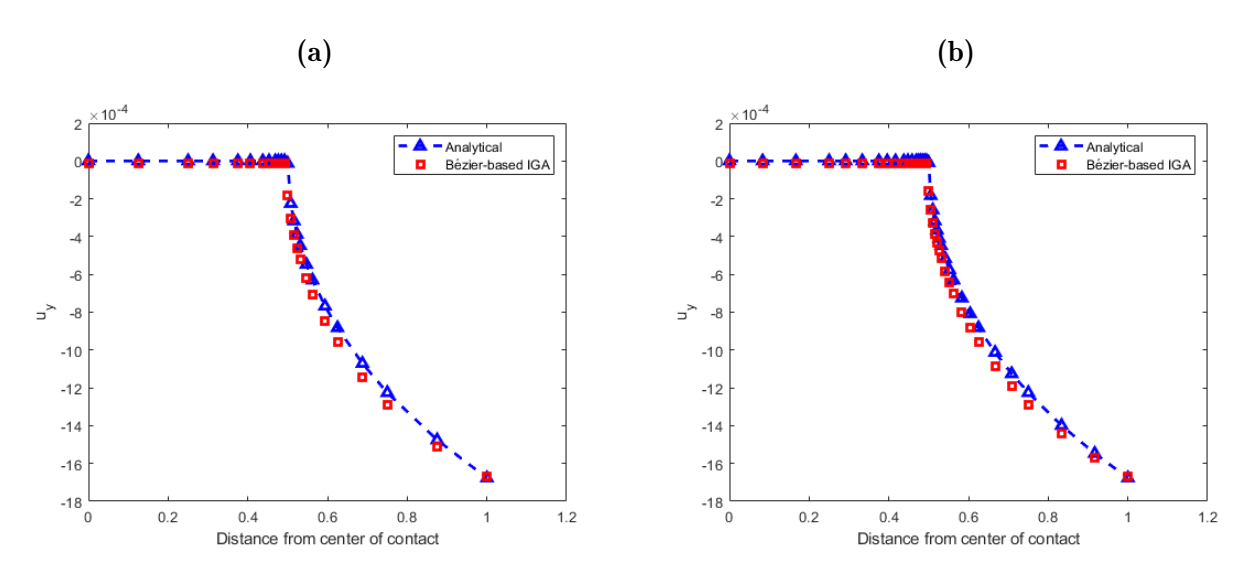


Figure 4.18 – Comparison of the numerical solution, in terms of the vertical displacement of the surface outside the punch, to the analytical solution for the quadratic and cubic case, $\varepsilon_N = 100E$: (a) quadratic mesh, and (b) cubic mesh.

The numerical results from the simulation are in good agreement with the analytical solution. A

relative error (relative to the analytical solution) of 3.7 % on the contact pressure at the center of contact is obtained with quadratic discretization. With the cubic discretization we have a 2.9 % relative error. Evidently we under predict the maximum contact pressure (pressure at the edge of the punch). This is because of the stress concentration and would therefore require a finer mesh to better capture the stresses at this area. Even so, this may seem a futile task numerically because the stresses are infinite.

Again comparing the results with the Abaqus FEA model using penalty method with the default penalty stiffness (12 slave nodes on the contact interface, full model with 340 linear quad elements, and 862 total DOFs), we found the Bézier based method to be more accurate. With the Abaqus FEA model we obtained $p_0 = 3.84812 \times 10^8$ Pa. For the same number of degrees of freedom in the system, with the FEA model we have a relative error of ~ 12.6 % in comparison to the analytical solution. With the Bézier based approach, the error is only ~ 3.7 %.

4.3 Numerical Simulation of Frictional Contact Problems

In this section we use the developed Bézier-based discretization scheme to simulate frictional contact. Again the penalty method is used for the enforcement of contact constraints and the node to surface method for the collocation of contact integrals.

4.3.1 Compression of an Elastic Cylinder on a Rigid Substrate

Consider the frictional contact of an infinitely long elastic cylinder with a rigid plane, schematic in fig. 4.19.

The cylinder is being compressed by displacement $\bar{u}=-2.7$ mm, has a radius R=0.05 m, and is made of a linear elastic isotropic material with a Young's modulus E=200 GPa and Poisson's ration $\nu=0.3$, with coefficient of friction $\mu=0.8$. Taking into account symmetry, the problem can be modeled in 2D with only a quarter of the geometry, under plane strain assumptions (with the formulation detailed in section 4.2.2.1 and the discrete elastic stiffness and the internal force vector in eqs. (4.19) and (4.20)).

The uncoupled analytical solution for this problem has been outlined in [102, 105, 106], assuming purely stick conditions. This simplified solution approach of course leads into the underestimation of contact stresses. However, if the friction coefficient is set large enough, which it is in our case, we can reduce the error arising as a result of the uncoupled approximation of the analytical solution [105]. Using the uncoupled solution approach, and assuming purely stick conditions, for the prescribed compressive displacement which is equivalent to a total applied load $F_N = 1.49 \times 10^8$ N. The analytical solution is computed in appendix III, and found as:

• the contact area semi width a is found to be 6.5708 mm

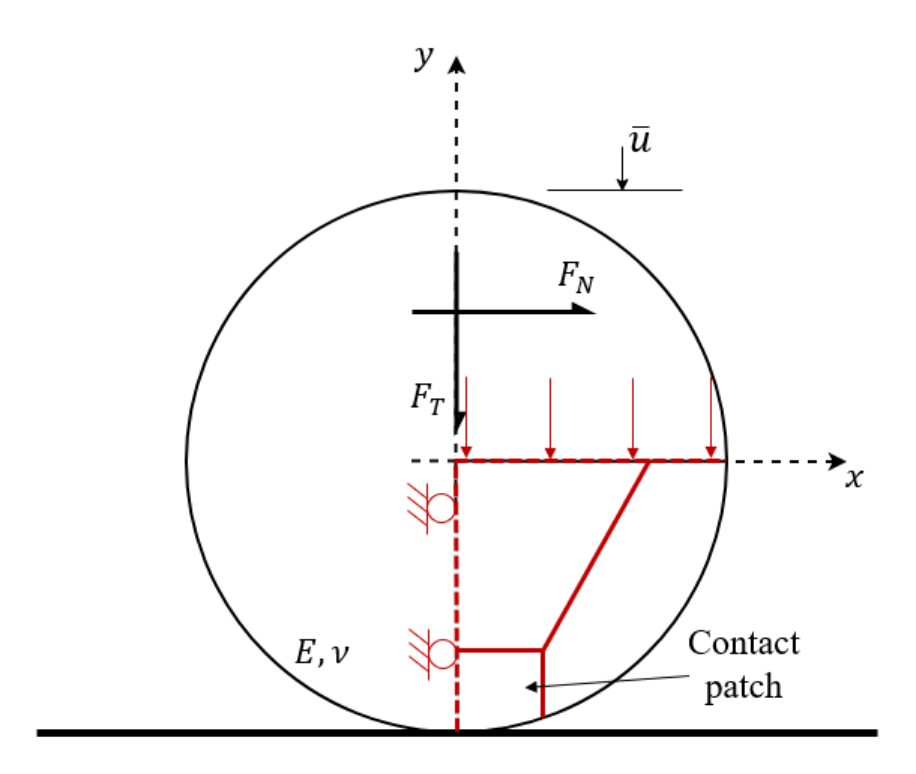


Figure 4.19 – Elastic cylinder compressed on to a rigid plane.

- the subsequent maximum normal contact pressure is $p_0 = 1.4441 \times 10^{10} \text{ Pa}$
- and the maximum tangential contact pressure is 0.32698×10^{10} Pa

Under the infinitesimal deformation conditions the contact stiffness terms and its force vector in eqs. (3.109) to (3.112) reduce into :

$$\mathbf{K}_{c}^{\text{stick}} = \varepsilon_{N} \mathbf{N} \mathbf{N}^{\text{T}} + \varepsilon_{T} m_{11} \mathbf{D}_{1} \mathbf{D}_{1}^{\text{T}} + 2\varepsilon_{T} \mathbf{D}_{1} \tilde{\mathbf{T}}_{1}^{\text{T}} \left(\bar{\xi} - \bar{\xi}_{n} \right)$$
(4.21)

$$\mathbf{F}_c^{\text{stick}} = \varepsilon_N g_N \mathbf{N} + t_{T_1}^{trial} \mathbf{D}_1 \tag{4.22}$$

for stick conditions, and

$$\mathbf{K}_{c}^{\text{slip}} = \varepsilon_{N} \mathbf{N} \mathbf{N}^{\text{T}} + \mu \varepsilon_{N} \operatorname{sign} \left(t_{T_{1}}^{trial} \right) \left[\sqrt{m_{11}} \mathbf{D}_{1} \mathbf{N}^{\text{T}} + \frac{g_{N}}{\sqrt{m_{11}}} \mathbf{D}_{1} \tilde{\mathbf{T}}_{1}^{\text{T}} \right]$$
(4.23)

$$\mathbf{F}_c^{\text{slip}} = \varepsilon_N g_N \mathbf{N} + t_{T_1} \mathbf{D}_1 \tag{4.24}$$

for sliding conditions.

The stick and slip tangential tractions write as:

$$t_{T_{1}}^{trial} = t_{T_{1n}} + \varepsilon_{T} \left[m_{11} \left(\bar{\xi} - \bar{\xi}_{n} \right) \right]$$

$$t_{T_{1}} = -\mu |t_{N}| \frac{t_{T_{1}}^{trial}}{\left\| t_{T_{1}}^{trial} \right\|}$$
(4.25)

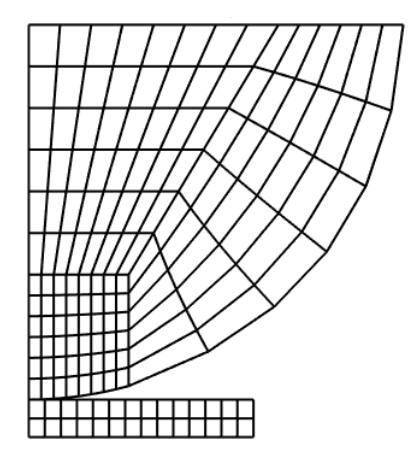


Figure 4.20 – Quadratic Bézier elements mesh used for the frictional contact problem between an elastic cylinder and a rigid substrate.

To simulate this interaction, we discretize the geometry with quadratic Bézier basis with the contact patch mesh of 4×3 elements; the mesh used for the computation is shown in fig. 4.20.

We set the tangential penalty parameter $\varepsilon_T = 10^2 E$ and normal penalty parameter $\varepsilon_N = 10^3 E$. The prescribed displacement \bar{u} is applied in 50 increments. The results obtained - the horizontal and vertical displacement field as well as the normal and tangential stress distribution - are shown in fig. 4.21.

The numerical semi width of the contact area was found to be in the vicinity of 6.578 mm, which is approximately 0.1% relative error, and the maximum normal contact pressure was found to be 1.46041×10^{10} Pa with $\sim 1\%$ relative error. The maximum tangential stress was found to be 0.3875×10^{10} Pa, which is much higher than the analytical value ($\sim 18.5\%$). To evaluate the effect of mesh refinements, we simulate this problem again : first using a 8×6 quadratic mesh, using a cubic 4×3 mesh, and finally a cubic 8×6 mesh. Results obtained are summarized in table 4.4.

Contact inter-	Max. tangential stress	Contact area semi	Max. normal pressure,	
face n_{elems}	$[\times 10^{10} \text{ Pa}]$	width, $a \text{ [mm]}$	$p_0^h \ [\times 10^{10} \ \mathrm{Pa}]$	
	Quadratic elements			
4	0.3875	6.5780	1.4604	
8	0.3862	6.5762	1.5149	
Cubic elements				
7	0.3899	6.5819	1.5201	
13	0.3692	6.5792	1.5582	

Table 4.4 – The effects of mesh refinement on the numerical solution for the frictional contact between an elastic cylinder and a rigid plane.

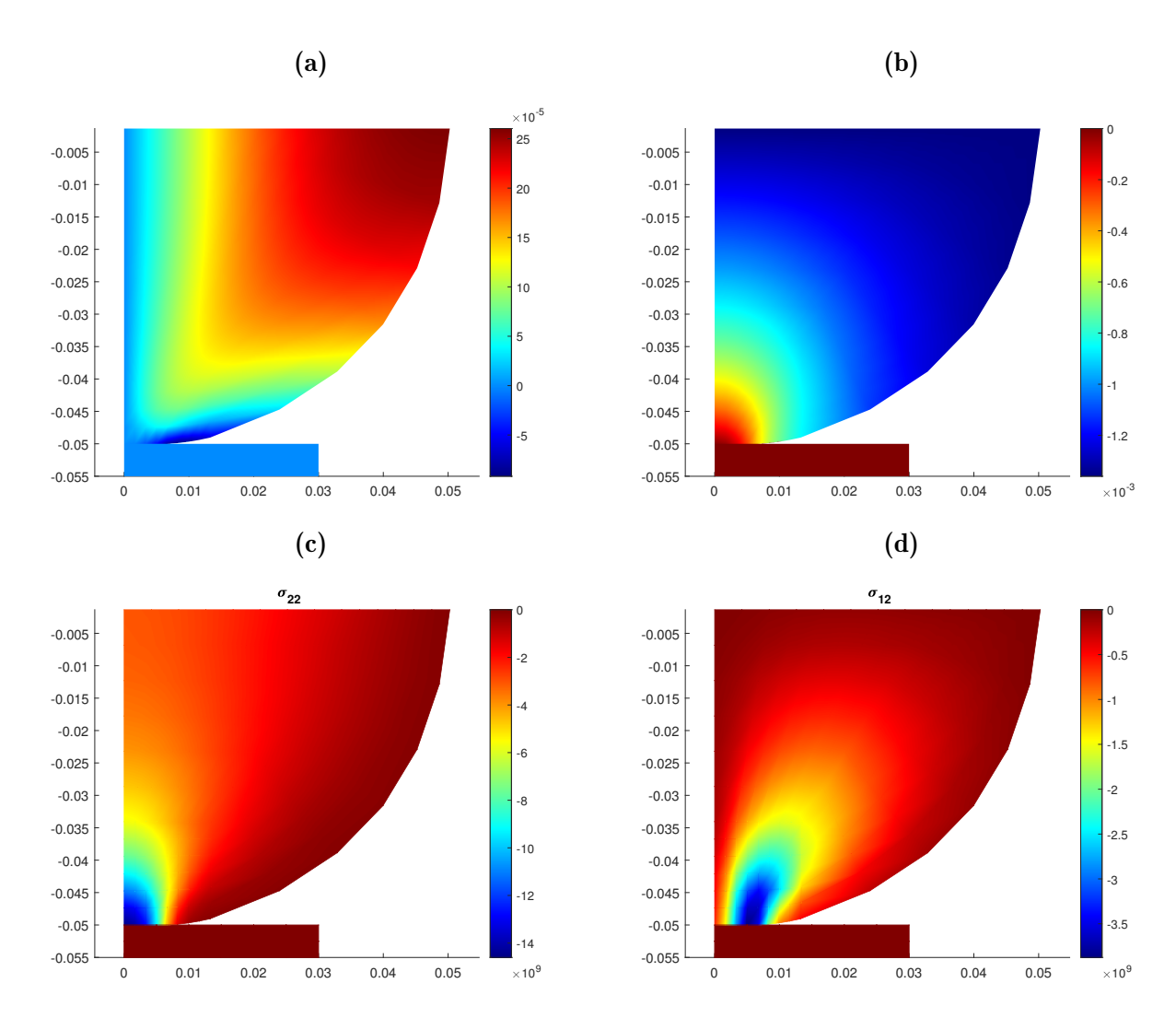


Figure 4.21 – Numerical results for the frictional contact of an elastic cylinder and a rigid plane obtained contact patch mesh 4×3 (mesh shown in fig. 4.4) : (a) *x*-component of the displacement, (b) *y*-component of the displacement, (c) normal stress distribution, σ_{22} , and (d) tangential stress distribution, σ_{12} .

Figure 4.22 shows the comparison of the numerical solution obtained using the Bézier-based IGA method to the analytical solution and the FEA solution from Abaqus (Abaqus mesh contains 21 slave nodes on the contact interface - model size as given in section 4.2.1.2).

Again the IGA Bézier based method proved to be more accurate that the Lagrange based FEA method, particularly in terms of the predicted contact area. From the Abaqus solution the contact area semi width was found to be 7.2785 mm leading to a relative error of $\sim 10.7\%$, whereas with IGA the error on the contact semi width is less than 1%. Likewise the quality of the recovered normal pressure from the IGA method is relatively more accurate, on per degree of freedom basis, than the normal pressure solution from Abaqus. Furthermore, the approximation of the tangential stress improves with mesh refinements.

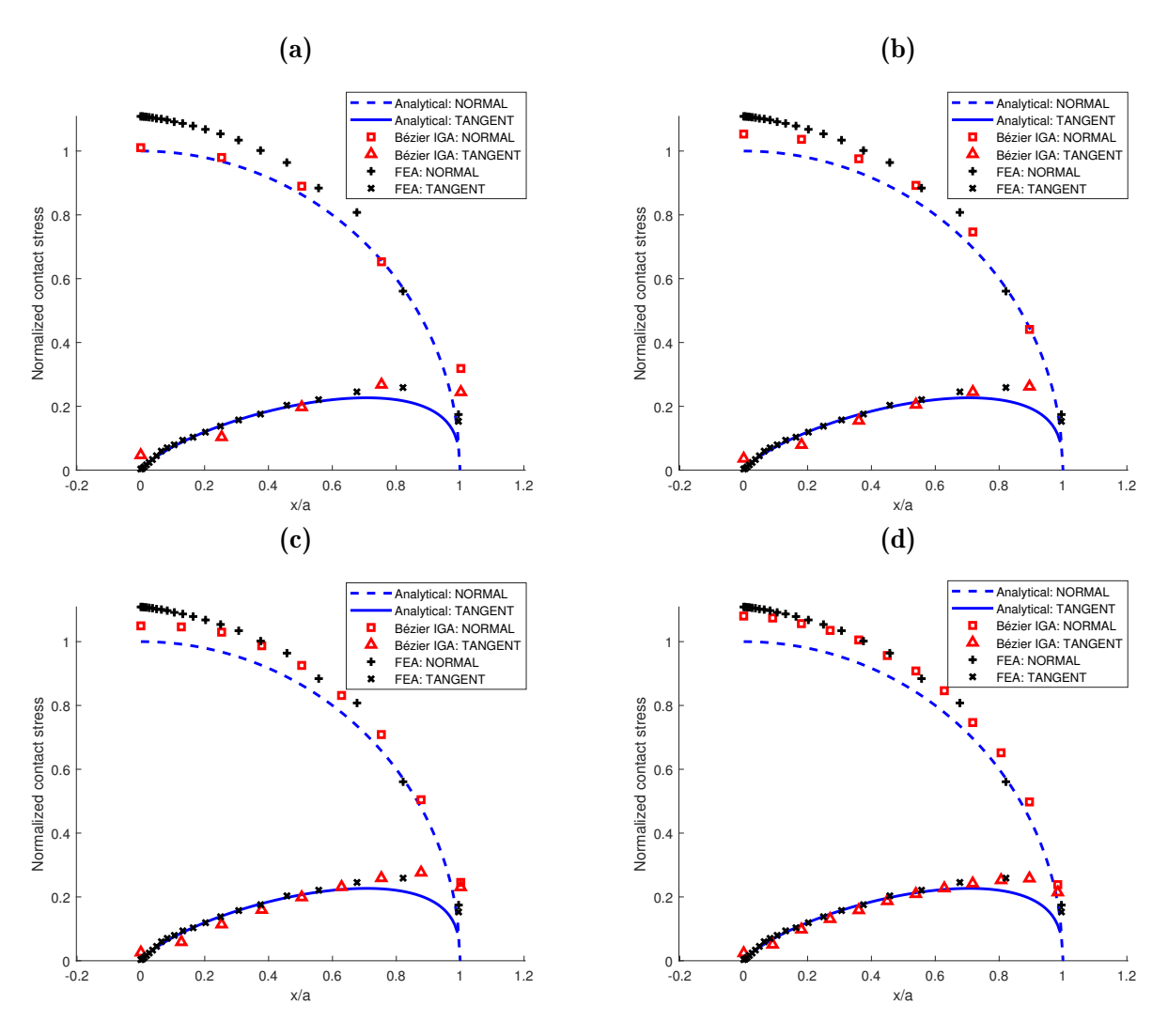


Figure 4.22 – Comparison of the Bézier-based numerical solution to the analytical solution (uncoupled approach) and Abaqus solution for the frictional contact between and elastic cylinder and rigid plane: (a) 4×3 quadratic mesh, (b) 4×3 cubic mesh, (c) 8×2 quadratic mesh, and (d) 8×6 cubic mesh.

4.3.2 Frictional Contact Between Deformable Bodies

In this numerical example we consider Hertzian contact, with friction, between a deformable body with a cylindrical lower surface (upper body) and a deformable plane (lower body) depicted in fig. 4.23.

Both bodies are made of an elastic isotropic material with a Young's modulus E=1 and Poisson's ratio $\nu=0.3$, and a coefficient of friction $\mu=0.2$. The upper body has a height of h=0.3, base width of b=0.5, and its cylindrical lower surface has a radius R=1. All units in SI units standard. The deformable plane has a height h=0.3 and base width h=0.5. The loading history of the problem depicted in fig. 4.23.

During the first analysis step a uniform downward vertical displacement is applied in increments

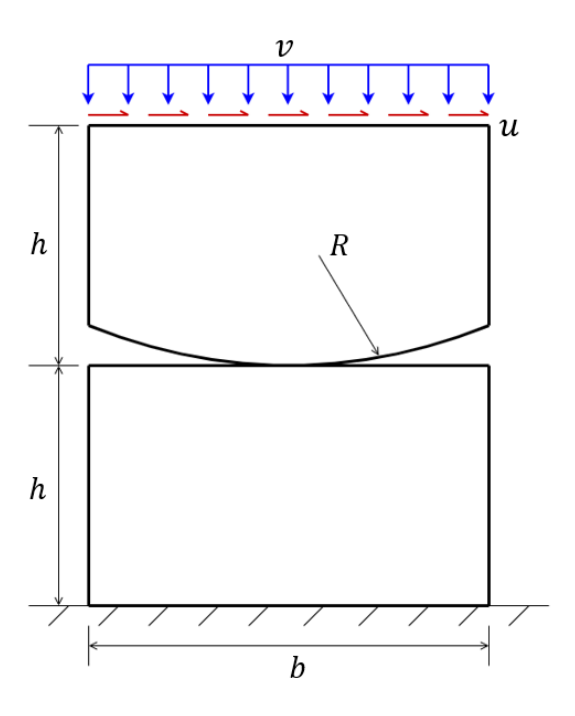


Figure 4.23 – Schematic of the frictional contact between a deformable cylinder and a deformable plane.

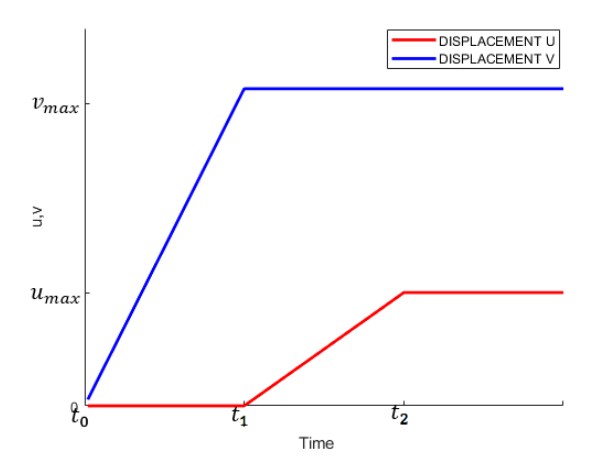


Figure 4.24 – Loading history for contact interaction in fig. 4.23.

up to $v_{max} = 2 \times 10^{-3}$ at the top surface of the upper body for time $T = [t_0, t_1]$. In the second analysis step the top surface of the upper body is then loaded in the horizontal direction, again in increments, with an applied displacement up to $u_{max} = 0.75 \times 10^{-3}$ during time $T = [t_1, t_2]$, while the vertical displacement is held constant at v_{max} . The bottom surface of the lower body is fixed in both x and y direction.

In the resolution of this problem we take the cylindrical surface of the upper body as the slave surface and upper surface of the plane as the master surface. The slave surface is discretized using cubic Bézier elements with its mesh containing 12 elements in the x-direction and 6 elements in

the y-direction. For the slave surface the mesh has been refined around the potential contact region, through the redistribution of the knot vector entries, such that 80% of the elements are located within half the total length of the knot vectors. Similarly the master surface is discretized with cubic Bézier elements (7×4 mesh), however with uniformly distributed knot entries both in the x,y-direction. Figure 4.25 shows the mesh used for the simulation.

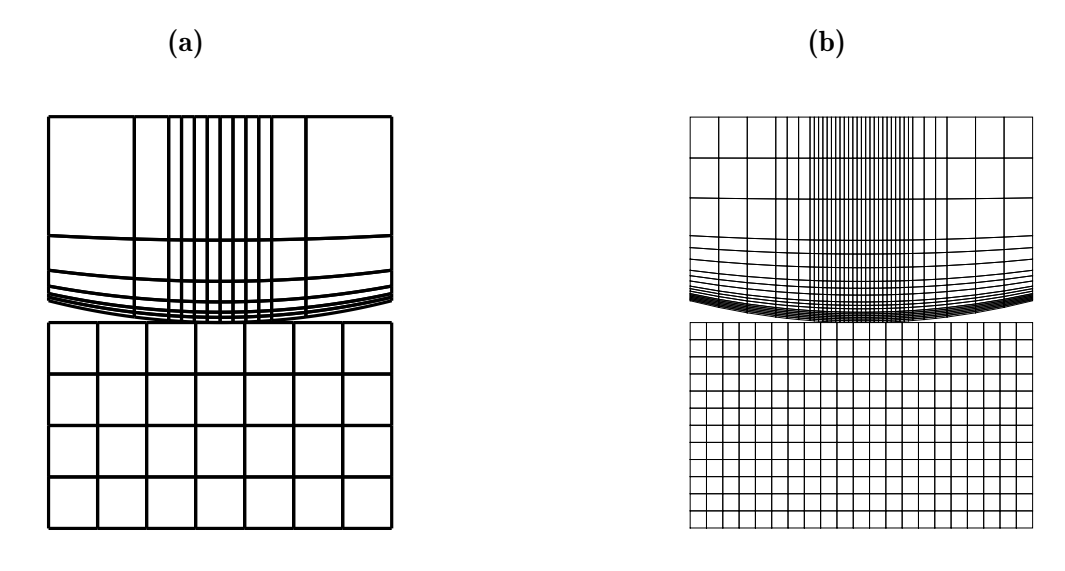


Figure 4.25 – The Bézier mesh of the problem in fig. 4.23 (visualization of elements and the actual location of the computation nodes), 12×6 mesh for the slave body, 7×4 mesh for the master body: (a) visualization of the Bézier elements in the mesh, and (b) the nodal mesh used for the computation.

The applied displacement in fig. 4.24 amounts to a total reaction force $F_N = 6.02 \times 10^{-4}$ N in the normal direction (y-direction) and $F_T = 1.08 \times 10^{-4}$ N in the tangential direction. Hills and Nowell [106] detailed the solution procedure for the analytical solution for this problem (uncoupled approach which assumes the tangential stresses has no effect on the normal contact pressure). The solution has been detailed in the appendix IV with the analytical normal and tangential contact pressure across the contact area shown fig. 4.26.

From fig. 4.26 we can see that contact interaction experiences both stick and slip conditions with maximum normal contact pressure $p_0 = 10.2587 \times 10^{-3}$ Pa. Both the normal and tangential contact pressure distribution are symmetric about the centre of contact area x = 0. The full contact area semi width is found to be $|a| = 3.73416 \times 10^{-2}$ m and the stick area semi width c is found to be $|c| = 1.18102 \times 10^{-2}$ m. Maximum tangential contact pressure is reached at the boundaries of the stick zone and is found to be 1.9457×10^{-3} Pa. At the centre of the contact zone the tangential contact pressure is found to be 1.4028×10^{-3} Pa.

To obtain the numerical solution; 50 load-steps are used for both analysis steps. We set both the normal penalty parameter and tangential penalty parameter to ε_N , $\varepsilon_T = 10^3 E$. The displacement field (horizontal and vertical components) obtained is shown in fig. 4.27.

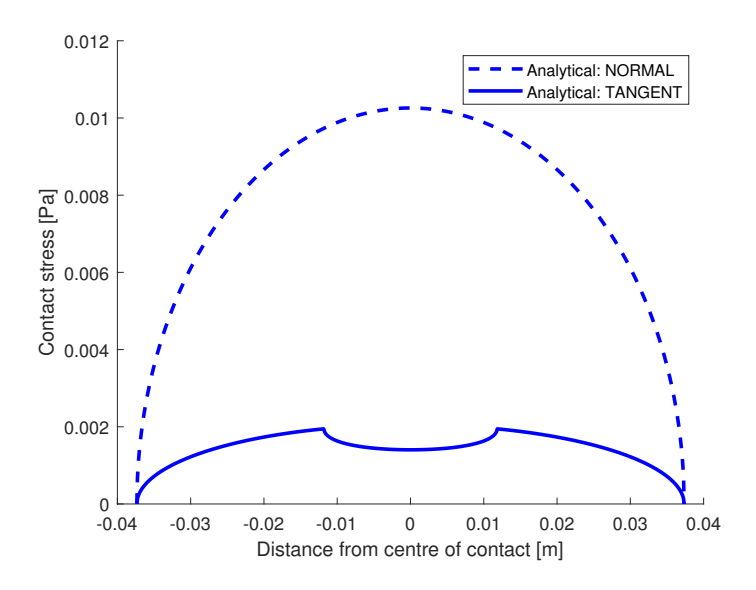


Figure 4.26 – Analytical contact pressure for the Hertz contact of the deformable cylinder on a deformable plane - see appendix IV.

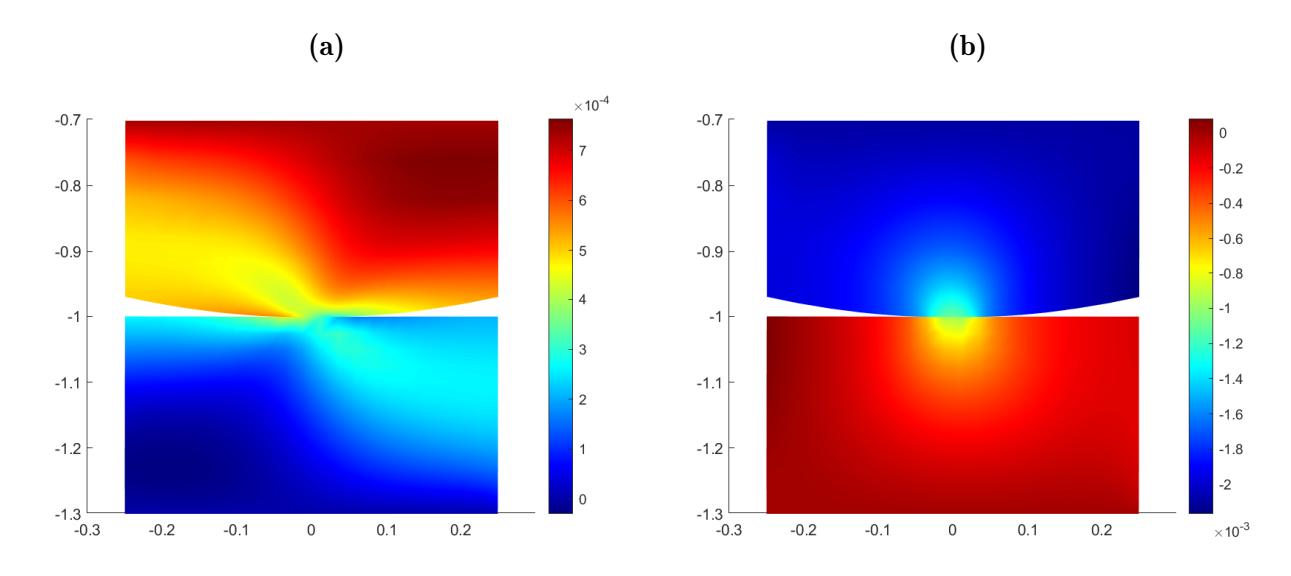


Figure 4.27 – Displacement field [m] obtained for contact between a deformable cylinder and deformable plane: (a) x- component of the displacement, and (b) y- component of the displacement.

Figure 4.28 shows the stress distribution (normal and tangential components) obtained, with maximum normal stress $\sim 1 \times 10^{-2}$ Pa and maximum tangential stress $\sim 3 \times 10^{-3}$ Pa.

The first observation from the results in fig. 4.27 and fig. 4.28 is the lack of symmetry of not only the deformation (with respect to the displacement fields), but both the normal and tangential contact stresses are skewed. This is especially apparent when looking at the comparison (fig. 4.29) of the contact stresses distribution across the contact area for both the analytical solution and the numerical solution obtained, as well as the numerical results summarized in table 4.5.

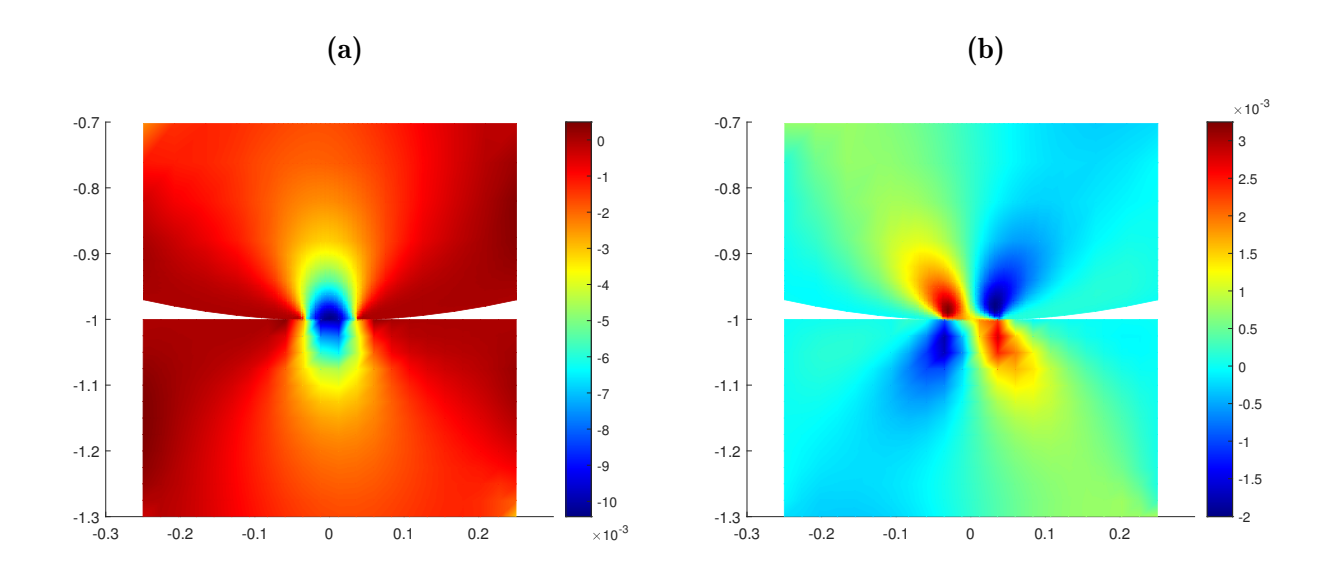


Figure 4.28 – Normal and tangential stress [Pa] distribution obtained for contact between a deformable cylinder and deformable plane : (a) normal stress, σ_{22} , distribution, and (b) tangential stress, σ_{12} , distribution.

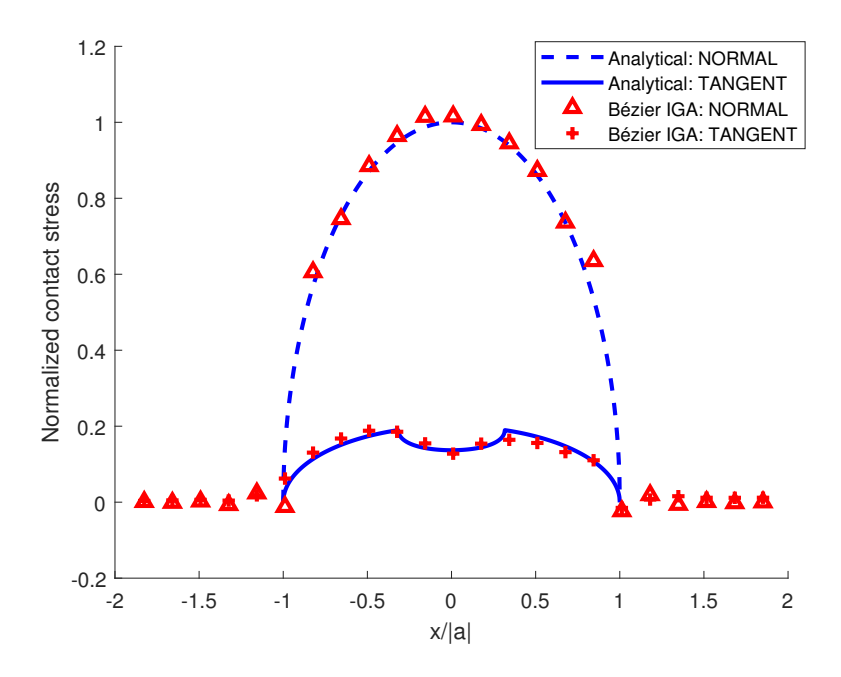


Figure 4.29 – Comparison of the analytical and numerical contact pressure (normalized) for the Hertz contact between the deformable bodies.

The maximum normal contact pressure was found to be 10.4224×10^{-3} Pa.

From fig. 4.27 and fig. 4.28 then we deduce that the presence of slip has an influence of the contact stresses and therefore the assumption made for the uncoupled solution approach (analytical solution in fig. 4.26) does not hold; the analytical solution is only approximate. This effect was also observed and is even more prominent in the Lagrange basis discretization solution which was obtained using the Penalty formulation in Abaqus with a default penalty stiffness. For this

Numerical results	Left	Right
Contact area semi-width $a \times 10^{-2}$	-3.6520	3.7650
Stick zone semi width $c \times 10^{-2}$	-1.8293	1.2812
Tangential contact pressure at $c \times 10^{-3}$	1.9295	1.6846

Table 4.5 – The contact area semi width a and the stick zone semi width c (contact between a deformable cylinder on an elastic plane) obtained using the Bézier-based method.

Abaqus model a 60×30 linear quads mesh was used for both the slave and master bodies. Again the mesh was refined in the vicinity of the contact region. Since we know that in standard FEA the finer the mesh, the closer we will get to the true solution, hence the use of the very fine mesh for the Abaqus model. This provides us with a good benchmark for verification of our IGA model specifically for this problem as the analytical solution is only approximate. The comparison of these results is shown in fig. 4.30 and fig. 4.31.

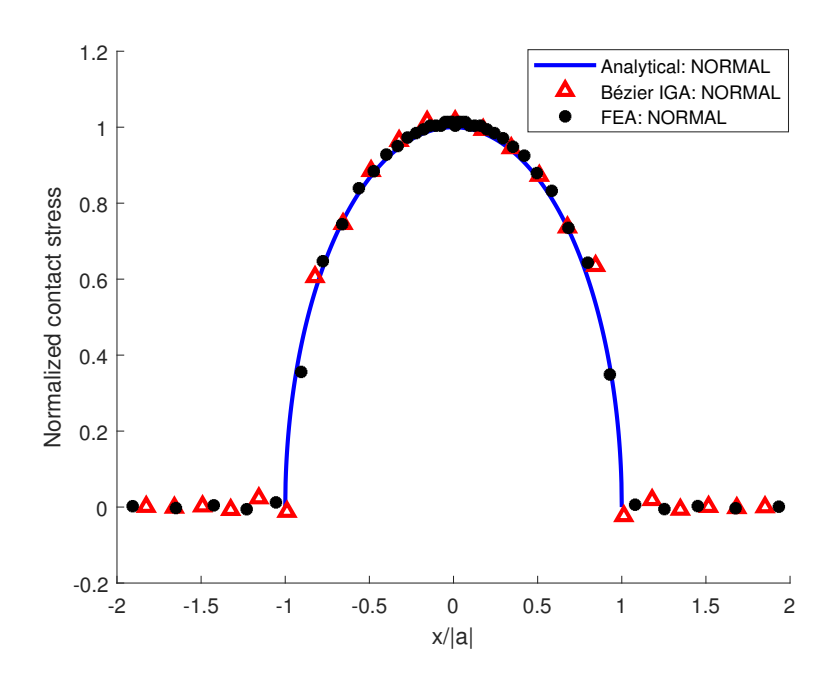


Figure 4.30 – Comparison of the analytical and numerical normal contact pressure (normalized) for the Hertz contact between the deformable bodies.

In table 4.6 we summarize the results in fig. 4.27 and fig. 4.28.

We can see that the total contact area and normal contact pressure, for both IGA and FEA, are comparable with the analytical solution. However the IGA model is much smaller, in terms of DOFs, compared to the Abaqus model: IGA model contains 100 elements with a total of 1978 DOFs, and the Abaqus model contains 3600 elements with a total of 7808 DOFs. From the results we learnt that:

• The numerical p_0 is 10.4224×10^{-3} Pa using IGA and 10.4×10^{-3} Pa using FEA, with a relative error (with respect to the analytical value) of 1.6% and 1.4%, respectively.

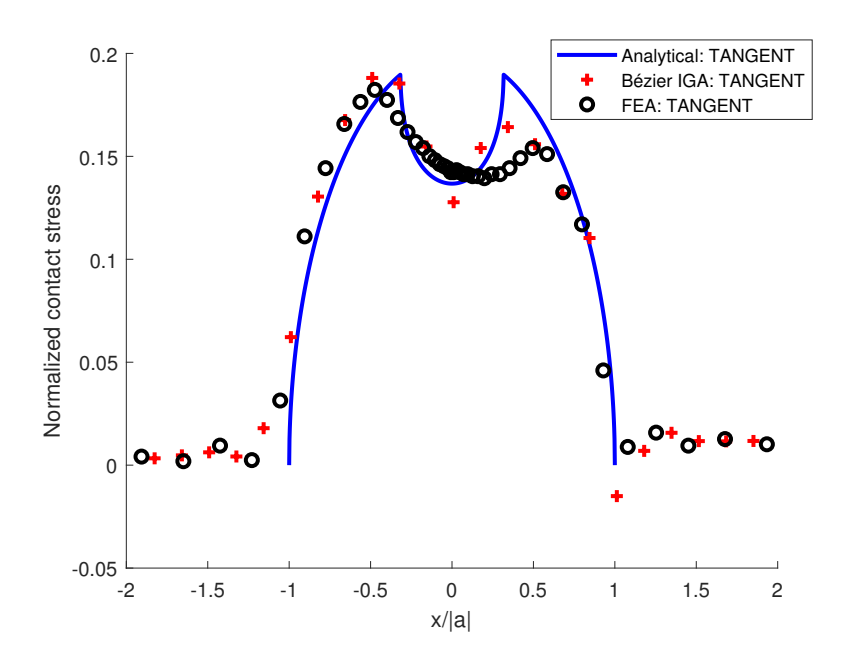


Figure 4.31 – Comparison of the analytical and numerical tangential contact pressure (normalized) for the Hertz contact between the deformable bodies.

	Left	Right	Left	Right
Method	IGA	A FEA		
Contact area semi-width $a \times 10^{-2}$ m	-3.6520	3.7650	-3.940	3.485
Stick zone semi width $c \times 10^{-2}$ m	-1.8293	1.2812	-1.770	1.850
Tangential contact pressure at $c \times 10^{-3}$ m	1.9295	1.6846	1.870	1.580

Table 4.6 – Results obtained in terms of the contact area semi width a and the stick zone semi width c (contact between a deformable cylinder on an elastic plane) from both the Bézier-based method and using Abaqus.

- The total contact area width 2a for both IGA and FEA is within 1% of the analytical solution : for IGA $2a = 7.417 \times 10^{-2}$ m, for FEA $2a = 7.425 \times 10^{-2}$ m, and the analytical total contact width is $2a = 7.46832 \times 10^{-2}$ m.
- The numerical total stick zone is however much higher than the analytical 2.36×10^{-2} m, with a width of $2c = 3.1105 \times 10^{-2}$ m and $2c = 3.62 \times 10^{-2}$ m, for IGA and FEA, respectively.

Again as mentioned the numerical tangential contact stress is non-symmetric with a larger slip zone to the right than on the left side.

4.4 Summary

In this chapter, we consider the Bézier-based IGA approach in [87] and introduced in chapter 2, suitable for existing FE codes data structures, which is based on the implementationally friendly isogeometric finite elements [76] and the transformation method in [88]. The main and interesting characteristic of this developed scheme is, unlike the standard NURBS/BSplines-based IGA, computation points now live on the physical geometry. This leads to a mesh identical to that of standard FEM which then greatly simplifies the application of boundary conditions, and thereafter the computation of contact integrals which have to be collocated at physicals points.

The Bézier based IGA method was then coupled with the node-to-surface method and developed in chapter 3.6 for the treatment of penalized contact problems. In this chapter the objective was to evaluate the performance of this scheme in terms of the quality of the solution as well as its performance relative to the classical Lagrange based FEA.

First we considered the classical frictionless Hertzian contact problem between an elastic sphere and a rigid block, under assumed axisymmetric conditions. The results were validated against the analytical solution. We found that even with a relatively coarse mesh we could predict both the contact radius and maximum contact pressure to within useful accuracy (less than 0.5% relative error on contact area radius, and a relative error of $\sim 1.5\%$ on the contact stress), and quality of the solution was far more superior than the quality of the solution obtained using the Lagrange based method (Abaqus).

In the second problem we studied the indentation of an elastic half space by a rigid flat punch, under plane strain assumptions with a quadratic discretization. The results obtained were then compared to the analytical solution and we found that with the Bézier-based method we could predict the contact pressure to within 4% of the analytical solution in terms of the contact pressure at the centre of the contact area. These results were further improved through degree elevation (cubic elements instead of quadratic discretization while maintaining the same number of degrees of freedom in the system); the relative error reduced from $\sim 4\%$ to just under 3%, a significant contrast to the $\sim 12\%$ relative error on the Abaqus results.

The third numerical example consisted of a pure stick contact interaction between an elastic cylinder and a rigid substrate. Again plain strain conditions hold for this problem, and due to double symmetry a quarter model was sufficient. The uncoupled solution of this problem exist and has been detailed in [102, 105, 106]. Comparing our numerical solution to the analytical solution, we found an excellent correlation in terms of the contact area semi width: the numerical semi width is with < 1% of the analytical value. A relatively good agreement of the numerical normal pressure and the analytical normal pressure was found as well.

The fourth and final numerical example considers a frictional Hertzian contact interaction between two deformable bodies (an elastic cylinder on an elastic plane) under partial slip conditions. The cylinder is first loaded in the vertical direction and then in the horizontal direction, such that in the contact area both the stick zone and slip zone are present. This problem has an existing analytical solution which is given in [105, 106] and given in fig. 4.26. One major observation from the numerical solution was, contrarily to the analytical solution, the contact pressure distribution (both the normal and tangential component) are non symmetric, however this skewness was more prominent in the tangential contact stresses. Consequently, the contact area is slightly skewed, however the total contact width is still with the 1% of the analytical total contact width. Furthermore the normal contact pressure was in good agreement with the analytical solution (relative error $\sim 1.7\%$). The skewness in the contact pressure was also observed in the Lagrange FEA solution.

Explicit Dynamics in Impact Simulation and Acoustic Radiation

5.1 Introduction

Vibration and noise control is an important subject in industry. Structural vibration is caused by the unbalanced inertial forces and noise generation is the result of such vibration. Whether it is the case of structural damaging vibrations, or vibrations generated by machines, moving vehicles, operational tools, the generated noise is not only detrimental to the machine life itself, but can also be harmful to the environment and pose a serious health and safety hazard to human life [8–11]. Hence the strict requirements on manufacturers to comply with the standards limiting unwanted noise emissions. This is the reason why noise control, and its reduction at the source, is an important step during the design phase of technical devices due to the impact it can have on the environment and humans [10, 107]. Consequently, good predictions of vibrations, and the understanding of the mechanisms of generation and propagation of noise, are so useful in this field, especially for noise induced by impacted structures. In particular, we consider the acoustic radiation of forced (excited) vibrating thin elastic plates (these are applicable in many sectors of industry). This excitation can be localized as typically encountered in impact problems, or moving as is generated by a passing vehicle.

As already mentioned, the recovery of contact stresses arising from surface/surface interactions such as impacted structures is the entry point for these type of analysis: noise control begins with a good prediction of the dynamics of the structure, including a good contact model. Numerical simulation of contact (static and dynamic), particularly in FEM and IGA, is well established and has been studied for many years [2, 3, 5, 22, 23, 97]. Similarly, research work dedicated to plate dynamics is plentiful and rich, ranging from modal analysis [108, 109], impact problems [10], and moving forces [110–112]. Focus on vibro-acoustics is also well advanced partly due to the emergence of new numerical techniques other than FEM, particularly the boundary element method (BEM) [113–115]. However, even with the progress made in research work for both contact analysis and vibro-acoustics, and despite the real interest from industry in

terms of impact induced noise control and reduction, very little effort has been made towards numerical simulation of the acoustic response of impacted structures [116–118]. The impact-acoustic problem of impacted plates has however been either partially addressed in time domain [119–121], or completely treated but in frequency acoustic formulation [122, 123] as implemented in [113, 114].

In transient acoustic response the most useful, sought out information is contained within a short duration at the beginning of the sound signal and for this reason, frequency methods are generally not sufficient [124]. For these type of problems, time-domain approaches are more appealing. Moreover, due to its complexity the impact-acoustic problem for plate like structures has been treated only in part. In fact, in the limited studies of this problem available in literature, the contact has been assumed to be punctual with the structure dependent contact forces estimated experimentally [120], analytically using the Hertzian contact law [121], or approximated by a Dirac pulse [119]. Furthermore, when it comes to predicting the noise generated from forced vibrating plates, the case studies were mainly limited to the acoustic radiation due to impact at the center of the plate [10, 118], and focused on the initial transient wave [125]. Hence the interest in a model that is both accurate and complete in time domain: (1) complete in the sense that the dynamic analysis of the impact problem based on a contact formulation is carried out jointly with the calculation of the acoustic response of the problem in time domain, (2) accurate in the sense that the contact force and the contact area are precisely calculated even for complex geometries and not only for plate like structures. This is the reason why isogeometric analysis is an interesting numerical approach for this class of problems [12]: not only has it been used for contact [37–40] and impact analysis [85], but it has also been used in acoustics [35, 126].

The main scope of this chapter is the analysis of the dynamic response, and the resulting acoustic radiation, of a forced-vibrating circular plate embedded in a rigid baffle using the Bézier-based IGA approach developed in chapter 2. The governing equations which constitute both the dynamic and acoustic behavior of the plate are detailed in section 5.2. This is followed by the derivation of the discrete model in section 5.3, using the Bézier elements, used for the numerical solution. In section 5.4 we give some details on the solution procedure and discuss the obtained results. Lastly, the performance of the complete model is analyzed, in terms of results quality, order of approximation, computational efficiency, and the effects of the choice of time integration scheme.

5.2 Problem Description

In this study we consider a circular elastic plate of radius R_p , and thickness h with material properties Young's modulus E_p , Poisson's ratio ν_p and density ρ_p , impacted by a small elastic sphere, as illustrated in fig. 5.1. This sphere has a radius R_s , Young's modulus E_s , Poisson's ratio ν_s , density ρ_s , and an initial velocity \mathbf{v}_0 . The impact, without friction, is perpendicular to the center O of the plate. The fluid medium surrounding the plate is assumed to be lossless and

homogeneous with a sound speed c_f and a density ρ_f smaller than ρ_p . Further, we assume that the propagation medium (air) is so light such that it neither alters the modes of the plates nor shifts its natural frequencies. Moreover, the plate is assumed initially at rest and is embedded in a rigid baffle thus fulfilling the necessary condition for the use of the Rayleigh integral equation.

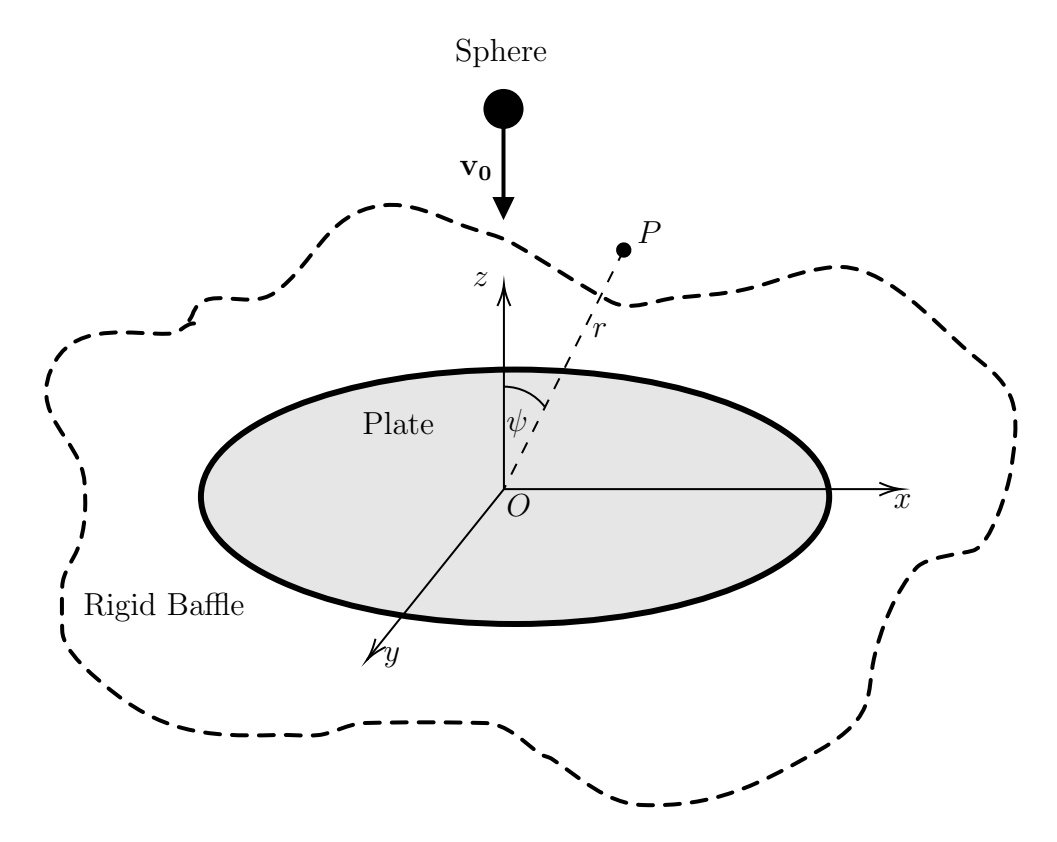


Figure 5.1 – Schematic of the impact of an elastic plate (embedded on a rigid baffle) by an elastic sphere : \mathbf{v}_0 the initial velocity of the sphere, and (r,ψ) are the polar coordinates defining the acoustic field point P.

The aim of this study is to perform numerical simulation of the impact between the plate and sphere, as well as the calculation of the resulting acoustic radiation in the surrounding fluid medium. Note that the circular shape chosen for the plate is motivated by the use of IGA which has been proven to be more accurate than the standard FEM approaches. The application of IGA for a rectangular plate would have brought very little compared to the standard method because of the shape of the plate. Moreover, in this problem only the deformation phase of impact is considered, the restitution phase is disregarded.

5.2.1 Governing Equations

Supposing there are no body forces, initial stresses, or initial strains present, the dynamic behavior of the elastic and homogeneous two-body system is governed by the following equilibrium and

boundary conditions equations:

$$\operatorname{div} \boldsymbol{\sigma}_{i} - \rho_{i} \frac{\partial^{2} \mathbf{u}_{i}}{\partial t^{2}} = \mathbf{0}, \quad \text{in } \Omega_{i}$$

$$\boldsymbol{\sigma}_{i} \cdot \mathbf{n}_{i} = \bar{\mathbf{t}}_{F_{i}}, \quad \text{on } \Gamma_{F_{i}}$$

$$\mathbf{u}_{i} = \mathbf{0}, \quad \text{on } \Gamma_{D_{i}}$$

$$(5.1)$$

where i = p, s (p for plate and s for sphere), and initial conditions

$$\mathbf{u}_{i}(\mathbf{x}_{i}, t_{0}) = \mathbf{u}_{0i}$$

$$\mathbf{v}_{i}(\mathbf{x}_{i}, t_{0}) = \mathbf{v}_{0i}$$
(5.2)

In eqs. (5.1) and (5.2) \mathbf{u} is the displacement field, t the time, \mathbf{n} the unit outward normal vector, and $\boldsymbol{\sigma}$ the stress tensor which is related to the strain tensor $\boldsymbol{\epsilon}$ through Hooke's law ($\boldsymbol{\sigma} = \mathbf{D} : \boldsymbol{\epsilon}$, with \mathbf{D} the elasticity matrix). Homogeneous boundary conditions are prescribed on the Dirichlet boundary Γ_D , with external loads acting on Γ_F , and the rest of the boundary Γ is assumed stress free. Assuming friction-less contact, that is, only normal traction \mathbf{t}_N (\bullet_N denotes a normal quantity) is taken into account, contact constraints are given by eq. (5.3)

$$g_N \ge 0, \quad t_N \le 0, \quad t_N g_N = 0$$
 (5.3)

with g_N the normal gap. Taking the sphere as the slave body and the plate as the master body, the normal gap $g_N = (\bar{\mathbf{x}}_p - \mathbf{x}_s) \cdot \bar{\mathbf{n}}_p$. Again, $\bar{\bullet}$ indicate quantities evaluated at the closest point projection parametric coordinates $\bar{\boldsymbol{\xi}}$.

The constitutive behavior of the plate is governed by the Reissner-Mindlin theory. With this plate theory, these main assumptions hold [127]:

• A plate of thickness h can be represented by its reference (middle) plane which is the xy-plane of surface A_p . The domain Ω_p of the plate then takes the form :

$$\Omega_p = \left\{ (x, y, z) \in \mathbb{R}^3 \mid z \in \left[-\frac{h}{2}, \frac{h}{2} \right], \quad (x, y) \in A_p \subset \mathbb{R}^2 \right\}$$
 (5.4)

• Any transverse loading on the plate induces deflection w (deflection does not vary through the thickness) and rotations θ_1, θ_2 of the normals to the reference plane. Moreover, a fiber initially normal to the reference plane rotates but remains straight after deformation. Thus the displacement field of any point on the plate is given by:

$$u_1(x,y,z) = z \ \beta_1(x,y) = z \ \theta_2(x,y)$$

$$u_2(x,y,z) = z \ \beta_2(x,y) = -z \ \theta_1(x,y)$$

$$u_3(x,y,z) = w(x,y)$$
(5.5)

• Plane stress hypothesis holds, that is, $\sigma_{33} = 0$

The stress-strain relationship, that is the relation of the in-plane strain κ and off-plane strain γ , to their corresponding stresses $\tilde{\sigma}$ and $\tilde{\tau}$, respectively, follows as:

$$\tilde{\boldsymbol{\sigma}} = z D_1 \boldsymbol{\kappa}, \quad \tilde{\boldsymbol{\tau}} = D_2 \boldsymbol{\gamma}$$
 (5.6)

where

$$\tilde{\boldsymbol{\sigma}} = \begin{cases} \sigma_{11} \\ \sigma_{22} \\ \sigma_{12} \end{cases}, \quad \tilde{\boldsymbol{\tau}} = \begin{cases} \sigma_{13} \\ \sigma_{23} \end{cases}, \quad \boldsymbol{\kappa} = \begin{cases} \frac{\partial \beta_1}{\partial x} \\ \frac{\partial \beta_2}{\partial y} \\ \frac{\partial \beta_1}{\partial y} + \frac{\partial \beta_2}{\partial x} \end{cases}, \quad \boldsymbol{\gamma} = \begin{cases} \frac{\partial w}{\partial x} + \beta_2 \\ \frac{\partial w}{\partial y} + \beta_1 \end{cases}$$
 (5.7)

and

$$D_{1} = \frac{E_{p}}{1 - \nu_{p}^{2}} \begin{bmatrix} 1 & \nu_{p} & 0 \\ \nu_{p} & 1 & 0 \\ 0 & 0 & \frac{1 - \nu_{p}}{2} \end{bmatrix}, \quad D_{2} = \frac{kE_{p}}{2(1 + \nu_{p})} \begin{bmatrix} 1 & 0 \\ 0 & 1 \end{bmatrix}$$
 (5.8)

k is the correction factor and is set to 5/6.

The sphere is assumed to be a 3D solid, with displacement field components $\mathbf{u}_s = \{u_s; v_s; w_s\}$, and its constitutive behavior described by the Hooke's law $\boldsymbol{\sigma}_s = \mathbf{D}_s : \boldsymbol{\epsilon}_s$. The stress $\boldsymbol{\sigma}_s$ and strain $\boldsymbol{\epsilon}_s$ tensor, in vectorial form, write as:

$$\sigma_{s} = \begin{cases} \sigma_{11} \\ \sigma_{22} \\ \sigma_{33} \\ \sigma_{12} \\ \sigma_{13} \\ \sigma_{23} \end{cases}, \quad \boldsymbol{\epsilon}_{s} = \begin{cases} \epsilon_{11} \\ \epsilon_{22} \\ \epsilon_{33} \\ \epsilon_{12} \\ \epsilon_{13} \\ \epsilon_{23} \end{cases} = \begin{cases} \frac{\partial u_{s}}{\partial x} \\ \frac{\partial v_{s}}{\partial y} \\ \frac{\partial w_{s}}{\partial z} \\ \frac{\partial u_{s}}{\partial z} + \frac{\partial v_{s}}{\partial x} \\ \frac{\partial u_{s}}{\partial z} + \frac{\partial w_{s}}{\partial x} \\ \frac{\partial v_{s}}{\partial z} + \frac{\partial w_{s}}{\partial y} \end{cases}$$

$$(5.9)$$

And the elasticity tensor \mathbf{D}_s given by :

$$\mathbf{D}_{s} = \frac{E_{s} (1 - \nu_{s})}{(1 + \nu_{s}) (1 - 2\nu_{s})} \begin{bmatrix} 1 & \frac{\nu_{s}}{1 - \nu_{s}} & \frac{\nu_{s}}{1 - \nu_{s}} & 0 & 0 & 0\\ \frac{\nu_{s}}{1 - \nu_{s}} & 1 & \frac{\nu_{s}}{1 - \nu_{s}} & 0 & 0 & 0\\ \frac{\nu_{s}}{1 - \nu_{s}} & \frac{\nu_{s}}{1 - \nu_{s}} & 1 & 0 & 0 & 0\\ 0 & 0 & 0 & \frac{1 - 2\nu_{s}}{1 - \nu_{s}} & 0 & 0\\ 0 & 0 & 0 & 0 & \frac{1 - 2\nu_{s}}{1 - \nu_{s}} & 0\\ 0 & 0 & 0 & 0 & 0 & \frac{1 - 2\nu_{s}}{1 - \nu_{s}} \end{bmatrix}$$

$$(5.10)$$

For the computation of the acoustic field of the forced-vibrating plate we use the Rayleigh integral equation, a well established method for calculating the acoustic radiation of flat structures embedded in an infinite rigid baffle [35, 113, 115, 128–131]. The Rayleigh integral equation represents a special case of the boundary integral equation, usually discretized using the boundary element method, in which the normal derivative of the Green's function is zero due to the presence of the infinite baffle [35]. This integral equation exists in both frequency and time domain form and can be formulated in terms of the acoustic pressure p or the acoustic potential ϕ . The advantage of using the Rayleigh integral equation is its efficiency in terms of computational time. Moreover, it does not require any memory as it does not rely on the resolution of a system of equations, but rather it consists only the evaluation of an integral:

$$p(\varsigma,t) = \int_{\Gamma} \frac{\rho_f}{2\pi r(\mathbf{x}_p,\varsigma)} a_3 \left(\mathbf{x}_p, t - \frac{r}{c_f}\right) dA$$
 (5.11)

In eq. (5.11), a_3 is the normal acceleration r is the distance separating the acoustic field point ς from the source point \mathbf{x}_p , and r/c_f is the time needed by the acoustic wave to propagate from source point to the acoustic field point.

5.2.2 Variational Formulation

The weak formulation of the contact-impact elasto-dynamics equations is given in eqs. (5.1) to (5.3). In what follows we drop the subscript i, however it should be understood that the weak formulation consists of both the plate and sphere contributions such that $\Omega = \Omega_p \cup \Omega_s$ and the external force term is the contact traction acting on $\Gamma_c = \Gamma_{c_p} = \Gamma_{c_p}$.

$$\int_{\Omega} \boldsymbol{\sigma} : \boldsymbol{\epsilon} \left(\delta \mathbf{u} \right) d\Omega + \rho \int_{\Omega} \mathbf{a} \cdot \delta \mathbf{u} d\Omega = \underbrace{\int_{\Gamma_c} t_N \left(\delta \mathbf{u}_p - \delta \mathbf{u}_s \right) \cdot \mathbf{n} d\Gamma}_{\text{contact force}}$$
(5.12)

where $\mathbf{n} = \mathbf{n}_p = -\mathbf{n}_s$.

To simplify the contact term in eq. (5.12), we adopt the convention of Zhong [4], where the contact tractions are replaced by a set of discrete nodal forces f_c which are considered as the primary unknowns. When these nodal forces are known, the contact tractions may be deduced as follows

$$\int_{\Gamma_c} t_N \left(\delta \bar{\mathbf{u}}_p - \delta \mathbf{u}_s \right) \cdot \bar{\mathbf{n}} \, d\Gamma = \sum_{k=1}^L \left[f_c \left(\delta \bar{\mathbf{u}}_p - \delta \mathbf{u}_s \right) \cdot \bar{\mathbf{n}} \right]_k$$
 (5.13)

The notation $[\bullet]_k$ in eq. (5.13) denotes the quantity $[\bullet]$ evaluated for each slave node k and L is the number of active slave nodes obtained through the local search algorithm. The penalty method is used to model these contact nodal forces, that is, $f_c \approx \varepsilon_N g_N$.

5.3 Discretization using Bézier Elements

In a similar manner to the contact problems in the previous chapter, the system is discretized with the Bézier-based IGA approach (with the Bézier inverse matrix introduced to allow for direct computation of physical quantities). If we redefine the element shape functions matrix \mathbf{Q} (defined in section 3.6.1 eq. (3.77)) at each node, as:

$$\mathbf{Q} = \begin{bmatrix} \phi(\xi)\mathbf{B}_{\text{bez}}^{-1} & \mathbf{0} & \mathbf{0} \\ \mathbf{0} & \phi(\xi)\mathbf{B}_{\text{bez}}^{-1} & \mathbf{0} \\ \mathbf{0} & \mathbf{0} & \phi(\xi)\mathbf{B}_{\text{bez}}^{-1} \end{bmatrix}$$
(5.14)

where $\phi(\xi)$ are the Bernstein basis, ξ the parametric coordinates, and $\mathbf{B}_{\text{bez}}^{-1}$ is the inverse Bézier matrix, and $\mathbf{0}$ is a row vector. It follows then that the discrete form of eq. (5.12) writes as:

$$KU + M\ddot{U} = F \tag{5.15}$$

where **K** is the global stiffness matrix, **M** the mass matrix, **U** the nodal vector containing physical displacements, $\ddot{\mathbf{U}}$ the corresponding nodal acceleration, and **F** is the force vector containing the externally applied loads including contact forces. The elemental stiffness matrix \mathbf{k}^e and mass matrix \mathbf{m}^e , for both the plate and the sphere, write as:

• the plate, $\boldsymbol{\xi} = \{\xi, \eta\}$

$$\mathbf{k}^{e} = \frac{h^{3}}{12} \int_{A_{e}} \mathbf{B}_{p}^{T} D_{1} \mathbf{B}_{p} \, dA + h \int_{A_{e}} \mathbf{S}_{p}^{T} D_{2} \mathbf{S}_{p} \, dA$$

$$\mathbf{m}^{e} = \rho_{p} \int_{A_{e}} \mathbf{Q}^{T} D \mathbf{Q} \, dA$$
(5.16)

 D_1 and D_2 are given in eq. (5.8), and

$$\mathbf{B} = \begin{bmatrix} \mathbf{0} & Q_{j,1} & \mathbf{0} \\ \mathbf{0} & \mathbf{0} & Q_{j,2} \\ \mathbf{0} & Q_{j,2} & Q_{j,1} \end{bmatrix}, \quad \mathbf{S} = \begin{bmatrix} Q_{j,1} & \mathbf{0} & Q_j \\ Q_{j,2} & Q_j & \mathbf{0} \end{bmatrix}, \quad D = \begin{bmatrix} h & 0 & 0 \\ 0 & \frac{h^3}{12} & 0 \\ 0 & 0 & \frac{h^3}{12} \end{bmatrix}$$
(5.17)

where $Q_j = \phi_j(\xi) \mathbf{B}_{\text{bez}}^{-1}, \ j = 1, \dots, n_{cpts}$

• the sphere, $\boldsymbol{\xi} = \{\xi, \eta, \zeta\}$

$$\mathbf{k}^{e} = \int_{\Omega_{s}^{e}} \mathbf{B}_{s}^{T} \mathbf{D}_{s} \mathbf{B}_{s} \, d\Omega$$

$$\mathbf{m}^{e} = \rho_{s} \int_{\Omega_{s}^{e}} \mathbf{Q}_{s}^{T} \mathbf{Q}_{s} \, d\Omega$$
(5.18)

where \mathbf{D}_s the elasticity tensor given in eq. (5.10) and

$$\mathbf{B}_{s} = \begin{bmatrix} \mathbf{Q}_{j,1} & \mathbf{0} & \mathbf{0} \\ \mathbf{0} & \mathbf{Q}_{j,2} & \mathbf{0} \\ \mathbf{0} & \mathbf{0} & \mathbf{Q}_{j,3} \\ \mathbf{Q}_{j,2} & \mathbf{Q}_{j,1} & \mathbf{0} \\ \mathbf{Q}_{j,3} & \mathbf{0} & \mathbf{Q}_{j,1} \\ \mathbf{0} & \mathbf{Q}_{j,3} & \mathbf{Q}_{j,2} \end{bmatrix}, \quad \mathbf{Q}_{s} = Q_{j}I_{6\times6}$$

$$(5.19)$$

The discrete contact force writes as

$$f_c \left(\delta \bar{\mathbf{u}}_p - \delta \mathbf{u}_s \right) \cdot \bar{\mathbf{n}} = \delta \mathbf{u}_c^T (\mathbf{Q}_c^T \mathbf{n} f_c)$$
 (5.20)

with

$$\mathbf{Q}_{c} = \begin{bmatrix} -I_{(3\times3)} & \bar{\mathbf{Q}}_{s1} & \bar{\mathbf{Q}}_{s2} & \bar{\mathbf{Q}}_{s3} \end{bmatrix}, \quad \bar{\mathbf{Q}}_{sj} = \begin{bmatrix} \phi_{j}(\bar{\boldsymbol{\xi}})\mathbf{B}_{\text{bez}}^{-1} & \mathbf{0} & \mathbf{0} \\ \mathbf{0} & \phi_{j}(\bar{\boldsymbol{\xi}})\mathbf{B}_{\text{bez}}^{-1} & \mathbf{0} \\ \mathbf{0} & \mathbf{0} & \phi_{j}(\bar{\boldsymbol{\xi}})\mathbf{B}_{\text{bez}}^{-1} \end{bmatrix} \\
\mathbf{u}_{c} = \begin{bmatrix} u_{1}^{s}, \ u_{2}^{s}, \ u_{3}^{s}, \ u_{1}^{p1}, \ u_{1}^{p2}, \cdots, \ u_{1}^{pl}, \ u_{2}^{p1}, \ u_{2}^{p2}, \cdots, \ u_{2}^{pl}, \ u_{3}^{p1}, \ u_{2}^{p2}, \cdots, \ u_{3}^{pl} \end{bmatrix}^{T}$$
(5.21)

and $I_{(k \times k)}$ is an identity matrix of size $k \times k$.

The Rayleigh integral equation may be discretized in the same way, as is done in Alia [35], with the discrete acceleration (acceleration history of the plate at time t) writing as:

$$\mathbf{a}_3\left(\mathbf{x}_p, t\right) = \mathbf{Q} \ \mathbf{a}_3^{\text{nodal}} \tag{5.22}$$

Equation (5.11) is then solved numerically as a summation of contributions of each element, however now with the retarded time, using a full Gauss quadrature rule. This acceleration at retarded time $t - r/c_f$ is obtained from a linear interpolation of the acceleration history of the plate [113].

5.4 Numerical Solution

Here we replicate the problem studied in Akay and Latcha [118] with a steel plate of center O, which is impacted by a small acrylic ball. The mechanical properties and input parameters of both the plate and the sphere, as well the radiating medium, are summarized in table 5.1.

Plate		Sphere	
Radius, R_p [m]	0.25	Radius, R_s [mm]	9.53
Thickness, h [mm]	1.59	Initial velocity, v_0 [m/s]	0.22
Young's modulus, E_p [GPa]	210	Young's modulus, E_s [GPa]	3.1
Poisson's ratio, ν_p	0.3	Poisson's ratio, ν_s	0.37
Density, $\rho_p [\mathrm{kg/m^3}]$	7850	Density, ρ_s [kg/m ³]	1190
Fluid medium (air)			
Density, ρ_f [kg/m ³]		1.021	
Sound velocity, c_f [m/s]		343	

Table 5.1 – Input parameters and mechanical characteristics of the impacted plate and the impactor sphere as well as the radiating medium.

The plate is modeled with five patches whose central is a square and each patch containing the same number of elements. The solid sphere is also modeled as multiple patches: seven patches are used, the central patch is a cube. Recall that with the Bézier-based approach used in this work, the entry point is a BSplines representation of the geometry patches (NURBS with unity weights) from which the Bézier elements are derived. BSplines are not exact for conic sections, hence the reason we have introduced the interpolation in section 2.2.3 eq. (2.16) and demonstrated in fig. 2.11. For this reason, when the BSplines (patch level interpolation) are used for the sphere or the plate result in a varying discrete radius for different angles. The implication is then that bending waves will not arrive simultaneously at the center of the plate after their reflection at the edge. To remedy this problem, a second interpolation (Bézier) similar to the patch level interpolation is now performed at element level.

Cubic Bézier elements are used to discretize both the plate and sphere, with : 320 2D elements with 2929 control points mesh for the plate, and 56 3D elements with 1651 control points mesh for the sphere. The acoustic analysis is also conducted using the cubic discretization. The mesh generated for the numerical model is shown in fig. 5.2.

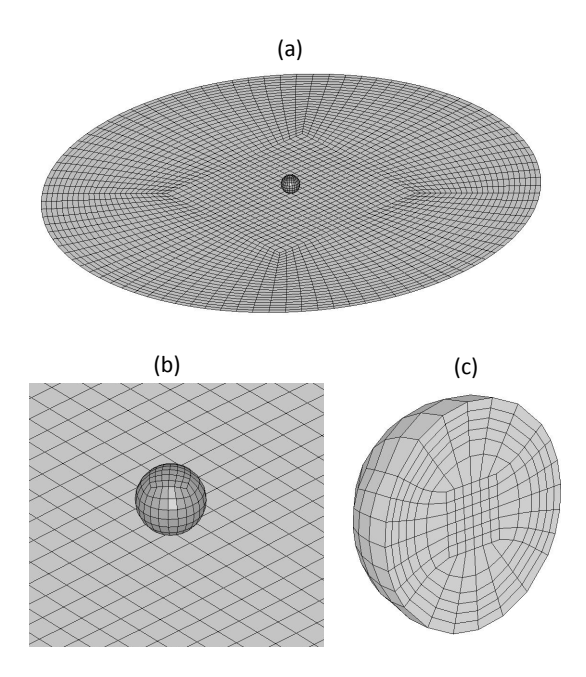


Figure 5.2 – (a) Mesh of the plate and sphere due to Bézier extraction, (b) sphere zoom and (c) mesh of the half of the sphere.

As both the sphere and plate are elastic, the mass matrix and the stiffness matrix are computed once at the beginning, and stored for use. For the global time-stepping algorithm, the conditionally stable central differences scheme is used for time integration. The time step size is set as $\Delta t = 0.0154~\mu s$. This value is derived using the criteria in Zhong [4], where for central differences scheme the critical time step size derives from $\Delta t_{cr} = \min \left[\Delta t_p; \ \Delta t_s; \ \Delta t_i\right]_{i=1, \dots, \ n_{dof}}$, with $\Delta t_p = 2/\omega_{p_{max}}, \ \Delta t_s = 2/\omega_{s_{max}}$, and $\Delta t_i = 2\sqrt{m_{ii}}/\omega_i$ the critical time step of the i^{th} DOF involved in contact. The penalty parameter for the contact tractions is chosen as $\varepsilon_N = (1/E_p + 1/E_s)^{-1}$. It is important to note that the Reissner-Mindlin plate theory is written for the reference plane, whereas contact interaction takes place on the surface of the plate. This then necessitates an offset of h/2 be accounted for when computing the penetration. Otherwise, contact will take place on the reference surface which is incorrect.

The solution procedure for the contact-impact vibro acoustics problem is designed in such a way, that for each time step $t + \Delta t$, first we compute the dynamic response (the solution to the contact-impact) in terms of the displacement, velocity and acceleration calculation. Once the current time step dynamic solution is obtained, acceleration is used to compute the acoustic pressure. However before we can compute the acoustic pressure, the plate geometry is updated (the displacement of the plate u_1 and u_2 is obtained, it is then added to the nodal positions

x and y, respectively). Moreover, we also have to introduce the plate thickness h/2 again, to truncate the spatial position of the nodes to the appropriate radiating upper surface of the plate. When the effective geometry has been recovered, we can then proceed to the Rayleigh integral equation in eq. (5.11) to compute the acoustic radiation at any point. The dynamic response and the acoustic response obtained are shown in the next sections.

5.4.1 The Dynamic Response

Figure 5.3 shows the obtained transverse displacement of the plate as a function of the radial distance r, at different times after impact.

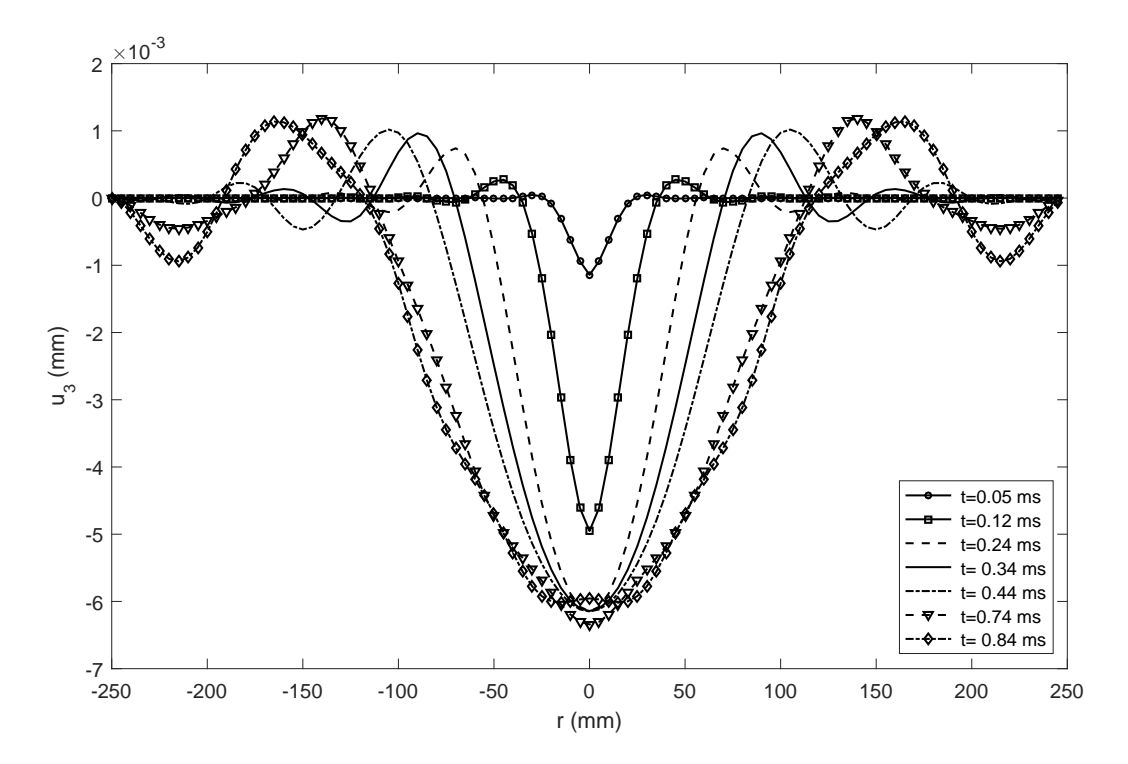


Figure 5.3 – Variation of the transverse displacement with respect to the radial distance for different times after impact.

From fig. 5.3, we observe that the transverse displacement is composed of: (1) a main deformation lobe (centered about the axis of the plate) which corresponds to the initial deformation due to contact, and (2) wavelets symmetric about the z-axis, called ripples by Oulmane and Ross [10] which correspond to the bending waves propagating through the plate following impact. The amplitude of the main deformation lobe and the ripples increase with time, with the main lobe reaching its maximum value. This maximum value is maintained as long as the bending waves are not reflected at the edges of the plate. When the reflection takes place, the reflected bending waves propagate until they reach the center of the plate and thus modifying the amplitude of the main lode due to interference.

The dynamic response of a forced vibrating plate may be seen as not only as forced vibrations

which gives rise to rapid deformation but also as free vibrations due to propagation of bending waves [118]. Taking a closer look at the time variation of the transverse displacement and velocity at different locations of the plate, particularly at the center of the plate, we can distinguish clearly the previously mentioned different deformation phases of the plate. From fig. 5.4a, at first we see that during contact the transverse displacement at the center of the plate increases progressively in the negative direction - this is the initial deformation phase. This first phase is followed by a constant displacement phase (sustained maximum main lobe displacement so long as bending waves are not reflected). Following the second phase, oscillations start to appear which indicates the arrival of the reflected bending waves at the center of the plate. Evolution of the velocity with time at the same location (fig. 5.4b), center of the plate, shows a first peak, which is followed by a zero velocity phase before the appearance of the oscillations.

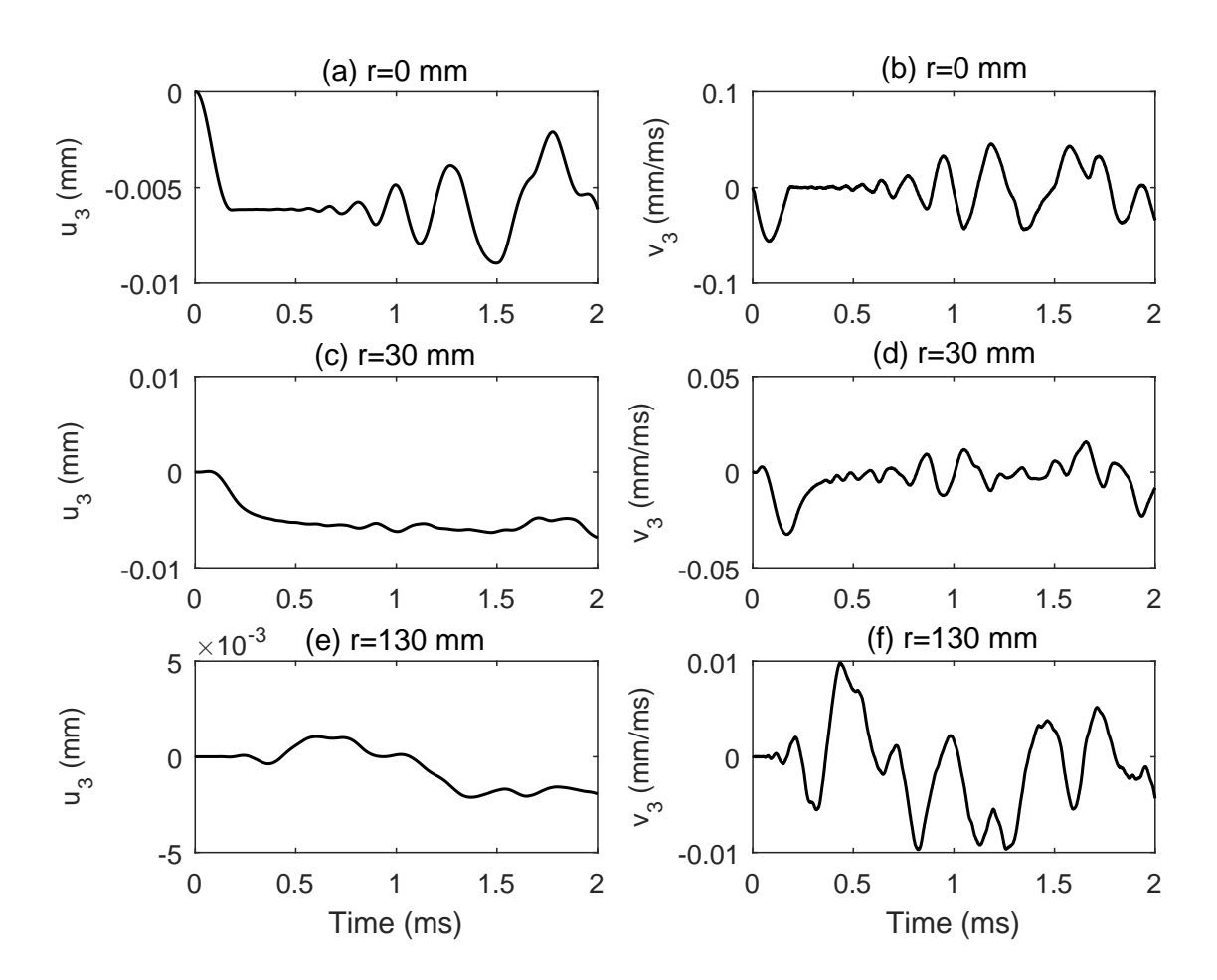


Figure 5.4 – Variation of the transverse displacement (left) and velocity (right) for the impact point (a,b), and two points located at 30 mm (c-d), and 130 mm (e-f) from the impact point.

Moreover, we notice that, in both the transverse displacement and velocity, as the observation points moves away from the axis of impact (z-axis) the intermediate zone (second phase) becomes smaller and smaller until it completely disappears (fig. 5.4c and fig. 5.4d). This is due to the overlapping of the bending waves and initial deformation wave. Outside the initial deformation

zone (the main deformation lobe extent in fig. 5.3), or rather at the regions near the edge of the plate, only the incident and reflected bending waves reach these points. This is evident in the lack of distinction between the three phases in fig. 5.4e and fig. 5.4f.

5.4.2 The Acoustic Response

Figure 5.5 shows the radiated acoustic pressure variation, with time, at different observation points located at a distance z = 60 mm from the plate, and polar angles $\psi = \{0^{\circ}, 25^{\circ}, 50^{\circ}, 75^{\circ}\}$.

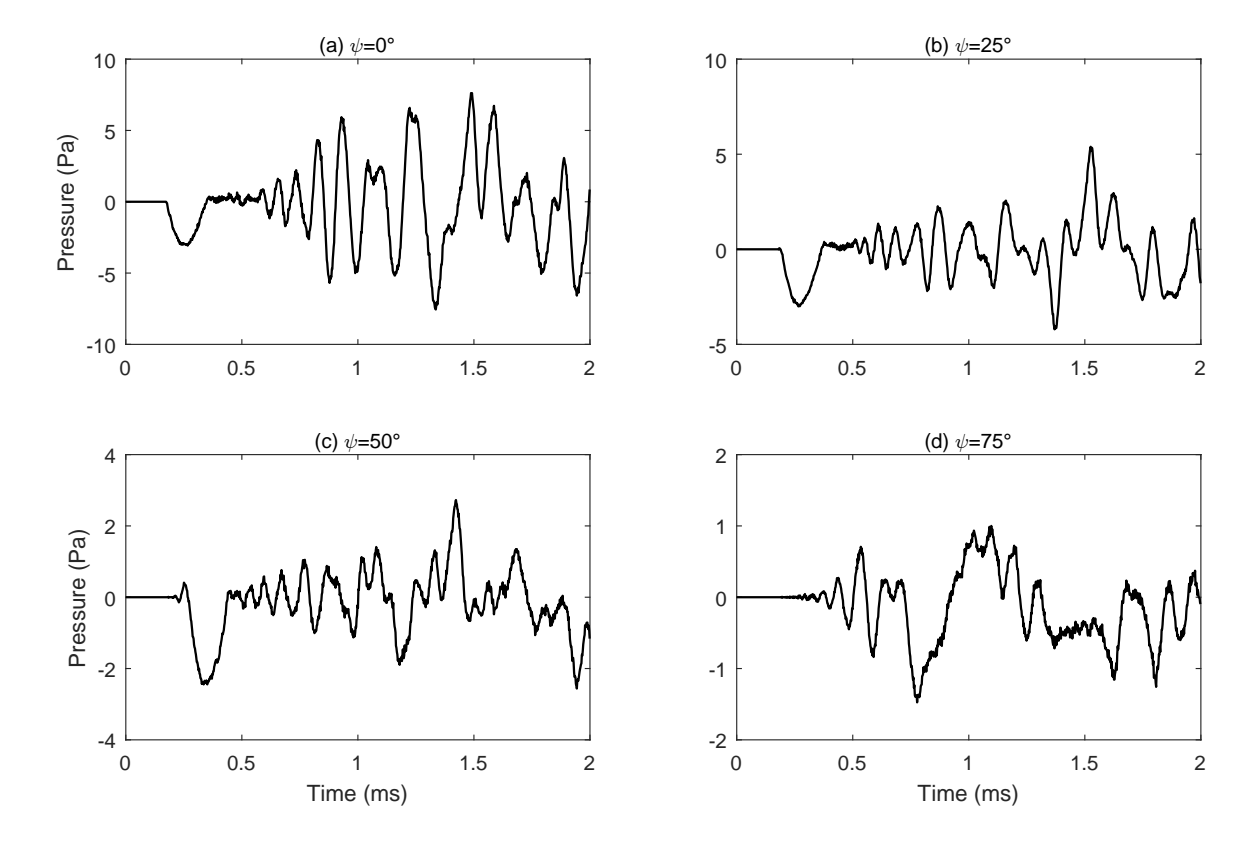


Figure 5.5 – Acoustic pressure at field points located at z = 60 mm and polar angles $\psi = \{0^{\circ}, 25^{\circ}, 50^{\circ}, 75^{\circ}\}.$

In literature, a similarity between the time variation of the velocity of an impacted plate and the radiated acoustic pressure has been found in both analytical and experimental studies [11, 118, 132]. At the observation point located on the z-axis (fig. 5.5a), again, we can discern three different phases which correlate with the dynamic response in fig. 5.3. The first phase is the so called *initial transient wave* which results directly from the contribution of the initial deformation following the contact. A second phase characterized by an almost zero acoustic pressure follows after - Troccaz et al. [121] call this the silent phase. The silent phase corresponds to the propagation of bending waves, of higher frequency than the critical frequency, towards

the edges of the plate. These waves have an oblique wavefront and therefore do not reach the observation point located on the z-axis. However, once these waves have been reflected, their oblique wavefront eventually reaches the on-axis observation point which constitutes the third phase known as the ringing noise. Off-axis (acoustic pressure variation in fig. 5.5b-d), it becomes increasingly difficult to distinguish between the three phases as the observation point moves further away from the axis of symmetry; these points are reached first by the acoustic wave due to bending waves before and after reflection at the edges of the plate.

The trends in our findings, in terms of the dynamic response and the acoustic pressure variation, correlate very well with the findings in literature, particularly in the works of Akay and Latcha [118], Ross and Ostiguy [132], and Oulmane and Ross [10].

5.4.3 Sensitivity Analysis

In this section we discuss and analyses the numerical implementation aspects for the resolution of the impact event and the subsequent generated acoustic wave. Bézier elements are used for the discretization.

5.4.3.1 Discretization Order

To evaluate the accuracy of the model, with respect to the order of the basis used for the discretization, a study on the error committed on the computation of the first 40 natural frequencies of the plates was conducted. The error is quantified against the analytical values in Blanch [133] and Leissa [134], and the estimated error is shown in fig. 5.6a. It can be seen that the cubic approximation is more accurate than the quadratic approximation. The relative error on the cubic approximation decreases at a faster rate, compared to the quadratic approximation, with increasing number of points on the edge nd of each patch of the plate. The error seems to stabilize from $nd \approx 25$, and then plateaus beyond this value.

In order to verify the behavior of the estimated error at nd = 25 and beyond, particularly for the cubic discretization, we recompute the acoustic radiation pressure field. The plate is discretized first with nd = 25 and then with nd = 28 which corresponds to 8 and 9 cubic elements per edge of the patch, respectively. For simplicity, the impact excitation is introduced as an analytical contact force proposed by Ross and Ostiguy [132], that is:

$$F(t) \approx F\left\{\frac{1.1}{1 + \Lambda + 2\Lambda^2} \sin{(0.97T)^{1.5}} \exp{\left[-(0.4T)^4\right]} + \left(\frac{1 + 2/\Lambda}{1 + \Lambda}\right) \left(\frac{T}{T + 1/\Lambda}\right)^{1.5} \exp{\left(-\frac{T}{\Lambda}\right)}\right\}$$
(5.23)

where $T = \pi t/\tau$, with τ the impact contact duration, and F is Hertzian contact force which depends on the mass and initial velocity of the sphere, the geometry, and elastic properties of both the plate and sphere (detailed computation of the magnitude F can be found in Akay and

Latcha [118]). Parameter Λ is related to the flexibility of the plate and the energy of the impact, and is defined as:

$$\Lambda = 1.15 \left(\frac{R_s}{h}\right)^2 \left(\frac{v_0}{C_L}\right)^{0.2} \left(\frac{\rho_s}{\rho_p}\right)^{0.6} \left(\frac{E'_s}{E'_s + E'_p}\right), \quad E' = \frac{E}{1 + \nu^2}$$
 (5.24)

with C_L the speed of longitudinal waves with the plate (5060 m/s for steel). The resulting pressure field is shown in fig. 5.6b-c at two observation points at distance z = 50 mm, from the plate, and polar angle $\psi = 0^{\circ}$ (on-axis) and $\psi = 75^{\circ}$ (off-axis). We can see that the obtained pressure field variation with time at these observation points, for both nd = 25 and nd = 28, is similar (effectively superimposed on top of each other). This means that refining the match beyond 8 cubic elements across the edge of the patch does not enrich the solution nor will it improve the error any further.

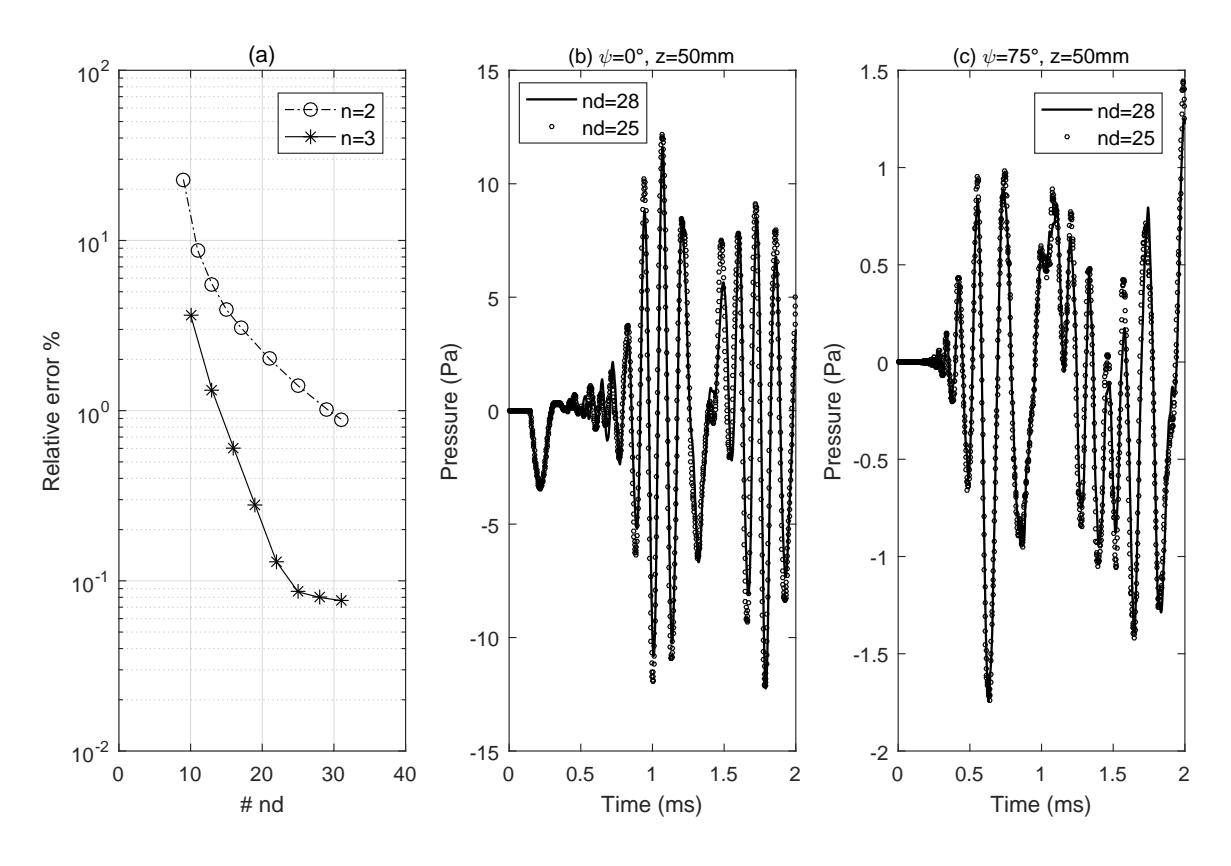


Figure 5.6 – Effect of the number of nodes nd per patch edge of the plate on : (a) the relative error committed on the 46 first natural frequencies of the plate for quadratic (n = 2) and cubic (n = 3) elements, the acoustic pressure (b) on-axis and (c) off-axis.

5.4.3.2 Time Integration Scheme

In section 5.4.1, the dynamic analysis was conducted using the explicit, conditionally stable, central differences method. According to literature central differences scheme are prone to

spurious oscillations when used for numerical simulation structural dynamics problems and wave propagation problems [135, 136]. To evaluate the choice of explicit time integration scheme we adopt the explicit schemes proposed by Noh and Bathe [135] and Kim and Lee [137], which appear more suitable for wave propagation problems. The two explicit schemes, abbreviated NB for Noh and Bathe [135] and KL for Kim and Lee [137], are tested against the central differences (CD) scheme. For both NB and KL schemes, the computation of the unknown dynamic fields (displacements, velocities, and acceleration only for NB; KL scheme does not require computation of the acceleration) during the time increment Δt is performed in two steps. In the NB scheme, the effective displacement and effective loading at $t + q\Delta t$ and $t + \Delta t$, with 0 < q < 1, is calculated via a linear interpolation [135]. On the other hand the KL scheme is based on an unconventional interpolation technique using three parameters τ_1 , τ_2 and β in which the displacement and velocity values are given at τ_1 and τ_2 and then recalculated at $t + \beta \Delta t$ and $t + \Delta t$ [137].

Again the five patch plate model, with nd=25 (cubic elements) is used. The sphere has seven patches with each patch edge divided into two cubic elements (small dimension sphere with respect to the plate size). The time step used is that of central differences method $\Delta t = 0.0154 \ \mu s$.

As mentioned in the KL scheme the calculation of the acceleration is not required. Even though the exclusion of the acceleration term from the computation of the displacement vector allows for the minimization of the high frequency modes [137], acceleration still remains an important physical quantity for the computation of the acoustic pressure field in eq. (5.11) - we need the acceleration field for the computation of the acoustic response. In this case we can then derive the acceleration from the obtained velocities through the use of a finite difference scheme. We set parameter values for both NB and KL to those used by the respective authors in their work: q = 0.54 for NB, and $\tau_1 = 0.2684$, $\tau_2 = 0.5$, $\beta = 0.4219$ for KL. Figure 5.7 shows the comparison of the displacement and velocity at the center O of the plate (impact point, r = 0) and at an off-axis points (r = 30 mm) for the three schemes (CD,NB, and KL).

The transverse displacement and velocity variation with time at the two points r=0 and r=30 mm in fig. 5.7, the three schemes are the same. In terms of computational time, the NB scheme is more efficient compared to KL which requires additional operation to access the acceleration. However both methods appear more computationally heavy compared to the CD scheme as the CD scheme does not require any interpolation, whereas the NB and KL schemes require one and two interpolations, respectively. These difference in computational time is further compounded by the calculation of the effective loading vector at the next time step, which for the present contact formulation is unknown thus rendering the interpolation impossible. Indeed, as the contact force is the only external force taken into account, each interpolation of the force is replaced by the evaluation of the gap function at the requested intermediate instant; the contact force follows then from $\varepsilon_N g_N$. Hence the heavier computational time, particularly for the KL scheme which is ~ 3.2 times that of CD, whereas the NB schemes is ~ 1.3 times the computational time of the CD scheme.

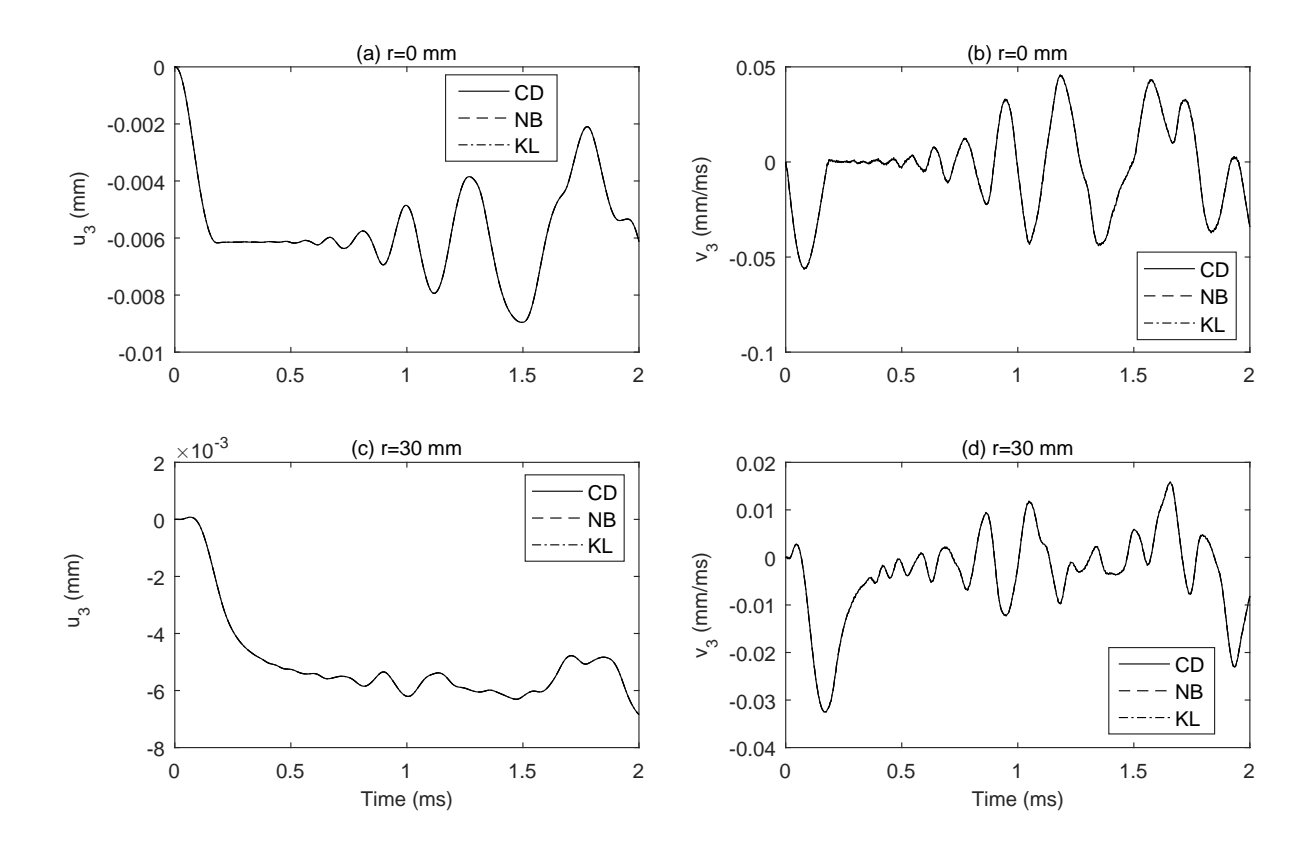


Figure 5.7 – Variation of the transverse displacement (left) and velocity (right) for the impact point (a,b) and at 30 mm from the impact point (c-d) calculated by central difference scheme (CD), Noh and Bathe (NB), and Kim and Lee (KL) schemes. (CD), (NB) and (KL) curves are the same.

5.4.3.3 Time Step Size

Thus far all the explicit simulations were conducted using Δt derived using the central difference method critical time step criteria in Zhong [4]. Let this be $\Delta t_1 = \Delta t = 0.0154~\mu s$. However, if we use a time step corresponding to the most finely meshed part, here the sphere, the time step size is then $\Delta t_2 = 0.1243~\mu s$. The results obtained using Δt_2 , for the NB and KL scheme, are shown in fig. 5.8.

From fig. 5.8, we see that for both time steps, the obtained contact force as well as the acoustic pressure field are similar for both the NB and KL scheme. With Δt_2 we obtain the same results however in less computational time. The computational time using the NB and KL scheme was found to be ~ 0.17 and ~ 0.46 times that of the original CD scheme (Δt_1), respectively. Essentially, the use of the explicit NB and KL schemes allows for the use of a larger time step than CD schemes while achieving the same quality of results. This is a great advantage in terms of computational efficiency.

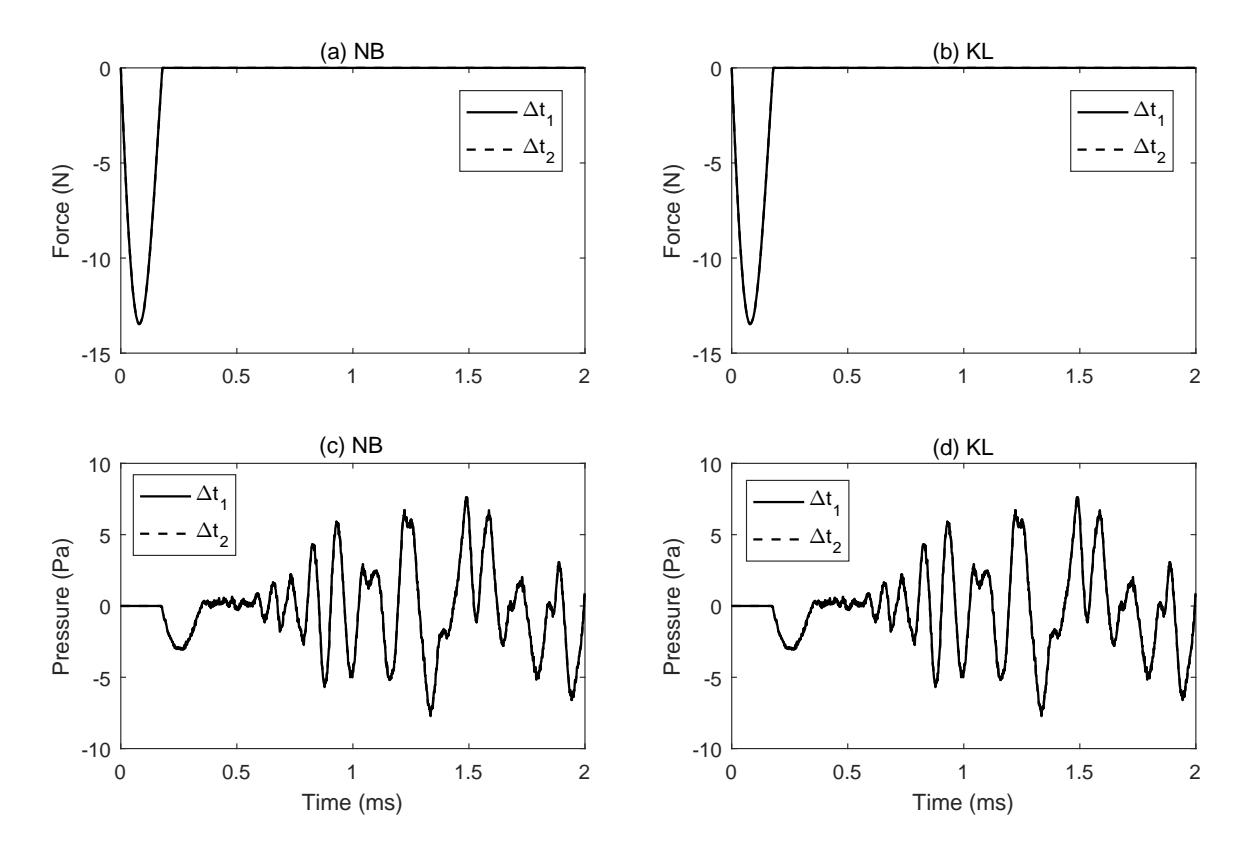


Figure 5.8 – Effect of the time step on the contact force between plate and sphere (a-b) and the acoustic pressure (c-d) when Noh and Bathe (NB) (left) and Kim and Lee (KL) (right) schemes are used for two time steps Δt_1 and Δt_2 .

5.5 Summary

In this chapter we have used the Bézier-based IGA numerical scheme, developed in chapter 2, to calculate dynamics and the acoustic radiation of forced-vibrating plates due to impact in time domain. Both the plate and sphere are modeled explicitly. The use of IGA allows for a relatively coarse mesh as already seen in the numerical simulation of contact problems in the previous chapter. So even though the mesh used for the analysis was relatively coarse, the mesh quality was still sufficient enough the adequately capture both the dynamic and acoustic response. The results obtained were in line with the observation from literature [118, 132, 10], in that, the acoustic radiation on the axis of symmetry (center of the plate), is characterized by three consecutive phases: the initial transient wave, the silent phase and the ringing phase. These characteristics correlated with the vibratory response of the plate which constitutes the initial deformation (localized about the plate center), followed by the propagation of bending waves and then their reflection at the edges of the plate. However, as the observation point moves away from the axis of symmetry, the three phases were no longer distinguishable. This is due to the dispersive character of bending waves.

In the initial complete model, time integration is performed using an explicit central differences

scheme, which can lead to spurious oscillations particularly for wave propagation problems in linear FEM. We then adopted the Noh and Bathe [135] (NB) and Kim and Lee [137] (KL) explicit schemes, which aim to address the drawbacks of the central difference method. We found all three schemes give the same results, both the dynamic and acoustic response, however the computational effort required varies for each of the schemes. Though, it is important to note that here, the impact simulated of a low energy impact. So it could interesting to observe the behavior of the schemes, but now with high energy impact (high velocities) and the effect of the mechanical material properties of both the plate and sphere.

Even though the complete model developed allowed us to capture the essential vibratory and acoustic characteristics of the plate, it still has some limitations. For instance, the model does not account for large deformations (linear impact assumptions) of the plate which are observed experimentally at the contact for certain initial velocities of the sphere [120] nor does it account for plasticity [121, 138] and material damping [124, 139]. Addressing these limitations by taking into consideration the inelastic effects of impact should improve the robustness of this model and therefore the quality of the results. Another limitation arises from the use of the Rayleigh integral equation, which is suitable only under the assumption that the plate is embedded in a rigid baffle which is not the always case. The idea of using IGA for this impact-acoustic problem is that it can allow us to study more complex geometries, which can only be possible for a less limiting method rather than the Rayleigh integral equation used in this work.

Acoustic Radiation of Forced-Vibrating Plates

6.1 Introduction

In this chapter we study the acoustic radiation of a forced vibrating circular elastic plate in chapter 5, however now with implicit dynamics. In the fist part (section 5.4) we compute the vibratory and acoustic response of the plate impacted at its center (localized excitation), with the contact force estimated using the analytical expression proposed by Ross and Ostiguy [132]. The dynamic response of the plate, computed using the implicit Newmark scheme (section 6.2.1), is then used to calculate and characterize the acoustic response of the impacted plate using the Rayleigh integral equation (section 6.2.2). This forms the reference case which is later used to correlate the complete model in section 6.2.3.

The subject of plate dynamics, from the FEM point of view, has been well researched and studied by many authors: from modal analysis [108, 109] to impact problems [10] to moving forces [110–112]. When it comes to predicting the noise generation from forced-vibrating plates, the cases studied were mainly limited to the acoustic radiation due to impact at the center of the plate [10, 118], and focused on the initial transient wave [132]. In fact, these studies have either been experimental [119, 120, 132, 140] or analytical [118, 121, 125, 132]. Certainly noise generation due to impact is very interesting because of its characteristics, i.e. the large peak and short duration. However, impact is not the only mechanism that can generate noise within the plate. Moving excitations, such as a moving force on a plate, have aroused much interest in dynamics [110–112], however very little has been done from the acoustic point of view [125]. Even with the progress made in FEM in different fields of mechanics, FEM has seldom been used in this type of application [10]. Hence our main focus in the second part of this chapter-section 6.3: we extend our study to the numerical simulation of the dynamic (section 6.3.1) and acoustic response (section 6.3.2) of the plate but now subjected to a moving force (moving excitation).

6.2 Application to Impacted Plates

Again, we consider a circular elastic plate of radius R_p , and a thickness h with material properties Young's modulus E_p , Poisson's ratio ν_p and density ρ_p , subjected to a localized excitation as depicted in fig. 5.1. Likewise, the fluid medium surrounding the plate is assumed to be lossless and homogeneous with a sound speed c_f and a density ρ_f smaller than ρ_p . Further, we assume that the propagation medium (air) is so light such that it neither alters the modes of the plates nor shifts its natural frequencies. Moreover, the plate is assumed initially at rest and is embedded in a rigid baffle thus fulfilling the necessary condition for the use of the Rayleigh integral equation. The contact is supposed to be punctual and occurs between a small elastic sphere and the plate at a point with coordinates (x_O, y_O) . The sphere has a radius R_s , Young's modulus E_s , Poisson's ratio ν_s , density ρ_s , and an initial velocity \mathbf{v}_0 . Here the contact force is computed using the expression proposed by Ross and Ostiguy [132] and shown in eqs. (5.23) and (5.24) with its evolution with time t shown in fig. 6.1a. In fig. 6.1b we sown the initial patches used for the representation of the plate geometry.

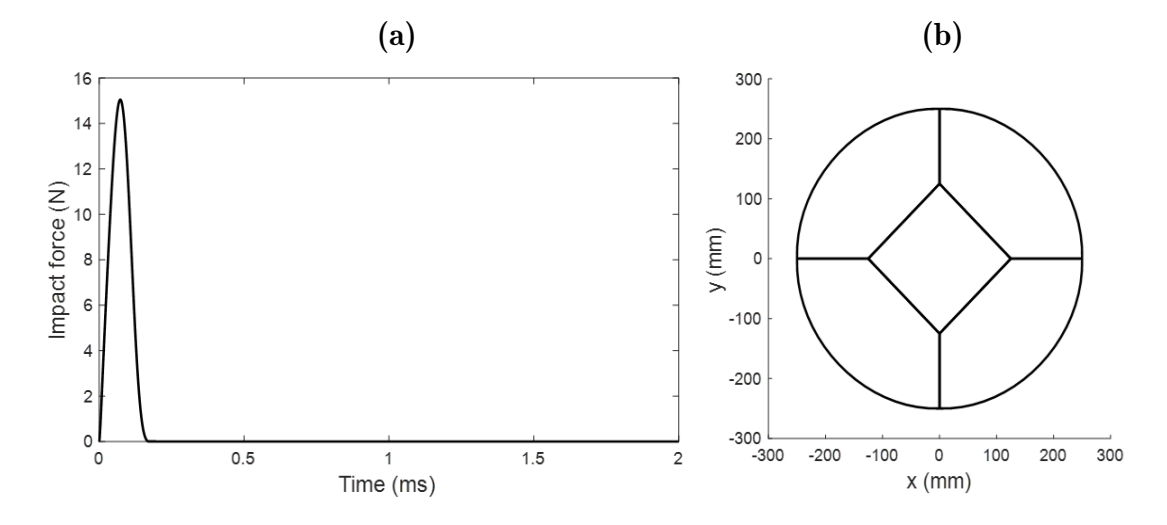


Figure 6.1 – Illustration of the problems considered : (a) the impact force computed using eq. (5.1), (b) multi-patch model of the circular plate geometry.

Since now contact force is modeled using an analytical expression, the contact between the sphere and the plate is no longer of interest. The main interest in this chapter is the plates dynamics, its vibratory response, and the acoustic radiation as a result. Therefore the system is still governed by the elasto-dynamics equations in eqs. (5.1) and (5.2), however now only the plate is considered. Its variational form and its discrete form follow accordingly from eq. (5.12) and eq. (6.1), respectively. However in eq. (5.12) the contact force is replaced by the analytical force computed from eqs. (5.23) and (5.24) prescribed as point load, acting at the center point O.

An unconditionally stable implicit Newmark scheme is used for the time integration of eq. (5.12) and computation of the dynamic response (the displacement history, and corresponding velocity

and acceleration history). Even though the use of implicit methods for structural dynamics problems allow for a larger critical time step size, for wave propagation problems (essentially acoustic radiation), a small time step is required in order to accurately track the high frequency waves in the body [85]. For this reason the time step here is chosen such that it satisfies the conditions stipulated for the conditionally stable explicit central differences scheme in accordance with the criteria given by Zhong [4] - see also section 3.6.6.2 and section 5.4. The mechanical properties and input parameters of both the plate and the sphere, as well the radiating medium, are summarized in table 5.1, now with initial velocity $v_0 = 0.22$ m/s.

The circular plate is modeled using 5 patches whose central one is a square and all patches contain the same number of elements. It is discretized with a mesh composed of 720 quadratic elements with 2929 nodes. For the time integration, a time-step of size $\Delta t = 0.287 \ \mu s$ is used in the simulation.

6.2.1 The Dynamic Response

First, we analyze the dynamic response, in terms of the transverse displacement and velocity, for the on-axis impact problem of the plate. This response is later correlated with the acoustic field radiated. The obtained variation of the transverse displacement of the plate and its velocity, with respect to time, at the impact point O and two points P_1 and P_2 at a distance $R_p/10$ and $R_p/2$ from O respectively, is shown in fig. 6.2. **Note**: calculations were considered for the impacted side of the plate, hence the negative values of the displacement and later the acoustic pressure.

From fig. 6.2a we distinguish the three phases of the dynamic response, which were also observed in the previous chapter section 5.4:(1) during contact, the impact point O moves in the direction of imposed force until it reaches a certain position at the end of the action of the contact force, (2) the impact point O sustains its position for a certain time before (3) it experiences oscillations due to the arrival of the bending waves reflected at the edge of the plate. These phases can also be distinctly observed from the velocity plot in fig. 6.2b: the initial impulse velocity due to the rapid (forced) deformation of the plate at O is followed by a range of zero velocity until the bending waves are reflected back to the impact point O.

Away from the impact point O, specifically at point P_1 , from the displacement variation (fig. 6.2c) we observe (1) a time lag in the response compared to that of the impact point O due to the time required for the waves to reach P_1 , (2) a slight presence of positive transverse displacement initially which then becomes negative, and (3) finally an overlap of phase 2 and 3, in both the transverse displacement and velocity variation in fig. 6.2d. Even more further away at P_2 , we can see only the bending waves are observed (only phase 3 present here) - see fig. 6.2e-f.

For a better visualization of the of the generation and reflection of the bending waves in fig. 6.3 we show the variation of the transverse displacement with the radial distance r of the plate at the different time instants. In the first moments of the impact the transverse displacement

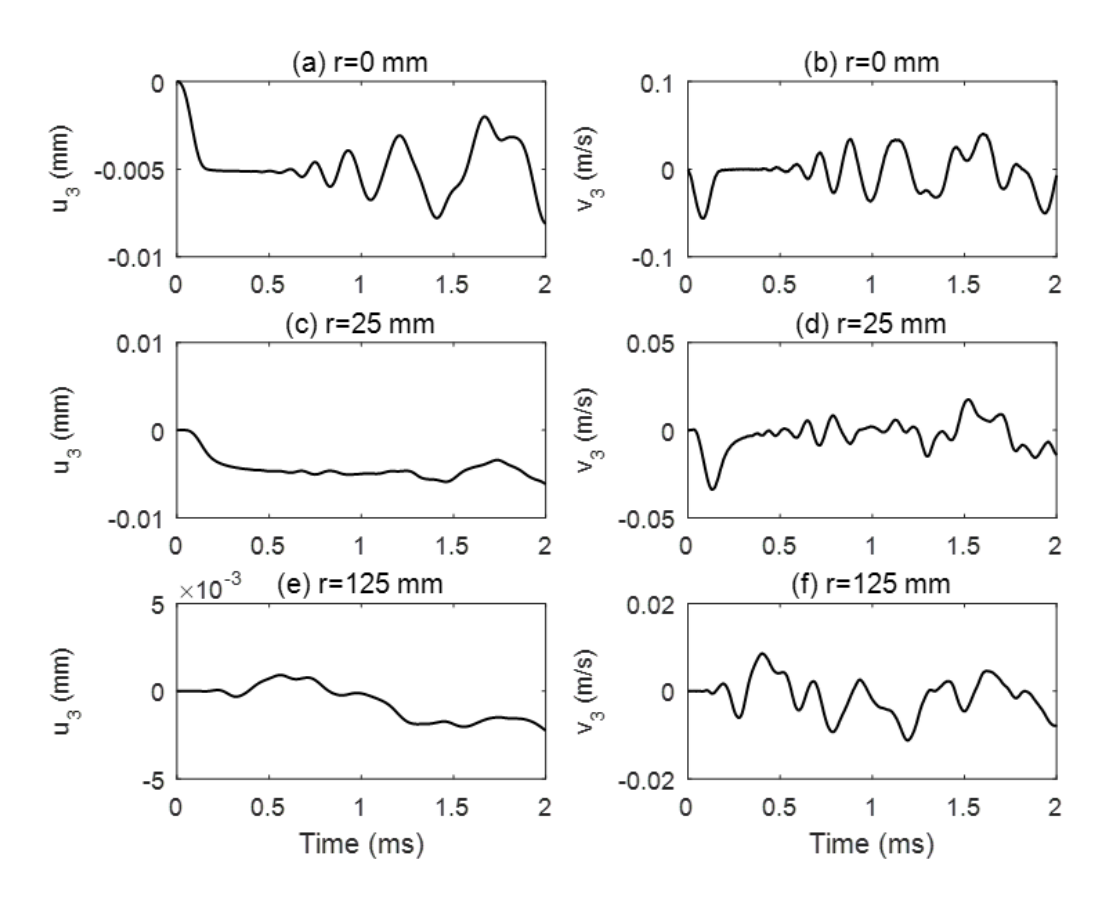


Figure 6.2 – Variation, with respect to time, of the transverse displacement (left) and velocity (right) of three points on plate : O (a-b), P_1 (c-d) and P_2 (e-f).

is characterized by small amplitude main lobes as seen in fig. 6.3a. Even early during impact we can already see the appearance of the ripples which correspond to the propagation of the bending waves. The amplitude and spread of the main lobes of deformation and the ripples increase progressively with time - see fig. 6.3b - this corresponds to phase 1 described above. At the end of contact action, the main lobe of deformation reaches a maximum value which it then maintains until the ripples have reached the edge of the plate (fig. 6.3c), this corresponds to the plateau observed in fig. 6.2a which is phase 2 of the dynamic response. Once the ripples are reflected back from the edge of the plate, they propagate towards the centre (O), modifying the amplitude of the transverse displacement and thus reaching phase 3 (fig. 6.3d).

Furthermore, we can see that the transverse displacement remains symmetric about axis of impact at all time instants. Moreover, the origin of the slight presence of positive displacement observed at P_1 (mentioned above on the analysis of fig. 6.2) becomes apparent. This is because point P_1 is located between the impact point O and the edge of the plate; it is reached by bending waves of dispersive nature (ripples) even before the waves are reflected back from the edge. Indeed after reflection the bending waves will still pass through this point. These results are in line with the findings in the works of [10, 132, 140] and correlate very well with response found using the explicit dynamics in fig. 5.3.

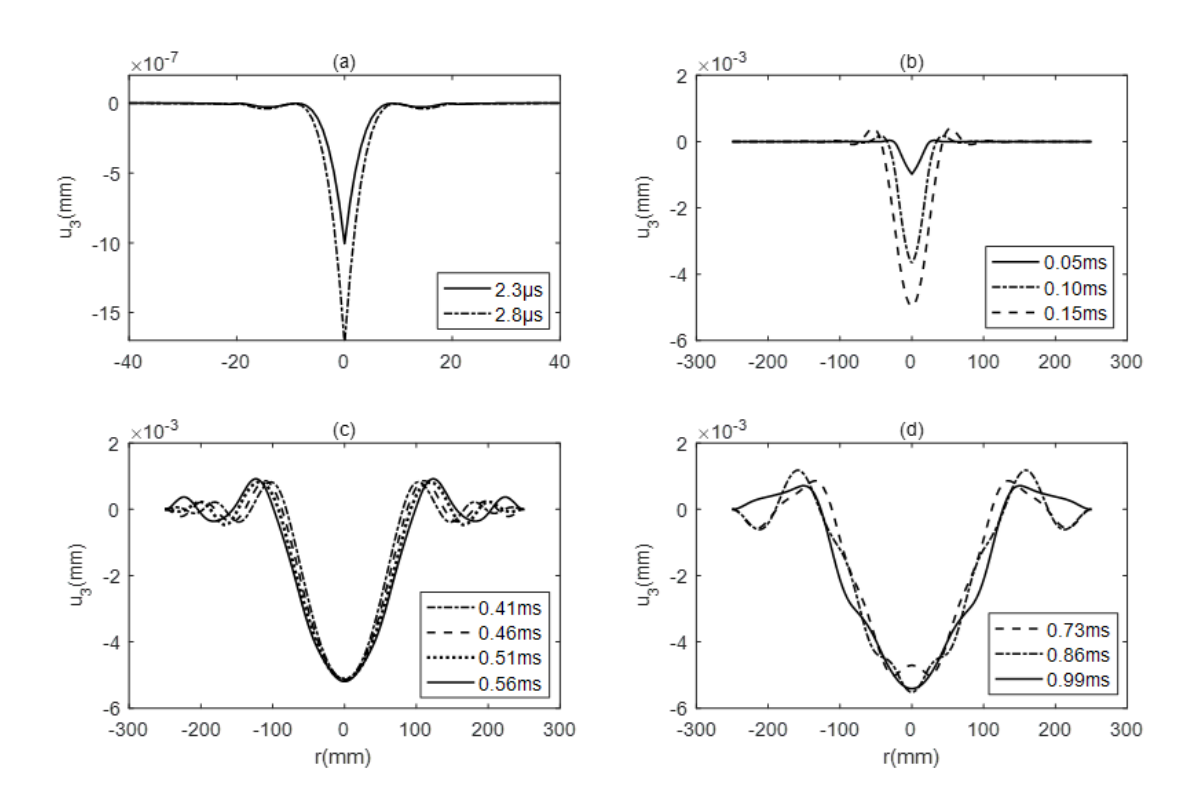


Figure 6.3 – Variation, with respect to the radial distance r, of the transverse displacement of the plate for different instants.

6.2.2 The Acoustic Response

We have already observed that the acoustic response correlates with the dynamic response, in terms of the evolution of the being waves and the resulting acoustic field pressure. We again observed this from the calculated acoustic pressure at different observation points (z=50 mm) shown in fig. 6.4. From fig. 6.4a we can distinguish the 3 different phases which are well correlated with the ones ascertained in the analysis of the dynamic response. At an observation point located on the impact axis (x=0 mm, z=50 mm) the acoustic field is composed of a peak, the initial transient wave, resulting from the initial rapid deformation of the plate at the impact point. The initial transient wave is then followed by a silent zone which is not subjected to the effects of the bending waves propagating towards the edges of the plate. This silent zone is succeeded by the gradual appearance of oscillations which signify the arrival of the bending waves reflected from the edge of the plate - the ringing noise.

The three phases of acoustic radiation become increasingly difficult to distinguish off axis, and even more so with increasing distance from the axis of impact, for the same reasons previously mentioned in the analysis of the dynamic response - see fig. 6.4b-d. As the observation point moves away from the impact axis (axis of symmetry), it is reached by the radiation of the bending waves even before they are reflected from the edges of the plate. Additionally, depending on its position, the observation point may be reached by the acoustic wave due to the bending waves even before the arrival of the initial transient wave. To better illustrate this phenomenon, in fig. 6.5 we have

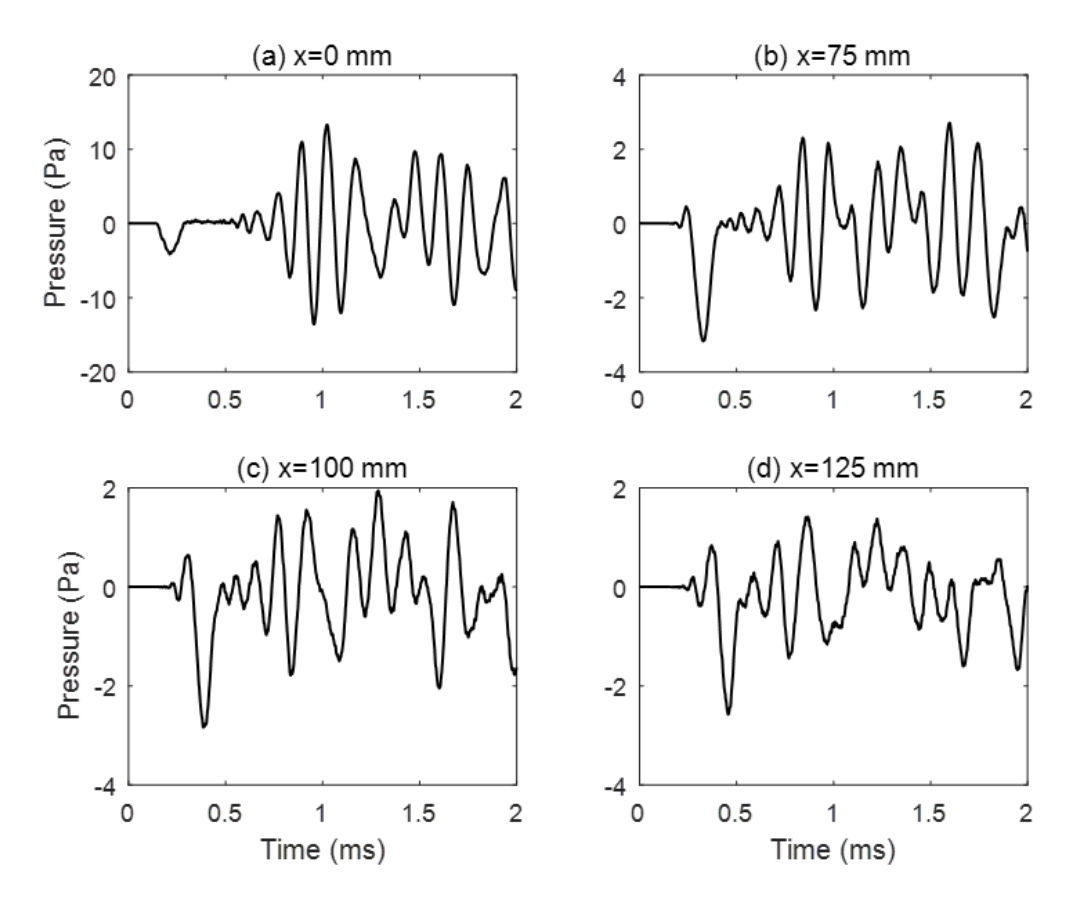


Figure 6.4 – Variation, with respect to time, of the acoustic pressure for field points located at a distance z = 50 mm from the plate.

shown the variation of the acoustic pressure for four field points situated at a distance of radius R = 50 mm (from the center of the plate and polar angle) $\psi = \{0^{\circ}, 30^{\circ}, 60^{\circ}, 89^{\circ}\}$. Note that since these points are located at the same distance from the impact point O, they are reached simultaneously by the initial transient wave.

In fig. 6.5a, at $\psi=0^\circ$, we can see that the initial transient wave is well separated from the ringing noise by the silent phase. The silent phase continues to exist at $\psi=30^\circ$, however now the initial transient wave is modified - this implies that the bending waves have already reached this point. This dispersive effect of the bending waves is even more apparent at $\psi=60^\circ$ and $\psi=89^\circ$ (fig. 6.5c-d) where the bending waves reach these field point before the initial transient wave, again corroborating the findings in the dynamic response.

Finally in fig. 6.6 we give an overview of the acoustic field, radiated by the force impacted plate, in the form of the pressure distribution in the xz-plane. The acoustic pressure distribution is shown at three different time instants after the beginning of the impact action. Due to axisymmetry, only half of the xz-plane is represented.

From fig. 6.6a, at $t = 24 \mu s$ after the impact, far from the impact we observe the development of an acoustic wave in the vicinity of the plate. This acoustic wave results from the bending waves rather than the initial rapid deformation of the plate at the point of contact. The bending

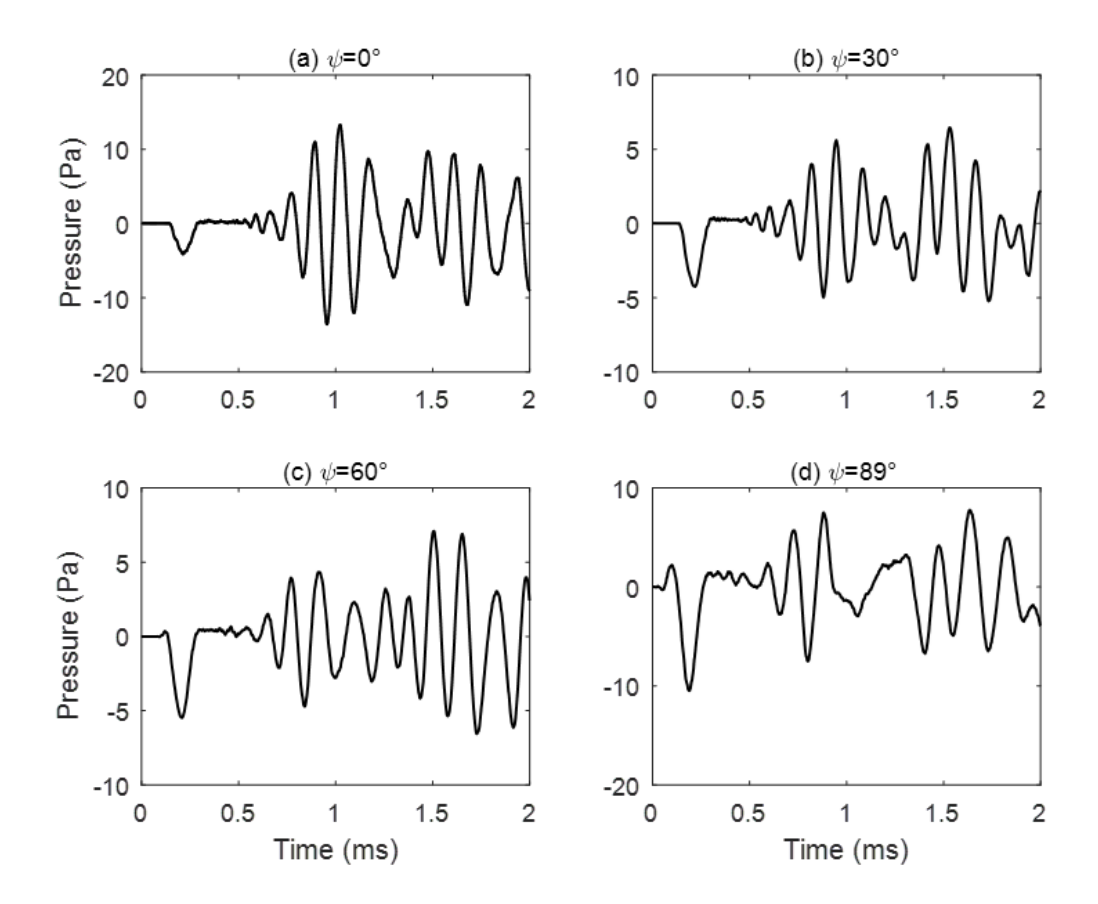


Figure 6.5 – Variation, with respect to time, of the acoustic pressure for field points located at a distance R = 50 mm from the plate center with different polar angles ψ .

waves have frequencies that exceed the critical frequency and propagate at speeds greater than those of the acoustic waves in air. This is the reason why the acoustic wave from the bending waves precedes the arrival of the acoustic wave due to the initial deformation for some points, particularly points located far enough from the axis of impact. With time, other acoustic waves of oblique wavefront due to bending waves as well as circular wavefront from the initial transient wave are observed - see fig. 6.6b. Both waves progress, with time, in the air until the first bending wave arrives at the edge of the plate, at which point the oblique waves reflect in succession and interfere with the incident waves - see fig. 6.6c. The interference of the oblique waves and incident waves makes the interpretation of the field difficult, hence the off-axis pressure pattern during the ringing phase.

6.2.3 Comparison to Explicit Dynamics

In the previous chapter we found that nd = 25 (8 cubic elements per patch edge of the plate) was sufficient to capture the acoustic radiation with a relatively good accuracy. To compare the results obtained using the implicit scheme with the analytical Ross and Ostiguy [132] contact force (taken as the reference case Ref.) and to our full explicit dynamics (with CD, NB, and KL schemes in section 5.4.3) and acoustic radiation model, we plot the acoustic pressure field

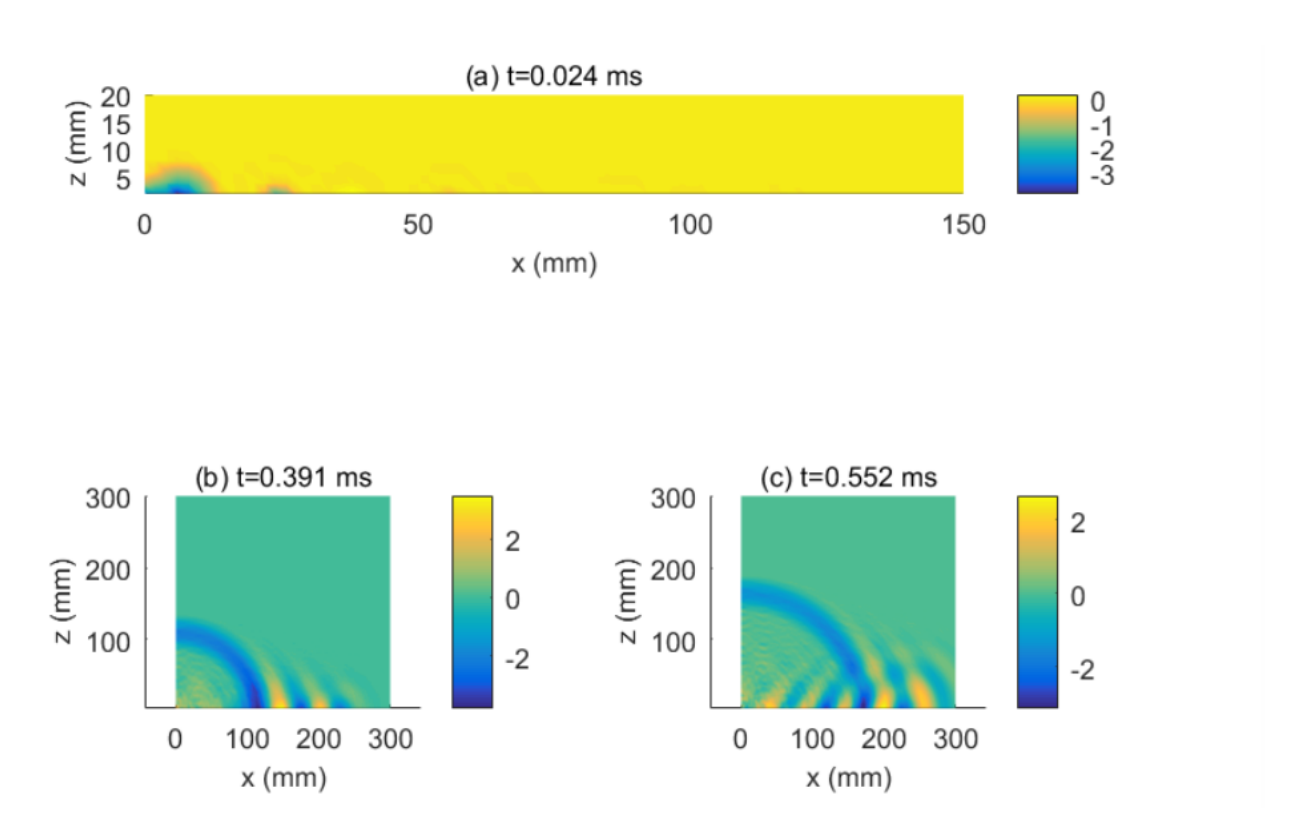


Figure 6.6 – Sound pressure distribution in the xz-plane at the vicinity of the plate at three instants after impact start. Pressure is given in Pa.

variation obtained with time. $\Delta t = 0.0154~\mu s$ for the explicit schemes and $\Delta t = 0.287~\mu s$ for the implicit scheme. Note that even though the implemented code has the capability to compute the acoustic pressure based on actual deformation of the plate (the effective geometry), here the undeformed plate geometry is used for the computations in the effort to reduce computational time. This choice can be justified by the small deformation of the plate.

Figure 6.7 shows the acoustic pressure field at an on-axis observation (z = 60 mm), variation with time, obtained from the dynamic response of the three explicit schemes in fig. 5.7. Again, we observe the three explicit schemes give similar results which is expected we have seen already that the acoustic wave propagation has the same distribution as the dynamic response, particularly the velocity. Comparing the three schemes results to the reference case, we notice the duration of the initial transient wave is longer and that the acoustic pressure in the third zone is lower. Nevertheless, the amplitude of the initial transient wave is well captured and the oscillations of the last zone correspond well.

To explain the difference in the acoustic pressure field in fig. 6.7 between that obtained using the explicit schemes and that of the reference case, we look at the contact force for the three schemes and that of Ross and Ostiguy [132]. These contact forces are shown in fig. 6.8. Once more, the three explicit schemes result in a similar contact force with an amplitude larger than that of the reference case, and a longer contact duration - fig. 6.8a - hence the larger amplitude and longer duration of the transient acoustic wave for the explicit schemes. In the case of explicit schemes, the contact is both punctual and elastic which corresponds very well with Hertz contact theory

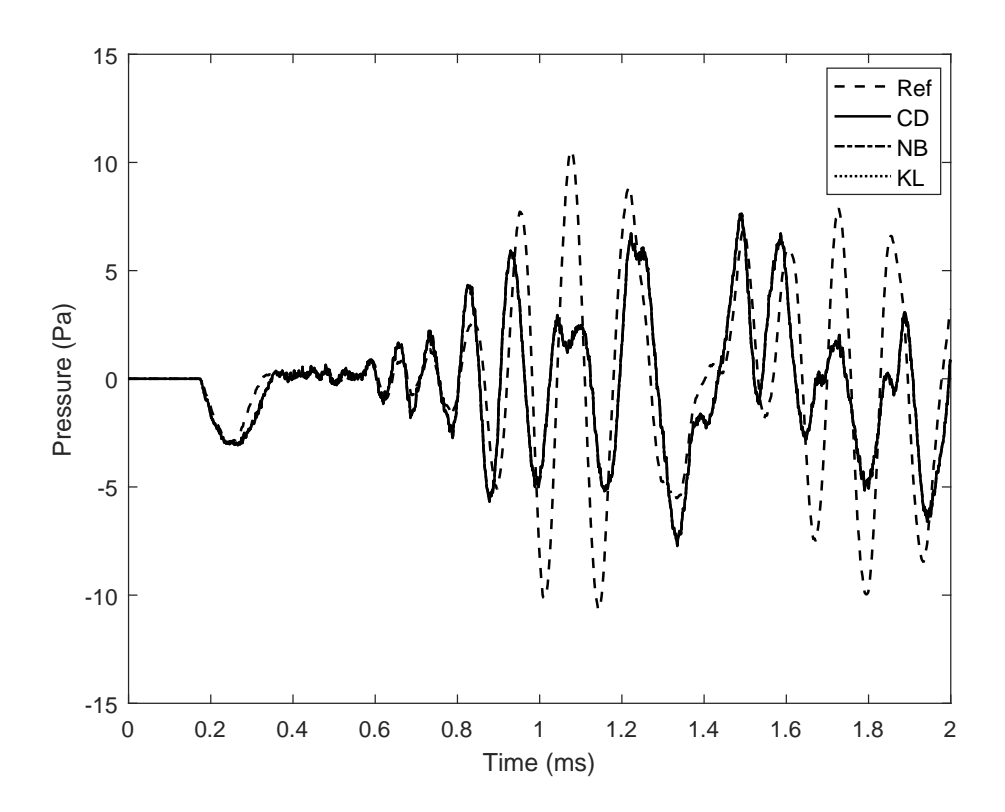


Figure 6.7 – Acoustic pressure on-axis at z = 60 mm using central difference scheme (CD), Noh and Bathe (NB), and Kim and Lee (KL) schemes in comparison to pressure (Ref) due to applying Ross and Ostiguy contact force directly to the plate without considering the sphere into calculations. (CD), (NB) and (KL) curves are the same.

in that: the contact force is symmetrical, of finite duration and amplitude greater than that of an inelastic case.

Looking at the penetration in fig. 6.8b, we note that it is symmetrical (expected as the contact force is directly proportional to the gap), and sufficiently small relative to the thickness of the plate (penetration $\sim 0.27\%$ of the plate thickness); this is satisfactory for the penalized explicit scheme applied.

6.3 Application to Vibrating Plates due to a Moving Force

Here, we analyze the dynamic response and the radiated acoustic field thereafter, of a plate subjected to a moving force, depicted in section 6.3. The radius of plate R_p has been reduced to 0.05 m. The constant amplitude F_{imp} is taken as the maximum amplitude of the impact force impulse in fig. 6.1a. We assume F_{imp} moves along the x-axis from the edge point $(-R_p, 0, 0)$ at a uniform translation velocity of $v_m = 100$ m/s. The reduced plate radius allows us to analyze

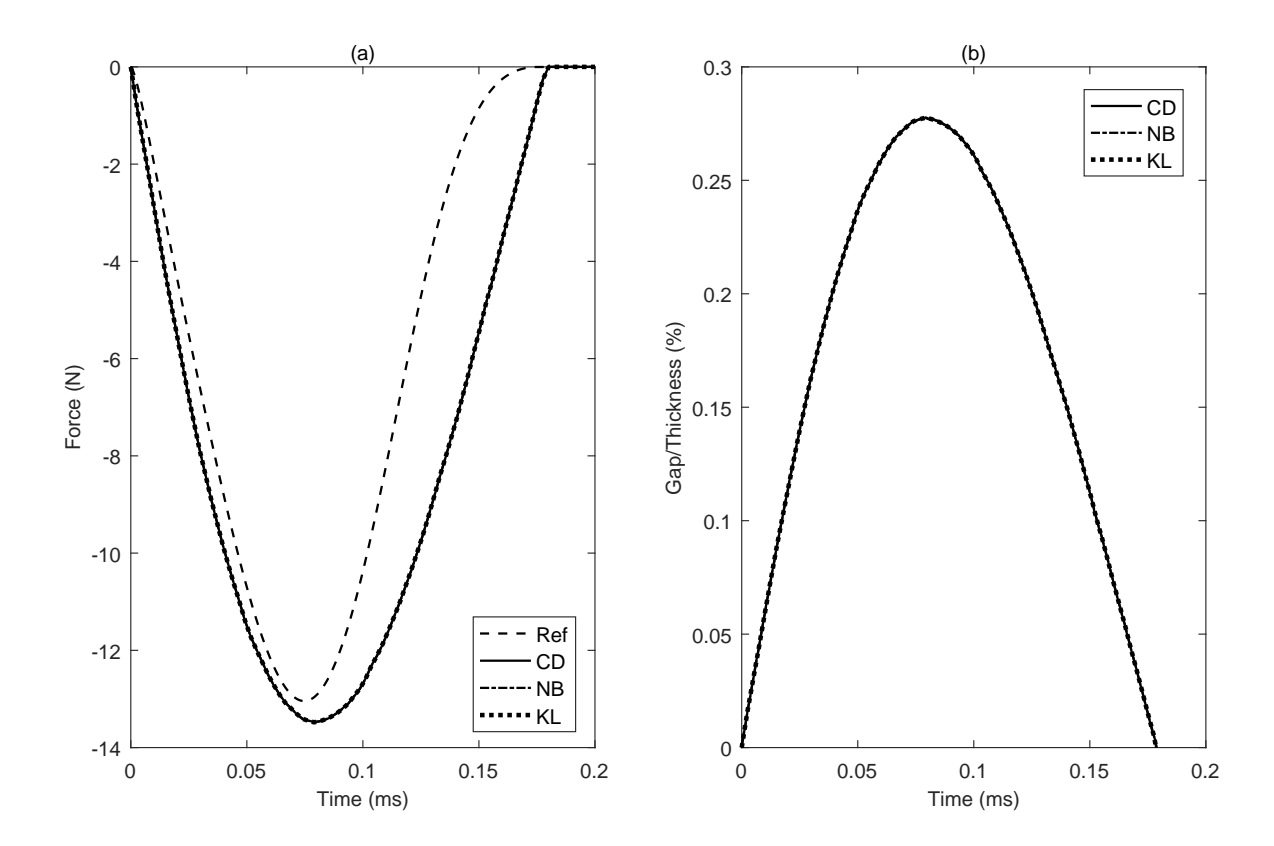


Figure 6.8 – Contact force between sphere and plate (a) and the effective penetration (b) when central difference (CD), Noh and Bathe (NB), and Kim and Lee (KL) schemes are used. (Ref) is the Ross and Ostiguy contact force. (CD), (NB) and (KL) curves are the same.

the acoustic radiation with a duration of 2 ms after the force starts moving; the force transits the plate diameter in 1 ms, thus leaving enough time to analyze the behavior of the plate post passage of the force.

Again, the system is governed by the elasto-dynamics equations in eqs. (5.1) and (5.2), however now only the plate is considered. Its variational form and its discrete form follow accordingly from eq. (5.12) and eq. (6.1), respectively. However in eq. (5.12) the contact force is replaced by the moving force F_{imp} . In section 6.2 the impact force is applied to a point coinciding with a node of the discretized geometry, in this case the computation of the force vector \mathbf{F} becomes trivial. We simply assign the value of the applied impact force directly to the corresponding component in the global force vector. However, if the external force is applied at any point other than the node, the computation of the force vector becomes a bit more sophisticated, as is typically done with consistent nodal loads [141]. This is particularly the case for the moving force.

To compute the force vector for the moving force involves two steps. First we must know the current position of the moving force, that is, we locate the point of application for the force on the element. To do this, the closest point projection method typically used for contact problems [142] is used. Once the parametric coordinates $\bar{\xi}$ of the closest projection point, or rather the

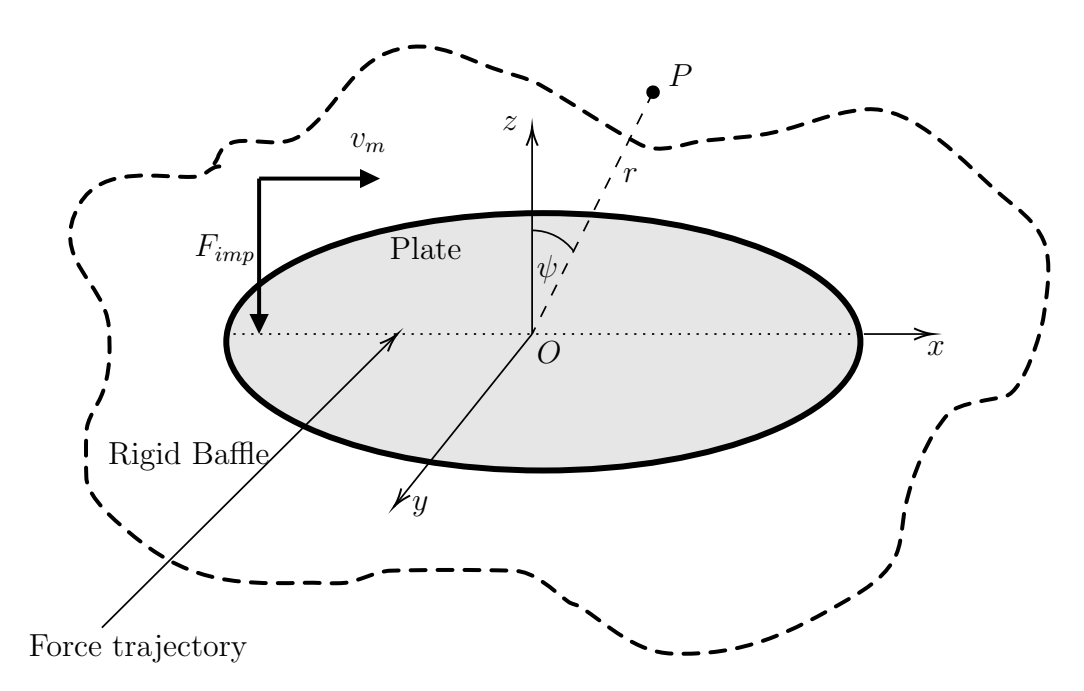


Figure 6.9 – Illustration of the problems considered : plate subjected to a moving force. v_m denotes the velocity of the imposed moving force F_{imp} , (r,ψ) are the polar coordinates of the field point belonging to the xz-plane.

parametric coordinates of the location of the force, are found, each node belonging to this same element are involved in the computation of the elemental force vector \mathbf{f}^e . If we denote by InodFe the nodes of this element involved and assuming only normal forces are present: the normal force at the closest point projection $f_N(\bar{\boldsymbol{\xi}})$ can be approximated as follows

$$\mathbf{f}_{N}^{e}\left(\bar{\boldsymbol{\xi}}\right) = \phi\left(\bar{\boldsymbol{\xi}}\right) \mathbf{f}_{N}^{\text{cntrl}}$$

$$= \phi\left(\bar{\boldsymbol{\xi}}\right) \mathbf{B}_{\text{bez}}^{-1} \mathbf{f}_{N}^{\text{phy}}$$

$$= \mathbf{Q}\left(\bar{\boldsymbol{\xi}}\right) \mathbf{f}_{N}^{\text{phy}}$$
(6.1)

Finally, for the applied F_{imp} as shown in fig. 5.1, the normal force contribution for each element into the global force vector right as:

$$\mathbf{f}^e = F_{imp} \bar{\mathbf{Q}}^T \bar{\mathbf{n}} \tag{6.2}$$

$$\mathbf{F}(InodFe) = \mathbf{F}(InodFe) + \mathbf{f}^e \tag{6.3}$$

Note, as previously done in the contact formulation, $(\bar{\bullet})$ indicates quantities evaluated at the projection point parametric coordinates $\bar{\xi}$. The rest of the global matrices follow in the same as in section 6.2.

In this case we now discretize the plate using 320 quadratic Bézier elements with 1313 nodes for the simulation. The material properties of the plate are as given in table 5.1, however now with the reduced radius. The implicit Newmark scheme with time step size $\Delta t = 0.131 \ \mu s$ is used. The dynamic and acoustic response are discussed in the next sections.

6.3.1 The Dynamic Response

Figure 6.10 shows the transverse displacement along the x-axis and y-axis of the plate at different time instants. From these results we can see that : (1) during the transit of the force, the main deformation lobe moves in the same direction as the force, (2) in the first milliseconds the amplitude, of the main deformation lobe, increases with the distance traveled by the force until it reaches a limit distance at which point it starts to decrease, and (3) the points in the x-axis appear to vibrate harmonically after the passage of the force. However, this vibration is not completely harmonic due to the appearance of a transient phase which can be observed in time instants 0.85 ms and 0.90 ms (fig. 6.10c) at the beginning of each sign change of the transverse displacement.

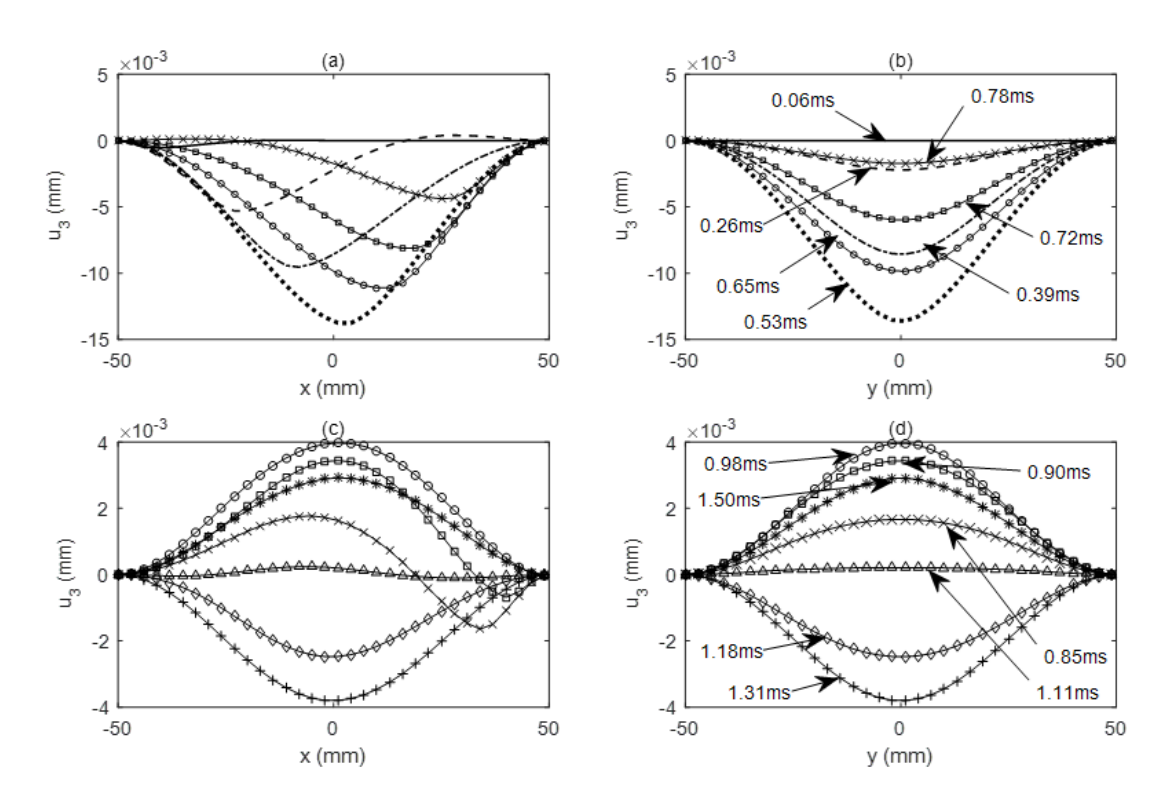


Figure 6.10 – Variation, with respect to x (left, y = 0 mm) and y (right, x = 0 mm), of the transverse displacement of the plate for different instants.

The appearance of the transient phase is further illustrated in the transverse displacement distribution at different time instants (fig. 6.11) as well as in the variation of the transverse displacement at observation point P(25, 0) in fig. 6.12e.

Looking at the variation, with time, of the transverse displacement and velocity shown in fig. 6.12, we observe the influence of the bending waves during and after the passage of the force. This is clearly reflected in: (1) the early arrival of the bending waves at the observation point even before the arrival of the deformation due to the force itself, and (2) the appearance of oscillations in the velocity even when the transverse displacement seems to smooth. In fact, from the first

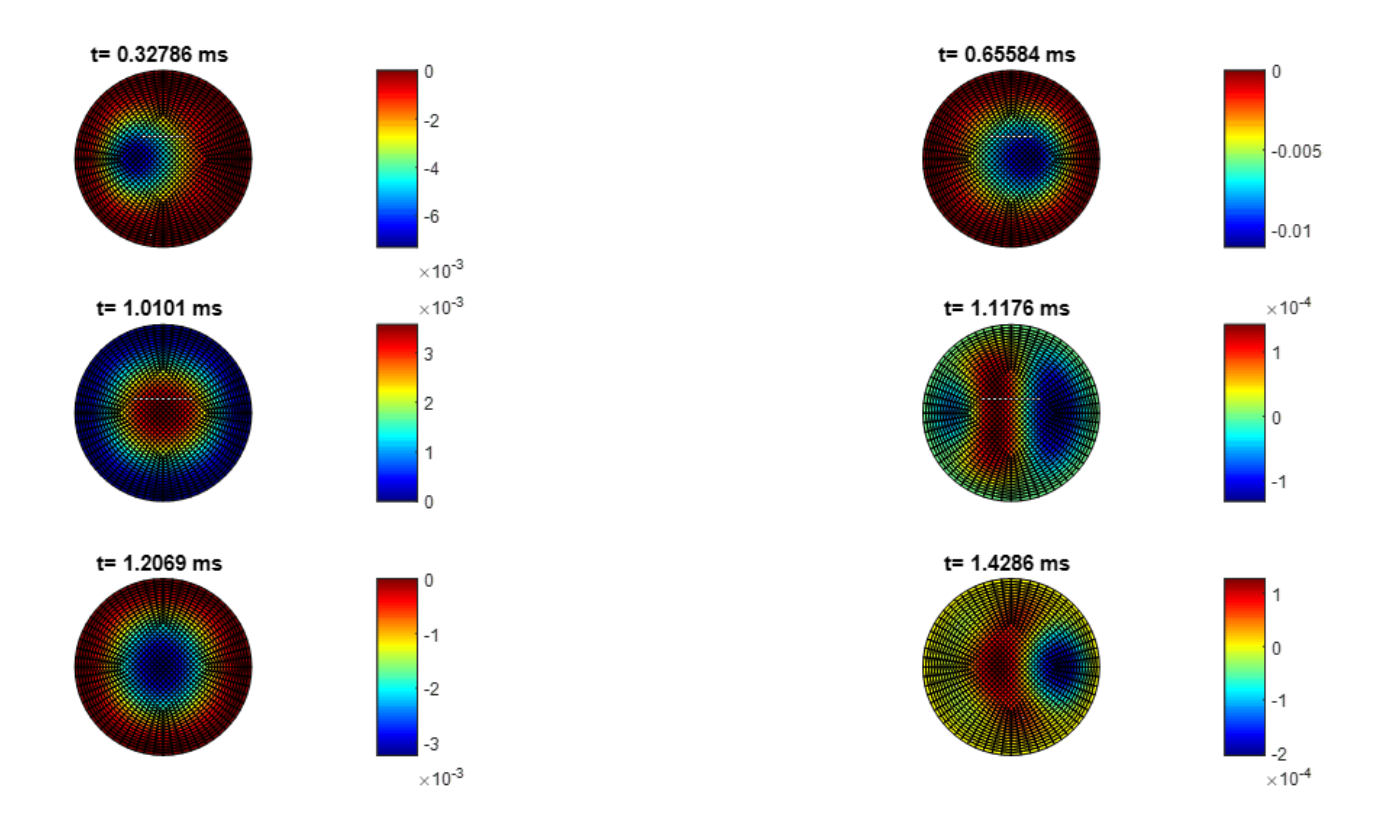


Figure 6.11 – Transversal displacement distribution of plate at different instants after the movement of the force start. Displacement is given in mm.

time step of the computation, bending waves of small amplitude start to propagate through the whole plate and also reflect on its edges, as can be seen from fig. 6.13.

At each new position of the moving force new bending waves appear and are reflected, and in the absence of damping these waves persist in the plate. Their influence depends on their interference as well as the point at which the velocity is considered - see for instance fig. 6.12d for which this influence is less prominent compared to fig. 6.12f. The amplitude of these bending waves can also be seen as a precursor in the transverse displacement and velocity as observed in fig. 6.12e-f, and sometimes their effect is only visible if we are interested in the velocity and consequently the acceleration. Moreover, as seen in the variation of velocity of some nodes (fig. 6.12b, fig. 6.12f), high frequency oscillations are superimposed on the velocity resulting from the global deformation of the plate. This phenomenon does not occur for the centered impact problem studied in the previous section. Here, the bending waves are generated at the same point and are all synchronous, both in their generation and their reflection.

6.3.2 The Acoustic Response

As already observed, the dynamic response of the plate has repercussions on its acoustic response. In fig. 6.14 we show the acoustic pressure at a field point located at z=25 mm on the

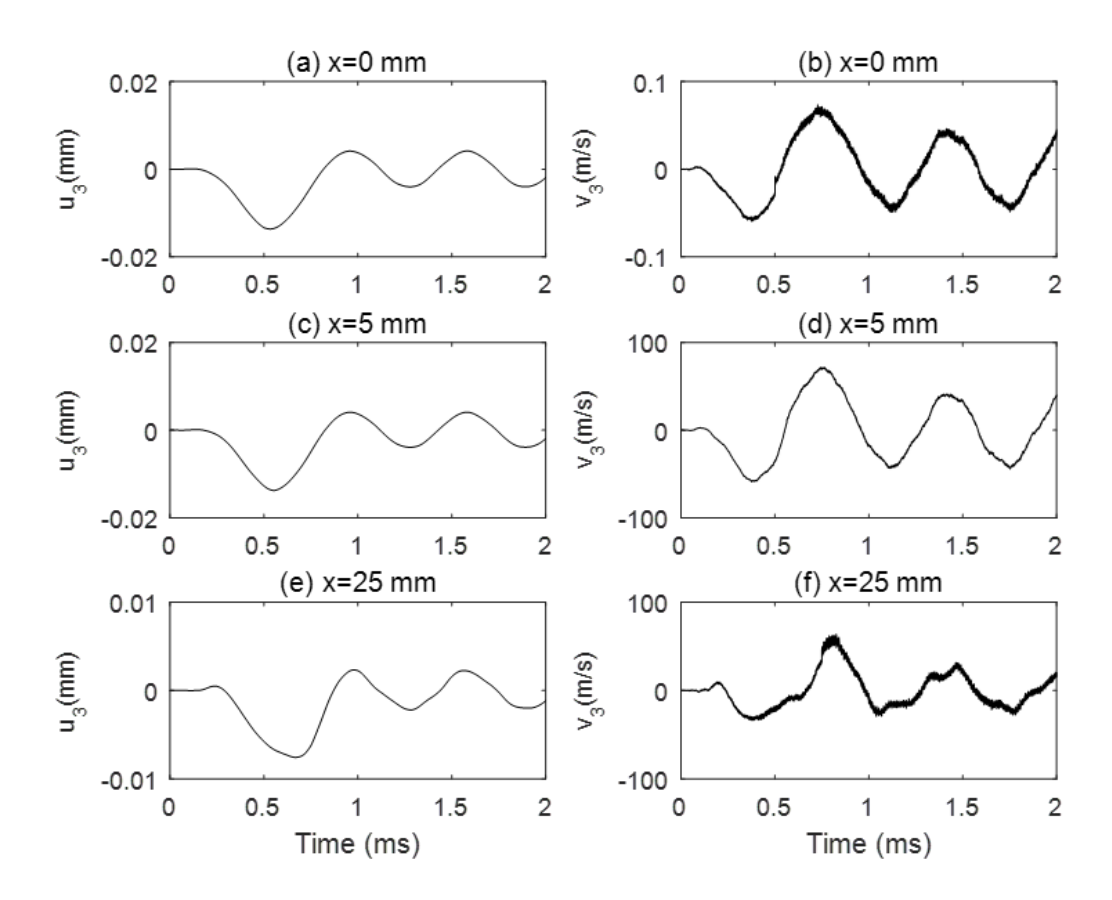


Figure 6.12 – Variation, with respect to time, of the transverse displacement (left) and velocity (right) of three points on the x-axis of the plate (y = 0 mm).

axis $\psi_0 = 0^\circ$, as well as the normalized spectrum with respect to its maximum. In line with expectation, we seen a correlation between the acoustic pressure variation and that of the velocity, in that (fig. 6.14a): (1) the variation of acoustic pressure is almost harmonic, (2) we see the appearance of the precursor due to the dispersive effects of the bending waves, and finally (3) the presence of oscillations in the distribution. Unlike the centered impact problem, here we notice the lack of the intermediate silent phase. This is due to the continuous movement of the force, thus leading to the propagation and multiple reflections of the bending waves throughout the plate from the beginning of the loading. Hence, the acoustic wave originating from the local deformation (due to the loading force) at a given time is interfered with by the acoustic waves arising from the propagation of the bending waves of the plate.

Contrary to the centered impact problem, the acoustic pressure is no longer axisymmetric, but rather, the pressure is symmetric about the xz-plane (see fig. 6.15). This can be seen in fig. 6.15 where we show the acoustic pressure at different field points, located at a distance R=25 mm from the center point O and polar angles $\psi_1=\pm 30^\circ$, $\psi_2=\pm 60^\circ$, and $\psi_3=\pm 89^\circ$. Moreover, we observe the effect of bending waves, in terms of the presence of oscillations, is more pronounced in the vicinity of the plate (fig. 6.15a and fig. 6.15f). This is particularly the case at observation points closest to the first point of application of the force - fig. 6.15a. This can also be confirmed by comparing the peaks from the spectrum of the on-axis point in fig. 6.14b and those of field

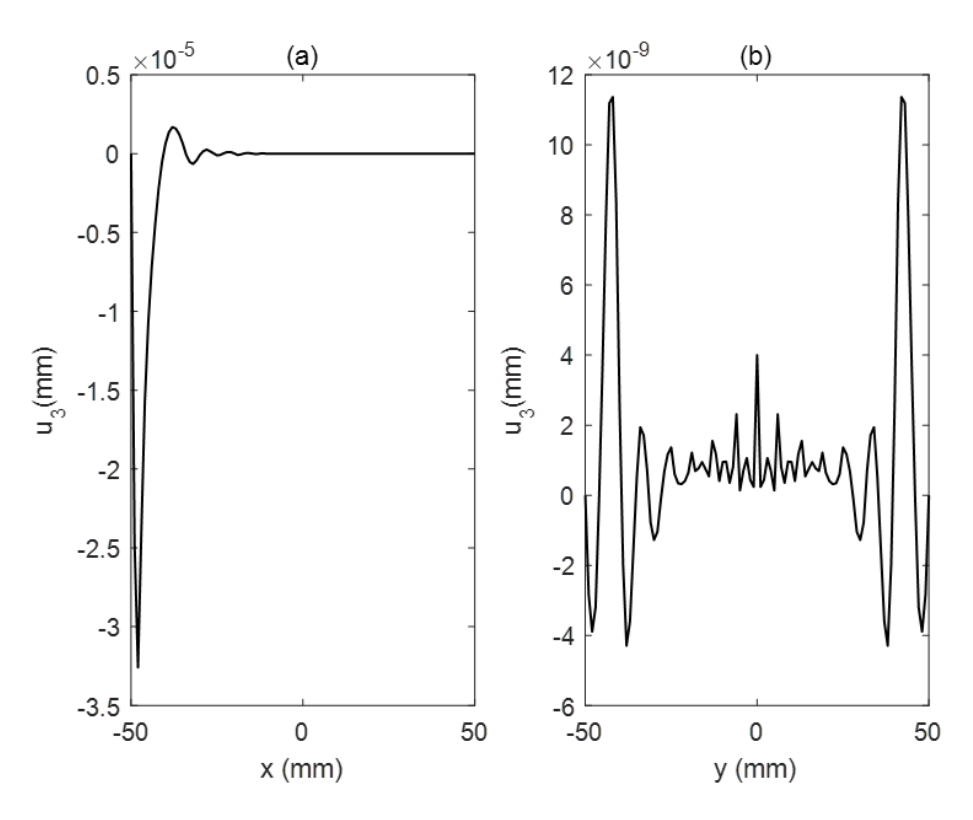


Figure 6.13 – Variation, with respect to x (left, y = 0 mm) and y (right, x = 0 mm), of the transverse displacement of the plate for $t = 6.56 \mu s$.

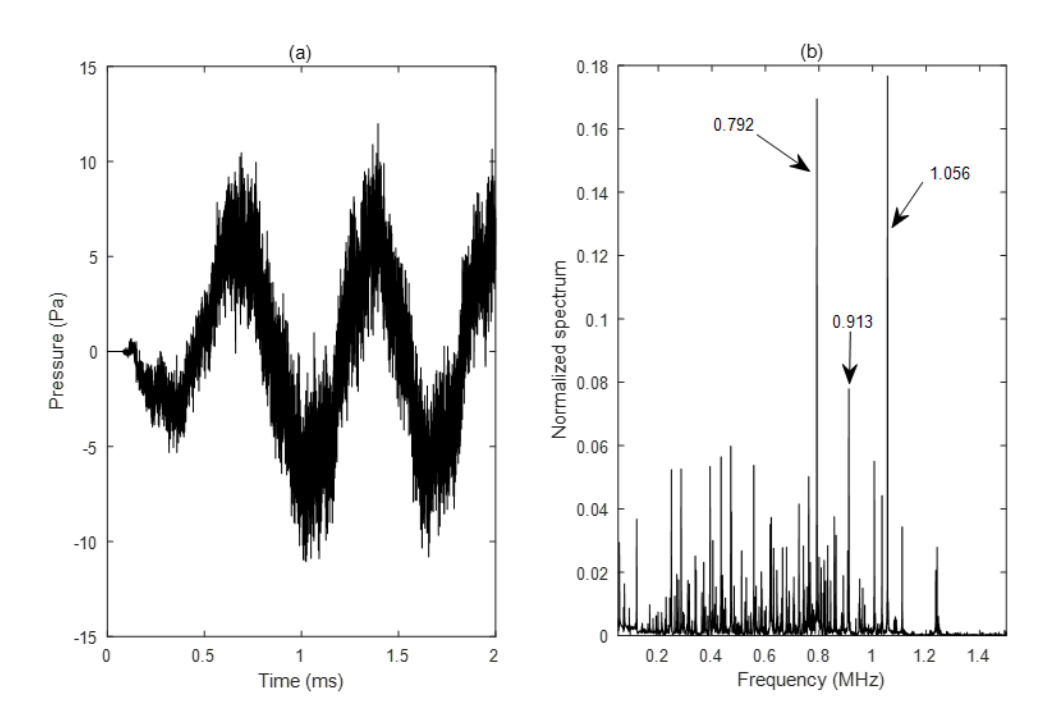


Figure 6.14 – (a) Variation, with respect to time, of the acoustic pressure for a field point located on the plate axis at a distance R = 25 mm from its center ($\psi_0 = 0^{\circ}$) and (b) its corresponding normalized spectrum with respect to its maximum value. The corresponding plate natural frequencies are indicated by rows in (b) for the more significant peaks.

points near the plate at $\pm \psi_3$ shown in fig. 6.16.

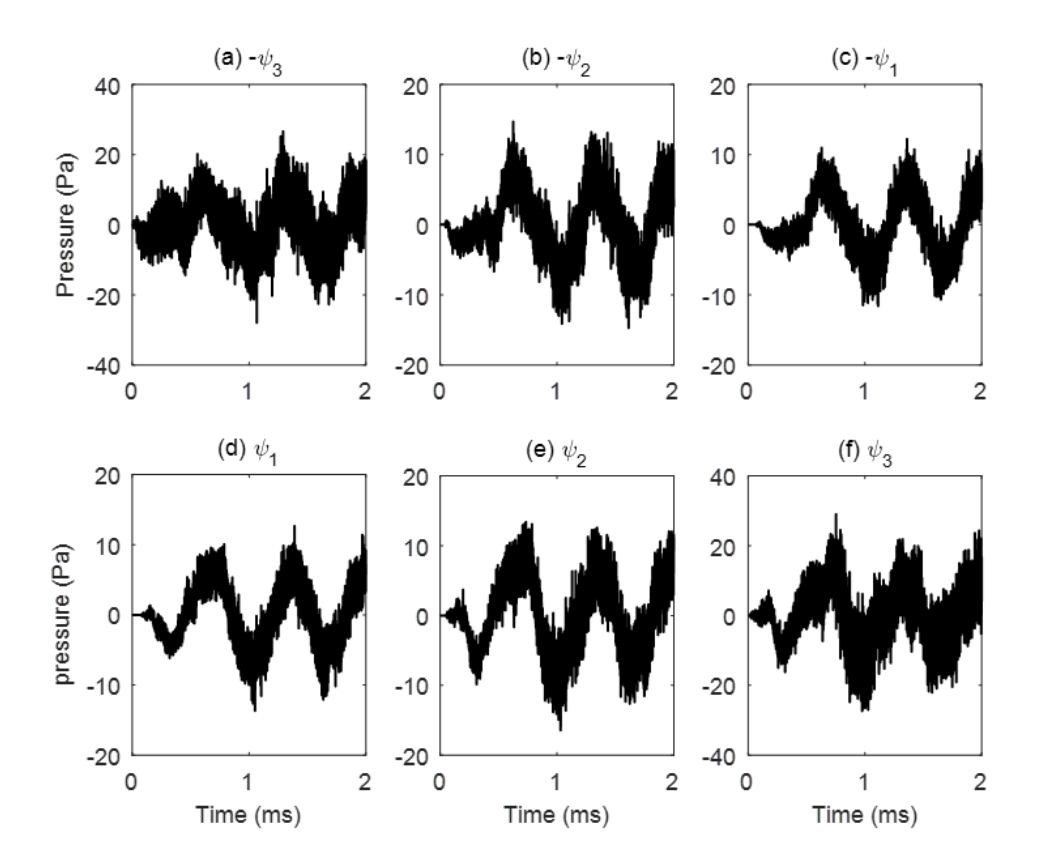


Figure 6.15 – Variation, with respect to time, of the acoustic pressure for different field points located in xz-plane at a distance R=25 mm from the plate center. $\psi_1=30^\circ$, $\psi_2=60^\circ$, $\psi_3=89^\circ$. The negative values of the angle ψ designate the negative values of the x-coordinate.

From fig. 6.14b we can see only three significant natural frequencies are present in the on-axis acoustic response. Their contribution with respect to the spectrum amplitude of the first frequency is almost 18%. At $-\psi_3$, the spectrum shows more high amplitude peaks at high frequencies compared to ψ_3 and ψ_0 . This point is not only close to the plate like ψ_3 but it is also close to the starting point of the force.

To get a better understanding of the process of generation and reflection of acoustic waves, we look at the spatial distribution (xz-plane) of the acoustic pressure in the vicinity of the plate shortly after the beginning of motion of the force and after complete travel of across the plate-fig. 6.17 and fig. 6.18. At $t = 9.4 \,\mu s$ (fig. 6.17a), we observe the development of the acoustic wave from bending waves downstream of the action field of the moving force (action field indicated by the circle on the figure). The acoustic wave due to the local deformation of the plate, following the application of the force, is at this moment small because of the embedding conditions (plate is embedded into a rigid baffle). Some $0.8 \,\mu s$ later, fig. 6.17b, at the left edge of the plate we notice the appearance of an acoustic wave of oblique wavefront that is parallel to the wavefront observed on the right side of the force action field. This implies that the acoustic wave due to the bending waves has been reflected on the left edge of the plate. At $t = 14.6 \,\mu s$, reflections on the left edge persist and the acoustic waves due to bending waves continue to propagate towards

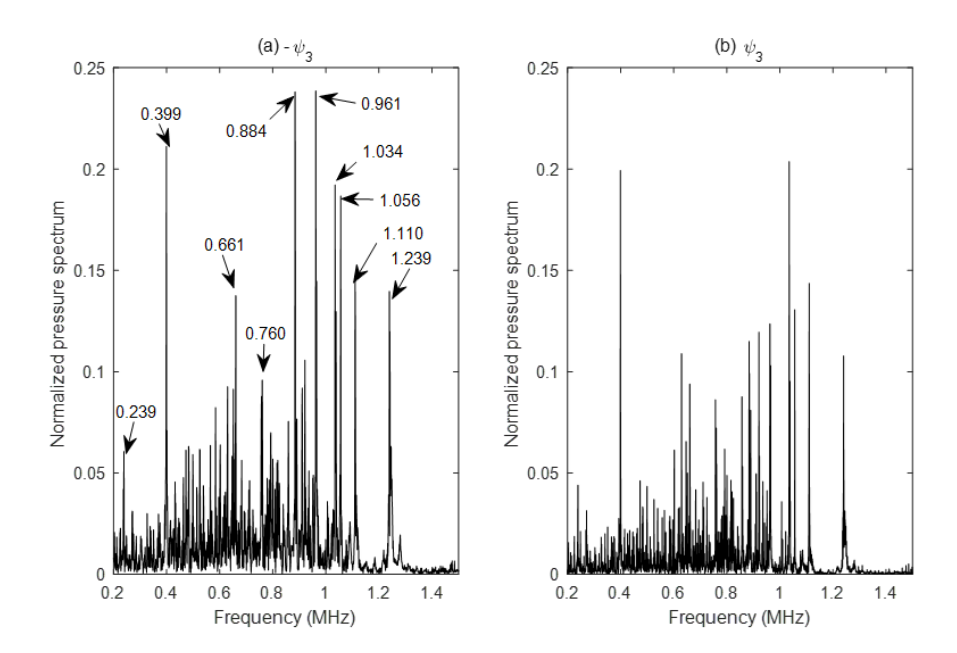


Figure 6.16 – Normalized spectrum, with respect to its maximum value, of the pressure of two field points located at a distance of 25 mm from the plate center where $\psi_3 = 89^{\circ}$. Some plate natural frequencies are indicated by rows in (a).

the right edge. At this time, however, shortly after the start of force motion, it is impossible to differentiate between acoustic waves due to the local deformation of the plate and those arising from the bending waves.

At $t=37~\mu s$, fig. 6.18a, the acoustic wave continues to grow and reaches the right edge of the plate, where a second reflection of the acoustic wave occurs. During this time instant, we can no longer interpret the wave-fronts because this is only a plane representation of the phenomenon and therefore does not show the propagation process outside the xz-plane. After the passage of the moving force (fig. 6.18b-d), the acoustic wave appears almost harmonic, that is, we have alternating positive and negative pressure of circular wave-fronts. This corroborates the residual effect of the bending waves on the acoustic pressure distribution which previously were observed as oscillations on its time variation. In addition, unlike the acoustic pressure distribution for the centered impact problem in fig. 6.6, here fig. 6.18b-d clearly show a non-homogeneous distribution of the acoustic pressure.

Finally, we look into the effect of the time step and mesh size on the oscillations observed in the variation of acoustic pressure with time. Since the time integration scheme used is unconditionally stable, we increase the time step to that $10 \times$ larger than has been used so far : $\Delta t_2 = 10 \Delta t_1$. The results obtained, in terms of the acoustic pressure and spectrum, are shown in fig. 6.19. From these results we observe (1) the decrease in the acoustic pressure oscillations, (2) the shift of the spectrum towards the low frequencies, and (3) the decrease in the amplitude of the most significant peaks of the spectrum. These findings correspond well with the expectations; decreasing the time step size allows for the elimination of high frequencies and accordingly the corresponding bending waves as well as the corresponding acoustic waves.

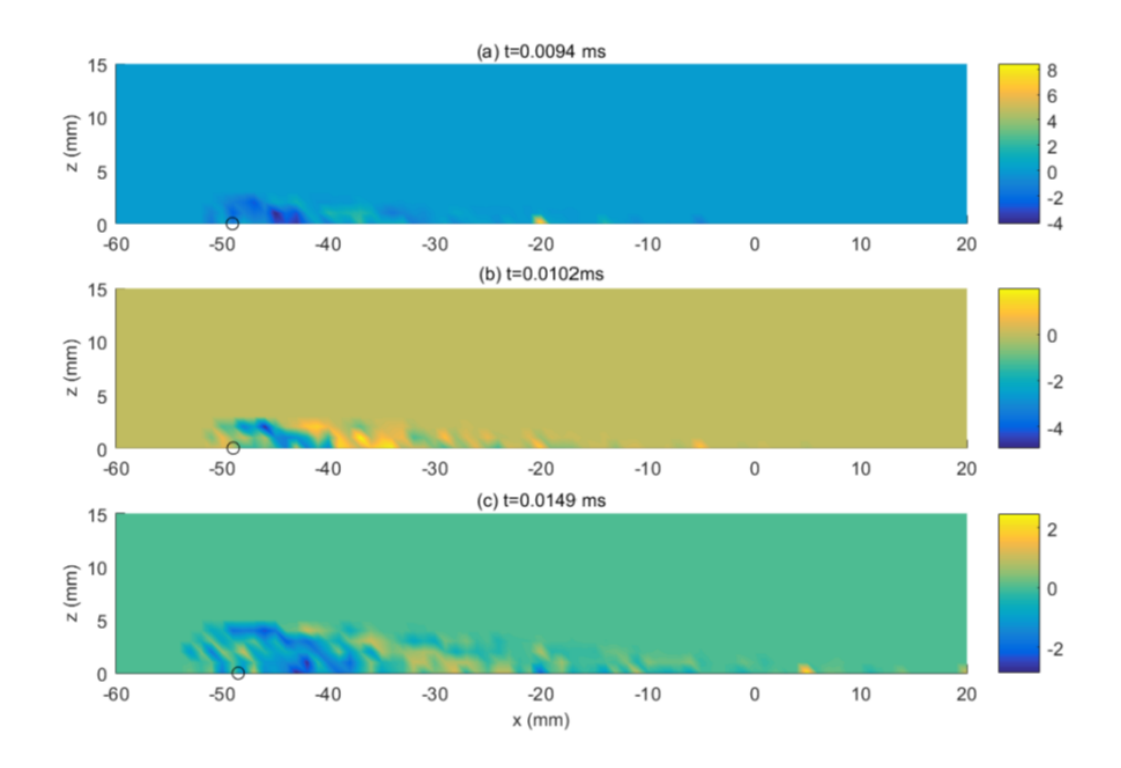


Figure 6.17 – Sound pressure distribution in the xz-plane at the vicinity plate at (a) $t = 9.4 \mu s$; (b) $t = 10.2 \mu s$; (c) $t = 14.9 \mu s$ after the force start to move. The circles show the current positions of the force. Pressure is given in Pa.

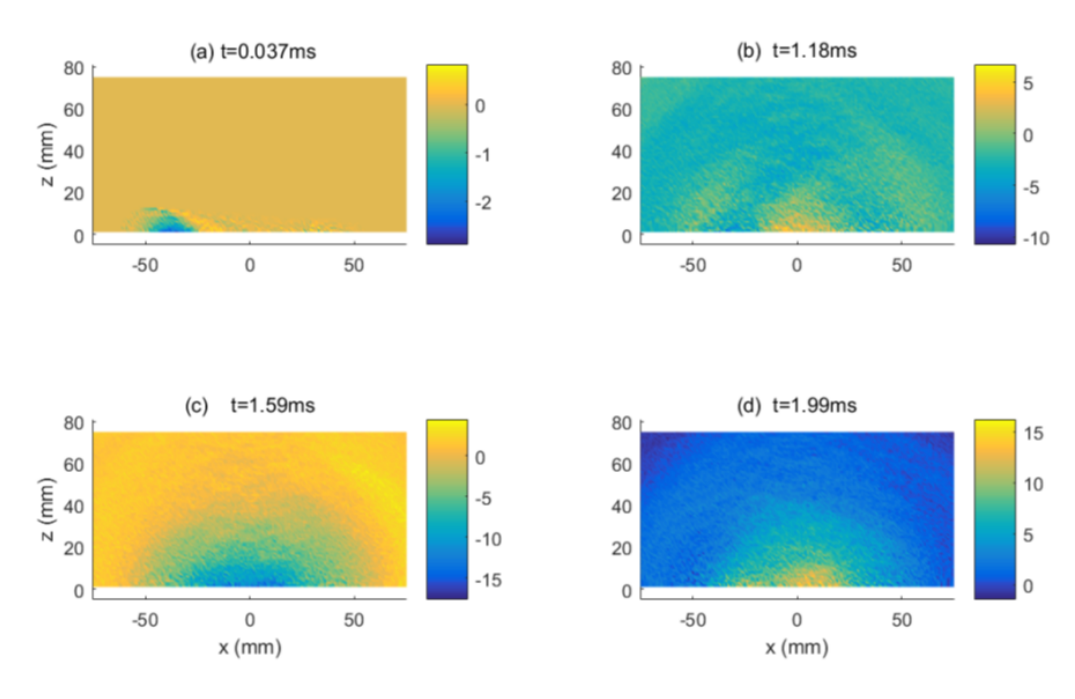


Figure 6.18 – Sound pressure distribution in the xz-plane at different instants during the movement of the force (a) and after its passage (b-d). Pressure is given in Pa.

Conversely, increasing the elements size (making the mesh coarse by reducing the number

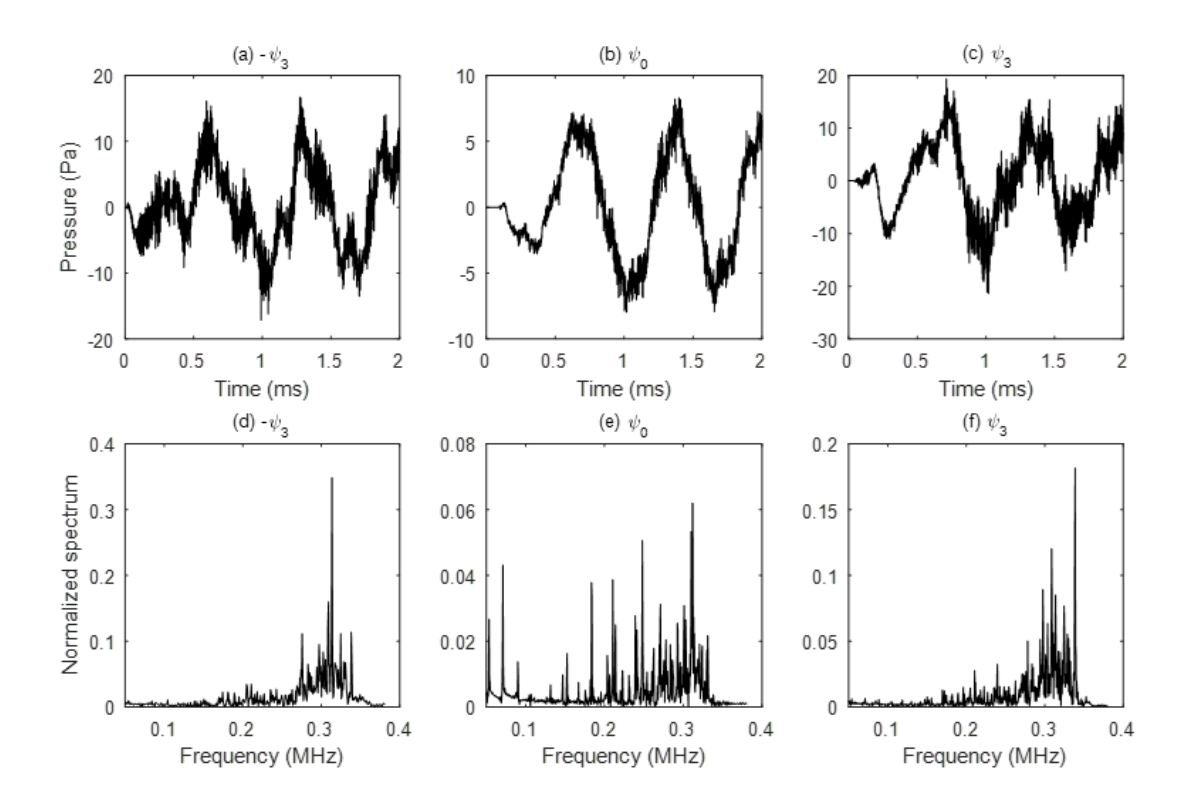


Figure 6.19 – Effect of the time step ($\Delta t_2 = 10\Delta t_1$) on the pressure : (a-c) Variation, with respect to time, of the acoustic pressure for three field points located on xz-plane at a distance R = 25 mm from its center ($\psi_0 = 0^{\circ}$, $\psi_3 = 89^{\circ}$) and (d-f) their corresponding normalized spectra with respect to their maximum values.

of nodes to 1009) while maintaining the same time step Δt_1 increases the amplitude of the oscillations in the acoustic pressure - see fig. 6.20. The spectrum on the other hand is less rich in frequencies compared to the spectra in figs. 6.14 and 6.16. This is due to loss of mesh quality, in terms of precision, compared to the original finer mesh. It is interesting to note that the overall shape of the acoustic pressure variation with time and its level is preserved for the three observation points, despite the coarser time step and computation mesh.

6.4 Summary

In this chapter we have used the developed Bézier-based IGA numerical scheme to calculate dynamics and the acoustic radiation, in time domain, of forced-vibrating plates. A thin elastic circular plate embedded in a baffle, vibrating first due a localized impact force and then vibrating due to a moving force, was studied. The Reisnsner-Mindlin plate theory used to model the plate and the Rayleigh integral equation for the acoustic response. The numerical dynamic and acoustic analysis mainly focused on the near field acoustic radiation.

In terms of the results obtained, many similarities were found between the two cases, including:
(1) the displacement field constitutes of an initial deformation which is then followed by free

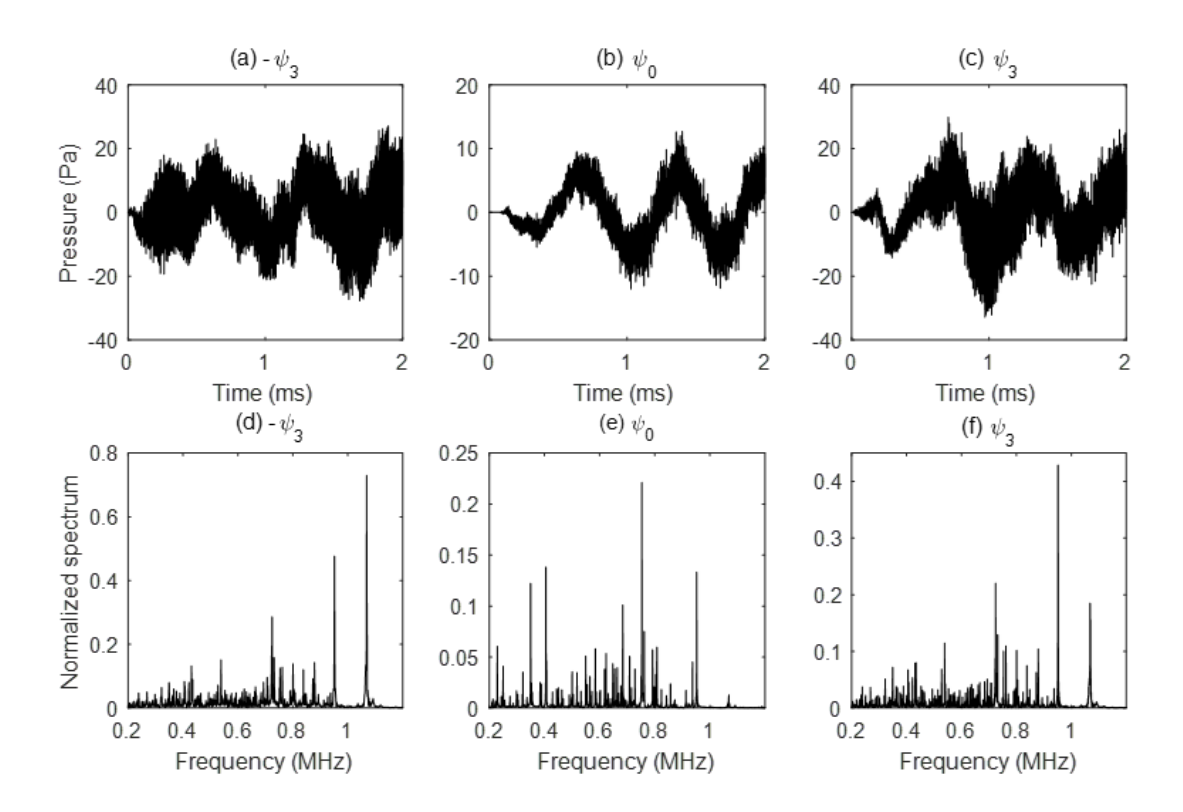
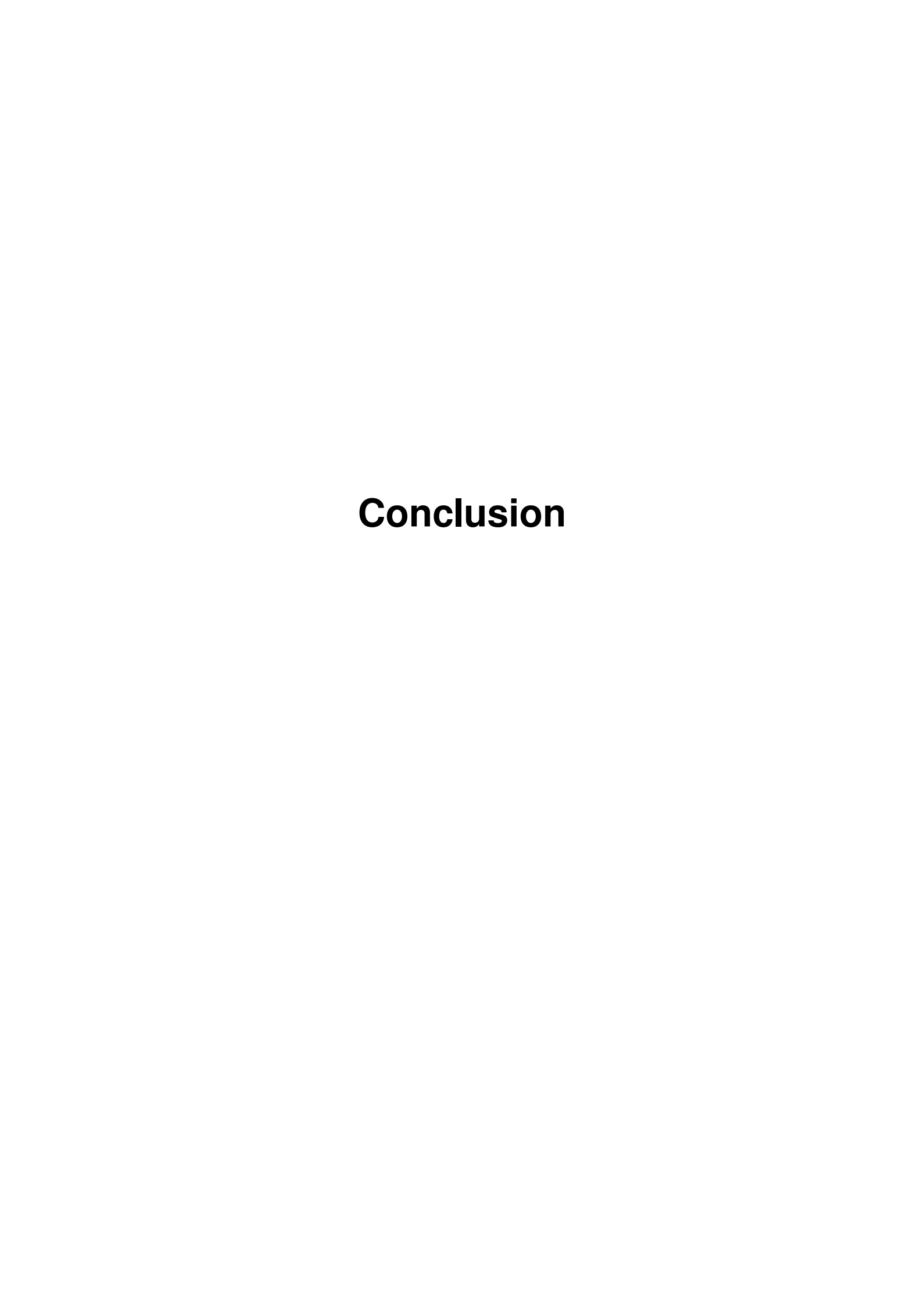


Figure 6.20 – Effect of the mesh (1009 nodes): (a-c) Variation, with respect to time, of the acoustic pressure for three field points located on xz-plane at a distance R=25 mm from its center ($\psi_0 = 0^\circ$, $\psi_3 = 89^\circ$) and (d-f) their corresponding normalized spectra with respect to their maximum values.

vibration of the plate, and (2) the presence of dispersive effects due to the generation of bending waves while the force is acting on the plate. Some differences were also observed, first being in the case of the moving force the absence of the silent zone and appearance of oscillations that are superimposed on the global response of the plate, in both the dynamic and acoustic response. Second, in the case of the localized excitation force, since the initial impact deformation is localized around the center of the plate, the dispersive effects exhibited by the bending waves as they propagate through the plate and the resulting acoustic waves are perfectly discernible. However, due to the size of the plate, lack of damping and the embedding boundary conditions, the continuous generation of the bending waves and their reflection at the edge of the plate causes the appearance of high frequency oscillations that are superimposed on the deformation due to the passage of the force and the free vibration of the plate. These oscillations were found to be sensitive to the model parameters such as mesh size and time step size.



Summary and Perspectives

Summary

In this thesis we have developed a Bézier-based IGA approach, with data structures suitable for existing FE codes, for the treatment of contact problems. This scheme couples the implementationally friendly isogeometric finite elements (Bézier extraction concept) with the Bézier inverse matrix (Bézier interpolation) to transform the computational space from that of control space to the physical space. The main and interesting characteristic of the Bézier-based method is, unlike the standard NURBS/BSplines-based isogeometric methods, with this scheme computation points now live on the physical geometry. The data structures are not only suitable for existing FE codes but also the computation mesh is identical to the more familiar standard FEA, thus granting direct access to the physical boundaries which then greatly simplifies the application of boundary conditions. Note, the connection with the original NURBS/BSplines is never lost. Just like we have deduced the Bézier form from the BSplines, we can equally recover the BSplines from the Bézier elements. A comparison of this Bézier based scheme with the traditional NURBS/BSplines based approach found that, in terms of the quality of the solution, both methods yield the same results. Naturally, the Bézier-based approach is slightly expensive as it introduces more DOFs into the system.

The Bézier based IGA approach allows for the use of the NTS contact formulation as now the contact integrals can be easily collocated at physical points. The full development of the NTS contact formulation with the penalty method, as well as the solution procedure algorithm is the main focus of chapter 3.6. In chapter 4 the developed NTS contact discretization scheme is applied to friction-less and frictional 2D contact problems, with quadratic and cubic discretizations. The multi-patch framework allowed us the ease to represent the relatively complex geometries as well as control over the computation meshes such that high density of elements were within the potential contact area, and a very coarse element distribution away from this area. A small deformation framework was assumed, thus allowing us to verify and validate our developed numerical scheme against analytical solutions. We found our scheme to be accurate, even for coarse meshes, particularly for the friction-less problems and with a cubic discretization. In the

classical Hertz problem we could predict both the contact area and contact stresses to within $\sim 1.5\%$ of the analytical solution, and in the rigid punch problem to $\sim 3\%$ of the analytical solution. We also compared our formulation to the standard FEA, NTS with penalty method, solution obtained using Abaqus: we found that for the same number of DOFs in the system, a relative error of $\sim 10\%$ on the classical Hertz problem with standard FEA, particularly on the contact area, is committed. This error was even higher for the rigid punch problem. Attempts to refine the mesh in Abaqus, to improve the results, quickly led to prohibitively large penalty stiffness. In fact, the Abaqus solver had to switch to Lagrange multipliers as the required penalty stiffness exceeded the threshold. On the other hand with IGA a penalty parameter of 100E was sufficient enough for allowed penetrations of order $< 1 \times 10^{-7}$. This is because of the coarseness of the mesh, recall that the penalty stiffness is a function of the surface lengths of the elements. The smaller the element size, the higher the penalty stiffness required. And as we know with the penalty method, high penalty parameters lead to ill-conditioning, which leads to instabilities and poor quality results. Hence the reason with standard FEA model, when the mesh was refined, the penalty formulation was no longer suitable.

In terms of the frictional contact problems, we compared our results to the ideal uncoupled analytical solutions. A good correlation, in terms of the contact area radius was found between our numerical models and analytical solution. A relatively good agreement between the normal contact tractions was found as well, particularly for the purely stick case. A slight deviation in the tangential tractions was observed. This deviation is to be expected due to the assumptions made on the analytical solution - uncoupling the tangential tractions and normal tractions. In fact, for the frictional problems, a good reference point is the standard FEA results: we know that with a sufficiently fine mesh, the numerical solution converges towards the true solution. Comparing our relatively coarse numerical model with a fine mesh resolution in standard FEA, we found both results, in terms of the distribution of contact stresses across the contact area, to be similar. This is even more evident in the case of partial slip (deformable on deformable frictional contact problem), where the analytical solution (again uncoupled, and therefore idealized) predicts a symmetric distribution of both the normal and tangential contact stresses. However, looking at both IGA and standard FEA, we observed this not be the case. The stress distribution was skewed for both normal and tangential stresses. Similarly, the contact area, stick zone and slip zone were found not to be symmetric. However the total contact area was in good correlation with the analytical solution. Of course, the results for the IGA model were obtained with a much coarser mesh, compared to standard FEA Abagus models. Note: due to the improved accuracy observed with the cubic discretization in the friction-less contact and purely stick case, cubic Bézier elements were used for the partial slip case.

Having successfully verified and validated our numerical scheme for the resolution of contact problems, particularly its ability to recover accurately the contact stresses, Bézier-based method is then extended into contact-impact vibro-acoustics. This is main subject of the two final chapter. The Bézier-based scheme was used to calculate, in time domain, the dynamics and acoustic radiation of forced vibrating plates embedded in a baffle. In chapter 5 we apply the NTS contact formulation, coupled it with the explicit central differences method and Bézier-based

IGA, to model the impact of the plate embedded in a rigid baffle, by a small sphere. The contact was assumed friction-less and therefore unilateral. With this explicit time integration, the contact force and the dynamic response are computed for each time step, with the dynamics (acceleration) then used in the evaluation of the Rayleigh integral equation to obtain the acoustic pressure field. In fact, the code performs a joint contact-impact and acoustic response numerical simulation. A multi-patch framework again was adopted for the ease of representing the geometry of the plate and the sphere. The results obtained were similar to that of the reference case (with analytical contact force and implicit time integration), both for the dynamic response and the acoustic pressure field. This proves our model, particularly the contact-impact algorithm is accurate. Again, we found that with the cubic Bézier elements and even with a coarse mesh, particularly for the contact region, we could still recover good quality results.

The last section of chapter 5 is dedicated towards sensitivity analysis. We have evaluated the influence of (1) the order of the Bézier elements and mesh size, (2) the choice of the time integration scheme used, and finally (3) the time step size. For (1) the error committed on the prediction on the natural frequency was used to characterize the mesh parameters, which compared the evolution of the error with respect to the number of nodes per patch edge of the plate as well as the discretization order. The cubic discretization was superior and it was found that beyond 8 elements across the edge of the patch, the refinement does not bring any more improvement on the quality of the solution. For the full model (the joint contact-impact and acoustics) we used the central differences which is prone to spurious oscillations for this class of problems. This scheme was compared to those proposed by Noh and Bathe [135] (NB) and Kim and Lee [137] (KL), which are meant to be an improvement of the central differences. Not much difference was observed in terms of the results obtained for the dynamic response and the acoustic pressure field, though the two schemes, NB and KL, were found to be more expensive than the central differences method. However, increasing the time step size, we found that the NB and KL, gave the same result as the original central differences scheme, in terms of the calculated contact forces, impact contact duration and the acoustic pressure field, at only a fraction of the resolution time of the central differences scheme.

In the first part of chapter 6 we characterize the dynamics and visualize the acoustic field: first of a plate impacted by a small sphere however with the contact force assumed analytical, and second we simulate the phenomena of a moving force (think of a moving vehicle) and study its dynamics and the resulting acoustic radiation. The dynamic response was obtained using the implicit Newmark method, and the acoustic response calculated using the Rayleigh integral equation. Even though the temporal discretization used is unconditionally stable, due to the nature of the problem being studied (impact event and wave propagation), we know that a large portion of the interesting characteristics, in terms of the dynamic response, is contained within a short duration, and therefore we need fine time steps to capture this transient phase. Hence, the time step size is still limited by the critical time step of the explicit central differences method stability criteria. In terms of our findings, in line with literature, the dynamic response correlated well with the acoustic response, specifically for the observation point at the axis of impact, we could distinctly discern the three phases of the dynamic response and the resulting acoustic

radiation: from the propagation of the transient acoustic wave as a result of the initial rapid deformation of the plate at the impact point, and the appearance of ripples due to generation and outward propagation of the bending waves, the silent phase (almost zero acoustic pressure) that follows as the bending waves of higher frequency than the critical frequency propagate towards the edge of the plate and reflect back, and finally the ringing phase as the reflected bending waves reach the observation point. These bending waves have an oblique wave front, which is why they do not reach the on-axis observation point as they propagate towards the edge of the plate, only once reflected back do they reach the center axis. As the observation point moves further away from the axis of impact, these three phases becomes increasingly difficult to distinguish as these points are simultaneously reached by propagating the reflecting bending waves. This chaotic nature of the acoustic field where propagating and reflected bending waves simultaneously reach the observation point, is even more amplified in the case of the moving force - the silent phase is non existent. Where in the case of centered impact there is delay before the bending waves are reflected back from the edge, with the moving force, almost immediately after the beginning of the transit of the force, bending waves are being reflected. The information learned here, particularly for the centered impact part was especially useful and used to verify the results of chapter 5, where now we explicitly model the impact event instead of using an analytical contact force. We found that our full model correlated very well with the is reference case.

Observations and Future Works

Even though the developed scheme gave superior results compared to standard FEA, in particular for the friction-less case, and offered a better performance on per degree of freedom basis, it is not without limitations. In the section we highlight some of these drawbacks and propose some recommendations on how they can be remedied. These include:

• In the implementation the contact search was performed locally, element wise. In fact, even the closest point projection is conducted element wise. Recall that the Bézier elements are C^0 continuous. The implication of this element wise projection is the possibility of having the same problem encountered in standard FEA: loss of uniqueness of the normals, thus leading to numerical instabilities and spurious nonphysical oscillations, particularly in large deformation sliding conditions. A quick fix for this, without employing contact smoothing techniques, it to perform the projection at patch level. Remember with this Bézier model, we have localized the global smooth topology information into the local element level. However, the Bézier extraction operator allows us to switch between the two levels, it is the link between the NURBS/BSplines and the local Bézier elements. In the same way, the Bézier inverse matrix projects the control quantities into the physical geometry. Therefore, the projection algorithm can be modified to search for contact patch-wise; once the projection point is known, it can then be projected back into the Bézier space. Care would still need to be taken when handling the patch boundaries (these are C^0 at patch

level) in the case of a multi-patch model, should the projection jump across the patch boundaries.

- The dynamic contact-impact problem considered in this thesis was friction-less, and therefore both explicit and implicit global time integration schemes were appropriate. However, dynamic friction, particularly with an explicit scheme, is not trivial. It could be interesting to evaluate how this scheme behaves under dynamic frictional contact.
- The motivation behind the use of the Bézier-based IGA model for the characterization of the dynamic and acoustic response, in the full joint model, is the accurate recovery of contact forces. In doing this, it gives us capabilities of studying even more complex geometries, compared to the plate/sphere model considered here, where access to the analytical forces is not a possibility. We have observed that our model is capable of predicting the physics of this contact-impact vibro-acoustics problem, and this should be transferable for the more complex geometries undergoing the same contact interaction. So, it could be interesting to explore more geometries.
- The numerical scheme developed has been designed in such a way that it should easily fit into existing FE codes, particularly the solvers. In fact, one of the motivation for this approach is its practicality. Majority of the effort goes towards geometry manipulation and mesh generation, and finally constructing the data structures to fit into existing FE codes. If all this is done successfully, and with the appropriate basis functions in the shape functions routine, this method can be easily integrated into existing codes, i.e. as a plug in module. This can also be the next step. In this work, we had to write all code, from geometry and its discretization, to the solver and the post-processing routine. If the scheme can work in conjunction with commercial code or any FE code, it could open up even more possibilities.
- Lastly, due to the critical importance of contact in many industries, from civil engineering, mechanics to environmental and medical applications, the numerical scheme developed in this thesis could have a wide range of applications. On top of the noise generation and propagation study conducted here, we envision this method could be extended to, for instance, friction induced vibrations modeling, progressive damage or premature damage prediction. In essence, the developed scheme is ultimately applicable to any problem where the description of contacting surfaces is of high importance. In the future, it could be interesting to explore the use of this methods for more of these applications.



Linearized Contact Integrals

The linearization of contact integrals in the weak formulation in eq. (3.91) writes as:

$$\Delta G_c = \int_{\Gamma_c^{normal}} \left(\Delta t_N \delta g_N + t_N \Delta \delta g_N \right) d\Gamma + \int_{\Gamma_c^{tangent}} \left(\Delta t_{T\alpha} \delta \bar{\xi}^{\alpha} + t_{T\alpha} \Delta \delta \bar{\xi}^{\alpha} \right) d\Gamma \tag{A.1}$$

Linearized contact variables $\Delta \delta g_N$ and $\Delta \delta \bar{\xi}^{\alpha}$ derive from variation of the normal gap. Starting from eq. (3.48), the gap normal can be rearranged as follows:

$$\mathbf{x}^1 - \bar{\mathbf{x}}^2 = g_N \bar{\mathbf{n}} \tag{A.2}$$

Taking the variation of eq. (A.2) leads to:

$$\delta \mathbf{x}^1 - \delta \bar{\mathbf{x}}^2 - \bar{\mathbf{x}}^2_{\alpha} \delta \bar{\xi}^{\alpha} = \delta g_N \bar{\mathbf{n}} + g_N \delta \bar{\mathbf{n}}$$
(A.3)

The linearization of eq. (A.3) gives us:

$$\underbrace{\Delta \delta \mathbf{x}^{1} - \Delta \delta \bar{\mathbf{x}}^{2}}_{=0} - \left(\delta \bar{\mathbf{x}}_{,\alpha}^{2} \Delta \bar{\xi}^{\alpha} + \Delta \bar{\mathbf{x}}_{,\alpha}^{2} \delta \bar{\xi}^{\alpha} + \bar{\mathbf{x}}_{,\alpha\beta}^{2} \Delta \bar{\xi}^{\alpha} \delta \bar{\xi}^{\beta} + \bar{\mathbf{x}}_{,\alpha}^{2} \Delta \delta \bar{\xi}^{\alpha}\right) = \Delta \delta g_{N} \bar{\mathbf{n}} + \delta g_{N} \Delta \bar{\mathbf{n}} + \Delta g_{N} \delta \bar{\mathbf{n}} + g_{N} \Delta \delta \bar{\mathbf{n}}$$
(A.4)

Taking the dot product of eq. (A.4) and the unit normal vector $\bar{\mathbf{n}}$ gives us the expression for $\Delta \delta g_N$. Since $\bar{\mathbf{x}}^2_{,\alpha} \cdot \bar{\mathbf{n}} = 0$ and identity $\bar{\mathbf{n}} \cdot \delta \bar{\mathbf{n}} = 0$, we have :

$$\Delta \delta g_N = \underbrace{-\left(\delta \bar{\mathbf{x}}_{,\alpha}^2 \Delta \bar{\xi}^{\alpha} + \Delta \bar{\mathbf{x}}_{,\alpha}^2 \delta \bar{\xi}^{\alpha} + \bar{\mathbf{x}}_{,\alpha\beta}^2 \Delta \bar{\xi}^{\alpha} \delta \bar{\xi}^{\beta}\right) \cdot \bar{\mathbf{n}}}_{\text{Term 1}} + \underbrace{g_N \bar{\mathbf{n}} \cdot \Delta \delta \bar{\mathbf{n}}}_{\text{Term 2}}$$
(A.5)

All quantities in eq. (A.5) are known except for the quantity $\Delta \delta \bar{\mathbf{n}}$ in Term 2. Variation and linearization of the projection point convective coordinate $\bar{\xi}^{\alpha}$ have been derived and can be found in eq. (3.54) and eq. (3.93), respectively. To derive the expression for $\Delta \delta \bar{\mathbf{n}}$, from the identity $\bar{\mathbf{n}} \cdot \delta \bar{\mathbf{n}} = 0$ we can write:

$$\Delta \left(\bar{\mathbf{n}} \cdot \delta \bar{\mathbf{n}} \right) = \Delta \bar{\mathbf{n}} \cdot \delta \bar{\mathbf{n}} + \bar{\mathbf{n}} \cdot \Delta \delta \bar{\mathbf{n}} = 0 \quad \Rightarrow \quad g_N \bar{\mathbf{n}} \cdot \Delta \delta \bar{\mathbf{n}} = -g_N \Delta \bar{\mathbf{n}} \cdot \delta \bar{\mathbf{n}} \tag{A.6}$$

The linearization and variation of the normal vector follows from the orthogonality condition $\bar{\mathbf{x}}_{,\alpha}^2 \cdot \bar{\mathbf{n}} = 0$, which gives :

$$\delta(\bar{\mathbf{n}} \cdot \boldsymbol{\tau}_{\alpha}) = \bar{\mathbf{n}} \cdot \delta \boldsymbol{\tau}_{\alpha} + \delta \bar{\mathbf{n}} \cdot \boldsymbol{\tau}_{\alpha} \quad \Rightarrow \quad \delta \bar{\mathbf{n}} = -(\bar{\mathbf{n}} \cdot \delta \boldsymbol{\tau}_{\alpha}) \, \boldsymbol{\tau}^{\alpha}$$

$$= -(\bar{\mathbf{n}} \cdot \delta \boldsymbol{\tau}_{\alpha}) \, m^{\alpha\beta} \boldsymbol{\tau}_{\beta}$$
(A.7)

with

$$\delta \boldsymbol{\tau}_{\alpha} = \delta \bar{\mathbf{x}}_{,\alpha}^2 + \bar{\mathbf{x}}_{,\alpha\beta}^2 \delta \bar{\xi}^{\beta} \tag{A.8}$$

The linearization $\Delta \bar{\mathbf{n}}$ and $\Delta \boldsymbol{\tau}_{\alpha}$ follow in the same way as in eq. (A.7) and eq. (A.8). Finally, we have :

$$\Delta \delta g_N = -\left[\delta \bar{\mathbf{x}}_{,\alpha} \Delta \xi^{\alpha} + \Delta \bar{\mathbf{x}}_{,\alpha} \delta \xi^{\alpha} + \bar{\mathbf{x}}_{,\alpha\beta} \Delta \xi^{\alpha} \delta \xi^{\beta}\right] \cdot \bar{\mathbf{n}} + \frac{g_N}{m_{\alpha\beta}} \left[\left(\delta \bar{\mathbf{x}}_{,\alpha} + \bar{\mathbf{x}}_{,\alpha\gamma} \delta \xi^{\gamma}\right) \bar{\mathbf{n}} \otimes \bar{\mathbf{n}} \left(\Delta \bar{\mathbf{x}}_{,\beta} + \bar{\mathbf{x}}_{,\beta\delta} \Delta \xi^{\delta}\right) \right]$$
(A.9)

 $\Delta \delta \bar{\xi}^{\alpha}$ also derives from eq. (A.4); we take the product of eq. (A.4) with the tangential vector τ_{α} , which yields:

$$-m_{\alpha\beta}\Delta\delta\bar{\xi}^{\beta} = \underbrace{\left(\delta\bar{\mathbf{x}}_{,\beta}^{2}\Delta\bar{\xi}^{\beta} + \Delta\bar{\mathbf{x}}_{,\beta}^{2}\delta\bar{\xi}^{\beta} + \bar{\mathbf{x}}_{,\beta\gamma}^{2}\Delta\bar{\xi}^{\beta}\delta\bar{\xi}^{\gamma}\right)\cdot\boldsymbol{\tau}_{\alpha}}_{\text{Term 1}} + \underbrace{\delta g_{N}\Delta\bar{\mathbf{n}}\cdot\boldsymbol{\tau}_{\alpha}}_{\text{Term 2}} + \underbrace{\Delta g_{N}\delta\bar{\mathbf{n}}\cdot\boldsymbol{\tau}_{\alpha}}_{\text{Term 3}} + \underbrace{g_{N}\Delta\delta\bar{\mathbf{n}}\cdot\boldsymbol{\tau}_{\alpha}}_{\text{Term 4}}$$
(A.10)

Term 1 in eq. (A.10) is known; it remains to expand and give expression for Terms 2-3. Starting with term 3, we need the expression of $\Delta \delta \bar{\mathbf{n}} \cdot \boldsymbol{\tau}_{\alpha}$. From :

$$\Delta \left[\delta \left(\boldsymbol{\tau}_{\alpha} \cdot \bar{\mathbf{n}} \right) \right] = \Delta \left(\delta \boldsymbol{\tau}_{\alpha} \cdot \bar{\mathbf{n}} + \boldsymbol{\tau}_{\alpha} \cdot \delta \bar{\mathbf{n}} \right) = 0$$

$$= \Delta \delta \boldsymbol{\tau}_{\alpha} \cdot \bar{\mathbf{n}} + \delta \boldsymbol{\tau}_{\alpha} \cdot \Delta \bar{\mathbf{n}} + \Delta \boldsymbol{\tau}_{\alpha} \cdot \delta \bar{\mathbf{n}} + \boldsymbol{\tau}_{\alpha} \cdot \Delta \delta \bar{\mathbf{n}}$$
(A.11)

We can rearrange eq. (A.11) to write $\tau_{\alpha} \cdot \Delta \delta \bar{\mathbf{n}}$

$$\boldsymbol{\tau}_{\alpha} \cdot \Delta \delta \bar{\mathbf{n}} = -\left(\Delta \delta \boldsymbol{\tau}_{\alpha} \cdot \bar{\mathbf{n}} + \delta \boldsymbol{\tau}_{\alpha} \cdot \Delta \bar{\mathbf{n}} + \Delta \boldsymbol{\tau}_{\alpha} \cdot \delta \bar{\mathbf{n}}\right) \tag{A.12}$$

where

$$\Delta \delta \boldsymbol{\tau}_{\alpha} = \Delta \left(\delta \bar{\mathbf{x}}_{,\alpha}^{2} + \bar{\mathbf{x}}_{,\alpha\beta}^{2} \delta \bar{\xi}^{\beta} \right)
= \delta \bar{\mathbf{x}}_{,\alpha\beta}^{2} \Delta \bar{\xi}^{\beta} + \Delta \bar{\mathbf{x}}_{,\alpha\beta}^{2} \delta \bar{\xi}^{\beta} + \bar{\mathbf{x}}_{,\alpha\beta\gamma}^{2} \Delta \bar{\xi}^{\beta} \delta \bar{\xi}^{\gamma} + \bar{\mathbf{x}}_{,\alpha\beta}^{2} \Delta \delta \bar{\xi}^{\beta}$$
(A.13)

It remains to expand on term 2 and term 3 in eq. (A.10) as well as the last 2 components in eq. (A.12). Since :

$$\Delta \left[(\delta g_N \bar{\mathbf{n}}) \cdot \boldsymbol{\tau}_{\alpha} \right] = \underbrace{\Delta \delta g_N \bar{\mathbf{n}} \cdot \boldsymbol{\tau}_{\alpha}}_{=0} + \delta g_N \Delta \bar{\mathbf{n}} \cdot \boldsymbol{\tau}_{\alpha} + \delta g_N \bar{\mathbf{n}} \cdot \Delta \boldsymbol{\tau}_{\alpha} = 0$$

$$\Rightarrow \delta g_N \Delta \bar{\mathbf{n}} \cdot \boldsymbol{\tau}_{\alpha} = -\delta g_N \bar{\mathbf{n}} \cdot \Delta \boldsymbol{\tau}_{\alpha}$$
(A.14)

We then have:

$$(\delta g_{N} \Delta \bar{\mathbf{n}} + \Delta g_{N} \delta \bar{\mathbf{n}}) \cdot \boldsymbol{\tau}_{\alpha} - g_{N} \left(\delta \boldsymbol{\tau}_{\alpha} \cdot \Delta \bar{\mathbf{n}} + \Delta \boldsymbol{\tau}_{\alpha} \cdot \delta \bar{\mathbf{n}} \right)$$

$$= - \left[\delta \left(g_{N} \bar{\mathbf{n}} \right) \cdot \Delta \boldsymbol{\tau}_{\alpha} + \Delta \left(g_{N} \bar{\mathbf{n}} \right) \cdot \delta \boldsymbol{\tau}_{\alpha} \right]$$

$$= - \left[\delta \left(\mathbf{x}^{1} - \bar{\mathbf{x}}^{2} \right) \cdot \Delta \boldsymbol{\tau}_{\alpha} + \Delta \left(\mathbf{x}^{1} - \bar{\mathbf{x}}^{2} \right) \cdot \delta \boldsymbol{\tau}_{\alpha} \right]$$

$$= - \left(\delta \mathbf{x}^{1} - \delta \bar{\mathbf{x}}^{2} \right) \cdot \Delta \boldsymbol{\tau}_{\alpha} - \left(\Delta \mathbf{x}^{1} - \Delta \bar{\mathbf{x}}^{2} \right) \cdot \delta \boldsymbol{\tau}_{\alpha} + \bar{\mathbf{x}}_{,\beta}^{2} \delta \bar{\xi}^{\beta} \cdot \Delta \boldsymbol{\tau}_{\alpha} + \bar{\mathbf{x}}_{,\beta}^{2} \Delta \bar{\xi}^{\beta} \cdot \delta \boldsymbol{\tau}_{\alpha}$$

$$(A.15)$$

Substituting eq. (A.8) into eq. (A.15) and then combining with eq. (A.15), we can substitute the final expressions of terms 2,3,4 in eq. (A.10) to obtain:

$$(m_{\alpha\beta} - g_N k_{\alpha\beta}) \, \Delta \delta \bar{\xi}^{\alpha} = -\left(\Delta \bar{\mathbf{x}}_{,\alpha}^2 \delta \bar{\xi}^{\alpha} + \delta \bar{\mathbf{x}}_{,\alpha}^2 \Delta \bar{\xi}^{\alpha}\right) \cdot \boldsymbol{\tau}_{\beta} - \left(\boldsymbol{\tau}_{\alpha} \cdot \boldsymbol{\tau}_{\alpha,\beta} - g_N \bar{\mathbf{n}} \cdot \boldsymbol{\tau}_{\alpha,\alpha\beta}\right) \, \Delta \bar{\xi}^{\gamma} \delta \bar{\xi}^{\gamma} - g_N \left(\Delta \bar{\mathbf{x}}_{,\alpha\beta}^2 \delta \bar{\xi}^{\alpha} + \delta \bar{\mathbf{x}}_{,\alpha\beta}^2 \Delta \bar{\xi}^{\alpha}\right) \cdot \bar{\mathbf{n}} - \left(\delta \bar{\mathbf{x}}_{,\alpha}^2 + \boldsymbol{\tau}_{\alpha,\gamma} \delta \bar{\xi}^{\gamma}\right) \cdot \boldsymbol{\tau}_{\alpha} \Delta \bar{\xi}^{\beta} - \left(\Delta \bar{\mathbf{x}}_{,\alpha}^2 + \boldsymbol{\tau}_{\alpha,\gamma} \Delta \bar{\xi}^{\gamma}\right) \cdot \boldsymbol{\tau}_{\alpha} \delta \bar{\xi}^{\beta} + \left(\delta \mathbf{x}^1 - \delta \bar{\mathbf{x}}^2\right) \cdot \left(\Delta \bar{\mathbf{x}}_{,\beta}^2 + \boldsymbol{\tau}_{\beta,\alpha} \Delta \bar{\xi}^{\alpha}\right) + \left(\Delta \mathbf{x}^1 - \Delta \bar{\mathbf{x}}^2\right) \cdot \left(\delta \bar{\mathbf{x}}_{,\beta}^2 + \boldsymbol{\tau}_{\beta,\alpha} \delta \bar{\xi}^{\alpha}\right)$$

$$(A.16)$$

Return Mapping Algorithm

Consider the graphical representation of the unregularized Coulomb's friction law in fig. B.1. In fig. B.1 (a) we have the relation between the tangential traction and the tangential slip velocity; the blue line represent stick state and the red line represents the slip state. Figure B.1 (b) shows the relation between the contact pressure and the tangential contact traction (the Coulomb's friction cone) - shaded region represents stick state, its closure represents the stick state.

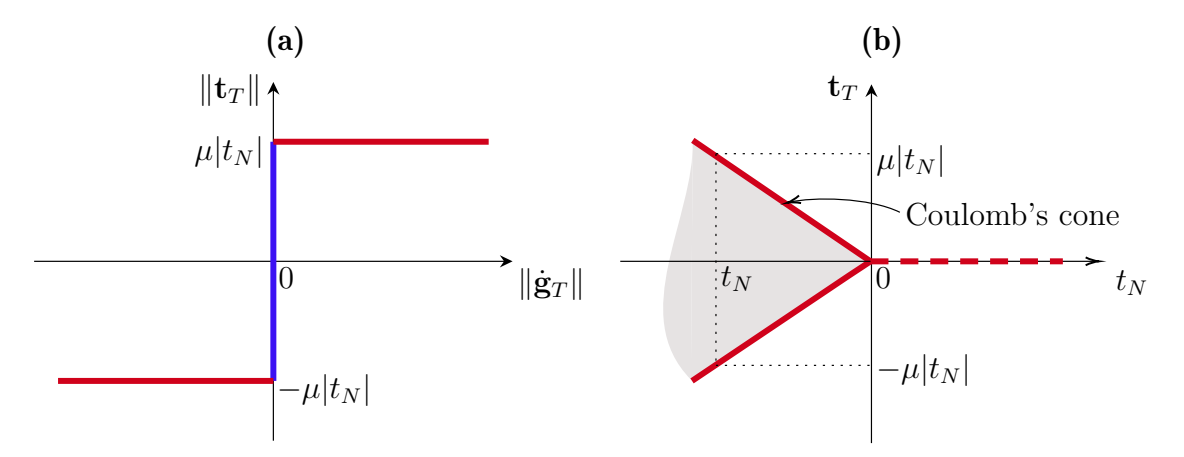


Figure B.1 – Unregularized Coulomb's law of friction : (a) Evolution of the frictional traction $\|\mathbf{t}_T\|$ with the tangential slip velocity $\|\dot{\mathbf{g}}_T\|$, and (b) Coulomb's cone.

A stress-state that fulfills these frictional conditions then corresponds to a unique point either on the interior of the Coulomb's cone or its closure. This behavior is analogous to plasticity formulation, particularly rigid-perfectly plastic constitutive formulation (obtained from elasto plastic constitutive law by setting the hardening modulus to zero and allowing the elasticity modulus to tend towards infinity) [5].

Due to the multivariate and non smoothness nature of the friction conditions in fig. B.1, it is common practice in numerical implementation to regularize these relations to remove this difficulty. And here we regularize the relations in the same way as elasto-perfectly-plastic constitutive law - see chapter B - where the stress is bounded by the yield stress σ_y and at this point plastic flow may occur (plastic strains are accumulated). Table B.1 summarizes the

analogy between friction and plasticity.

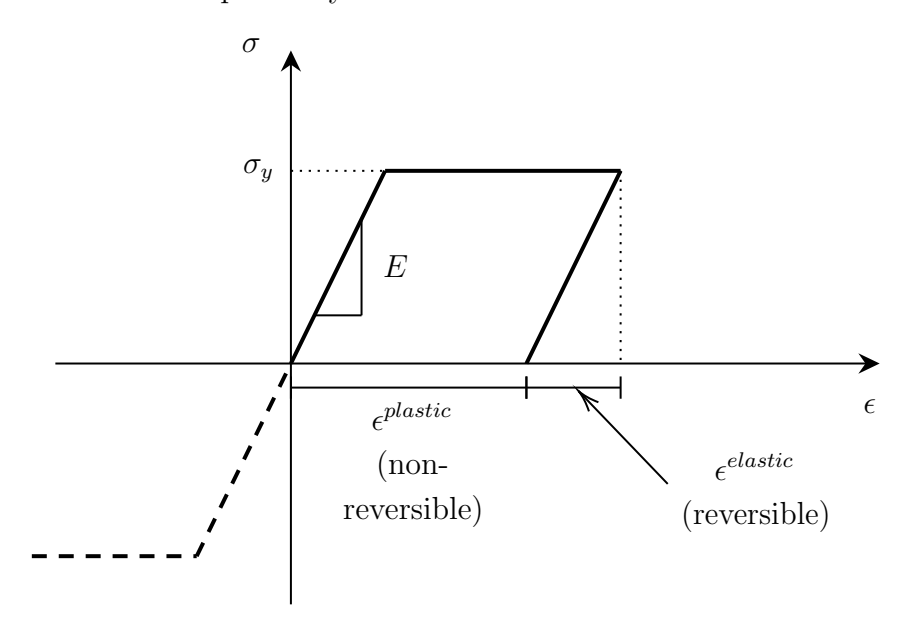


Figure B.2 – One dimensional schematic of the elasto-perfectly-plastic constitutive law, with σ_y the yield strength, E the Young's modulus.

Plasticity	Friction
Yield function : $f(\sigma, \sigma_y) \leq 0$	Slip function : $\Phi(t_N, \mathbf{t}_T) = \mathbf{t}_T - \mu t_N \le 0$
Plastic flow : $\dot{\epsilon}^{plastic} = \dot{\gamma} \frac{\partial f(\sigma, \sigma_y)}{\partial \sigma}$	Slip rate: $\dot{\mathbf{g}}_T^{slip} = \dot{\gamma} \frac{\mathbf{t}_T}{\ \mathbf{t}_T\ }$
Stress-strain : $\sigma = E(\epsilon - \epsilon^{plastic})$	Frictional traction: $\dot{\mathbf{t}}_T = \varepsilon_T \left(\dot{\mathbf{g}}_T - \dot{\gamma} \frac{\mathbf{t}_T}{\ \mathbf{t}_T\ } \right)$
Elastic deformation	Stick state
Yield surface	Coulomb's cone

Table B.1 – Analogies between friction and plasticity constitutive relations, with γ the plastic multiplier/slip [2].

The Kuhn-Tucker conditions for the Coulomb friction in the tangential direction write as:

$$\Phi \le 0, \quad \dot{\gamma} \ge , \quad \dot{\gamma}\Phi = 0 \tag{B.1}$$

The constitutive relations for friction in table B.1 involve rate quantities which, similarly to elasto-plasticity may be discretized using the backward Euler integration scheme and therefore can be solved using the trial state/radial return strategy (return mapping in one dimension). In this strategy, the departure point is the known normal contact traction in current time step t_N^{n+1} . Assuming no slip in the time step, we evaluate the time discretized equations thus giving rise to the trial state. This is then followed by a correction if necessary, the return map, such the predicted traction is situated in the admissible region.

The graphical representation of the strategy for 2D frictional problems is shown in fig. B.3. As it can be seen from fig. B.3 (a), the predicted trial states $[\mathbf{t}_T^{n+1}]^{trial}$ is non-admissible, the traction is located outside the Coulomb's cone. A correction is then necessary to return the surface of the slip function as is done in fig. B.3 (b).

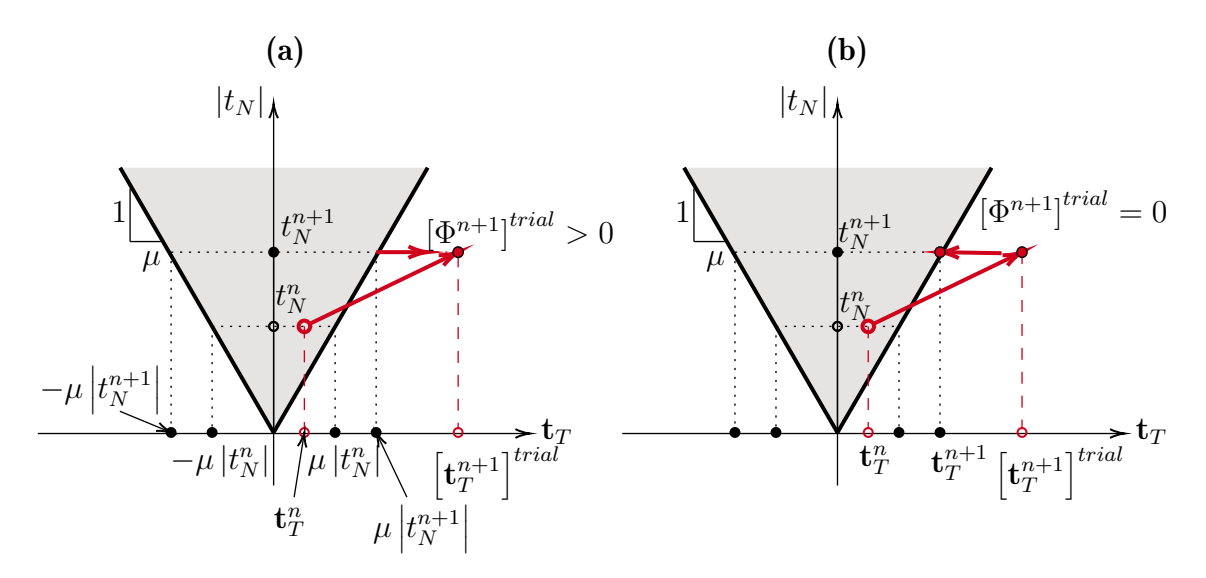


Figure B.3 – Return mapping algorithm in the stress space : (a) initial state - trial state, (b) trial state - solution state.



Analytical Solution for Hertzian Contact Problems

I Classical Hertz Contact Between an Elastic Sphere and a Rigid Plane

Here we detail the analytical solution for the friction-less contact between an elastic sphere and a rigid block. The input parameters for this problem are given in table C.1.

Young's Modulus, E [GPa]	200
Poisson's ratio, ν	0.3
Radius of the sphere, R [m]	0.05
Applied displacement, \bar{u} [m]	2.7×10^{-3}

Table C.1 – Input parameters for the contact between an elastic sphere and a rigid plane.

From the Hertzian analytical solution in [102, 103], the contact area radius a can be computed as follows:

$$a = \sqrt{R^* d} \tag{C.1}$$

where $d \equiv \bar{u}$ is the total prescribed displacement and R^* the effective radius, $R^* = \frac{R}{2}$. The contact pressure (normal) distribution across the contact area is given by

$$p(r) = p_0 \sqrt{1 - \left(\frac{r}{a}\right)^2} \tag{C.2}$$

where $0 \le r \le a$, and p_0 is the maximum contact pressure computed as:

$$p_0 = \frac{3F}{2\pi a^3} \tag{C.3}$$

with

$$F = \frac{4}{3} E^* \sqrt{R} d^{\frac{3}{2}}$$
 (C.4)

where

$$\frac{1}{E^*} = 2\left[\frac{1-\nu^2}{E}\right] \tag{C.5}$$

 E^* is the effective contact stiffness.

The contact radius obtained through the Hertzian solution procedure above is found to be a = 8.21 mm, the maximum contact pressure is found to be $p_0 = 2.3 \times 10^{10}$ Pa. Figure C.1 shows the normalized contact pressure distribution across the contact area.

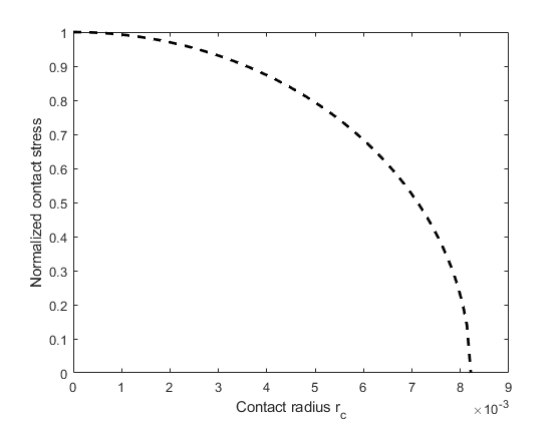


Figure C.1 – The normalized contact pressure of the sphere across the contact area.

II Rigid Punch on an Elastic Half-Space Contact Problem

Consider the contact between a flat ended rigid punch with an elastic half space, schematic in fig. C.2.

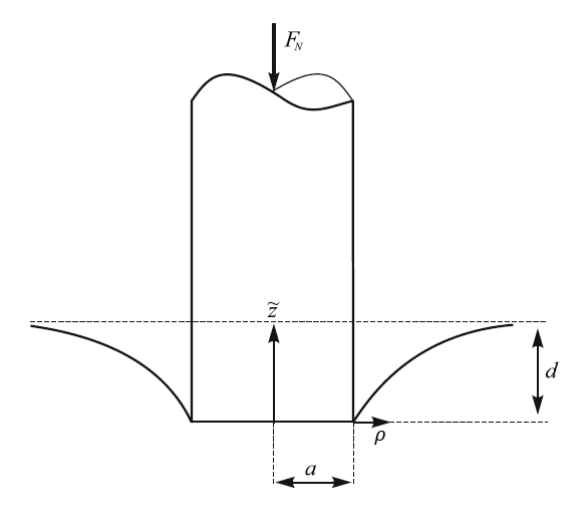


Figure C.2 – Indentation by a cylindrical flat punch.

The input parameters and material parameters are given in table C.2

Young's Modulus, E [GPa]	200
Poisson's ratio, ν	0.3
Half base width, a [m]	0.5
Indentation d [m]	2×10^{-3}

Table C.2 – Input parameters for the contact between a rigid punch and an elastic half space.

Following the method of dimensionality reduction (MDR) detailed in [104]: the analytical contact area equals to half the base of the rigid indenter. In our given problem we have a = 0.5 m. To compute the contact pressure at x = 0, first we compute the effective stiffness E^* as:

$$\frac{1}{E^*} = \frac{1 - \nu^2}{E} \Rightarrow \boxed{\mathbf{E}^* = 2.1978 \times 10^{11} \text{ Pa}}$$
 (C.6)

The normal contact pressure distribution across the contact area is given by:

$$p(\rho) = \frac{p_0}{\sqrt{1 - \left(\frac{\rho}{a}\right)^2}} \tag{C.7}$$

In eq. (C.7) p_0 is the contact pressure at $\rho = 0$ and is computed from

$$p_0 = \frac{E^* d}{\pi a} \tag{C.8}$$

where d in eq. (C.8) is the indentation depth (prescribed as a vertical displacement $\bar{u} = -2$ mm in the rigid problem in section 4.2.2). Substituting the effective stiffness calculated in eq. (C.6) and the contact area radius a, we find $\mathbf{p_0} = \mathbf{279.83}$ MPa.

Figure C.3 shows the contact pressure distribution across the contact area.

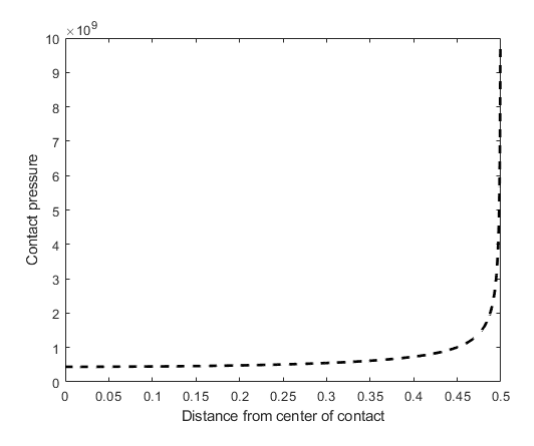


Figure C.3 – Analytical contact pressure distribution across the contact area due to the indentation of the elastic half space.

The corresponding normal force is computed from :

$$F_N = 2\pi a^2 p_0 \tag{C.9}$$

III Compression of Elastic Cylinder on a Rigid Substrate

Consider the schematic in fig. 4.19: an elastic cylinder in contact with a rigid substrate (frictional Hertz contact). The material properties and input parameters are given in table C.3.

Young's Modulus, E [GPa]	200
Poisson's ratio, ν	0.3
Coefficient of friction, μ	0.8
Dundur's constant, β_0	0.5
Radius of the cylinder, R [m]	0.05
Applied displacement \bar{u} [m]	2.7×10^{-3}

Table C.3 – Input parameters for the frictional contact problem between an elastic cylinder and a rigid plane.

To obtain the contact pressure distribution as well as the contact area semi width a, we follow the uncoupled solution approach detailed in [102, 105, 106].

Depending on the value of the tangential forces, the contact area may consist of a mixture of stick zones (where points in contact adhere to each other) and slip zones (tangential relative motion occurs between the contacting point). The tangential traction is limited by friction. Figure C.4 shows the contact interface configuration, made up of the stick zone and slip regions, for contact for dissimilar cylinders (idealized as plane contact).

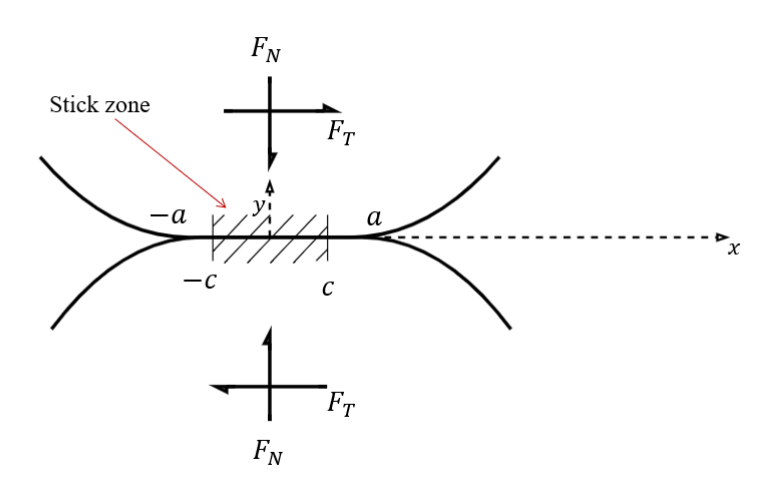


Figure C.4 – Contact configuration : stick zone and slip region.

From Coulomb's law of friction, we have:

$$\begin{cases} \text{stick zone} : |F_T| < \mu F_N, |x| < c \\ \text{slip zone} : |F_T| = \mu F_N c < |x| < a \end{cases}$$
 (C.10)

Johnson [102] gives a relationship of the extent of slip region of dissimilar solids, based on the ratio between the Dundurs' constant β_0 and the coefficient of friction μ . With β_0 and μ values in table C.3, we find the ratio c/a > 0.95. Assumption of pure stick conditions (with uncoupled normal and tangential tractions) may then be sufficient for obtaining a good approximation of the analytical solution. Of course in theory some slip will occur around the edge of contact $|x| \to a$.

The normal contact pressure distribution is given by:

$$p(x) = p_0 \sqrt{1 - \left(\frac{x}{a}\right)^2} \tag{C.11}$$

where

$$\kappa = \frac{1}{R_1} + \frac{1}{R_2} = \frac{2}{R} \text{ and } A = 2\left[\frac{1-\nu_1^2}{E_1} + \frac{1-\nu_2^2}{E_2}\right] = 2\left(2\frac{1-\nu^2}{E}\right)$$
(C.12)

Using the dimensions and properties give above $\kappa = 40$ and $A = 1.82 \times 10^{-11}$. For an applied displacement in fig. 4.19, the total normal reaction force is $F_N = 1.49055 \times 10^8$ N. We can compute the contact area semi width a as follows:

$$a = \sqrt{\frac{2F_N A}{\pi \kappa}} = 6.57083 \text{ mm}$$
 (C.13)

The maximum normal contact pressure follows from

$$p_0 = \frac{\kappa a}{A} = 1.44414 \times 10^{10} \text{ Pa}$$
 (C.14)

For purely stick conditions, the tangential traction is given by:

$$q(x) = \frac{\beta_0 p_0}{\pi a} \left[\sqrt{a^2 - x^2} \ln \left| \frac{a + x}{a - x} \right| + x \ln \left\{ \frac{a + \sqrt{a^2 + x^2}}{a - \sqrt{a^2 - x^2}} \right\} \right]$$
(C.15)

The obtained solution is shown in fig. C.5

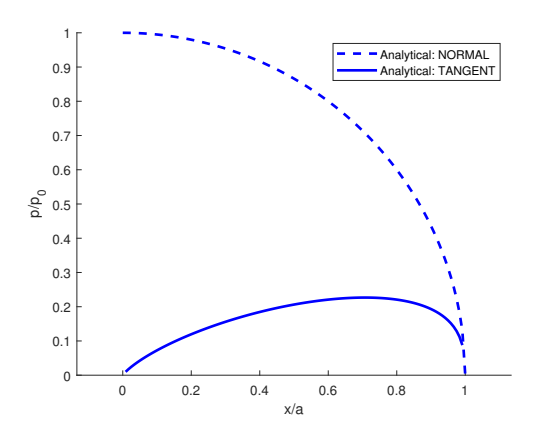


Figure C.5 – Purely stick contact analytical solution.

IV Hertz Contact Between Deformable Bodies

The solution for the problem in fig. 4.23 derives from the analytical solution detailed in [105, 106] for the case of two elastically similar cylinders, uncoupled (assume that the tangential traction has no effect on the normal pressure). Here, we have contact under partial slip conditions.

Table C.4 contains the input parameters and material properties for the problem in fig. 4.23.

Young's Modulus, E [Pa]	1
Poisson's ratio, ν	0.3
Coefficient of friction, μ	0.2
Radius of the cylinder, R [m]	1
Normal force F_N [N]	6.02×10^{-4}
Tangential force F_T [N]	1.08×10^{-4}

Table C.4 – Input parameters for the frictional Hertz contact between two deformable bodies.

From eq. (C.10) it is apparent that for sliding conditions:

$$|q(x)| = -\mu p(x) \tag{C.16}$$

where the normal pressure is Hertzian (see eq. (C.11)) and p_0 as computed from eq. (C.14). The tangential traction is then the composite of the stick zone shear tractions and slip zones traction in eq. (C.16).

$$q(x) = \begin{cases} \mu p_0 \sqrt{1 - \left(\frac{x}{a}\right)^2} - \mu p_0 \left(\frac{c}{a}\right) \sqrt{1 - \left(\frac{x}{c}\right)^2} & : |x| \le c \\ \mu p_0 \sqrt{1 - \left(\frac{x}{a}\right)^2} & : c < |x| \le a \end{cases}$$
 (C.17)

We compute the ratio c/a as

$$\frac{c}{a} = \sqrt{1 - \left| \frac{F_T}{\mu F_N} \right|} \tag{C.18}$$

For the total normal and tangential reaction forces obtained from the loading in fig. 4.24, and the material properties in table C.4, we have :

- Maximum normal pressure $p_0 = 10.2587 \times 10^{-3}$
- Contact area semi width $a = 3.7342 \times 10^{-2}$
- Stick zone semi width $c = 1.18102 \times 10^{-2}$

BIBLIOGRAPHY

- [1] M.E. Matzen. Isogeometrische Modellierung und Diskretisierung von Kontaktproblemen. PhD thesis, Universität Stuttgart, Germany, 2015.
- [2] V.A. Yastrebov. Computational Contact Mechanics: Geometry, Detection and Numerical Techniques. PhD thesis, École Nationale Supérieure des Mines de Paris, France, 2011.
- [3] P. Wriggers. Computational Contact Mechanics. Springer-Verlag, 2nd edition, 2006.
- [4] Z.H. Zhong. Finite Element Procedures for Contact-Impact Problems. Oxford science publications. Oxford University Press, 1993.
- [5] T.A. Laursen. Computational Contact and Impact Mechanics. Fundamentals of Modeling Interfacial Phenomena in Nonlinear Finite Element Analysis. Springer-Verlag, 1st edition, 2003.
- [6] V.A. Yastrebov. Numerical Methods in Contact Mechanics. John Wiley & Sons Inc, 2013.
- [7] A. Meziane, L. Baillet, and B. Laulagnet. Experimental and Numerical Investigation of Friction-Induced Vibration of a Beam-On-Beam in Contact with Friction. *Applied Acoustics*, 71:843–853, 2010. doi: 10.1016/j.apacoust.2010.04.012.
- [8] R.A. Ibrahim. Friction-Induced Vibration, Chatter, Squeal, and Chaos Part II: Dynamics and Modeling. *ASME Applied Mechanics Reviews*, 47(7):227–253, 1994. doi: 10.1115/1.3111080.
- [9] R.A. Ibrahim. Friction-Induced Vibration, Chatter, Squeal, and Chaos Part I: Mechanics of Contact and Friction. *ASME Applied Mechanics Reviews*, 47(7):209–226, 1994. doi: 10.1115/1.3111079.
- [10] A. Oulmane and A. Ross. Effects of Material Parameters on the Transient Dynamics of an Impacted Plate with Partial Constrained Layer Damping Treatment. The Journal of the Acoustical Society of America, 147(3):1939–1952, 2020. ISSN 0001-4966. doi: 10.1121/10.0000890. URL http://asa.scitation.org/doi/10.1121/10.0000890.
- [11] A. Akay. A Review of Impact Noise. The Journal of the Acoustical Society of America, 64(4):977-987, 1978. ISSN 0001-4966. doi:10.1121/1.2773928. URL http://asa.scitation.org/doi/10.1121/1.2773928.
- [12] T.R.J. Hughes, Y. Cottrell, and Y. Bazilevs. Isogeometric Analysis: CAD, Finite Elements, NURBS, Exact Geometry and Mesh Refinement. Computer Methods in Applied Mechanics and Engineering, 194:4135–4195, 2005. doi: 10.1016/j.cma.2004.10.008.
- [13] J.A. Cottrell, T.J.R. Hughes, and Y. Bazilevs. *Isogeometric Analysis : Toward Integration of CAD and FEA*. John Wiley & Sons Ltd, 2009. ISBN 978-0-470749-09-8.

- [14] B. Szabos, A. Duster, and E. Rank. The p-Version of the Finite Element Method, in: E. Stein, R. de Boorst, T.J.R. Hughes, 2004.
- [15] P. Wriggers, L. Krstulovic-Opara, and J. Korelc. Smooth C¹-Interpolations for Two-Dimensional Frictional Contact Problems. *International Journal for Numerical Methods in Engineering*, 51(12):1469–1495, 2001. doi: https://doi.org/10.1002/nme.227. URL https://onlinelibrary.wiley.com/doi/abs/10.1002/nme.227.
- [16] L. Krstulović-Opara, P. Wriggers, and J. Korelc. A C¹-Continuous Formulation for 3D Finite Deformation Frictional Contact. Computational Mechanics, 29(1):27–42, 2002. ISSN 1432-0924. doi: 10.1007/s00466-002-0317-z. URL https://doi.org/10.1007/s00466-002-0317-z.
- [17] V. Padmanabhan and T.A. Laursen. A Framework for Development of Surface Smoothing Procedures in Large Deformation Frictional Contact Analysis. *Finite Elements in Analysis and Design*, 37(3):173–198, 2001. ISSN 0168-874X. doi: https://doi.org/10.1016/S0168-874X(00)00029-9. URL https://www.sciencedirect.com/science/article/pii/S0168874X00000299.
- [18] R.A. Sauer. Local Finite Element Enrichment Strategies for 2D Contact Computations and a Corresponding Post-Processing Scheme. *Computational Mechanics*, 52(2):301–319, 2013. doi: 10.1007/s00466-012-0813-8.
- [19] C.J. Corbett and R. A. Sauer. NURBS-enriched Contact Finite Elements. Computer Methods in Applied Mechanics and Engineering, 275:55-75, 2014. ISSN 0045-7825. doi: https://doi.org/10.1016/j.cma.2014.02.019. URL https://www.sciencedirect.com/science/article/pii/S0045782514000760.
- [20] M. Stadler, G. A. Holzapfel, and J. Korelc. C^n Continuous Modelling of Smooth Contact Surfaces using NURBS and Application to 2D Problems. *International Journal for Numerical Methods in Engineering*, 57(15):2177–2203, 2003. doi: https://doi.org/10.1002/nme.776. URL https://onlinelibrary.wiley.com/doi/abs/10.1002/nme.776.
- [21] M. Al-Dojayli and S.A. Meguid. Accurate Modeling of Contact using Cubic Splines. Finite Elements in Analysis and Design, 38(4):337–352, 2002. ISSN 0168-874X. doi: https://doi.org/10.1016/S0168-874X(01)00088-9. URL https://www.sciencedirect.com/science/article/pii/S0168874X01000889. Multi-field Finite Elements.
- [22] L. De Lorenzis, P. Wriggeres, and T.J.R. Hughes. Isogeometric Contact: A Review. Gesellschaft f. Angewandte Mathematik und Mechanik, 37:85–123, 2014. doi: 10.1002/gamm.201410005.
- [23] L. De Lorenzis, P. Wriggers, and C. Weißenfels. Computational contact mechanics with the finite element method. In Erwin Stein, René de Borst, and Thomas J R Hughes, editors, Encyclopedia of Computational Mechanics Second Edition, pages 1–45. John Wiley & Sons, Ltd, Chichester, UK, 2017. URL http://doi.wiley.com/10.1002/9781119176817. ecm2033.

- [24] V. Agrawal and S.S. Gautam. IGA: A Simplified Introduction and Implementation Details for Finite Element Users. *Journal of The Institution of Engineers (India): Series C*, 100 (3):561–585, 2019. doi: 10.1007/s40032-018-0462-6.
- [25] V. Agrawal and S.S. Gautam. Varying-Order NURBS Discretization: An Accurate and Efficient Method for Isogeometric Analysis of Large Deformation Contact Problems. Computer Methods in Applied Mechanics and Engineering, 367:113–125, 2020. doi: 10.1016/j.cma.2020.113125.
- [26] J.A. Evans, Y. Bazilevs, I. Babuska, and T.J.R. Hughes. n-Widths Sup-Infs and Optimality Ratios for the k-Version of the Isogeometric Finite Element Method. Computer Methods in Applied Mechanics and Engineering, 198(21):1726-1741, 2009. ISSN 0045-7825. doi: https://doi.org/10.1016/j.cma.2009.01.021. URL https://www.sciencedirect.com/science/article/pii/S0045782509000280.
- [27] D. Grossmann, B. Jüttler, H. Schlusnus, J. Barner, and A-V. Vuong. Isogeometric Simulation of Turbine Blades for Aircraft Engines. *Computer Aided Geometric Design*, 29:519—531, 10 2012. doi: 10.1016/j.cagd.2012.03.002.
- [28] C. Verhoosel, M.A. Scott, R. Borst, and T.J.R. Hughes. An Isogeometric Approach to Cohesive Zone Modeling. *International Journal for Numerical Methods in Engineering*, 87:336–360, 2011. doi: 10.1002/nme.3061.
- [29] R. Dimitri, L. De Lorenzis, P. Wriggers, and G. Zavarise. NURBS- and T-spline-based Isogeometric Cohesive Zone Modeling of Interface Debonding. *Computational Mechanics*, 54(2):369–388, 2014. ISSN 1432-0924. doi:10.1007/s00466-014-0991-7. URL https://doi.org/10.1007/s00466-014-0991-7.
- [30] R. Dimitri and G. Zavarise. Isogeometric Treatment of Frictional Contact and Mixed Mode Debonding Problems. *Computational Mechanics*, 60(2):315–332, 2017. ISSN 1432-0924. doi:10.1007/s00466-017-1410-7. URL https://doi.org/10.1007/s00466-017-1410-7.
- [31] G. Bhardwaj, S. K. Singh, I. V. Singh, B. K. Mishra, and Timon Rabczuk. Fatigue Crack Growth Analysis of an Interfacial Crack in Heterogeneous Materials using Homogenized XIGA. *Theoretical and Applied Fracture Mechanics*, 85:294–319, 2016. ISSN 0167-8442. doi: https://doi.org/10.1016/j.tafmec.2016.04.004. URL https://www.sciencedirect.com/science/article/pii/S0167844215302421.
- [32] S. K. Singh, I. V. Singh, B. K. Mishra, and G. Bhardwaj. Analysis of Cracked Functionally Graded Material Plates using XIGA based on Generalized Higher-Order Shear Deformation Theory. *Composite Structures*, 225, 2019. ISSN 0263-8223. doi: https://doi.org/10.1016/j.compstruct.2019.111038. URL https://www.sciencedirect.com/science/article/pii/S0263822319301217.
- [33] Y. Bazilevs, V. M. Calo, T. J. R. Hughes, and Y. Zhang. Isogeometric Fluid-Structure Interaction: Theory, Algorithms, and Computations. *Computational Mechanics*, 43(1):

- 3-37, 2008. ISSN 1432-0924. doi: 10.1007/s00466-008-0315-x. URL https://doi.org/10.1007/s00466-008-0315-x.
- [34] J.A. Cottrell, A. Reali, Y. Bazilevs, and T.J.R. Hughes. Isogeometric Analysis of Structural Vibrations. *Computer Methods in Applied Mechanics and Engineering*, 195(41):5257–5296, 2006. doi: https://doi.org/10.1016/j.cma.2005.09.027. John H. Argyris Memorial Issue. Part II.
- [35] A. Alia. Ultrasonic Diffraction by a Circular Transducer: Isogeometric Analysis Sensitivity to Full Gauss Quadrature Points. *The Journal of the Acoustical Society of America*, 147(2):EL74–EL79, 2020. ISSN 0001-4966. doi: 10.1121/10.0000591. URL http://asa.scitation.org/doi/10.1121/10.0000591.
- [36] R. N. Simpson, M. A. Scott, M. Taus, D. C. Thomas, and H. Lian. Acoustic Isogeometric Boundary Element Analysis. Computer Methods in Applied Mechanics and Engineering, 269:265-290, 2014. doi: 10.1016/j.cma.2013.10.026. URL http://dx.doi.org/10.1016/ j.cma.2013.10.026.
- [37] M.E. Matzen, T. Cichosz, and M. Bischoff. A Point to Segment Contact Formulation for Isogeometric, NURBS based Finite Elements. *Computer Methods in Applied Mechanics and Engineering*, 255:27–39, 2013. doi: 10.1016/j.cma.2012.11.011.
- [38] I. Temizer, P. Wriggers, and T.J.R. Hughes. Contact Treatment in Isogeometric Analysis with NURBS. *Computer Methods in Applied Mechanics and Engineering*, 200:1100–1112, 2011. doi: 10.1016/j.cma.2010.11.020.
- [39] I. Temizer, P. Wriggers, and T.J.R. Hughes. Three-dimensional Mortar-based Frictional Contact Treatment in Isogeometric Analysis with NURBS. *Computer Methods in Applied Mechanics and Engineering*, 209(201):115–128, 2012. doi: 10.1016/j.cma.2011.10.014.
- [40] J. Lu. Isogeometric Contact Analysis: Geometric Basis and Formulation for Frictionless Contact. Computer Methods in Applied Mechanics and Engineering, 200:726–741, 2011. doi: 10.1016/j.cma.2010.10.001.
- [41] L. De Lorenzis, I. Temizer, P. Wriggers, and G. Zavarise. A Large Deformation Frictional Contact Formulation using NURBS-based Isogeometric Analysis. *International Journal for Numerical Methods in Engineering*, 87:1278–1300, 2011. doi: 10.1002/nme.3159.
- [42] L. De Lorenzis, İ. Temizer, P. Wriggers, and G. Zavarise. A Large Deformation Frictional Contact Formulation using NURBS-based Isogeometric Analysis. *International Journal for Numerical Methods in Engineering*, 87(13):1278–1300, 2011. doi: https://doi.org/10.1002/nme.3159. URL https://onlinelibrary.wiley.com/doi/abs/10.1002/nme.3159.
- [43] N. Kikuchi and J.T. Oden. Contact Problems in Elasticity: A Study of Variational Inequalities and Finite Element Methods. Studies in Applied Mathematics. SIAM, 1988.

- [44] R.L. Taylor and O. Papadopoulos. On a Patch Test for Contact Problems in Two Dimnension. In P. Wriggers and W. Wagner, editors, *Nonlinear Computational Mechanics*, pages 690–702, Berlin, 1991. Springer-Verlag.
- [45] T.J.R. Hughes, R.L. Taylor, and W. Kanoknukulchai. A Finite Element Method for Large Displacement Contact and Impact Problems. In K.J. Bathe, J.T. Oden, W. Wunderlich, and E.L. Wilson, editors, Formulations and Computational Algorithms in FE Analysis, U.S.-German Symposium, pages 468–495. MIT Press, 1977.
- [46] J.C. Simo, T. Wriggers, and R.L. Taylor. A Perturbed Lagrangian Formulation for the Finite Element Solution of Contact Problems. Computer Methods in Applied Mechanics and Engineering, 50(2):163–180, 1985. ISSN 0045-7825. doi: https://doi.org/10.1016/ 0045-7825(85)90088-X. URL https://www.sciencedirect.com/science/article/pii/ 004578258590088X.
- [47] J.O. Hallquist. NIKE2D: An Implicit, Finite-Deformation, Finite-Element Code for Analyzing the Static and Dynamic Response of Two-Dimensional Solids. Technical Report UCRL-52678, Lawrence Livermore Laboratory, University of Carlifonia, United States, March 1979. URL https://www.osti.gov/biblio/6208469.
- [48] K.J. Bathe and A.B. Chaudhary. A Solution Method for Planar and Axisymmetric Contact Problems. *International Journal for Numerical Methods in Engineering*, 21(1):65–88, 1985. doi: 10.1002/nme.1620210107.
- [49] A.B. Chaudhary and K.J. Bathe. A Solution Method for Static and Dynamic Analysis of Three-dimensional Contact Problems with Friction. *Computers and Structures*, 24(6): 855–873, 1986. doi: 10.1016/0045-7949(86)90294-4.
- [50] A.B. Chaudhary. A Solution Method for Two- and Three-Dimensional Contact Problems. PhD thesis, Massachusetts Institute of Technology, United States, 1985.
- [51] P. Wriggers, T. Vu Van, and E. Stein. Finite Element Formulation of Large Deformation Impact-Contact Problems with Friction. *Computers & Structures*, 37(3):319–331, 1990. doi: 10.1016/0045-7949(90)90324-U.
- [52] G. Zavarise and P. Wriggers. A Segment-to-Segment Contact Strategy. Mathematical and Computer Modelling, 28(4):497–515, 1998. ISSN 0895-7177. doi: https://doi. org/10.1016/S0895-7177(98)00138-1. URL https://www.sciencedirect.com/science/ article/pii/S0895717798001381. Recent Advances in Contact Mechanics.
- [53] K.A. Fischer and P. Wriggers. Frictionless 2D Contact Formulations for Finite Deformations based on the Mortar Method. Computational Mechanics, 36(3):226-244, 2005. ISSN 1432-0924. doi: 10.1007/s00466-005-0660-y. URL https://doi.org/10.1007/s00466-005-0660-y.
- [54] K.A. Fischer and P. Wriggers. Mortar based Frictional Contact Formulation for Higher Order Interpolations using the Moving Friction Cone. *Computer Methods in Applied*

- Mechanics and Engineering, 195(37):5020-5036, 2006. ISSN 0045-7825. doi: https://doi.org/10.1016/j.cma.2005.09.025. URL https://www.sciencedirect.com/science/article/pii/S0045782505005359. John H. Argyris Memorial Issue. Part I.
- [55] P. Papadopoulos, R.E. Jones, and J.M. Solberg. A Novel Finite Element Formulation for Frictionless Contact Problems. *International Journal for Numerical Methods in Engineering*, 38(15):2603–2617, 1995. doi: 10.1002/nme.1620381507. URL https://onlinelibrary.wiley.com/doi/abs/10.1002/nme.1620381507.
- [56] R.A. Sauer and L. De Lorenzis. A Computational Contact Formulation based on Surface Potentials. Computer Methods in Applied Mechanics and Engineering, 253:369–395, 2013. ISSN 0045-7825. doi: 10.1016/j.cma.2012.09.002. URL https://www.sciencedirect.com/science/article/pii/S0045782512002769.
- [57] C. Bernardi, Y. Maday, and A.T. Patera. Domain Decomposition by the Mortar Element Method. In H.G. Kaper, M. Garbey, and G.W. Pieper, editors, Asymptotic and Numerical Methods for Partial Differential Equations with Critical Parameters, pages 269–286, Dordrecht, 1993. Springer Netherlands. doi: 10.1007/978-94-011-1810-1_17. URL https://doi.org/10.1007/978-94-011-1810-1_17.
- [58] F.B. Belgacem, P. Hild, and P. Laborde. The Mortar Finite Element Method for Contact Problems. *Mathematical and Computer Modelling*, 28(4):263–271, 1998. ISSN 0895-7177. doi:10.1016/S0895-7177(98)00121-6. URL https://www.sciencedirect.com/science/article/pii/S0895717798001216. Recent Advances in Contact Mechanics.
- [59] T.W. McDevitt and T.A. Laursen. A Mortar-Finite Element Formulation for Frictional Contact Problems. *International Journal for Numerical Methods in Engineering*, 48 (10):1525–1547, 2000. doi: 10.1002/1097-0207(20000810)48:10<1525::AID-NME953> 3.0.CO;2-Y. URL https://onlinelibrary.wiley.com/doi/abs/10.1002/1097-0207% 2820000810%2948%3A10%3C1525%3A%3AAID-NME953%3E3.0.CO%3B2-Y.
- [60] M.A. Puso and T.A. Laursen. A Mortar Segment-to-Segment Frictional Contact Method for Large Deformations. Computer Methods in Applied Mechanics and Engineering, 193(45):4891-4913, 2004. ISSN 0045-7825. doi: 10.1016/j.cma.2004.06.001. URL https://www.sciencedirect.com/science/article/pii/S0045782504002518.
- [61] B. Yang, T.A. Laursen, and X.N. Meng. Two Dimensional Mortar Contact Methods for Large Deformation Frictional Sliding. *International Journal for Numerical Methods in Engineering*, 62:1183–1225, 2005. doi: 10.1002/nme.1222.
- [62] M.A. Puso and T.A. Laursen. A Mortar Segment-to-Segment Contact Method for Large Deformation Solid Mechanics. *Computer Methods in Applied Mechanics and Engineering*, 193(6):601–629, 2004. ISSN 0045-7825. doi: 10.1016/j.cma.2003.10.010. URL https://www.sciencedirect.com/science/article/pii/S0045782503005802.

- [63] C. Weißenfels. Contact Methods Integrating Plasticity Models with Application to Soil Mechanics. Institut für Kontinuumsmechanik, Leibniz Universität Hannover. Inst. f. Kontinuumsmechanik, 2013. ISBN 978-3-941302-06-8. URL https://books.google.fr/books?id=8Lf4ngEACAAJ.
- [64] G. Zhao, W. Zhang, R.and Wang, and X. Du. Two-Dimensional Frictionless Large Deformation Contact Problems using Isogeometric Analysis and Nitsche's Method. *Journal of Computational Design and Engineering*, 9(1):82–99, 2021. ISSN 2288-5048. doi: 10.1093/jcde/qwab070. URL https://doi.org/10.1093/jcde/qwab070.
- [65] J-Y. Kim and S-K. Youn. Isogeometric Contact Analysis using Mortar Method. International Journal for Numerical Methods in Engineering, 89(12):1559–1581, 2012. doi: https://doi.org/10.1002/nme.3300. URL https://onlinelibrary.wiley.com/doi/abs/10.1002/nme.3300.
- [66] L. De Lorenzis, P. Wriggers, and G. Zavarise. A Mortar Formulation for 3D Large Deformation Contact using NURBS-based Isogeometric Analysis and the Augmented Lagrangian Method. *Computational Mechanics*, 49(1):1–20, 2012. ISSN 1432-0924. doi: 10.1007/s00466-011-0623-4. URL https://doi.org/10.1007/s00466-011-0623-4.
- [67] M. Dittmann, M. Franke, İ. Temizer, and C. Hesch. Isogeometric Analysis and Thermomechanical Mortar Contact Problems. Computer Methods in Applied Mechanics and Engineering, 274:192–212, 2014. ISSN 0045-7825. doi: https://doi.org/10.1016/j.cma.2014.02.012. URL https://www.sciencedirect.com/science/article/pii/S0045782514000693.
- [68] A. Seitz, P. Farah, J. Kremheller, B.I. Wohlmuth, W.A. Wall, and A. Popp. Isogeometric Dual Mortar Methods for Computational Contact Mechanics. *Computer Methods in Applied Mechanics and Engineering*, 301:259–280, 2016. ISSN 0045-7825. doi: https://doi.org/10.1016/j.cma.2015.12.018. URL https://www.sciencedirect.com/science/article/pii/S0045782515004247.
- [69] F. Auricchio, L. Beirão da Veiga, T.J.R. Hughes, A. Reali, and G. Singalli. Isogeometric Collocation Methods. *Mathematical Models and Methods in Applied Sciences*, 20(11): 2075–2107, 2010. doi: 10.1142/S0218202510004878. URL https://doi.org/10.1142/S0218202510004878.
- [70] F. Auricchio, L. da Veiga, T.J.R. Hughes, A. Reali, and G. Sangalli. Isogeometric Collocation for Elastostatics and Explicit Dynamics. Computer Methods in Applied Mechanics and Engineering, 249–252:2–14, 2012. doi: 10.1016/j.cma.2012.03.026.
- [71] D. Schillinger, J.A. Evans, A. Reali, M.A. Scott, and T.J.R. Hughes. Isogeometric Collocation: Cost Comparison with Galerkin Methods and Extension to Adaptive Hierarchical NURBS Discretizations. *Computer Methods in Applied Mechanics and Engineering*, 267:170–232, 2013. ISSN 0045-7825. doi: 10.1016/j.cma.2013.07.017. URL https://www.sciencedirect.com/science/article/pii/S004578251300193X.

- [72] L. De Lorenzis, J.A. Evans, T.J.R. Hughes, and A. Reali. Isogeometric Collocation: Neumann Boundary Conditions and Contact. *Computer Methods in Applied Mechanics and Engineering*, 284:21–54, 2015. doi: 10.1016/j.cma.2014.06.037.
- [73] R. Kruse, N. Nguyen-Thanh, and T.J.R. De Lorenzis, L.and Hughes. Isogeometric Collocation for Large Deformation Elasticity and Frictional Contact problems. *Computer Methods in Applied Mechanics and Engineering*, 296:73–112, 2015. ISSN 0045-7825. doi: https://doi.org/10.1016/j.cma.2015.07.022. URL https://www.sciencedirect.com/science/article/pii/S0045782515002406.
- [74] N. Nguyen-Thanh, W. Li, J. Huang, N. Srikanth, and K. Zhou. An Adaptive Isogeometric Analysis Meshfree Collocation Method for Elasticity and Frictional Contact Problems. *International Journal for Numerical Methods in Engineering*, 120(2):209–230, 2019. doi: https://doi.org/10.1002/nme.6132. URL https://onlinelibrary.wiley.com/doi/abs/10.1002/nme.6132.
- [75] V.P. Nguyen, C. Anitescu, S.P.A. Bordas, and T. Rabczuk. Isogeometric Analysis: An Overview and Computer Implementation Aspects. *Mathematics and Computers in Simulation*, 117:89–116, 2015. doi: 10.1080/17797179.2017.1354575.
- [76] M.J. Borden, M.A. Scott, J.A. Evans, and T.J.R. Hughes. Isogeometric Finite Element Data Structures Based on Bézier Extraction of NURBS. *International Journal for Numerical Methods in Engineering*, 87:15–47, 2011. doi: 10.1002/nme.2968.
- [77] M.J. Borden. Isogeometric Analysis of Phase-Field Models for Dynamic Brittle and Ductile Fracture. PhD thesis, The University of Texas, United States, 2012.
- [78] M.A. Scott, M.J. Borden, C.V. Verhoosel, T.W. Sederberg, and T.J.R. Hughes. Isogeometric Finite Element Data Structures based on Bézier extraction of T-splines". *International Journal for Numerical Methods in Engineering*, 88(2):126–156, 2011. ISSN 0029-5981. doi: 10.1002/nme.3167.
- [79] R. Dimitri. Isogeometric Treatment of Large Deformation Contact and Debonding Problems with T-splines: A Review. Curved and Layered Structures, 2(1):59–90, 2015. doi: 10.1515/cls-2015-0005.
- [80] R. de Borst and L. Chen. The Role of Bézier Extraction in Adaptive Isogeometric Analysis: Local Refinement and Hierarchical Refinement. *International Journal for Numerical Methods in Engineering*, 113(6):999–1019, 2018. doi: 10.1002/nme.5696. URL https://onlinelibrary.wiley.com/doi/abs/10.1002/nme.5696.
- [81] T.J.R. Hughes, R.L. Taylor, J.L. Sackman, A. Curnier, and W. Kanoknukulchai. A Finite Element Method for a Class of Contact-Impact Problems. *Computer Methods in Applied Mechanics and Engineering*, 8(3):249–276, 1976. doi: 10.1016/0045-7825(76)90018-9.

- [82] T. A. Laursen and V. Chawla. Design of Energy Conserving Algorithms for Frictionless Dynamic Contact Problems. *International Journal for Numerical Methods in Engineering*, 40(5):863–886, 1997.
- [83] F. Armero and E. Petocz. Formulation and Analysis of Conserving Algorithms for Frictionless Dynamic Contact/Impact Problems. Computer Methods in Applied Mechanics and Engineering, 158(3-4):269-300, 1998. doi: 10.1016/S0045-7825(97)00256-9.
- [84] J. Lu and C. Zheng. Dynamic Cloth Simulation by Isogeometric Analysis. Computer Methods in Applied Mechanics and Engineering, 268:475-493, 2014. ISSN 0045-7825. doi: 10.1016/j.cma.2013.09.016. URL https://www.sciencedirect.com/science/article/pii/S0045782513002430.
- [85] P. Otto, L. De Lorenzis, and J.F. Unger. Explicit Dynamics in Impact Simulation using a NURBS Contact Interface. *International Journal for Numerical Methods in Engineering*, 121:1248–1267, 2020. doi: 10.1002/nme.6264.
- [86] R. Vázquez, G. Sangalli, and A. Buffa. An Introduction to Isogeometric Analysis. http://www.usc.es/dmafm/eventos_organizados/texto_conferencias_cursos/RafaelVazquez/Santiago_part1.pdf, April 2019.
- [87] N.P. Khanyile, A. Alia, P. Dufrenoy, and G. De Saxcé. Bézier-based isogeometric analysis (iga) suitable for existing fe data structures. 14th WCCM and ECCOMAS Congress (Oral Presentation), January 2021. URL https://slideslive.com/38944458.
- [88] L.M. Kamoso. Intégration de la Modélisation Géométrique dans la Méthode des Éléments Finis de Frontière, Application à l'Optimisation de Forme des Pièces Tridimensionnelles. PhD thesis, Université Laval, Canada, 1999.
- [89] G.E. Farin. Curves and Surfaces for CAGD: A Practical Guide. Academic Press, San Diego, CA, 4th edition, 1996.
- [90] L. Piegl and W. Tiller. *The NURBS Book*. Monographs of Visual Communication. Springer Berlin Heidelberg, 2^{nd} edition, 1997.
- [91] Hong, D. Effects of weights in nurbs. https://citeseerx.ist.psu.edu/viewdoc/download?doi=10.1.1.538.4700&rep=rep1&type=pdf, October 2018.
- [92] Q. Hu, F. Chouly, P. Hu, G. Cheng, and S.P.A. Bordas. Skew-symmetric Nitsche's Formulation in Isogeometric Analysis: Dirichlet and Symmetry Conditions, Patch Coupling and Frictionless Contact. *Computer Methods in Applied Mechanics and Engineering*, 341: 188–220, 2018. doi: 10.1016/j.cma.2018.05.024.
- [93] J-S. Chen and H-P. Wang. New Boundary Condition Treatments in Meshfree Computation of Contact Problems. *Computer Methods in Applied Mechanics and Engineering*, 187 (3–4):441–468, 2000. doi: 10.1016/j.cma.2012.03.026.

- [94] E. Marino, J. Kiendl, and L. De Lorenzis. Isogeometric Collocation for Implicit Dynamics of Three-Dimensional Beams Undergoing Finite Motions. *Computer Methods in Applied Mechanics and Engineering*, 356:548–570, 2019. doi: 10.1016/j.cma.2019.07.013.
- [95] J. Kopacka, D. Gabriel, R. Kolman, and J. Plesek. Isogeometric contact analysis: A study of an explicit dynamic contact algorithm. In *Vypocty Konstrukci Metodou Konecnych Prvku*, Institute of Thermomechanics AS CR, v. v. i., November 2015.
- [96] V.A. Yastrebov. Introduction to Computational Contact Mechanics, February 2019.
- [97] A. Popp. State-of-the-Art Computational Methods for Finite Deformation Contact Modeling of Solids and Structuress. In A. Popp and P. Wriggers, editors, Contact Modeling for Solids and Particles, volume 585 of CISM International Centre for Mechanical Sciences (Courses and Lectures). Springer International Publishing, 2018.
- [98] A. Konyukhov and R. Izi. *Introduction to Computational Contact Mechanics*. A Geometrical Approach. John Wiley & Sons Ltd, 2015.
- [99] A. Konyukhov and K. Schweizerhof. *Computational Contact Mechanics*. Lecture Notes in Applied and Computational Mechanics. Springer, 2013.
- [100] M.A. Crisfield. *Nonlinear Finite Element Analysis of Solids and Structures*. Volume 2 : Advanced Topics. John Wiley & Sons Ltd, Chichester, 1997.
- [101] J.C. Simo and T.J.R. Hughes. *Computational Inelasticity*. Interdisciplinary Applied Mathematics. Springer, New York, 1998.
- [102] K.L. Johnson. Contact Mechanics. Cambridge University Press, 1985.
- [103] J.C. Charmet. Mécanique du Solide et des Matériaux : Elasticité-Plasticité-Rupture, May 2021. URL https://cours.espci.fr/site.php?id=318&fileid=1242.
- [104] V.L. Popov, M. Heß, and E. Willert. Handbook of Contact Mechanics: Exact Solutions of Axisymmetric Contact Problems. Springer-Verlag GmbH, Berlin, 2019. ISBN 978-3-662587-08-9. doi: 10.1007/978-3-662-58709-6.
- [105] D. Nowell, D.A. Hills, and A. Sackfield. Contact of Dissimilar Elastic Cylinders Under Normal and Tangential Loading. *Journal of the Mechanics and Physics of Solids*, 36(1): 59–75, 1988. doi: 10.1016/0022-5096(88)90020-8.
- [106] D.A. Hills and D. Nowell. Mechanics of Fretting Fatigue. Springer, Dordrecht, 1994. ISBN 978-94-015-8281-0. doi: 10.1007/978-94-015-8281-0.
- [107] J. Du and N. Olhoff. Topological Design of Vibrating Structures with Respect to Optimum Sound Pressure Characteristics in a Surrounding Acoustic Medium. *Structural and Multi-disciplinary Optimization*, 42(1):43–54, 2010. ISSN 1615-147X, 1615-1488. doi: 10.1007/s00158-009-0477-y. URL http://link.springer.com/10.1007/s00158-009-0477-y.

- [108] Z.H. Zhou, K.W. Wong, X.S. Xu, and A.Y.T. Leung. Natural Vibration of Circular and Annular Thin Plates by Hamiltonian Approach. *Journal of Sound and Vibration*, 330(5):1005–1017, 2011. ISSN 0022460X. doi: 10.1016/j.jsv.2010.09.015. URL https://linkinghub.elsevier.com/retrieve/pii/S0022460X10006206.
- [109] A. Pouladkhan. Fundamental Natural Frequency Analysis of Axisymmetric Vibrations of a Solid Circular Plate by using Ritz and FEM Methods. *Journal of Sound and Vibration*, 5(4):6, 2021.
- [110] J-J. Wu, A.R. Whittaker, and M.P. Cartmell. The Use of Finite Element Techniques for Calculating the Dynamic Response of Structures to Moving Loads. *Computers and Structures*, page 11, 2000.
- [111] B. Dyniewicz and C.I. Bajer. New Consistent Numerical Modelling of a Travelling Accelerating Concentrated Mass. World Journal of Mechanics, 02(6):281–287, 2012. doi: 10.4236/wjm.2012.26034.
- [112] E. Uzal and L.E. Sakman. Dynamic Response of a Circular Plate to a Moving Load. *Acta Mechanica*, 210(3):351–359, 2010. ISSN 0001-5970, 1619-6937. doi: 10.1007/s00707-009-0207-y. URL http://link.springer.com/10.1007/s00707-009-0207-y.
- [113] A. Alia. Simulation Numérique en Vibroacoustique et en Interaction Fluide Structure. phdthesis, Université des Sciences et Technologies de Lille, France, 2006.
- [114] A. Alia and M. Souli. Simulation of Acoustic and Vibroacoustic Problems in LS-DYNA using Boundary Element Method. In 6th European LS-DYNA Conference, Gothenburg, 2007. URL https://www.dynalook.com/conferences/european-conf-2007/simulation-of-acoustic-and-vibroacoustic-problems.pdf.
- [115] S. Kirkup. The Boundary Element Method in Acoustics: A Survey. *Applied Sciences*, 9(8), 2019. ISSN 2076-3417. doi: 10.3390/app9081642. URL https://www.mdpi.com/2076-3417/9/8/1642.
- [116] L.L. Koss and R.J. Alfredson. Transient Sound Radiated by Spheres Undergoing an Elastic Collision. *Journal of Sound and Vibration*, 27(1):59–75, 1973. ISSN 0022460X. doi: 10.1016/0022-460X(73)90035-7. URL https://linkinghub.elsevier.com/retrieve/pii/0022460X73900357.
- [117] L.L. Koss. Transient Sound from Colliding Spheres—Inelastic Collisions. *Journal of Sound and Vibration*, 36(4):555-562, 1974. ISSN 0022460X. doi:10.1016/S0022-460X(74)80121-5. URL https://linkinghub.elsevier.com/retrieve/pii/S0022460X74801215.
- [118] A. Akay and M. Latcha. Sound Radiation from an Impact-Excited Clamped Circular Plate in an Infinite Baffle. *The Journal of the Acoustical Society of America*, 74(2):640–648, 1983. ISSN 0001-4966. doi:10.1121/1.389787. URL http://asa.scitation.org/doi/10.1121/1.389787.

- [119] S. Schedin, A.O. Wåhlin, and P.O. Gren. Transient Acoustic Near Field in Air Generated by Impacted Plates. *The Journal of the Acoustical Society of America*, 99(2):700–705, 1996. ISSN 0001-4966. doi:10.1121/1.414646. URL http://asa.scitation.org/doi/10.1121/1.414646.
- [120] S. Schedin, C. Lambourg, and A. Chaigne. Transient Sound Fields from an Impacted Plates: Comparison between Numerical Simulations and Experiments. *Journal of Sound and Vibration*, 221(3):471–490, 1999. ISSN 0022460X. doi:10.1006/jsvi.1998.2004. URL https://linkinghub.elsevier.com/retrieve/pii/S0022460X98920041.
- [121] P. Troccaz, R. Woodcock, and F. Laville. Acoustic Radiation due to the Inelastic Impact of a Sphere on a Rectangular Plate. *The Journal of the Acoustical Society of America*, 108(5):2197–2202, 2000. ISSN 0001-4966. doi:10.1121/1.1312358. URL http://asa.scitation.org/doi/10.1121/1.1312358.
- [122] S. Delaye, P. Streeter, E. Morales, P. Wood, T. Senior, J. Hart, and T. Allen. Modelling the Sound of a Golf Ball Impacting a Titanium Plate. *Procedia Engineering*, 147:354–359, 2016. ISSN 18777058. doi: 10.1016/j.proeng.2016.06.309. URL https://linkinghub.elsevier.com/retrieve/pii/S1877705816307561.
- [123] T. Mase, R. Sharpe, N. Volkoff-Shoemaker, and S. Moreira. Modeling the Sound of a Golf Club Impact. Proceedings of the Institution of Mechanical Engineers, Part P: Journal of Sports Engineering and Technology, 226(2):107–113, 2012. ISSN 1754-3371, 1754-338X. doi: 10.1177/1754337112442782. URL http://journals.sagepub.com/doi/10.1177/1754337112442782.
- [124] A. Chaigne and C. Lambourg. Time-Domain Simulation of Damped Impacted Plates. I. Theory and Experiments. *The Journal of the Acoustical Society of America*, 109(4): 1422–1432, 2001. ISSN 0001-4966. doi: 10.1121/1.1354200. URL http://scitation.aip.org/content/asa/journal/jasa/109/4/10.1121/1.1354200.
- [125] F.T.K. Au and M.F. Wang. Sound Radiation from Forced Vibration of Rectangular Orthotropic Plates Under Moving Loads. *Journal of Sound and Vibration*, 281(3):1057–1075, 2005. ISSN 0022460X. doi:10.1016/j.jsv.2004.02.005. URL https://linkinghub.elsevier.com/retrieve/pii/S0022460X04001427.
- [126] L. Coox, F. Greco, O. Atak, D. Vandepitte, and W. Desmet. A Robust Patch Coupling Method for NURBS-based Isogeometric Analysis of Non-Conforming Multipatch Surfaces. Computer Methods in Applied Mechanics and Engineering, 316:235–260, 2017. doi: 10.1016/j.cma.2016.06.022.
- [127] T.J.R. Hughes. The Finite Element Method: Linear Static and Dynamic Finite Element Analysis. Prentice Hall, New Jersey, 1987.
- [128] D.W. Herrin, F. Martinus, T.W. Wu, and A.F. Seybert. A New Look at the High Frequency Boundary Element and Rayleigh Integral Approximations. In SAE 2003

- Noise & Vibration Conference and Exhibition. SAE International, May 2003. doi: https://doi.org/10.4271/2003-01-1451. URL https://doi.org/10.4271/2003-01-1451.
- [129] D.W. Herrin, F. Martinus, T.W. Wu, and A.F. Seybert. An Assessment of the High Frequency Boundary Element and Rayleigh integral Approximations. *Applied Acoustics*, 67(8):819–833, 2006. ISSN 0003682X. doi: 10.1016/j.apacoust.2005.12.006. URL https://linkinghub.elsevier.com/retrieve/pii/S0003682X06000041.
- [130] J.W. Wind and Y.H. Wijnant. Fast Evaluation of the Rayleigh Integral and Applications to Inverse Acoustics. *Journal of Physics Conference Series*, page 9, 2006.
- [131] Y. Qian and N.R. Harrisa. Direct Solution of the Rayleigh Integral to Obtain the Radiation Pattern of an Annular Array Ultrasonic Transducer. *Procedia Engineering*, 47:861–864, 2012. ISSN 18777058. doi: 10.1016/j.proeng.2012.09.283. URL https://linkinghub.elsevier.com/retrieve/pii/S1877705812043469.
- [132] A. Ross and G. Ostiguy. Propagation of the Initial Transient Noise from an Impacted Plate. *Journal of Sound and Vibration*, 301(1):28–42, 2007. ISSN 0022460X. doi:10.1016/j.jsv.2006.09.016. URL https://linkinghub.elsevier.com/retrieve/pii/S0022460X06007449.
- [133] G. Blanch. Notes on Zeros of $I_{n+1}(x)J_n(x) + J_{n+1}(x)I_n(x)$. Mathematical Tables and Other Aids to Computation, 6(37):58-61, 1952. URL http://www.jstor.org/stable/2002751.
- [134] A.W. Leissa. Vibration of Plates. N70-18461. Scientific and Technical Information Division, Office of Technology Utilization, National Aeronautics and Space Administration, Washington, 1969.
- [135] G. Noh and K.J. Bathe. An Explicit Time Integration Scheme for the Analysis of Wave Propagations. *Computers & Structures*, 129:178–193, 2013. ISSN 00457949. doi: 10.1016/j.compstruc.2013.06.007. URL https://linkinghub.elsevier.com/retrieve/pii/S0045794913001934.
- [136] L. Mahéo, V. Grolleau, and G. Rio. Numerical damping of spurious oscillations: a comparison between the bulk viscosity method and the explicit dissipative Tchamwa-Wielgosz scheme. *Computational Mechanics*, 51(1):109–128, 2013. doi: 10.1007/s00466-012-0708-8. URL https://hal.archives-ouvertes.fr/hal-00879942.
- [137] W. Kim and J.H. Lee. An Improved Explicit Time Integration Method for Linear and Nonlinear Structural Dynamics. *Computers & Structures*, 206:42–53, 2018. ISSN 00457949. doi:10.1016/j.compstruc.2018.06.005. URL https://linkinghub.elsevier.com/retrieve/pii/S0045794918302104.
- [138] K. Khorshidi. Elasto-Plastic Response of Impacted Moderatly Thick Rectangular Plates with Different Boundary Conditions. *Procedia Engineering*, 10:1742–1747, 2011. ISSN 18777058. doi:10.1016/j.proeng.2011.04.290. URL https://linkinghub.elsevier.com/retrieve/pii/S1877705811004784.

- [139] C. Lambourg, A. Chaigne, and D. Matignon. Time-Domain Simulation of Damped Impacted Plates. II. Numerical Model and Results. *The Journal of the Acoustical Society of America*, 109(4):1433–1447, 2001. ISSN 0001-4966. doi: 10.1121/1.1354201. URL http://scitation.aip.org/content/asa/journal/jasa/109/4/10.1121/1.1354201.
- [140] A.O. Wåhlin, P.O. Gren, and N-E. Molin. On Structure-Borne Sound: Experiments Showing the Initial Transient Acoustic Wave Field Generated by an Impacted Plate. *The Journal of the Acoustical Society of America*, 96(5):2791–2797, 1994. ISSN 0001-4966. doi: 10.1121/1.411285. URL http://asa.scitation.org/doi/10.1121/1.411285.
- [141] S. Kok. Geometrically Nonlinear Finite Element Analysis Including an Assumed Stress Formulation, July 2013.
- [142] A. Konyukhov and K. Schweizerhof. On the Solvability of Closest Point Projection Procedures in Contact Analysis: Analysis and Solution Strategy for Surfaces of Arbitrary Geometry. Computer Methods in Applied Mechanics and Engineering, 197(33):3045–3056, 2008. ISSN 00457825. doi: 10.1016/j.cma.2008.02.009. URL https://linkinghub.elsevier.com/retrieve/pii/S0045782508000649.